



IMPROVING TEMPERATURE CAPACITY OF TNM-BASED TiAl ALLOYS

by

Bo Liu

A thesis submitted to the University of Birmingham for the degree of
DOCTOR OF PHILOSOPHY

School of Metallurgy and Materials
College of Engineering and Physical Sciences
University of Birmingham
February 2019

UNIVERSITY OF
BIRMINGHAM

University of Birmingham Research Archive

e-theses repository

This unpublished thesis/dissertation is copyright of the author and/or third parties. The intellectual property rights of the author or third parties in respect of this work are as defined by The Copyright Designs and Patents Act 1988 or as modified by any successor legislation.

Any use made of information contained in this thesis/dissertation must be in accordance with that legislation and must be properly acknowledged. Further distribution or reproduction in any format is prohibited without the permission of the copyright holder.

Preface

This project was carried out by Bo Liu in the School of Metallurgy and Materials, University of Birmingham (from March 2015 to February 2019), under the supervision of Dr. Dawei Hu and Dr. Yulung Chiu. The present work is original and no part of this work has been submitted for a degree at any other university.

The following study has been published in Intermetallics.

Bo Liu, Jing Li, Dawei Hu, Solidification and grain refinement in Ti(48–50)Al₂Mn₂Nb₁B alloys, Intermetallics, Volume 101, 2018, Pages 99-107.

Synopsis

A TNM alloy based on the nominal composition of Ti-43.5Al-4Nb-1Mo-0.1B (at%) is the typical third-generation alloy which has been commercially tested on aero-engines. As an alloy for the production of LPT blades, the alloy must meet the requirements of forging small parts as blade preforms. The amount of stored heat energy is low during the process of extruding small diameter rods and rolling thin sheets. Thus, it is necessary that the selected alloy comes with a fine-grained, globular and isotropic casting microstructure. To realise the above microstructure, a new Ti-44.4Al-4Nb-1Mo-0.8B (at%) has been designed and heat treated.

The solidification pathway of Ti-44.4Al-4Nb-1Mo-0.8B (TNM-0.8B) follows $L+\beta\rightarrow\beta$ and avoids the peritectic solidification of $L+\beta\rightarrow\alpha$, that is, the concentration of Al is defined in the range of 39%-45%. The addition of β phase stabilising elements Nb and Mo can stabilise the β phase by extending the β phase region to higher Al contents. Also, the strength and creep resistance of TiAl alloys are significantly enhanced at high temperature, meanwhile, the corrosion and pitting resistance of TiAl alloys in some acid and neutral chloride solutions are also increased at various temperatures. With the addition of the element B, the grain size of TiAl alloys is refined significantly^[168].

Although the TNM-B alloy has been commercially tested on aero-engines, its creep resistance and mechanical properties still need to be improved for the further application in future aero-engines. The solidification pathway of most TNM alloys follows $L \rightarrow L + \beta \rightarrow \beta \rightarrow \beta + \alpha \rightarrow \alpha + \beta/B_2 + \gamma \rightarrow \alpha + \alpha_2 + B_2 + \gamma \rightarrow \alpha_2 + B_2 + \gamma$. There is a β or B_2 phase in the full temperature range. The creep resistance properties are sensitive to the size and morphology of the β/B_2 phase at colony boundaries. Thus, the manipulation of the size and morphology of the β/B_2 phase is an effective method to improve the creep resistance. The mechanical properties have been found to be sensitive to the microstructure, and the microstructure has been found to be sensitive to the heat treatment. Therefore, the control of the microstructure via heat treatment is an effective method to enhance the relative mechanical properties.

The phase diagram and different heat treatment methods have been carefully studied for manipulating the size and morphology of grain colonies. Through the heat treatment of the alloys at different temperatures and quenching conditions, the phase diagram has been mapped for the relative alloys to understand the phase transformation sequence. The effects of Continuous Cooling Transformation (CCT) and Time Temperature Transformation (TTT) on the microstructure have been studied in order to manipulate the microstructure of the alloys. The B_2 particles in aging TNM-0.8B alloys are unavoidable. However, the morphology and composition of the B_2 particles could be manipulated by

heat treatment. The uniform fully lamellar microstructure with fine lamellae in the TNM-0.8B alloy can be achieved by ageing after α phase solution treatment (1290°C 1h AC 889°C 4h AC). Compared with the original TNM-B alloy, the heat treated TNM-0.8B alloy has excellent creep resistance at the condition of 250MPa, 750°C, and the working temperature capacity has been successfully improved by adjusting the composition and heat treatment.

Acknowledgements

I am indebted to the excellent supervision, invaluable assistance and continuous encouragement from Dr. David Hu during all four years. I appreciate the opportunity to study with him and learn how to do research sensibly from him. A grateful acknowledgement to Dr. Yulung Chiu and Dr. Rengen Ding for their support and supervision of the Ph.D projects. Many thanks are expressed for the assistance of the secretarial and technical staff in the School of Metallurgy and Materials.

I wish to thank my parents, my wife X. Bai and my auntie F. Liu especially, for their constant support on finance and life, I could never be able to face the life bravely without their help. Also, a great thank is to following friends who helped me during the four years: X. Zhang, C. Li, W. Yang, Z. Pan, Z. Chen and all the office mates in 1B20.

Contents

CHAPTER 1 INTRODUCTION	1
CHAPTER 2: LITERATURE REVIEW	4
2.1 Introduction	4
2.1.1. Intermetallic Compounds	4
2.1.2 Titanium Aluminide Compounds	5
2.2 Basic Crystallography and Slip System of Titanium Aluminide Compounds	8
2.2.1 Crystallography and Slip System of Ti_3Al Intermetallic Compound	9
2.2.2 Crystallography of $TiAl$ Intermetallic Compound	9
2.2.3 Crystallography of $TiAl_3$ Intermetallic Compound	10
2.2.4 Crystallography of Borides in $TiAl$ Alloy System	10
2.3 $TiAl$ Alloy Constitution and Binary $Ti-Al$ Phase Diagram	11
2.4 Phase Transformation and Microstructure	13
2.4.1 Solidification Pathway and Ordering Transformations of $Ti-Al$ Based Alloy	13
2.4.2 β to α Transformation	14
2.4.3 Formation of Lamellar $\alpha_2+\gamma$ Colonies	20
2.4.4 Phase Transformation in Boron-containing $Ti-Al$ Based Alloy	26
2.4.5 Phase Transformation and Microstructure of the TNM alloy	29
2.5 Factors effect on $TiAl$ alloy microstructure	31
2.5.1 Heat Treatment Effect on Microstructure	32
2.5.2 Cooling Rate Effect on Microstructure	34
2.5.3 Alloy Composition Effect on Microstructure	36
2.6 Discontinuous Coarsening in Full Lamellar Microstructure	37
2.7 Mechanical Properties of $TiAl$ alloy	39
2.7.1 Deformation Mechanisms Relative to Mechanical Properties	39
2.7.2 Factors Effect on Mechanical Properties	40
2.8 TNM-B alloy Composition and the Effect	52
2.8.1 Design strategy	52
2.8.3 Microstructure and Engineering Properties	54

2.8.4 Recommended Heat Treatments for Balanced Mechanical Properties	54
2.9 Background and Aims of This Project	55
CHAPTER 3 EXPERIMENTAL METHOD AND EQUIPMENT	74
3.1 Alloys Used in This Study	74
3.2 Heat-Treatment Method and Furnace Details	75
3.3 Preparation of Specimens	77
3.4 Equipment Used for Microstructure and Crystal Structure Observation	78
3.4.1 The SEMs Used for Microstructure Observation	79
3.4.2 Equipment and Method Used for Microstructure and Crystal Structure Identification	80
3.5 Mechanical Testing	81
CHAPTER 4 THE STUDY ON PHASE DIAGRAM	86
4.1 Experimental Alloy Selection and Phase Diagram Study	87
4.2 Phase Fractions Diagram of TNM-B Alloys	87
4.3 The Assessment of α Grain Size Stability	91
4.4 Summary	92
CHAPTER 5 STUDY OF CONTINUOUS COOLING TRANSFORMATION AND TEMPERATURE TIME TRANSFORMATION	107
5.1 Continuous Cooling Transformation on TNM-B Alloy	107
5.1.1 Jominy End Quenching on Ti-44.2Al-4Nb-1Mo-0.8B and Ti-45Al-2Mn-2Nb-1B	107
5.1.2 Air and Furnace Cooling on Ti-44.2Al-4Nb-1Mo-0.8B	109
5.1.3 Interrupting Furnace Cooling Temperature Effect on Microstructure and Phase	109
5.2 Temperature Time Transformation on Ti-44.2Al-4Nb-1Mo-0.8B Alloy	111
5.2.1 Ageing with Different Times and Temperatures after Solution Heat Treatment	111
5.2.2 Double Ageing on Solution Treated Ti-44.2Al-4Nb-1Mo-0.8B Alloy	116
CHAPTER 6 β PHASE AND GRAIN BOUNDARY ANALYSIS ON TI-44.2AL-4NB-1MO-0.8B ALLOY	128
6.1 Precipitates of the β Phase in Ti-44.2Al-4Nb-1Mo-0.8B Alloy during Cooling and Ageing	128

6.1.1 Precipitation of the β Phase at Grain Boundaries and Triple Points.....	128
6.1.2 Precipitation of the β Phase in Lamellar Colonies.....	132
6.2 Analysis of Grain Boundary Morphologies.....	134
6.2.1 Coarsening of the γ Phase at the Grain Boundary	135
6.2.2 Interlocked-lamellar Colonies	136
CHAPTER 7 HEAT TREATMENT FOR THE IMPROVEMENT OF TEMPERATURE CAPACITY	158
7.1 Heat Treatment Conditions and Microstructures.....	158
7.2 Tensile Testing on Heat Treated Ti-44.2Al-4Nb-1Mo-0.8B Alloy	159
CHAPTER 8 GENERAL DISCUSSION.....	167
8.1 Study on Ti-44.2Al-4Nb-1Mo-0.8B Alloy.....	167
8.1.1 Phase Diagram of TNM-B Alloys	168
8.1.2 CCT and TTT on Ti-44.2Al-4Nb-1Mo-0.8B Alloy	169
8.2 Temperature Capacity Improvement via Heat Treatment	171
CHAPTER 9 CONCLUSIONS AND FUTURE WORK	176
9.1 Conclusions.....	176
9.2 Future Work.....	177

List of Figures

Figure 2. 1 Field of use with the temperature of Ti ₃ Al and TiAl base intermetallic as well as composites using these alloys as the matrix.[18]	57
Figure 2. 2 Crystal structure of Ti ₃ Al intermetallic alloy system, Dark black dot represents Ti atom, white circle represents Al atom.....	57
Figure 2. 3 Crystal structure of TiAl intermetallic alloy system, Dark black dot represents Ti atom, white circle represents Al atom.....	57
Figure 2. 4 Schematic diagrams of the trigonal prism stacking and resultant unit cell projections for: (a) TiB-B27, projection along [010]; (b) TiB-Bf, projection along [100]; (c) Ti ₃ B ₄ -D7b, projection along [100]; and (d) TiB ₂ -C32, projection along [0001][102]	58
Figure 2. 5 Binary Ti-Al phase diagram assessed by Schuster and palm [44]	59
Figure 2. 6 (a) Backscattered electron image for lath or plate martensite, Ti-44Al-4Nb-4Hf-0.1Si which iced-brine quenched from 1410°C, (b) backscattered electron image for acicula martensite, Ti-38Al-5V which water quenched from 1400°C[57, 58]......	59
Figure 2. 7 Basket wave microstructure of Ti-6Al-4V alloy after cooling from β phase range at the cooling rate of 99°C/s-1[179].	60
Figure 2. 8 Backscattered electrons image of the alloy Ti-45Al-7Nb-1Mo; (a) lower magnification (b) higher magnification.	60
Figure 2. 9 Morphology and crystallography of a colony of widmannstätten α plates growing method from β grain boundary.[12]	60
Figure 2. 10 (a) Schematic image of crystallographic alignment between Ti ₃ Al α_2 and TiAl γ platelets within the lamellar microstructure. (b) orientation relationships of the six rotational variants of γ lamellae with respect to the parent α_2 phase[180]......	61
Figure 2. 11 Schematic image of the transformation from α phase to γ lamellae following Denquin et. al[82]......	61
Figure 2. 12 (a) Schematic illustration of the morphology of widmannstätten lath colonies, (b) fine microstructure from aged (1300°C) feathery lamellar of Ti-46Al-8Nb (BSE image), (c) schematic illustration of the morphology of feathery structure, (d) coarsened widmannstätten lamellar microstructure of aged (1300°C) Ti-46Al-8Nb (BSE image).	62
Figure 2. 13 Schematic representation of massive gamma grains growth process [86].	62
Figure 2. 14 Back-scattered scanning electron convoluted microstructure of Ti-46Al-8Nb developed in a 20-mm diameter bar which was oil quenched from 1360 ° C and then aged for 2 h at 1320 ° C via Hu et al.[92].	63
Figure 2. 15 Distribution of TiB ₂ morphologies in Ti-(45-49) Al-(0-2) B.	63
Figure 2. 16 (a) Phase diagram of Ti-(35-50) Al-4Nb-1Mo-0.1B (b) phase fractions with temperature for the investigated alloy composition Ti-43.67Al-4.08Nb-1.02Mo-0.1B [113]......	64
Figure 2. 17 BSE image of As-cast and hot isostatically pressed TNM alloy. (a) microstructure of as-cast and hot isostatically pressed TNM alloy, coarse α_2/γ colony	

indicated by the white arrow. (b) View at a high magnification.....	64
Figure 2. 18 (a) Bi-modal (b) equiaxed (c) lamellar microstructure created by different heat treatment on α_2 phase based alloy[181]......	65
Figure 2. 19 Typical microstructures of post-hot work heat treated γ titanium aluminide alloys. (a) near γ , (b) duplex, (c) near lamellar and (d) fully lamellar[122]......	65
Figure 2. 20 Central portion of the TiAl phase diagram[115]......	66
Figure 2. 21 Micrographs of the heat treated Ti-46.8Al-1.7Cr-1.8Nb at 1380 °C for 30 min and then furnace cooled, air cooled, sand cooled, oil quenched, water quenched, and ice-water quenched [96].	66
Figure 2. 22 Schematic representation of the possible development mechanisms of lamellar microstructure[86]......	67
Figure 2. 23 Schematic sketches for Widmannstätten laths nucleation and growth via both twinning then sympathetic nucleation and sympathetic only[117].	67
Figure 2. 24 Backscattered electron morphologies of γ_f - γ_b structures and γ_f -int structures. (a) γ_f - γ_b structures from ice-water quenched and (b) γ_f -int structures in sand cooled GE alloy specimens[182]......	67
Figure 2. 25 Schematic of feathery like nucleation and growth mechanisms of (a) γ_f - γ_b structures (b) γ_f -int structures [182]......	68
Figure 2. 26 Variation of tensile ductility with temperature for varies microstructures[136].	68
Figure 2. 27 Schematic illustration of the processes determining crack propagation in a lamellar ($\alpha_2 + \gamma$) alloy at temperatures below the brittle to ductile transition temperature. (a) A crack in a macroscopic component; (b) continuum plastic zone involving enough grains; (c) crystal plasticity zone due to dislocation glide and mechanical twinning; (d) actual separation process at the atomic level[12].	69
Figure 2. 28 Curves 1: Crack growth resistance curves of investment-cast Ti-48Al-2Cr with duplex microstructure at 20 °C and 700°C, □, ○ compact tension (CT)-50 specimens with fatigue pre-cracks and displacement rates of 10 $\mu\text{m/h}$ and 600 $\mu\text{m/h}$, respectively. △ CT50 specimens with ECM-slit notch (radius -50 μm) and 600 $\mu\text{m/h}$. ◆: CT-2.6 specimen. 10 $\mu\text{m/h}$. Curves 2: KR curves of FL Ti-47Al-2.6Nb-2(Cr + V) at 20 and 800°C; displacement rate 4.2×10^{-2} /s. Data summarized by F. Apple and R. Wagner [154]......	69
Figure 2. 29 Dependence of the fracture toughness on temperature for two-phase γ -alloys with different microstructures. ■ Ti47Al-2Cr-0.2Si, lamellar microstructure ($d_L \sim 330 \text{ nm}$, $\lambda_L \sim 0.05 \text{ }\mu\text{m}$); ○ Ti-47Al-2Cr-0.2Si, near gamma microstructure ($d_\gamma \sim 11 \text{ }\mu\text{m}$); * Ti-47Al-1Cr - (Nb, Mn, Si, B), duplex microstructure ($d_\gamma \sim 30 \text{ }\mu\text{m}$, $d_L \sim 200 \text{ }\mu\text{m}$) [154]......	70
Figure 2. 30 S-N curves of a binary Ti-36.5Al alloy with a lamellar structure at different temperatures[154].	70
Figure 2. 31 S-N curves of alloys with varies microstructures [154].	71
Figure 2. 32 Dependence of the minimum strain rate on stress for different single γ -phase alloys [154]......	71
Figure 2. 33 Schematic drawing of a designed NL+ γ microstructure which can be adjusted	

by a two-step heat treatment in a forged TNM alloy (see text). The influence of the microstructural constituents on the mechanical properties is indicated [168].	72
Figure 3. 1 XRD scan result for raw alloy of Ti-44.2Al-4Nb-1Mo-0.8B. It indicates α , β and γ phases contained in this alloy.	83
Figure 3. 2 SEM images of raw alloy of Ti-44.2Al-4Nb-1Mo-0.8B under BSE mode. Three phases and boride are indicated by the red arrow.	83
Figure 3. 3 Correspondence diagram of measured temperature and reading temperature.	84
Figure 3. 4 Furnace cooling rate diagram.	84
Figure 3. 5 Dimensions of Jominy end quenching specimen.	85
Figure 4.1 Experimental quasi-binary section through the TNM alloying system by Schwaighofer et al. a) The Al-content of the Ti-43.5Al-4Nb-1Mo-0.1B alloy is indicated by a vertical line. b) Course of phase fractions with temperature for the investigated alloy composition Ti-43.67Al-4.08Nb-1.02Mo-0.1B.	94
Figure 4.2 The image of long time ageing samples, the oxide layer or oxide effect area up to 2 mm deep from outside to inside.	95
Figure 4.3 BSE images of Ti-44Al-4Nb-1Mo-0.3B and Ti-44.5Al-4Nb-1Mo-0.3B, heat treated at different temperatures and cooled by water quench.	97
Figure 4.4 BSE images of Ti-44.6Al-4Nb-1Mo-0.1B and Ti-44.2Al-4Nb-1Mo-0.8B, heat treated at different temperatures and cooled by water quench.	100
Figure 4.5 Phase diagram of Ti-44Al-4Nb-1Mo-0.3B. The area fraction represents the volume fraction, single α phase from 1270°C to 1285°C.	100
Figure 4.6 Phase diagram of Ti-45.5Al-4Nb-1Mo-0.3B. The area fraction represents the volume fraction, single α phase from 1295°C to 1350°C.	101
Figure 4.7 Phase diagram of Ti-44.6Al-4Nb-1Mo-0.1B. The area fraction represents the volume fraction, single α phase from 1270°C to 1310°C.	101
Figure 4.8 Phase diagram of Ti-44.2Al-4Nb-1Mo-0.8B. The area fraction represents the volume fraction, single α phase from 1270°C to 1300°C.	102
Figure 4.9 XRD curves for 0.8B quenched samples. The heat treatment conditions and phases are indicated in the Figure.	102
Figure 4.10 Phase diagram of Ti-44.2Al-4Nb-1Mo-0.8B, which is mapped by XRD result compared with the phase diagram mapped by area fraction.	103
Figure 5. 1 BSE images of β phase Jominy quenched 0.8B alloy, α phase Jominy quenched 0.8B alloy and 4522XD alloy. The images were taken at different distances away from the quench end, as indicated at the bottom of images.	118
Figure 5. 2 BSE mode SEM images of 0.8B alloy with different cooling rates after α phase solution treatment: (a) Air cooling with hydrofluoric (HF) acid corrosion and (b) Furnace cooling to 889°C and then air cooling.	119
Figure 5. 3 BSE mode SEM images of 0.8B alloy with interrupting furnace cooling at different temperatures after α phase solution treatment. (a) 1290°C 2h FC 1182°C AC,	

(b) 1290°C 2h FC 1085°C AC, (c) 1290°C 2h FC 987°C AC and (d) 1290°C 2h FC 889°C AC.....	120
Figure 5. 4 SEM BSE mode images of 0.8B sample heat treated with the same solution (1290°C 2h AC) and subsequently aged at different temperatures for different times.	122
Figure 5. 5 Diagram of β precipitates per 100 μm^2 grain boundary against different ageing times for 0.8B alloy aged at 792°C and 889°C.	123
Figure 5. 6 Diagram for the grain size of β precipitates against different ageing times for 0.8B alloy aged at 792°C and 889°C.....	123
Figure 5. 7 Diagram for the Vickers hardness of 0.8B samples heat treated under the condition of 1290°C 2h AC and subsequently aged at 792°C and 889°C for different times and then air cooling.	124
Figure 5. 8 SEM BSE mode images of 0.8B samples heat treated with the same solution (1290°C 2h FC 1182°C AC) but different ageing temperatures ((a),(b),(e) and (g) ageing at 792°C, (a),(b),(e) and (g) ageing at 889°C) and times (1 hour on (a) and (b), 2 hours on (c) and (d), 4 hours on (e) and (f) and 8 hours on (g) and (h))......	126
Figure 5. 9 SEM BSE images for 0.8B alloy double aged after α phase solution treatment, which (a) 1290°C 2h AC 792°C 2h AC 889°C 2h AC and (b) 1290°C 2h AC 792°C 2h AC 889°C 4h AC.....	126
Figure 6. 1 BF-STEM image from and EDS mapping for 0.8B alloy heat treated by condition of 1290°C 2h AC 889°C 2h AC.....	139
Figure 6. 2 BF-STEM image and EDS spectra from the 0.8B alloy heat treated by condition of 1290°C 2h AC 889°C 2h AC. (a) BF-STEM image showing the positions of EDS spectra. Spot A, C and B located at boride, unknown phases and γ phase respectively. (b) EDS spectra with the highest concentration of Nb, Mo and B but the lowest concentration of Al among spot A, B and C. Spot C contained a higher concentration of Nb and Mo but a lower concentration of Al than spot B.....	140
Figure 6. 3 BF-STEM image from and EDS line-scan for 0.8B alloy heat treated by condition of 1290°C 2h AC 889°C 2h AC. (a) BF-STE image showing the overview of the position for EDS line-scan. (b) EDS line-scan path way indicated by the yellow arrow, the scan started from the predicted β phase, crossed particle B and ended in the γ phase. (c) EDS line-scan results showing that the particle B might be a ω phase.	141
Figure 6. 4 (a) HAADF STEM image of grain boundary β /B2 phase precipitates (bright grain) in 0.8B alloy heat treated with 1290°C 2h AC 889°C 96h AC, and corresponding SAD patterns with a zone axis of [110] (b), [111] (c) and [131] (d) respectively. The tilting angles between (b) / (c), (b) / (d) and (c) / (d) were 35.26°, 31.48° and 29.50° respectively.	142
Figure 6. 5 Identification of ω phase precipitated in the B2 phase in 0.8B alloy heat treated with 1290°C AC 2h 889°C 2h AC. (a) BF-STEM image, (b) HAADF STEM image of the ω phase precipitated in the B2 phase, (c) HRTEM images of ω and B2 phases, (d) FFTed diffraction pattern from the ω phase, (e) FFTed diffraction pattern from the B2	

phase, (f) FFTed diffraction pattern from ω and B2 phases.	144
Figure 6. 6 (a) BF-STEM image showing the overview of the grain boundary B2 phase in heat treated 0.8B alloy (1290°C 2h AC 889°C 96h AC), (b) HAADF and (c) BF STEM images of the grain boundary B2 phase, (d) [110] SAD pattern from a grain boundary B2 phase in Figure 6.6b/c.	144
Figure 6. 7 β phase precipitates observed in long-time aged samples. The heat treatment conditions of samples were 1290°C 2h AC ageing at 889°C for (a) 4 hours, (b) 64 hours and (c) 96 hours with air cooling. (d) High magnification of (c).	145
Figure 6. 8 EDS map of the samples heat treated with 1290°C 2h AC 889°C 96h AC. Known phases were already indicated in (a).	146
Figure 6. 9 EDS line-scan result crossed β precipitates. (a) EDS line mapping started from the α_2 phase, crossed the β phase and ended in the parent α_2 phase. The scanning result is shown in (b). (c) EDS line mapping started from the γ phase, crossed the β phase, γ and α_2 lathes, and ended in the γ phase. The sample was not very stable during scanning and the real mapping track was indicated by the red arrow. The scanning result is shown in (d).	146
Figure 6. 10 EDS spot analysis at different areas of the sample heat treated by 1290°C 2h AC 889°C 96h AC. Spot 'a' and 'd' were located at lamellar β precipitates; spot 'b' and 'e' were located at the α_2 phase; spot 'c' and 'f' were located at the γ phase. Spot 'g', 'h' and 'i' were located at the grain boundary B2 phase. EDS scanning results are shown in (j).	148
Figure 6. 11 HAADF images of in-lamellar precipitated B2/ β particles. (a) B2/ β particles precipitated within α_2 lamellae and (b) B2/ β particles formed in γ lamellae.	149
Figure 6. 12 (a) [101] A SAD pattern from a B2 particle within γ lamella shown in Figure 6.11b and (b) a dark field TEM image of the B2 phase using (010) reflection.	149
Figure 6. 13 (a) HAADF STEM image of the analysed β /B2 particle (b) HRTEM image of a β /B2 particle within the α_2 lath, (c) and (d) FFTed diffraction patterns from the γ phase, the particle and two phases (the particle and neighbouring γ laths) respectively.	150
Figure 6. 14 BSE mode SEM image for (1290°C 2h AC 889°C 2h AC) 0.8B alloy, DC of the γ phase with three different morphologies were indicated in the image.	151
Figure 6. 15 BSE mode images for aged 0.8B samples after interrupting furnace cooling, the detailed heat treatment condition listed in the image.	153
Figure 6. 16 Statistics of the grain boundary γ phase and the width of the aged 0.8B samples after interrupting furnace cooling.	153
Figure 6. 17 The diagram of grain boundary γ phase volume fraction subject to aged 0.8B samples after interrupting furnace cooling and air cooling.	154
Figure 6. 18 EBSD scan of 0.8B sample treated with 1290°C 2h AC. The BSE image scan area shown in (a) and analysed grains marked with capital letters.	155
Figure 6. 19 EBSD scan of 0.8B sample treated with 1290°C 2h AC 889°C 2h AC. The BSE image scan area shown in (a) and analysed grains marked with capital letters.	157
Figure 6. 20 Feathery microstructure with around 15° angle between deviate γ lathes.	157
Figure 7. 1 BSE mode SEM images for tensile tested samples.	163

Figure 7. 2 Creep behaviour at 750°C and 250Mpa of mechanical tested samples. Corresponding microstructures were indicated in images.	163
Figure 7. 3 Low and high-magnification fracture surfaces SEM images for tensile tested samples. Interlamellar and translamellar cracking and debonding of boride were marked by black, white and red frames respectively.....	165
Figure 8. 1 Creep behaviour of the TNM-B (three black curves) and TNM-0.8B alloy (four colour curves). Reference by Figure 7.2 and Figure 8.4. [168].....	174
Figure 8. 2 Schematic CCT diagram for 0.8B alloy.....	174
Figure 8. 3 Schematic TTT diagram for 0.8B alloy.....	175
Figure 8. 4 Creep behaviour at 750°C and 185 Mpa of the TNM microstructure NL+ γ (original TNM alloy), NL+ β 1 and NL+ β 2[168].....	175

List of Tables

Table 2. 1 Crystallographic data for the four titanium boride phases ^[41]	73
Table 3. 1 Nominal and actual composition of used alloys during the study.	104
Table 4. 1 Heat treatment details of Ti-44 Al-4Nb-1Mo-0.3B and Ti-45.5Al-4Nb-1Mo-0.3B.....	104
Table 4. 2 Heat treatment details of Ti-44.6Al-4Nb-1Mo-0.1B and Ti-44.2Al-4Nb-1Mo-0.8B.....	104
Table 4. 3 The area fraction (representing the volume fraction) of the constituent phases for water quenched Ti-44Al-4Nb-1Mo-0.3B and Ti-45.5Al-4Nb-1Mo-0.3B after solution treatment.	105
Table 4. 4 The area fraction (representing the volume fraction) of the constituent phases for water quenched Ti-44.6Al-4Nb-1Mo-0.1B and Ti-44.2Al-4Nb-1Mo-0.8B after solution treatment.	105
Table 4. 5 The volume fraction table of Ti-44.2Al-4Nb-1Mo-0.8B.the result calculated by software Match automatically.....	105
Table 4. 6 Table of α grain growth stability assessment.	106
Table 5. 1 0.8B samples solution treated at 1290°C for 2 hours then air cooling, subsequently aged at 792°C and 889°C for different times then air cooling.....	127
Table 7. 1 Tensile testing condition and result for selected samples.	166

CHAPTER 1 INTRODUCTION

TiAl-based alloys have been well studied in the past 30 years. They represent a class of important high-temperature structural materials, providing excellent physical and mechanical properties that lead to substantial payoffs in the automotive industry, industrial gas turbines and aircraft engines^[1-3].

In the past few years, General Electric and Pratt & Whitney have successfully inserted TiAl-based blades into low-pressure turbines (LTP) in their commercial aero-engines. The TiAl-based application in aero-engines can save fuel and reduce the environmental impact by increasing fuel efficiency^[4]. Also, more advanced aero-engines are being designed for the requirements of further improvement on energy efficiency and environmental impact. The evolution of the LPT system is one of the critical technologies for advanced aero-engines. Moreover, the advanced aero-engines should have lighter weight but higher working temperature LPT system^[5]. The current TiAl-based LPT blade has the temperature capability up to 750°C, which is not enough to meet the requirement (up to 900°C) for the future aero-engines^[6]. Thus, it is a need for the next generation of aero-engines to improve the temperature capability of the current TiAl alloy.

Based on the commercial TNM-B alloy (Ti–43.5Al–4Nb–1Mo–0.1B, at%) on LPT of PW1100G aero-engine, the main purpose of this study is to explore how the

fine fully lamellar microstructure to improve temperature capability. In this study, the new TNM-B alloy (Ti-44.2Al-4Nb-1Mo-0.8B, at%) with the lamellar microstructure was introduced. Through the application of different heat treatment conditions in the TNM-0.8B alloy, the heat treated TNM-0.8B alloy with a fine fully lamellar microstructure was finally achieved, and it has excellent creep resistance at high temperature, which could meet the requirements of the design purpose.

In Chapter 2, a comprehensive literature review was presented, starting with a general introduction of the crystal structure of TiAl intermetallic compounds. The literature review on phase transformations and their effect on the microstructure of alloys, as well as the factors affecting mechanical properties were presented in detail. The main concern of this study is the manipulation of the phase transformation to achieve the expected microstructure and meet the required mechanical properties. The composition of the new TNM-B alloy and its effect were also described in this chapter. Finally, the background and purpose of the project were both summarised.

In Chapter 3, the alloys, experimental methods and equipments used in this research were introduced in detail. In Chapter 4, the phase diagrams of four alloys were analysed, as the phase diagram is essential to reveal the phase transformation sequence. In Chapter 5, different heat treatment conditions were

applied in the TNM-0.8B alloy, and this chapter consists of two sections considering the effect of Continuous Cooling Transformation (CCT) and Time Temperature Transformation (TTT) both on the microstructure. Factors affecting the microstructure were also summarised in this chapter. In Chapter 6, some interesting phases and their morphology were studied, as the phase or its morphology could both significantly affect the mechanical properties. The mechanical testing results were shown in Chapter 7. The samples under different heat-treatment conditions were subject to the tensile testing, and the testing results were also described in this chapter.

A general discussion was presented in Chapter 8, mainly focusing on the effect of phase transformation, CCT and TTT on the microstructure and heat treatment conditions, as the study is primarily related to these three themes. A main conclusion was shown in Chapter 9. Some future work that should be carried out was proposed for further study on the TNM-B alloys.

CHAPTER 2: LITERATURE REVIEW

2.1 Introduction

This thesis covers an experimental program aimed at the further improvement of the working temperature capacity of TNM-based TiAl alloys. The literature review focuses on the basic TiAl intermetallic knowledge, phase transformation leading to the microstructure evolution mechanism, heat treatment leading to microstructure evolution mechanism and the microstructure-property relationships of TiAl alloys. The particular TNM alloy studied with nominal composition Ti-43.5Al-4Nb-1Mo-0.1B (in at. %). The general areas cover design strategy, phase diagram, microstructure and engineering properties and recommended heat treatments for balanced mechanical properties.

2.1.1. Intermetallic Compounds

In 1967, Schulz clearly defined intermetallic compounds as the compounds of metals whose crystal structure was different from the constituent metals. They contain two or more metallic elements and can contain one or more non-metallic element^[7]. Intermetallic phases are formed when the metallic bonding between unlike metal atoms is stronger than that between like^[8].

Intermetallic compounds have better characteristics in both ceramics and metals, due to their long-range order and they have ionic, and highly directional covalent

bonds, rather than the non-direction metallic bonding of conventional metal. Depending on the difference of metal constituents, intermetallics contain both covalent and metallic bonds ^[9]. Furthermore, intermetallics are well known for their outstanding physical properties, which include high stiffness, strength and melting point, as well as being resistant to creep, oxidation and corrosion while being relatively lightweight. Their main weakness is the high cost of processing and is brittleness at room temperature. i.e., below their brittle to the ductile transition temperature, which lies between 800 and 1000°C ^[10]. Despite their weaknesses, intermetallics were used in structural applications such as in the automotive industry, space and aircraft engines, and especially in a high-performance turbine engine to reduce engine weight and increase service temperature ^[11].

2.1.2 Titanium Aluminide Compounds

In the Ti-Al system, there are three ordered titanium aluminides intermetallic compounds. They are Ti_3Al (α_2 phase); TiAl (γ phase); and TiAl_3 . TiAl -based alloys always design as two-phase alloy contain both α_2 (Ti_3Al) and γ (TiAl). Compared with monolithic constituents α_2 (Ti_3Al) and γ (TiAl), two-phase titanium aluminide alloys have much better mechanical properties, especially when the grain size and phase distribution have been suitably controlled ^[12].

2.1.2.1 Applications of Titanium Aluminide Compounds

As discussed, intermetallics can be used as the structural materials in various areas, especially in automobile, aircraft and aerospace.

In automobile industries, titanium aluminide compounds based on TiAl and Ti₃Al can be used as heat-resistant materials for engine components rotating or reciprocating at high speed, such as exhaust valves, turbocharger blades and turbine rotors. The lighter weight components is beneficial to quicker response and allow for the higher engine power output (Over 21,000rpm can be reached by TiAl rotors), this allows for the improved performance of automobiles while decreasing fuel consumption ^[13].

γ TiAl based alloys still suffer from difficult workability and manufacturing routes^[14]. However, a powder metallurgy processing route involving hot isostatic pressing (HIP) has been shown to be promising for the production of net shaped components^[15, 16].

In aircraft industries and aerospace, titanium aluminide compounds based on TiAl and Ti₃Al could be utilised, instead of nickel-based superalloys, with a working temperature range between 600 °C and 750 °C ^[17].

2.1.2.2 Basic Physical and Mechanical Properties of Titanium Aluminide Compounds

Titanium aluminide intermetallic compounds are well known for having low density, high modulus, and high tensile and creep strength in a high-temperature working environment.

Compared with other materials, TiAl based titanium aluminides are emerging as a revolutionary high-temperature material and provide a fantastic set of mechanical and physical properties, which lead to substantial payoffs in jet engines, power plant turbines and vehicle turbo wheels. Engineers have already spent more than 25 years in intensive research to introduce TiAl-based alloys into the market as engineering components ^[18]. They have outstanding mechanical and physical properties, which include: good structural stability; good resistance against corrosion; good resistance against oxidation; higher ignition temperature compared with traditional titanium alloys; , high elastic modulus (around 160GPa to 180GPa) ^[19]; high melting point (greater than 1440 °C); and low density (lower than 4.2g/cm³) ^[20]. Compared with other alloys (e.g. Steel, Al alloy, nickel-based superalloys and other Ti alloys), TiAl-based alloys widely used in temperature between 500°C and 900°C(Figure 2.1) ^[18]. However, the disadvantage of low ductility still is the biggest problem with TiAl alloy, since low ductility makes TiAl alloy brittle at room temperature. In addition

to that, TiAl-based alloys are difficultly processed into components [21, 22].

Similarly, γ -TiAl and TiAl_3 compounds also have the disadvantage of being brittle and tend to suffer from cleavage fracture. TiAl compound has the advantage of the best oxidation resistance^[23] and specific stiffness, among these three Ti-Al intermetallic compounds. Ti_3Al compound has outstanding strength to density ratio amongst these three Ti-Al intermetallic compounds, but the low creep strength and high risk of burning limit the application of the Ti_3Al compound. Similarly, to the other compounds, Ti_3Al exhibits limited ductility at room temperature, particularly in the binary state^[24, 25].

The two-phase (γ and α_2) TiAl based alloys are the most intensively studied materials, because this class of alloys have low density, high strength and modulus retention at high temperature, and some tensile ductility at room temperature. All these properties are very attractive in this new class of structural materials. TiAl based alloys can be manufactured through conventional processes, such as casting, forging, precision casting and ingot melting. Furthermore, some of them can be machined on conventional equipment at room temperature^[26, 27].

2.2 Basic Crystallography and Slip System of Titanium Aluminide Compounds

In the TiAl alloy system, there are two binary intermetallic compounds of interest.

They are a hexagonal α_2 phase with a DO_{19} structure which based on the composition of Ti_3Al ; face centred tetragonal (fct) γ phase with the $L1_0$ structure which based on the composition of $TiAl$. The further study is focused on the TNM alloy (with a nominal composition of Ti-43.5Al-4Nb-1Mo-0.1B in % (at.)) [28]. Usually, boron is always added in the TNM alloy as a grain refiner [29]. Therefore, the crystallography of Ti_3Al , $TiAl$ and borides are reviewed below.

2.2.1 Crystallography and Slip System of Ti_3Al Intermetallic Compound

As mentioned above, a Ti_3Al intermetallic compound has an ordered hexagonal crystal structure and normally referred to as α_2 phase in the $TiAl$ alloys. In this compound, twinning is not observed, and $\vec{c} + \vec{a}$ slip is not easy to occur. Furthermore, ordering reduces the likelihood of $(a/3) \langle 11\bar{2}0 \rangle$ slip on the basal plane because the movement of such a slip creates disorder. The crystal structures of Ti_3Al is shown in Figure 2.2. Ti_3Al has lattice parameters of $a = 0.575\text{-}0.577$ nm and $c = 0.462\text{-}0.48$ nm. The lattice is derived from the A3 type hcp (hexagonal close-packed) crystal structure but presents long-range order, only in the direction perpendicular to the c axis [30, 31].

2.2.2 Crystallography of $TiAl$ Intermetallic Compound

$TiAl$ intermetallic compound have a face centred tetragonal crystal structure and are normally referred to as γ phase. due to the difference between Ti and Al atomic radius, the long-range order in $TiAl$ $L1_0$ (space group $P4/mmm$, prototype

CuAu) crystal structure creates a slight tetragonal distortion in the disordered face centred cubic lattice. The lattice parameters of TiAl are $a = 0.3995\text{--}0.3997$ nm and $c = 0.4062\text{--}0.4079$ nm (Figure 2.3). The most favourable slip systems should involve Burgers vectors that correspond to the shortest translation vector in the planes and close-packed lattice planes. The perfect dislocations in $L1_0$ TiAl have the Burgers vectors $\vec{b}_{\langle 110 \rangle} = 1/2 \langle 110 \rangle$, $\vec{b}_{\langle 001 \rangle} = \langle 011 \rangle$ and $\vec{b}_{\langle 112 \rangle} = 1/2 \langle 11\bar{2} \rangle$ ^[32]. The dislocations preferentially glide on $\{111\}$ planes and have the potential to cross slip on to other low index planes^[12, 33, 34].

2.2.3 Crystallography of TiAl₃ Intermetallic Compound

Much like the simple cubic structure of CuAu₃^[9], TiAl₃ intermetallic compound shows a body-centred tetragonal structure. Yamaguchi et al. reported the major plastic deformation mode of the twinning of $\langle 111 \rangle \{112\}$ of TiAl₃ below 620°C. The structure can only provide four slip systems, thus leading to the very brittle polycrystalline specimens^[35, 36]. $[110]$, $[100]$ and $[010]$ type slips appear as augmentation of $\langle 111 \rangle \{112\}$ slip at temperature over 620°C. The observed lattice parameters of phase D0₂₂ TiAl₃ are $a = 0.384$ nm and $c = 0.858$ nm^[33].

2.2.4 Crystallography of Borides in TiAl Alloy System

There are four types of borides in equilibrium boron containing TiAl alloys. These borides are present in both α_2 and γ phase. They are TiB in B27 structure, TiB in B_f structure, Ti₃B₄ in D7_b structure and TiB₂ in C32 structure^[37-39]. In Ti-Al-B-X

alloys, there is another metastable phase in the Ti-Al-B ternary and a stable phase in quaternary and higher order Ti-Al-X-B alloys when X= Nb, Ta and Zr. This phase is in B_f structure. ^[40] These four boride phases share a common structural motif: a regular trigonal prism with one B atom at the centre and six metal atoms at the vertices. However, only TiB_2 has a hexagonal structure among them; others have the orthorhombic structures. The crystallographic structure and parameters of these four phases are summarised in Figure 2.4 and Table 2.1 ^[38, 41].

2.3 TiAl Alloy Constitution and Binary Ti-Al Phase Diagram

As the author mentioned above, there are several intermetallic phases which exist on the binary Ti-Al phase diagram. However, the recognised Ti-Al structured materials are only based on the Ti_3Al α_2 phase with the hexagonal DO_{19} structure or the TiAl γ phase with a cubic $L1_0$ structure. Furthermore, in some high-temperature engineering applications, the Ti-Al alloys contain β phase with a BCC A2 structure and its B_2 variant also play a significant role^[42]. Despite intensive research, binary phase diagrams are still the subject of controversy in recent years.

In 1987, Murry published the well-recognised binary phase diagram which has been considered useful as a standard reference since then ^[43]. Schuster and Palm reassessed the published experimental data and constituted the current

state of knowledge on the phase diagram ^[44]. See the detail phase diagram in Figure 2.5.

The above binary Ti-Al phase diagram shows the current knowledge concerning the constitution of binary Ti-Al alloys, but a specific feature of this diagram should be noted. γ (TiAl) phase Ti-Al alloys are always used as engineering alloys, with concentrations of Al usually between 44% to 48%^[45]. Depending on the cooling rate from high temperature, or after subsequent heat treatment, a variety of different phase transformations can occur. A wide range of microstructures can be obtained according to principles of solution heat treatment and subsequent ageing ^[46].

Most the engineering Ti-Al alloys are based on the γ phase and have Al content of 44-48 at.%. In order to enhance the mechanical properties, one or more elements are added to the Ti-Al alloys. Thus, the alloys can be described by the general formula of Ti-(42-49) Al-(0.1-10) X with the X such as Cr, Mn, V, Nb, W, Mo, Ta, B, and Si. As reported by Huang, additions of 2Cr, 3V and 2Mn can reduce the α transus temperature of Ti-(44-51) Al-X alloys. These elements also have a “ductilizing” effect, as reported in reference ^[47]. The TiAl alloy can achieve better oxidation resistance with the addition of element Nb, W, Mo and Ta^[47-49]. The cast TiAl alloys can be significantly refined by the B addition ranging from 0.1 to 1 at.%. Si is added to TiAl to improve the creep resistance through

precipitation hardening/microstructural stabilization^[50, 51] and oxidation resistance.

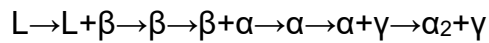
2.4 Phase Transformation and Microstructure

Melting and subsequent solidification were involved in almost all processing routes for metallic alloys. Thus, solidification determines the microstructure, texture and distribution of alloying elements in wrought, powder processing and cast alloys. During solidification, driving forces and complex heat transport or diffusion process govern the phase transformation rather than thermodynamic equilibrium^[52]. Thus, the subsequent heat treatment is needed to achieve desirable microstructure. Thus, the study on solid-state transformation is necessary.

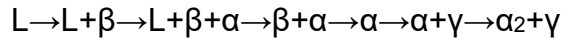
2.4.1 Solidification Pathway and Ordering Transformations of Ti-Al Based Alloy

According to the binary Ti-Al mentioned above, the existence of one (α phase) or two ($\alpha+\beta$) single phase high-temperature regions is a characteristic feature of γ (TiAl) alloys^[53]. Depending on the different concentrations of Al, several different solidification pathways will occur, according to the phase diagram in Figure 2.5 the solidification pathway can classify as the blow.

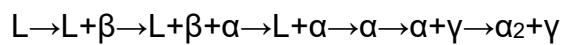
The solidification pathway of Ti-(39%-45%) Al alloys will follow:



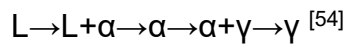
The solidification pathway of Ti-(45%-47%) Al alloys will follow:



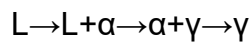
The solidification pathway of Ti-(47%-49%) Al alloys will follow:



The solidification pathway of Ti-(49%-51%) Al alloys will follow:



The solidification pathway of Ti-(51%-55%) Al alloys will follow:



The concentrations of Al in TiAl alloys play a significant role during the solidification process. If the concentration of Al lower than 49%, the first solidified solid phase is the β phase. With increasing Al content, the first solidified solid phase moves to the α phase, and then to γ phase. There are two peritectic reactions during these changes. $L + \beta \rightarrow \alpha$ and $L + \alpha \rightarrow \gamma$.

2.4.2 β to α Transformation

When the binary β solidifying γ TiAl alloy is cooled after solidification or treated

under the β phase field heat treatment, the high-temperature β phase will transform to the α phase. Depending on the different concentrations of Al and cooling rate, the transformation from β phase to α phase could be diffusion-less martensite transformation, composition invariant massive transformation involving short-range diffusion and precipitation of the Widmanstätten α transformation from β phase directly^[55].

- Martensite Transformation ($\beta \rightarrow \alpha'$ and α'')

The martensitic transformation, caused by the cooperative movement of atoms, is from the BCC to the other crystal lattice over a given volume, via a shear-type process^[56]. There are two morphologies of α' martensite: lenticular and acicular. Acicular martensite has a hexagonal close-packed structure and occurs in lower martensitic phase transformation temperature in TiAl alloys. For example, acicular martensite in Ti-38Al-5V produces by water quenching from 1400°C, as shown in Figure 2.6 (b). Lath or packet martensite in massive transformation occurs only in pure Ti or very dilute alloys, as shown in Figure 2.6 (a). Lath or plate martensite in Ti-44Al-4Nb-4Hf-0.1Si form via iced-brine quenched from 1410°C^[57, 58]. Usually, a high dislocation density and some twins come with the martensitic plates. Another martensite in TiAl alloys, named α'' martensite, can be found in higher solute content TiAl alloys. The crystal structure of α''

martensite is described as orthorhombic structure. As it lost its hexagonal symmetry, the structure is named face-centred orthorhombic structure [20, 59, 60].

The orthorhombic martensite in TiAl alloys was reported in the early 1990s by Feng et al., and treated as a phase transformation toughening mechanism since its formation was stress induced [61]. Hu et al. reported in 2015 that hexagonal martensite in a Ti-44Al-4Nb-4Hf alloy contains lenticular martensite with midribs, and its habit plane is close to {344} planes of the parent β phase. They also confirmed that continuously cooled martensitic transformation was only observed in beta (bcc) to alpha (hcp) transformation in TiAl alloys, but not in alpha (hcp) to gamma (fct) transformation [57].

- Massive Transformation from β phase to α phase

The massive transformation was occurring during cooling of crystalline materials. The crystal structure will change, but the composition will keep at a constant value during the transformation. The transformation is so-called "massive transformation" due to the appearance of the alloy phases being "blocky" or "massive" [62].

The massive transformation from β phase to the α phase occurring during cooling rate is slightly lower than those for martensitic transformation, such

as when Ti-40Al alloys are water quenched ^[63]. Compared with the precipitation reactions, the massive transformation growth kinetics are usually several orders magnitude faster, This is because there is no partition between the phase, but only short-range diffusion at the migrating interfaces takes place during the transformation ^[12].

The massive transformation from β phase to α_2 phase is never directly studied but only mentioned in the literature. As mentioned above, the β to α massive transformation occurs at cooling rate slightly lower than that for martensitic transformation. It usually occurs during water or oil quenching. However, Hu et reported the massive transformation in iced brine quenched Ti-44Al-4Nb-4Hf-0.1Si. These α_2 grains, with the $D0_{19}$ crystal structure, (the domains of massive α phase) obey no orientation relations with parent β phase. The orientation of the domains was chosen to rotate about their α -axes to minimise system elastic energy ^[57].

- β phase to Widmanstätten α phase

Upon slow cooling (i.e. slower than water or oil quenching), the β phase will transform from the β phase to Widmanstätten plates of the α phase. The α phase Widmanstätten plates precipitate from the β phase by diffusion-controlled mechanisms^[64]. The plate morphology of Widmanstätten α phase precipitates in β phase resembles the microstructure in near α or

$\alpha+\beta$ alloys, with a so-called “basket” wave microstructure^[65]. See Figure 2.8 for backscattered electrons image of basket wave microstructure, which from the arc-melted button of alloy Ti-45Al-7Nb-1Mo ^[12].

The reaction starts with the α phase nucleation and the Widmanstätten α plates precipitation mainly starts at β grain boundaries or grain boundary allotriomorphs. These α plate nucleations grow into β grains with the Burgers orientation relationship. New α colonies tend to nucleate not only on β -phase boundaries but also on boundaries of other colonies, growing perpendicularly to the existing lamellae. This leads to the formation of the ‘basket weave’ microstructure ^[66].

See Figure 2.9 for Widmanstätten α plates growing method. The Widmanstätten α lath and parent β grains have a Burgers orientation relationship of $\{110\}\beta \parallel (0001)\alpha$ and $\langle 1\bar{1}1 \rangle \beta \parallel \langle 11\bar{2}0 \rangle \alpha$.^[67]

The $\beta \rightarrow \alpha$ cooling transformation much depends on the cooling rate, Under the highest cooling rates, the α phase cannot decompose, but orders to the α_2 phase ^[63]. Many transformations and subsequent microstructure are observed when decreasing the cooling rate, such as composition invariant massive α to γ transformation; the different lamellar reaction, in which crystallographically orientated plates of the γ phase are precipitated from α phase; and α to γ transformation at very low cooling rates. ^[12, 54, 68, 69].

Also, a series of ordering transformations will occur during the cooling and heating process. Both of solid-state phase transformation form β (body centred cubic crystal structure) to α (hexagonal closed packed crystal structure) by cooling and from α to β by heating follows strict rules of burgers orientation relationship, which is: $\{110\}\beta \parallel (0001)\alpha$; $\langle 111 \rangle \beta \parallel \langle 2\bar{1}\bar{1}0 \rangle \alpha$ ^[70-72]. There are 12 possible variants of the Burgers orientation relationship relating the β matrix to the α product phase, due to each $\{110\}\beta$ plane have 2 $\langle 111 \rangle \beta$ directions and there being six $\{110\}\beta$ planes in the grains of β phase. As a result, five different rotation angles between α variants are inherited from the same parent β grain, giving angles of 90, 63.26, 60.83, 60, and 10.53 in degree ^[59, 73, 74].

The transformation from solid α phase to lamellae composing γ laths and α laths follows the rule of Blackburn orientation relationship^[75] which is $\{111\}\beta \parallel (0001)\alpha$; $\langle 110 \rangle \gamma \parallel \langle 11\bar{2}0 \rangle \alpha$. When γ precipitates from an α parent phase, a serious of complex variant and twin forms, this will state in next chapter ^[26, 76, 77].

The β to α phase transformation determines the grain/colony size of the α phase, which means it also determines the size of the final lamellar $\alpha_2+\gamma$ colonies. Furthermore, the borides can serve as nucleates to refine the grain size. Thus, the solution treatment from β phase range to the α phase provides an

opportunity to control the grain size of TiAl alloys.

2.4.3 Formation of Lamellar $\alpha_2+\gamma$ Colonies

The lamellar colonies contain $D0_{19}$ ordered hexagonal α_2 phase, and $L1_0$ ordered tetragonal γ phase. Since the α_2 phase and γ phase grow in lath and parallel to each other in each colony, they form a lamellar microstructure. The solid phase formation pathway at a medium cooling rate from α is $\alpha \rightarrow \alpha+\gamma \rightarrow \alpha_2+\gamma$ but varies with different alloy compositions^[78]. The γ lamellae formation starts in the $\alpha+\gamma$ two-phase region. The α to α_2 ordering reaction begins at the eutectoid temperature. The formation pathway of $\alpha \rightarrow \alpha_2 \rightarrow \alpha_2+\gamma$ will occur at high cooling rate in lean Al alloys, but still, lead to the same microstructure. The phase formation sequences listed above was determined by the T_0 curve to be at 44% Al in binary TiAl alloys^[77]. There is no eutectoid reaction of $\alpha \rightarrow \alpha_2+\gamma$ has been observed as a discontinuous transformation^[79].

The α phase to lamellar γ phase transformation is the process of lattice transformation from hexagonal close-packed to a face-centred tetragonal, and the composition will change via a diffusion process. The γ phase lamellae follow Blackburn's orientation relationship of $\{111\}_\gamma \parallel (0002)_{\alpha_2}$ and $\langle 1\bar{1}0 \rangle_\gamma \parallel \langle 11\bar{2}0 \rangle_{\alpha_2}$ ^[75]. The α to γ transformation proceeds via the formation of a stacking faulty in the α phase, that is formed by the splitting of a $1/3 \langle 11\bar{2}0 \rangle$ dislocated into two Shockley partials with $b=1/3 \langle 01\bar{1}0 \rangle$ and $1/3 \langle 01\bar{1}0 \rangle$. The fcc

structure is formed if stacking faults are formed on every second close-packed plane in the α phase. There are two possibilities of gliding of the partial dislocations on every even-numbered plane (AB|AB|AB|), which transforms the hcp stacking sequence ABABAB into ABCABC; or glide on every odd-numbered basal plane (A|BA|BA|B), which transforms the hcp stacking sequence ABABAB into ACBACB^[80-82]. Because of each of the two fcc orientation variants have three possible ways to align the c-axis of the $L1_0$ structure, six orientation variants of the γ phase can be ordered by the fcc phase, the orientations match Blackburn's orientation relationship of $\{111\}_\gamma \parallel (0001)_{\alpha_2}$ and $\langle 110 \rangle_\gamma \parallel \langle 11\bar{2}0 \rangle_{\alpha_2}$, and corresponds to rotations of multiples of 60° around $[0001]_{\alpha/\alpha_2}$ or $\langle 111 \rangle_\gamma$. See Figure 2.10 (a) for the schematic image of crystallographic alignment between Ti_3Al α_2 and TiAl γ platelets within the lamellar microstructure, and (b) orientation relationships of the six rotational variants of γ lamellae with respect to the parent α_2 phase. One prior α grain can only transform into one colony of $\alpha_2+\gamma$ parallel lamellae since there is only one basal plane for α and α_2 phases.

In lamellar microstructure, the interfaces of γ/γ and γ/α_2 are most often encountered. Following the orientation relationship mentioned above, three kinds of tetragonal γ/γ interfaces may occur. They are: true twin interface (rotation of 180° around $[111]$); pseudo-twin interface (rotation of 60° or 300° around $[111]$); or the domain boundaries divide single γ lamellae into domains of

different orientations, which have been found to separate by only 120° orientation variants (rotation of 0° , 120° and 240° around $[111]$) [26, 81, 83]. See Figure 2.11 for the schematic image of the transformation from the α phase to γ lamellae. (a) the growth of local face-centred cubic structure lath caused by propagation of Shockley partial dislocation. (b) $L1_0$ structure colony nucleation of orientation variants in the prenucleation fcc lath. (c) Ordered domain boundaries (odb) and anti-phase boundaries (APB) are formed inside lamellae lath with the growth of the orientation variants, true twin boundaries (TB) or pseudo-twin boundaries (PTB), which occur since the growth of the lamellae lathes results in the γ/γ lamellar interfaces. Mixed boundaries will occur if adjacent lamellae have a different stacking sequence of the close-packed planes since the anti-phase boundaries (APB) grow rapidly and lie at the other boundaries.

Zghal et al. reported the fine γ lamellae nucleation inside α grains was presumably homogenised at a temperature range of below α phase to α_2 phase ordering transition. However, most people still favour the consensus that γ lamellae are usually heterogeneously nucleated in the α phase, in particular at grain boundaries or grain boundaries allotriomorphs. Kim et al. reported that borides could act as the γ lamellae nucleation sites in 2001 [84]. The γ lamellae nucleate at a moving interface, named sympathetic nucleation, and has been observed and reported. The conclusion, summarised by Dey et al., is that γ TiAl alloys appear to be prone to sympathetic nucleation due to the anisotropic

elastic behaviour of the α phase, and the availability of low - energy interfaces between the phases [85, 86].

Both lattice transformation and diffusion are to equilibrate the composition between α/α_2 and the γ phase during the γ lamellae nucleation process. This process has been attributed to the migration of partial dislocations accompanied by diffusion [87, 88].

The lamellar microstructure can be characterised by varying structure parameters, such as the difference between colony size, the width of lamellar lathes, domain boundaries distance and α_2 volume fraction. All of these depends on the composition of the alloy and history of processing, especially regarding heat treatment temperature and cooling rate. Thus, solution treating and ageing are an effective way to get or refine the lamellar microstructure. Thermal treatment also can lead to recrystallisation and result in different microstructures, Kim summarised and reported that the microstructures of subsequently heat-treated samples are near- γ , duplex, near lamellar and full lamellar, which will be discussed later.

2.4.3.1 Feathery Structure and Widmanstätten Colonies

The characteristic alterations of the lamellar microstructure in γ TiAl alloy forms during an intermediate cooling rate from the α phase field. Widmanstätten lath colonies and feathery structure also will occur within the lamellar microstructure

as characteristic alterations. The Widmanstätten lath colonies contain α_2 and γ lamellae lathes and have a different interface orientation to the surrounding lamellae colony^[89]. The feathery structure has a similar microstructure to lamellar structure, it has the usual crystallographic-orientation relationship between the phase, but the feathery microstructure has a less than 15° misorientation concerning the surrounding lamellar lathes. See Figure 2.12 for the schematic illustration of the morphology of Widmanstätten lath and feathery structures. Hu et al. also reported the backscatter electron images for Widmanstätten lath and feathery structures^[90].

Hu et al. also reported the correlation between microstructures of Ti-46Al-8Nb and cooling rate during continuous cooling to confirm that the formation of Widmanstätten lath occurs at lower cooling rates than feathery structures.

2.4.3.2 Massive γ Phase Transformation

No composition change should take place during the massive transformation, and only short-range diffusion was required^[91]. Thus, the massive transformation is a composition invariant phase transformation that occurs discontinuously behind a migrating reaction front. The γ massive transformation has been observed by Dey et al. with sufficiently fast cooling of TiAl alloys from the α phase range, but the critical cooling rate varies with different compositions. The α phase to massive γ phase transformation in alloys of Ti-46Al to Ti-48Al have

been identified by Wu et al. [92, 93].

The nucleation of massive γ grains is a kind of heterogeneous reaction. The massive γ grains can be found at grain boundaries, grain boundary triple points, intragranular twins in the α phase, and existing lamellae or γ grains. The massive γ grains are nucleated, following Blackburn's orientation relationship, at α phase grain boundaries, and surrounding the parent α grains [94, 95]. Dey et al. reported the massively γ growth contains micro twinning of γ phase and α_2 plates. They suggested that the massive γ grains easily grow into the both of adjacent α grain and α nucleated grain after nucleation in the Blackburn orientation relationship. There is no simple orientation relationship between the massively formed γ phase and the parent α grain. This is because twinning results in the massively transformed γ phase losing the orientation relationship [96].

Furthermore, Dey et al. reported the schematic representation of a massive gamma grain growth process, as shown in Figure 2.13. The primary massive grain germinates on a favourable α grain (primary α grain) over the α/α grain boundary and follows the Blackburn orientation relationship. The first generation twins will form over the planes of the primary massive grains [86] and grow into the adjoined non-Blackburn orientation relationship α grains. The further second-generation twins will form over the $\{111\}$ planes of the first generation twins, and grow into the Blackburn orientation related B grain [97-99]. There are

misorientations between the later generated twins and the primary α grain [96].

The study of Ti-46Al to Ti-48Al by Wu and Hu at 2005, showed that the massively transformed γ phase has a larger number of faults and transformed in displacive transformation without long-range diffusion. The transformation starts from the high-temperature α phase with a sufficiently fast cooling rate (i.e. cooling rates that are faster than oil quenching but not as fast as to result in metastable α/α_2). very fine microstructure (named convoluted microstructure) consisting of fine α_2 plates within the γ matrix will be formed. See Figure 2.14 for Back-scattered scanning electron image of the convoluted microstructure.

The massive γ microstructures always contain high internal stress, because they are usually achieved by a quenching treatment. Thus, the quench cracking problems hinder the technical application of fine convoluted microstructure that develops via heat treatment in the phase of $\alpha + \gamma$ field.

2.4.4 Phase Transformation in Boron-containing Ti-Al Based Alloy

Borides will be formed in TiAl alloys with the addition of the element B, and the solidification behaviour will change with the formation of borides. Hyman et al. reported there are four distinct morphologies of (TiB_2) boride phases during the solidification of TiAl-(0-1) B. These are convoluted flakes, plates, needles, and blocky particles. The morphologies of (TiB_2) boride changes with the concentration of B and Al, see details from Figure 2.15 [100, 101].

Besides the concentration of B and Al, morphologies of (TiB₂) boride also related to the cooling rate. The morphologies of (TiB₂) boride in Ti-(45-52) Al-(0-1.6) B tend to exhibit plate and needle morphologies at slowest solidification rates. With increasing cooling rate, the morphologies of (TiB₂) boride become flakes, and finally, very fine equiaxed particles. The blocky borides nucleate and grow from the melt and are assumed to be the primary borides, which can be found in the rich B (>1 at. %) containing TiAl-B alloys. Flake, plates and needles are the secondary borides, which are concurrent with the matrix by irregular eutectic-like solidification along the L→M + TiB₂ monovariant line. They are subsequently trapped by the matrix which constrains their growth and causes them to develop anisotropic shapes [100, 101].

Boron has been identified to act as an effective grain refining alloying element in both cast and wrought TiAl alloys. The microstructure of TiAl alloys can be significantly refined, with a considerable fraction, with very little B addition (range of 0.1 to 2 at. %) during the solidification. Beside this, it has also been found to be useful concerning the hot working behaviour and the microstructure of wrought TiAl alloys. There are many studies devoted to explaining the mechanism for the grain size refinement of cast TiAl alloys. The essential reason for grain refinement of B in TiAl is the partitioning behaviour of boron between the solid phase and liquid phase. When the concentration of B in TiAl alloys is lower than 0.003 or equal to 0.011 at % [102], the boron can be dissolved in α_2

(Ti_3Al), and γ TiAl phase at room temperature respectively but there is a very low solubility B₂ phase. For example, there is about 0.1% boron solubility in the β phase even at the solidification temperature ($>1500^\circ\text{C}$ for Ti 44Al 8Nb 1b), and it forms to thin curvy boride in the interdendritic liquid of Ti-(43-45) Al-(5-8) Nb with a higher than 0.1% boron addition. The grain refinement study has been linked to the solidification path of these alloys since 2007. Since the previous studies have almost no dedicated effort to investigate grain refinement mechanisms, most of them have not been purposely verified by designed experiments. Hu continued to study and summarised the new grain refinement mechanism following the solidification path. The grain refinement study covered three solidification pathways, which are $\text{L} \rightarrow \beta$, $\text{L} + \beta \rightarrow \alpha$ and $\text{L} \rightarrow \alpha$, and varies with Al concentration ^[103]. A Ti-(<44.8)Al alloy with 0.1% B addition follows the solidification pathway $\text{L} \rightarrow \beta \rightarrow \alpha$. Boride precipitates will act as inoculants to help α phase nucleate if the boride precipitates during the $\text{L} \rightarrow \beta$ transformation ^[104]. The primary solidification phase is either borides or metallic phases depends upon the concentration of B in Ti-(43-52) Al-B alloys. The dividing value is close to 1% of B and being slightly reduced with increasing Al. The titanium boride is the primary solidification phase when concentration of B is higher than 1%^[101, 105], otherwise metallic β or α phase and titanium boride is the primary solidification phase. The boron will refine the lamellar colony size via titanium boride precipitates' inoculation of α phase ^[106-108].

For most studied B refinement TiAl alloys the primary solidification phase is β or α , the concentration is no more than 1%. The grain refinement has been found to closely related to solid β phase in alloys with Al concentration up to 45%, the refinement in β solidifying alloys was achieved during β to α solid transformation rather than the solidification^[104, 108]. The already existing boride precipitates that stimulate α phase nucleation and Burgers α variants generation, to achieve the fine α grains and transform to fine lamellar colonies. For some high-Nb containing alloys, the critical concentration of B is as low as 0.1%. the excess B forms boride particles from the liquid in the interdendritic area, resulting in the non-burgers β to α transformation. Thus, the extra boron does not lead to significant further reduction in grain refinement^[106-109].

2.4.5 Phase Transformation and Microstructure of the TNM alloy

Typical TNM alloy Ti-43.5Al-4Nb-1Mo-0.1B (at. %) ^[1, 110], based on γ phase TiAl and with multi-phases, is β solidifying TiAl alloys. With the addition of β stabilisation elements (such as Mo and Nb), the rough transformation pathway of Ti-43.5Al-4Nb-1Mo-0.1B is $L \rightarrow L+\beta \rightarrow \beta \rightarrow \beta+\alpha \rightarrow \alpha+\beta/B_2+\gamma \rightarrow \alpha+\alpha_2+B_2+\gamma \rightarrow \alpha_2+B_2+\gamma$ ^[111]. See detailed phase diagram of TNM alloys in Figure 2.16. Besides the addition of Mo and Nb, a small amount of B has also been added in the alloy to refine the microstructure and to achieve a balance of mechanical properties via subsequent heat treatment. At the normal cooling condition (air cooling). The

primary solidification phase of TNM alloy is still metallic phase, rather than borides, as the boron concentration is low. with the continuous cooling, the primary β phase precipitated via $L \rightarrow L + \beta$ firstly, then, the $L + \beta$ phase transform to fully β phase. The single β phase transform to α phase massively and $\alpha + \beta$ phase exist the alloy at the same time. The $L1_0$ structure γ TiAl phase comes out via diffusion-controlled precipitation during the further cooling^[112]. Depending on the cooling rate, γ phases with different morphologies of globular or lens-shaped, can be obtained in the β phase. Ordered α_2 -Ti₃Al and B₂-TiAl with D0₁₉ and B₂ structure with ω phase or their derivatives can be observed at room temperature [104, 113, 114].

The TNM alloy is commonly manufactured via cast/HIP. Thus, the microstructure after HIPing is the starting microstructure for the subsequence heat treatment. The microstructure of TNM alloy after HIPping is a near lamellar γ microstructure. See Figure 2.17 for more details. There are many coarse-grained α_2/γ colonies embedded in some otherwise fine-grained matrixes. The size of these coarse-grained α_2/γ colonies size is different from 30 μm to 150 μm . The reaction within the α_2/γ colonies, according to $\alpha \rightarrow \beta + \gamma$, took place during the HIPing process. This decomposition reaction will lead to the thickness increasing in γ lamellae, as well as to the formation of secondary precipitates of the B₂-phase (B₂, sec) within the α_2/γ colonies.

The typical microstructure of cast/HIP TNM alloy is ordered B₂-phase decorated on lamellar colony boundaries and globular γ grains decorated on B₂-phase grain boundaries. Furthermore, small (<10 nm) ω domains can be detected in B₂-phase phase by XRD [113].

2.5 Factors effect on TiAl alloy microstructure

Titanium aluminide alloys have been classified into three groups by the diversity of phases. They are single γ phase alloys; single α_2 phase alloys; and dual phase alloys. As shown in the previous diagram, when the concentration of Al more than 50% in TiAl alloys, the single γ phase alloy exist. The microstructure for this alloy composition is characterised by equiaxed γ grains causing poor ductility and fracture toughness, therefore, causing it to be neglected in the engineering industry. When the concentration of Al lower than 40% in TiAl alloys, the single α_2 (Ti₃Al) phase alloys exist, which exhibits better ductility at room temperature. However, the ductility is still unacceptable form an engineering standpoint. With the addition of the high amount of Nb (more than 10%), the low Al concentration (lower than 40%) alloys can also transform to dual phase ($\alpha_2+\gamma$) alloys and exhibit a range of desirable properties. Three microstructures can form in this kind alloys, which are full bi-modal, equiaxed and lamellar. See Figure 2.18 for the details of these microstructures. These kinds of alloys have been neglected in engineer industry due to the disadvantage in density

corrected strength compare with the Ni-based alloys and conventional TiAl alloys [115].

When the concentration of Al in TiAl alloys is between 40% and 48.5%, the dual phase $\alpha_2+\gamma$ phase alloys exist. Depending on the heat treatment condition, the microstructures of the dual phase titanium aluminides have been broadly classified into four categories: near γ ; duplex; near lamellar; and fully lamellar (Figure 2.19). As the microstructure is closely related to the mechanical properties, the duplex and fully lamellar microstructure exhibit more balanced mechanical properties, applicable to a range of commercial applications [46].

2.5.1 Heat Treatment Effect on Microstructure

As mentioned above, the dual phase titanium aluminide can be classified into four categories, which are near γ , duplex, near lamellar and fully lamellar.

When Ti (40-48.5) Al alloy is heat treated at the temperature (T_4 in Figure 2.20) which is in the $\alpha_2+\gamma$ phase field, the near γ microstructure is formed. On average, the grain size for this microstructure is usually between 30 μm to 50 μm . The microstructure is shown in Figure 2.19 a and is characterised by many relatively small α_2 -Ti₃Al grains located at coarse equiaxed γ -TiAl grain boundaries.

When Ti (40-48.5) Al alloy is heat treated at the temperature (T_3 in Figure 2.20), the duplex microstructure has been formed. The grain size for this microstructure

(both lamellar grains and γ grains) is about 10 μm on average. The microstructure shown in Figure 2.19 b is characterised by uniform α colonies along with equiaxed γ grains. Due to the heat treatment temperature, both of the $\alpha+\gamma$ phase field and α/γ volume ratio are very close to 1 for Ti48Al alloys, and the existing α_2 particles will dissociate. The γ phase continues to reduce in volume until the equilibrium volume fraction is reached and grain growth occurs. The dispersed α phase will limit the growth of γ grains, causing the grain size of the duplex microstructure to be smaller. TiAl alloys with duplex microstructures always have high tensile strength and ductility but have the disadvantage of poor fracture toughness and low creep strength.

When Ti (40-48.5) Al alloy is heat treated at temperature T_2 in Figure 2.20 which is higher than duplex microstructure forming temperature, the α grains will coarsen and finish the formation of the near-lamellar microstructure. The grain size for near-lamellar microstructure is usually between 150 μm to 200 μm on average. The microstructure (as shown in Figure 2.19 c) is characterised by a majority of lamellar colonies with some equiaxed γ grains. Near-lamellar microstructure contains equiaxed γ phase and $\alpha_2+\gamma$ lathes (lamellar grains). The $\alpha_2+\gamma$ lathes in lamellar grains follow Blackburn orientation relationship.

When Ti (40-48.5) Al alloy is heat treated above α transus temperature (T_1 in Figure 2.20), which is in the α phase field, the α_2 and γ lathes transform from α

phase, and these lathes obtain a fully lamellar morphology (as shown in Figure 2.19 d) during cooling to room temperature. The lamellar microstructure always coarsens, and the colony size is in the range of 200 μm to 1000 μm .

2.5.2 Cooling Rate Effect on Microstructure

Variants of the γ based microstructure can be generated via heat treating TiAl based alloys in single α phase followed by subsequent cooling at a different rate. Microstructure, such as lamellae, Widmanstätten laths, massive γ grains and feathery like blocks, can be observed alone or coexisting in the TiAl alloys [86, 116]. Hu et al. reported all these microstructures when studying Ti-46Al-8Nb in 2005. The Ti-46Al-8Nb Jominy bar quenched form after a solution treatment temperature of 1360°C, is in the α phase field. Dey et al. also reported and summarised the detail work on Ti-46.8Al-1.7Cr-1.8Nb as shown in Figure 2.21, The microstructure only contains coarse equiaxed lamellar grains, Widmanstätten laths and feathery like blocks in the lamellar microstructure, when increasing the cooling rate to the intermediate rate (1380°C 0.5h sand cooling or air cooling). Feathery structures coexisting with γ massive grains will be generated upon increased cooling rate (1380°C 0.5h oil, water quenching). Finally, γ massive grains along the prior α/α boundaries, together with residual α_2 phase, will result from the fastest cooling rates (1380°C 0.5h ice water quench). Thus, in general, the microstructure of lamellar grains, Widmanstätten laths,

feathery like structure and γ massive grains can be controlled by controlling the cooling rate. Furthermore, depending on the cooling rate they can be observed in TiAl alloys separately or together [117].

Lamellar grains can be observed in slow to fast cooled samples, ranging from furnace cooling to sand cooling. There are 6 γ variants in lamellar structures. The lamella width will decrease when increasing the cooling rate [82, 118, 119].

As mentioned above, lamellar grains can be generated in a range of cooling rate: the higher the cooling rate, the shorter the width of lamella lath. At higher cooling rates (sand cooling), the greater amount of undercooling leads to a higher driving force. The γ lamellae preferentially nucleate at the boundaries of untransformed α phases. During the $\alpha \rightarrow \alpha_2 + \gamma$ transformation, $\gamma/\alpha_2/\gamma$ interfaces are generated, and higher amounts of α_2 and fewer γ/γ interfaces are observed in alloys cooled at higher rates (sand cooling). The nucleation and growth process could be termed as growth by continuous nucleation (Figure 2.22 a). On the other hand, at the very slow cooling rates (furnace cooling), a lower driving force leads to a lower energy transformation. Less energy is need when nucleating at α/γ interfaces, unlike nucleating at the boundaries of untransformed α phase. Therefore, new γ lamellae nucleate over the laterally growing interfaces of the existing γ lamellae, during the stage of subsequent primary γ nucleated and its growing stage (Figure 2.22 c). At a slower cooling

rate (between furnace cooling and sand cooling), the γ growth is more likely to occur due to nucleation of another γ lamella with face to face true relationship, since the face-to-face true twin interface provides minimum interfacial energy among three γ/γ interface types. The new γ lamella is thinner than the primary γ lamella, caused by the lower temperature and later of nucleation. The nucleation and growth process could be termed as growth by twin generation (Figure 2.22 b) [82, 86].

2.5.3 Alloy Composition Effect on Microstructure

Much like the different heat treatments on one TiAl alloy can generate various microstructures, same treatment on TiAl alloys with different compositions will generate various microstructures [113]. Most of the as-cast TiAl alloys have lamellar microstructure, but third phases such as β or B_2 will introduce in the microstructure with the addition of large amount β -stabilizing elements. There are many β -stabilizing elements in TiAl alloys (such as Nb, Ta, W, Zr, Mo etc.) and different elements have varied β stabilising strength. Alloying effect on the phase transformation and microstructures have been much less studied than their effect on mechanical properties, and the effects alloying has on mechanical properties will be discussed later [54, 120]. The details of refinement mechanisms and phase transformation path of TNM-B alloys have been discussed before [38, 41].

Beside β stabilising elements and B, another set of α/α_2 stabilising elements such as O, N, C etc. also affect the phase transformation and microstructure. As the α/α_2 stabiliser elements in TiAl alloys, the oxygen solubility in α_2 phase can be as high as 10% to 15%, far more than the oxygen solubility in γ phase (0.025% to 0.05%). Higher oxygen content always results in higher α_2 volume fraction [85, 102, 121].

2.6 Discontinuous Coarsening in Full Lamellar Microstructure

The fully lamellar microstructure is essential for improvement of the fracture toughness and high temperature creep resistance of TiAl alloy. But the lamellar microstructure becomes unstable and lamella coarsening occurs at high temperature, the lamella coarsening can degrade the creep resistance significantly^[122, 123]. The discontinuous coarsening (DC) plays the dominant role below the eutectoid temperature in low Al content (<45% at. %) TiAl alloys^[124].

The DC proceeds via lamellar colony boundary migration leaving behind coarser lamellae. The DC cells nucleate randomly and homogeneously within lamellae or along the lamellar colony boundaries, and grow into the neighbouring lamellae or lamellar colonies at the expense of its fine lamellae. The driving force of the coarsening is mainly derived from the reduction on primary lamella interfacial energy and the chemical free energy.

Three types of morphology can be observed in discontinuously coarsened

lamellar structures. (a) A coarsened lamellar structure, which has the same lamellar direction as the original primary lamellae. The crystallographic orientation of the α_2 plates is the same as that of the original primary lamellae, and the interfaces of coarsened lamellae are the low energy habit plane. (b) A coarsened lamellae structure with irregular faceted interfaces, which have the same crystallographic orientation of α_2 plate as that of the original primary lamellae, but have a different lamellar direction as the original primary lamellae. The interfaces of coarsened lamellae are the high energy faceted rather than the low energy habit plane. This type of coarsened lamellae typically located at the adjacent primary lamellae are nearly perpendicular to the boundaries, and lamellar colony boundaries were nearly parallel to the secondary lamellae. (c) Coarsened lamellae without any orientation relationship to the primary lamellae. Furthermore, the crystallographic orientation of α_2 plate is different from that in the original primary lamellae, and the coarsened lamellae are considered to be formed by the α_2 plates re-precipitation with different variants with respect to the γ {111} planes. This type of lamella uses the low energy habit plane as their lamellar interfaces [68].

Upon the study of DC in Ti-(40-45) Al (soaked at 1000°C after solution heat treatment). The content of Al and DC are related, the Ti-44Al represent the most content of DC. Either a small amount of Si addition or slower cooling after α solution treatment can result in the remarkable improvement of the stability of

the primary lamellar structure, thereby can avoid the DC in TiAl based alloys at high temperature^{[125] [124]}.

2.7 Mechanical Properties of TiAl alloy

2.7.1 Deformation Mechanisms Relative to Mechanical Properties

TiAl alloys always have limited ductility and damage tolerance, and research on deformation properties of TiAl has been done in an attempt to improve these disadvantages. The deformation mechanisms for $\alpha_2+\gamma$ alloys at room temperature can be summarised as follows. The deformation is mainly confined to the γ (TiAl) phase rather than the microstructure (lamellar, equiaxed or other) ^[126, 127]. The γ (TiAl) deforms by octahedral glide of octahedral dislocation and super dislocation. The glide of octahedral dislocation follows the Burgers vector $\vec{b}=1/2\langle 110 \rangle$, and super dislocations follow the Burgers vectors $\vec{b}=\langle 101 \rangle$ and $\vec{b}=1/2\langle 11\bar{2} \rangle$. Another potential deformation mode is mechanical twinning along $1/6\langle 11\bar{2} \rangle\{111\}$. The alloy composition decides the dominant deformation mode. For $\alpha_2+\gamma$ alloys at room temperature, the primary deformation mode is ordinary dislocation glide, followed by mechanical twinning in the γ phase. The α_2 phase has localised glide which resulted in prism glide of $1/3\langle 11\bar{2}0 \rangle$ super dislocation ^[128, 129]. The deformation of $\alpha_2+\gamma$ alloys is much easier at elevated temperature. At elevated temperature, around 700°C to 800°C, γ phase deformation still plays the main roles rather than the α_2 phase. γ phase deformed by ordinary climb

dislocation and intensive mechanical twinning. The plasticity of α_2 phase has been enhanced, so significant glide can occur in the prismatic and pyramidal glide. In summary, these dislocations make the deformation of $\alpha_2+\gamma$ alloys much easier and ensure strain continuity ^[130].

TiAl alloy deformation is not only relative to the high intrinsic glide resistance and the plastic anisotropy but also impeded by the various interfaces occurring in the lamellar morphology. Perfect and twinning partial dislocation can overcome these interfaces. The barrier strength of an interface depends on its character and interface type. The α_2/γ boundaries provided the highest barrier strength. The barrier strength of the lamellae gives rise to an athermal stress part that is almost independent of temperature. Thus, strengthened $\alpha_2+\gamma$ TiAl alloys can be achieved by lamellar spacing refinement ^[99, 131, 132].

2.7.2 Factors Effect on Mechanical Properties

2.7.2.1 Tensile Properties

The tensile properties of two-phase γ TiAl alloys vary depending mainly on the microstructure and the grain size, and, to a lesser extent on the alloy composition. The tensile plastic elongation of two-phase γ TiAl alloys at room temperature ranges from 0.4% to 3.5%, the yield strengths vary from 350 MPa to 650 MPa at room temperature, and ultimate strength ranges from 400 MPa to 720MPa at room temperature ^[133-135].

The tensile strength is inversely proportional to the grain size square rooted, and the formula of yield stress is given by $\sigma = \sigma_0 + k_y / \sqrt{D}$. σ_0 is a materials constant for the starting stress for dislocation movement (or the resistance of the lattice to dislocation motion). K_y is a material constant (measures the difficulty of slip penetrates from one grain to the next), and D is the grain size, or the length of the dislocation slip path. Therefore, the tensile property for two-phase γ TiAl alloys is strongly dependent on the grain size or morphology of the phases. The duplex microstructures have the best ultimate tensile strengths, ductility and yield stress, with higher tensile elongations associated with the smaller grain size [136, 137]. The grain size in forged γ TiAl alloys with duplex microstructures varies from 10 μ m to 40 μ m. The tensile elongation ranges between 2% to 4% depending on alloy composition, interstitial impurity level and heat treatment processes [138].

Fully lamellar microstructures always have large grain size, thus generally exhibit poor ductility and lower strength at room temperature. Kim et al. reported that better strength and ductility could be achieved via decreases in the grain size and lamellar spacing of the lamellae [139]. However, the relationship mentioned above between ductility and lamellar colony size in wrought lamellar TiAl alloys is not always strictly followed in cast lamellar TiAl alloys. Hu et al. studied cast lamellar Ti-44Al-4Nb-4Hf-0.1Si-0.1B with different thermal processing conditions, and the tensile ductility of these fine-grained alloy with

fine boride precipitates was less than 0.45% ^[140]. The powder metallurgy processed two-phase γ TiAl alloys always has fine grain size and homogeneous microstructures, and are reported to have better strength and ductility than wrought and cast alloys. The superior properties were observed mainly in alloys that had been processed via a hot extruded powder metallurgy process, giving a lamellar structure. The influence of HIPing temperature on mechanical properties was smaller than the after-heat treatment, as heat treatment after HIPing could change fractions of lamellar colonies, lamellar spacing and grain size, which change both the strength and ductility of the alloy ^[141, 142].

Tensile properties of two-phase γ TiAl alloys are also significantly associated with the alloy composition. Same microstructure alloys with added elements of Nb, V, Mo, Ta, Zr, Hf and W could significantly increase tensile strength due to solid solution strengthening, whereas Cr, Mn and V improved the ductility ^[143, 144].

For polysynthetically twinned crystals, their tensile properties strongly depend on the angle θ between lamellar plane $\{111\}$ and loading axis ^[145]. When θ is 0° , the polysynthetically twinned crystals exhibited a good balance of strength and ductility (5 - 10 % at room temperature). When θ at 90° the polysynthetically twinned crystals exhibit the highest strength but the very poor ductility (almost 0). When the angle of θ is between 30° to 90° , ductility is relative to the volume of α_2

phase, since slip within α_2 is required [145].

Tensile ductility changes in two-phase γ TiAl alloys are characterised by a brittle to the ductile transition temperature. The brittle to ductile transition temperature varies depending on the microstructure, from 620 °C to 800 °C at low strain rates (lower than 10⁻⁴/s). The brittle to ductile transition temperature is highest for fine lamellar microstructure, and lowest for near γ and duplex microstructure. The ductility increases very slowly and tends to a constant below the brittle to the ductile transition temperature. however, once temperature increases above the brittle to the ductile transition temperature it increases steeply. From the study by Appel et al., the ductility of fine lamellar, near γ and fine-grained duplex microstructures commonly exceed 30% once over the brittle to the ductile transition temperature, which indicates creep strength being a problem. See Figure 2.26 for more details [136].

2.7.2.2 Fracture Toughness

The fracture behaviour of two-phase TiAl alloys is governed by several processes that occur over a wide range of length scales. The length scales encompass the various microstructural length scales that are associated with the cracked sample geometry, lamellar colonies, individual lamella, dislocations to twins as illustrated in Figure 2.27.

The crack tip stress distribution dependeds on the material properties when a

macroscopic distance from the crack tip applied imposed loading, and the resulting stress is greatly magnified in the crack tip region (Figure 2.27.a). The stress – intensity factor K describe the strength of the singularity, and K decays as the inverse square root of the distance r from the crack. The formula of K is $k = \sigma_a \sqrt{\pi a_c}$, where σ_a is the stress that acts perpendicular to the crack plane, and $2a_c$ is the crack length. The framework of this model is the resistance to crack growth only arises from the produced surface energy^[146]. The effects of microstructure become important at the smaller length scale which shows in Figure 2.27.b. Phase distribution and morphology of the constituents, crack interaction with phase and grain boundaries, lamellar spacing, and the elastic and plastic anisotropy of the constituents, will affect the fracture behaviour. These interactions will give rise to stress and strain fluctuations, and the fracture resistance is sensitive to the microstructure as the wavelengths are comparable to the grain or colony size. The overwhelming part of fracture characterisation in TiAl alloys has been performed at this mesoscopic scale. The influence of dislocation glide and mechanical twinning becomes noticeable at the finer scale, which is shown in Figure 2.27.c. The energy was needed for propagating and multiplying the dislocations with the crack advances. The dislocations and twins may play an ambivalent role in the fracture process. Local stress levels produced by dislocation pile-ups or immobilised twins may exceed the cohesive strength and cause crack nucleation. On the other hand, local dislocation and

twin plasticity may shield and blunt crack tips so that the crack driving force is reduced. Fracture in crystalline metals rarely occurs via cleavage when there is large-scale plasticity. The crack propagates by stretching and breaking individual bonds between the atoms at the atomic scale (Figure 2.27.d). The process may exhibit a significant crystallographic anisotropy, depending on the strength and directionality of the atomic bonding. The crack growth and failure in TiAl alloys are determined by various processes that occur on length scales ranging from the component dimensions down to the atomic level. It is the interaction of all these processes that determine if crack advance occurs and how much energy is dissipated along the crack path ^[12].

The yield point of metals will decrease, but the plastic deformation will increase when the alloys are in a high-temperature environment. Thus, energy dissipation by plastic deformation becomes more important for higher test temperatures during crack propagation.

Fracture resistance (K_R) curves have been frequently analysed on the fracture behaviour of TiAl alloys. The Figure 2.28 shows the K_R curves of Ti-48Al-2Cr and Ti-47Al-2.6Nb-2(Cr+V) with the corresponding microstructure of duplex and fully lamellar at different temperatures^[122, 147]. Under plain strain conditions, the initiation value is corresponding to the fracture toughness K_{IC} . At the room temperature, the Duplex microstructure materials show the brittle behaviour with

little resistance to crack growth or to tear, the behaviour revealed from the running almost flat of K_R values in the diagram. Depending on the volume of lamellar and γ colonies, the values of fracture toughness for the fine-grained duplex microstructure ranging from 10 $\text{MPa}\sqrt{m}$ to 16 $\text{MPa}\sqrt{m}$. The fully lamellar microstructure materials are suggested cracking initiation to be followed by stable crack growth, the behaviour revealed from the raising K_R values in the diagram. Depending on the randomised orientation of lamellar colonies, the values of fracture toughness of lamellar microstructure ranging from 20 $\text{MPa}\sqrt{m}$ to 40 $\text{MPa}\sqrt{m}$ [122]. The fracture toughness is found to increase continuously for all microstructures and alloys with the increasing the temperature (Figure 2.29). However, the fully lamellar microstructure exhibits better fracture toughness than duplex and near gamma alloys even though its dependence of KIC on temperature is less pronounced [136, 147].

There are lots of studies regarding the relationship between fracture toughness and lamellar alloys. The lamellar microstructure has a better fracture toughness and more stable crack growth behaviour. With the further study in cast and powder metallurgy alloys, the fracture toughness increases by increasing the lamellar colony size and decreasing lamellar spacing in general [139, 142, 148, 149]. Trans-lamellar fracture and decohesion of lamellar colonies are the main fracture mechanisms in lamellar alloys, whereas intergranular fracture and cleavage are the dominant fracture mechanisms during interfacial delamination in the duplex

microstructure.

In a lamellar microstructure, the fracture toughness can be improved by the presence of un-cracked ligaments bridging in the crack wake, which shield the crack tip from the far field loading. β -stabilizers (such as Cr or Nb) could lead to a three-phase microstructure, and the presence of a ductile β/B_2 phase may also contribute to the fracture toughness [150, 151].

2.7.2.3 Fatigue

Engineering application of TiAl alloys involves components that are subjected to fluctuating or cyclic loading. The fluctuating stresses produce cumulative damage and can lead to failure without warning. Fatigue cracks may grow when the crack driving force is much smaller than that is needed for the same crack to grow under monotonic loading. Therefore, the fatigue properties of TiAl alloys have an important implication on life prediction and design. Based on the relative sizes of the elastic and plastic components of the strain, two types of fatigue are usually distinguished. They are high cycle fatigue (HCF) and low cycle fatigue (LCF). The fluctuations in load and strain are relatively small in HCF, but the number of cycles during component life is measured in millions. The HCF will happen if the component vibrates. The fluctuations in load and strain are larger in LCF. LCF is a progressive failure phenomenon brought about by cyclic strains that extend into the plastic range. The LCF will happen when an aircraft takes off

or lands for example.

The fatigue life of TiAl alloys in the HCF range is usually displayed on a plot of cyclic stress level versus the logarithmic life and normally called S-N curves. The S-N curves of a binary Ti-36.5Al alloy with a lamellar structure at different temperatures as shown in Figure 2.30 ^[152]. Regardless of temperature, the fatigue life of Ti-36.5Al alloy has characterised by flat S-N curves. Thus, the number of cycles to failure is sensitive to the applied stress. The fatigue resistance is relatively insensitive to test temperature range room temperature to 800°C. Larsen and co-workers also reported the more S-N curves of alloys with various microstructures as shown in Figure 2.31 ^[153]. The result shows that S-N curve is strongly dependent on the microstructure. However, the fatigue stress at 10^7 cycles is higher than 75% of the ultimate tensile stress. This means the maximum applied stress during fatigue loading is higher than the TiAl yield stress of the alloy even at low-stress ratios ^[154].

Fatigue crack growth in γ based TiAl alloys is generally very rapid at low and intermediate temperatures. The Figure 2.30 shows the crack growth rate for alloys with different microstructures at various stress intensity. Normally, alloys with coarse lamellar microstructures exhibited superior FCG resistance than alloys with duplex microstructures for TiAl alloys with more than 5mm crack, which is attributed to the beneficial shielding effect from crack deflection. The

fatigue crack growth rate in TiAl alloys extremely depends on the cyclic stress intensity. The fully lamellar microstructure exhibits a less steep slope and higher fatigue crack growth threshold. Its FCG resistance consistent with the R-curve behaviour under monotonic loading. here is no improvement in fatigue performance with the refinement in lamellar colony size or lamellar spacing. Furthermore, there is no significant fatigue growth resistance difference between lamellar and duplex microstructures for TiAl alloys with 10 to 300 μ m cracks [155, 156].

Reported by Hénaff, the low cycle fatigue of TiAl alloys relates to composition and microstructure. Same grain size lamellar microstructure presented a better resistance than duplex microstructure. So far the highest resistance is observed for the low aluminium sample, with the finest lamellar microstructure [154]. The life of TiAl components under LCF is relatively insensitive to temperature and is largely determined by the amount of inelastic strain in each cycle. Cyclic softening occurs at an elevated temperature and cyclic hardening at room temperature. Also, stress-induced phase transformation will happen during the LCF in two-phase $\alpha_2+\gamma$ alloys, which will lead to significant structural change. The phase transformation is coupled with dynamic recrystallisation and degrades the lamellar morphology at high temperature [157].

Cyclic temperature changes also affect fatigue property. Changes in temperature

with cyclic strains and stresses can lead to thermomechanical fatigue (TMF). There are two types TMF regimes, which are: in-phase TMF, which implies that the maximum normal strain and the maximum temperature occur simultaneously; and out of phase TMF, which implies that the maximum normal strain coincides with the minimum temperature. Compare with isothermal LCF, in-phase thermomechanical fatigue leads to longer fatigue life, whereas out of phase TMF have the shortest life ^[158, 159]. Furthermore, In-phase TMF leads to negative mean stresses and out of phase TMF leading to positive (tensile) mean stresses. The generation of the mean stresses is attributed to cyclic softening and hardening, and independent of the microstructure. The generation of mean tensile stresses and oxidation will result in short fatigue life for out of phase TMF in a high-temperature environment. During the low- temperature tensile cycle, the oxide layer was thought to provide crack nucleation sites ^[159].

2.7.2.4 Creep Properties

Creep resistance and structural stability are important prerequisites for high-temperature application of TiAl alloys. The microstructure has a strong effect on the creep behaviour in TiAl alloys. Fully lamellar microstructure provides the best creep resistance. For the same alloy, the full lamellar microstructure reduces strain rates by at least one order of magnitude compared to a duplex microstructure. In broad terms, the fine spacing of lamellar reduces

the effective slip length for dislocations and twins, compared to that in the duplex and equiaxed microstructures [22, 133, 160].

Appel et al. summarised the effects of the lamellar morphology on the creep resistance as follows [12]:

Under low stress and temperature conditions, the creep curves of lamellar alloys are similar to those of single phase γ alloys as shown in Figure 2.32.

When γ grains are present along the colony boundaries, the minimum creep rate of lamellar alloys tends to increase, as a result of the dynamic recrystallisation occurring in these γ grains.

When the colony size of lamellar alloys is more than $100\mu\text{m}$, the creep rate is dependent on serrated colony boundaries rather than the colony size. The serrations result from incursions of lamellae into neighbouring colonies.

Higher creep resistance of lamellar microstructure can be achieved via lamellar spacing refinement, and lamellar spacing is sensitive to cooling rate.

The minimum creep rate is insensitive to the proportion of α_2 phase in Ti-(44-48) Al.

Oriented PST crystals show a significant anisotropy to creep resistance, and the creep resistance was found to be lowest for the 45° orientation and highest for

the 0° orientation of the lamellae against the compression axis.

The minimum creep rate of lamellar alloys increases progressively with stress.

Overall, the factors that mainly effect creep resistance are the thickness of lamellae, lamellar colony orientation concerning the loading axis, the volume of colony boundaries and colony size (less than 100µm).

2.8 TNM-B alloy Composition and the Effect

In the past few years, lowering impact on the environment by increasing fuel efficiency and reducing exhaust gases has been the main target in research. TNM based TiAl blades in LPT were successes used in PW1100G (Ti-43.5Al-4Nb-1Mo-0.1B in at.%) aero-engines by Pratt & Whitey. As the thesis focus on the TNM-B based alloy, the details/characteristic for TNM-B based alloys in the thesis covers design strategy, phase diagram, microstructure and engineering properties and recommended heat treatments for balanced mechanical properties summarised here again^[1].

2.8.1 Design strategy

TNM based alloy always contain Al concertation at 43.5% in at% to ensure a solidification follows $L+\beta\rightarrow\beta$ for achieving fine-grained, globular and isotropic casting microstructure^[161, 162].

A significant fraction of the dis-ordered β phase could suppress grain growth in the course of the hot working process or heat treatment process within the region of $\alpha+\beta$ phase field.

Minimal fractions of the ordered β_o phase needed are required in order embrittlement at room temperature but reduce creep resistance at elevated temperature [163-166].

Designed TNM TiAl have to meet the industrial feasibility, which means, small variations in the chemical alloy composition and the component geometry should be less sensitive to phase transition temperatures and phase volume fractions [167, 168].

Designed TNM TiAl must have a stability microstructure during long term exposure at a working temperature in the range of 600°C to 750°C [168].

Nb and Mo used for extending the β phase field region to higher Al contents. Also, the room temperature ductility of alloy will increase, the oxidation resistance will increase, and solid-state diffusion process will retard with the addition of Nb. High-temperature strength and creep resistance increased with the addition of Mo and Nb [169, 170].

Element B was always added in TNM alloys for refining grain size since [171] there is a remarkably coarser as-cast microstructure without the addition of B [29, 170].

For further improvement of the high-temperature capability, the yield strength and creep resistance can be significantly improved by adding C and Si [168, 172].

2.8.3 Microstructure and Engineering Properties

Alloys with NL microstructures and coarse-grained FL microstructures exhibit a relatively high fracture toughness and creep resistance, but poor tensile ductility and strength especially at room temperature [136, 170].

Depending on the cooling rate, the creep and tensile strengths are sensitive to the α_2/γ lamellar spacing [12, 173].

A specific microstructure concept of an NL microstructure established for TNM alloys exhibits a balanced mechanical property. The size of equiaxed α_2/γ colonies is ranging from 50 μm to 100 μm , with fine lamellar spacing, small amount globular γ and B_2 grains located at the grain boundaries and triple points [12, 174].

The influence of the microstructural constituents on the mechanical properties as shown in Figure 2.33 [16, 168, 175].

2.8.4 Recommended Heat Treatments for Balanced Mechanical Properties

By ignoring the homogenization treatment, the TNM alloys consist of two heat treatment steps.

The first step consists of annealing at high temperature, minimisation of the β/β_2 phase by heating the alloy to $\alpha+\beta+\gamma$ phase or $\alpha+\beta$ phase field followed by cooling at a balance cooling rate.

The second step consists of a continuous heating ramp or an isothermal stabilisation annealing between 850 and 950°C. The γ phase fraction is increasing with the form of the ultrafine lamellae during the annealing and leading to a significant increase in hardness [176-178].

2.9 Background and Aims of This Project

TiAl blades in LPT were successfully used in GENx (Ti-48Al-2Nb-2Cr) and PW1100G (TNM) aero-engines by General Electric and Pratt & Whitey. The GENx-1b engine contains two stages (stage6 and 7) of TiAl LPT blades. Compare with the prior engines in the same class. The GENx-1b engine delivers an 80% reduction in NOX emissions, a 50% reduction in noise and a 20% reduction in fuel consumption^[1, 168].

For developing future highly efficient engines, Geared Turbofan (GTF) has been designed and manufactured. The key component of GTF engine is the reduction gearbox that de-couples the fan from the turbine, that is low speed for the fan but high speed for the LPT. Due to the faster rotating LPT, the third-generation blade material used must be of higher strength, able to withstand higher mechanical loading and able to work at higher temperature up to range 650°C to 800°C.

The main aim for this project is trying to improve the temperature capacity of Ti-43.5Al-4Nb-1Mo-0.1B alloy. Compare with the commercial used Ti-43.5Al-4Nb-1Mo-0.1B alloy, the new alloy should achieve the target of better mechanical properties in the higher temperature (750°C to 850°C.) working environment by adjust the alloy composition and heat treatment.

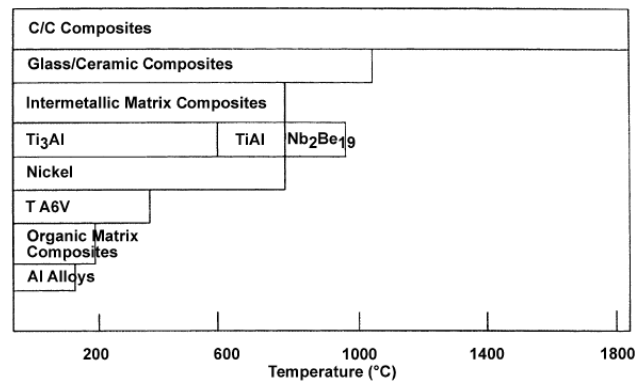


Figure 2. 1 Field of use with the temperature of Ti₃Al and TiAl base intermetallic as well as composites using these alloys as the matrix.^[18]

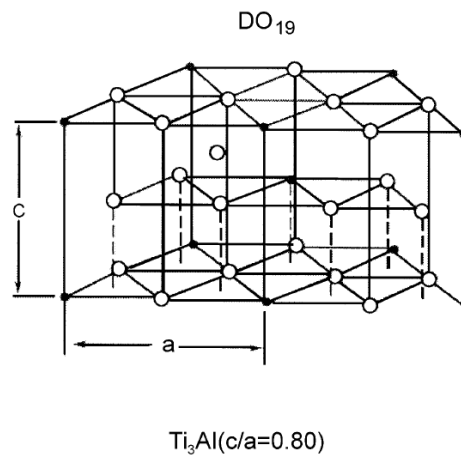


Figure 2. 2 Crystal structure of Ti₃Al intermetallic alloy system, Dark black dot represents Ti atom, white circle represents Al atom.

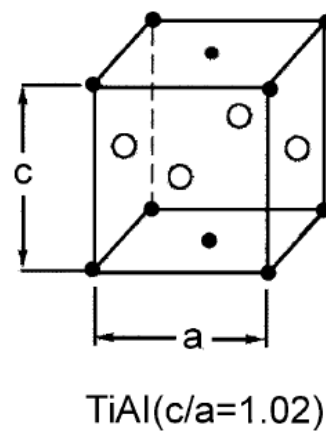


Figure 2. 3 Crystal structure of TiAl intermetallic alloy system, Dark black dot represents Ti atom, white circle represents Al atom.

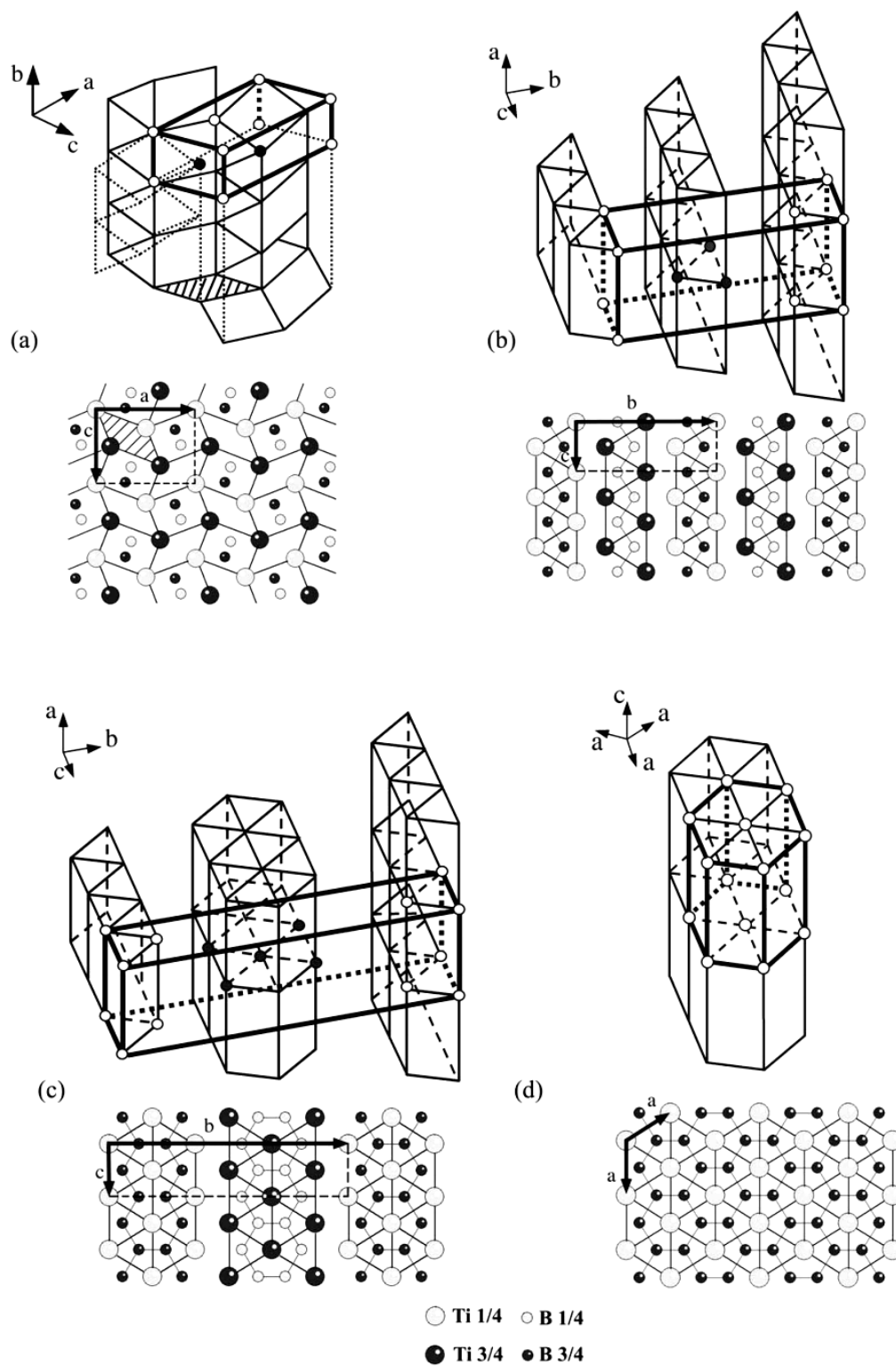


Figure 2. 4 Schematic diagrams of the trigonal prism stacking and resultant unit cell projections for: (a) TiB-B27, projection along $[010]$; (b) TiB-B₆, projection along $[100]$; (c) Ti₃B₄-D7_b, projection along $[100]$; and (d) TiB₂-C32, projection along $[0001]$ ^[102]

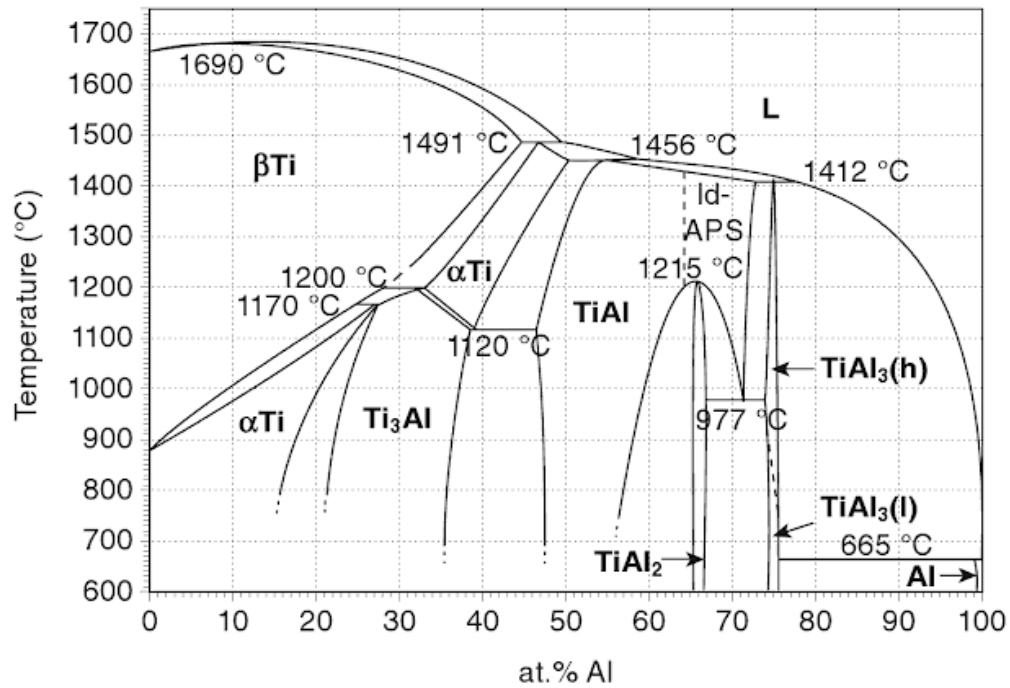


Figure 2. 5 Binary Ti-Al phase diagram assessed by Schuster and palm ^[44]

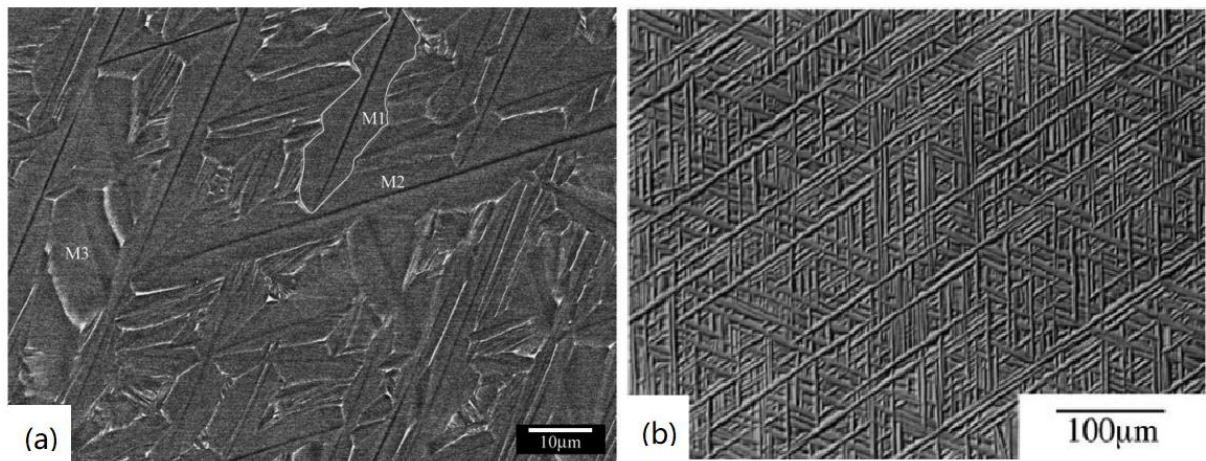


Figure 2. 6 (a) Backscattered electron image for lath or plate martensite, Ti-44Al-4Nb-4Hf-0.1Si which iced-brine quenched from 1410°C, (b) backscattered electron image for acicula martensite, Ti-38Al-5V which water quenched from 1400°C^[57, 58].

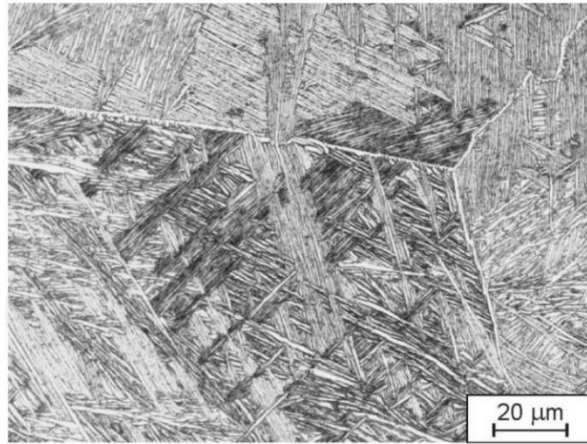


Figure 2. 7 Basket wave microstructure of Ti-6Al-4V alloy after cooling from β phase range at the cooling rate of $99^{\circ}\text{C/s}^{-1}$ [179].

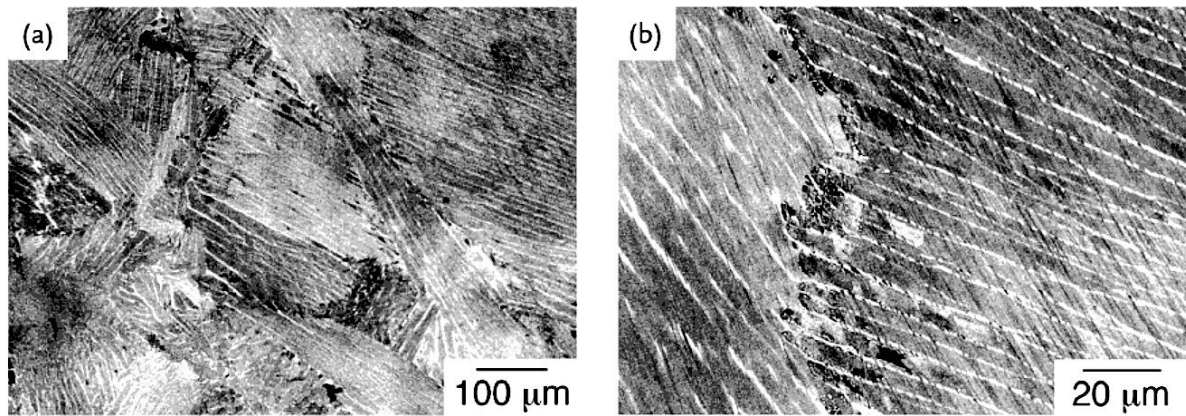


Figure 2. 8 Backscattered electrons image of the alloy Ti-45Al-7Nb-1Mo; (a) lower magnification (b) higher magnification.

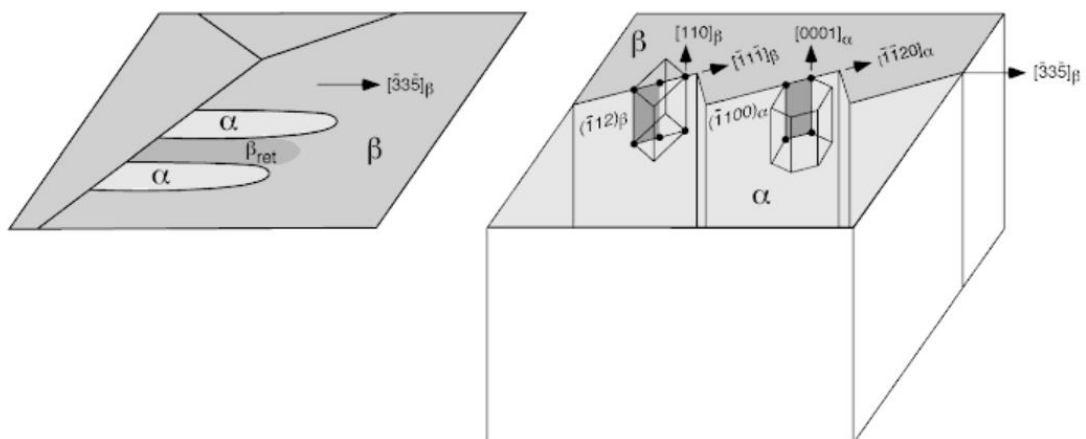


Figure 2. 9 Morphology and crystallography of a colony of Widmannstätten α plates growing method from β grain boundary.^[12]

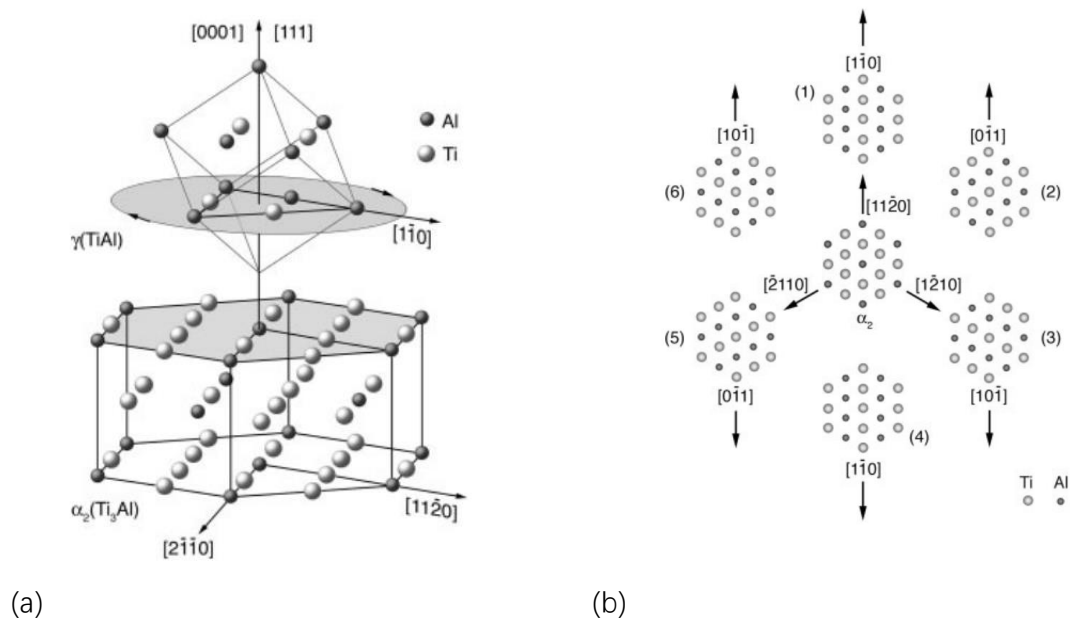


Figure 2. 10 (a) Schematic image of crystallographic alignment between Ti₃Al α_2 and TiAl γ platelets within the lamellar microstructure. (b) orientation relationships of the six rotational variants of γ lamellae with respect to the parent α_2 phase^[180].

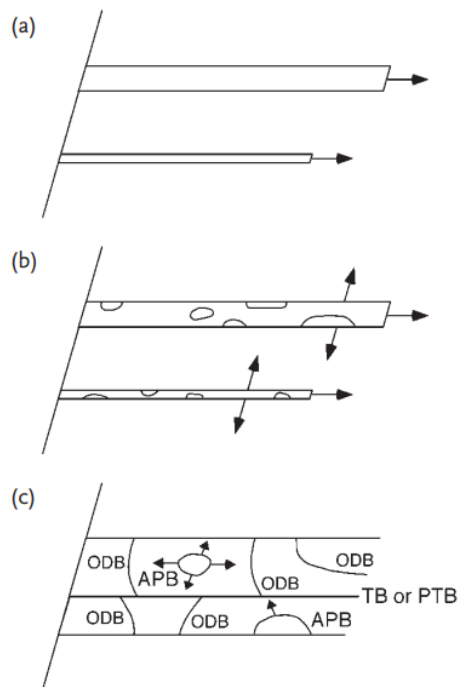


Figure 2. 11 Schematic image of the transformation from α phase to γ lamellae following Denquin et. al^[82].

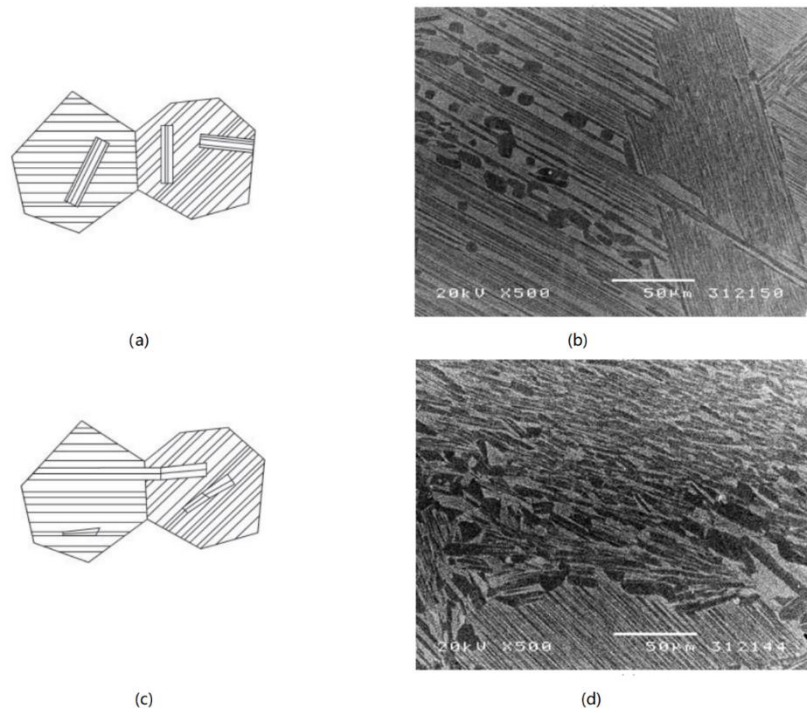


Figure 2. 12 (a) Schematic illustration of the morphology of widmannstätten lath colonies, (b) fine microstructure from aged (1300°C) feathery lamellar of Ti-46Al-8Nb (BSE image), (c) schematic illustration of the morphology of feathery structure, (d) coarsened widmannstätten lamellar microstructure of aged (1300°C) Ti-46Al-8Nb (BSE image).

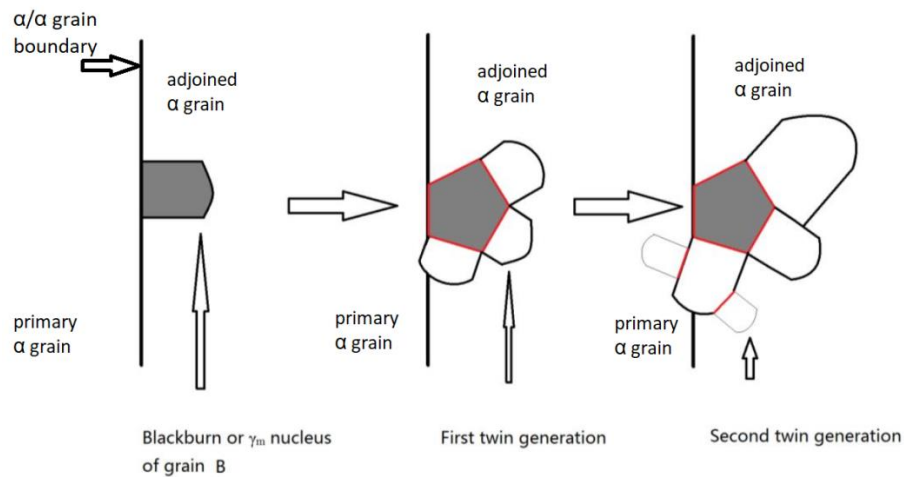


Figure 2. 13 Schematic representation of massive gamma grains growth process ^[86].

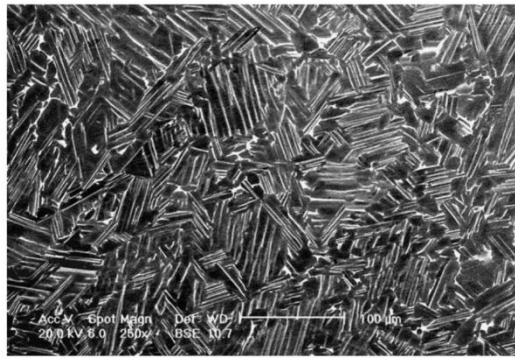


Figure 2. 14 Back-scattered scanning electron convoluted microstructure of Ti-46Al-8Nb developed in a 20-mm diameter bar which was oil quenched from 1360 ° C and then aged for 2 h at 1320 ° C via Hu et al.^[92].

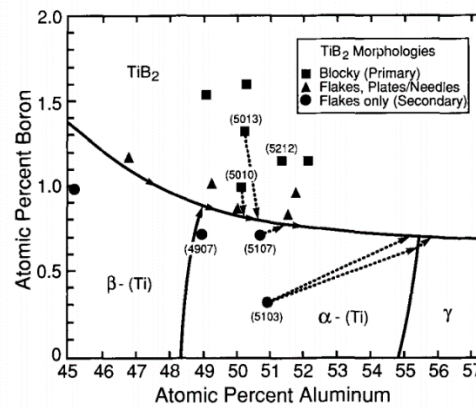


Figure 2. 15 Distribution of TiB₂ morphologies in Ti-(45-49) Al-(0-2) B.

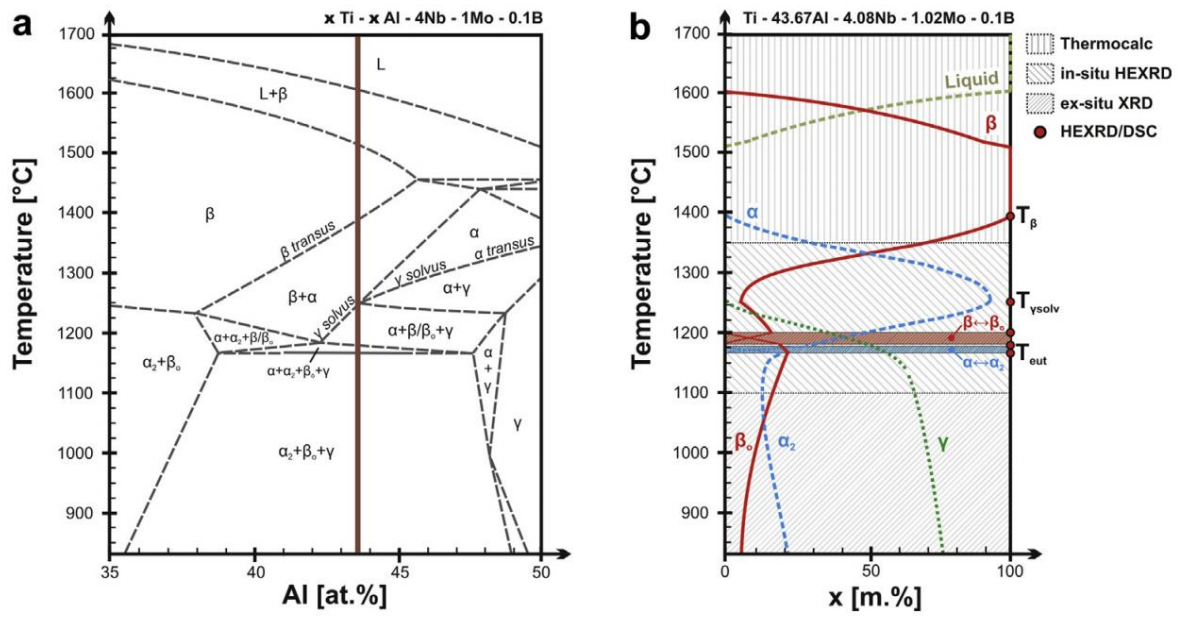


Figure 2. 16 (a) Phase diagram of Ti-(35-50) Al-4Nb-1Mo-0.1B (b) phase fractions with temperature for the investigated alloy composition Ti-43.67Al-4.08Nb-1.02Mo-0.1B ^[113].

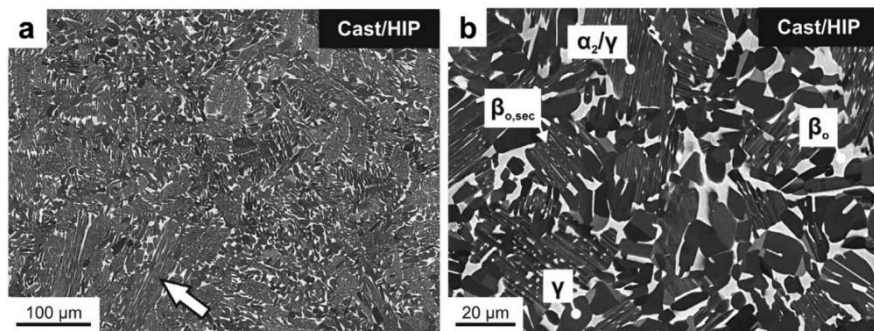


Figure 2. 17 BSE image of As-cast and hot isostatically pressed TNM alloy. (a) microstructure of as-cast and hot isostatically pressed TNM alloy, coarse α_2/γ colony indicated by the white arrow. (b) View at a high magnification.

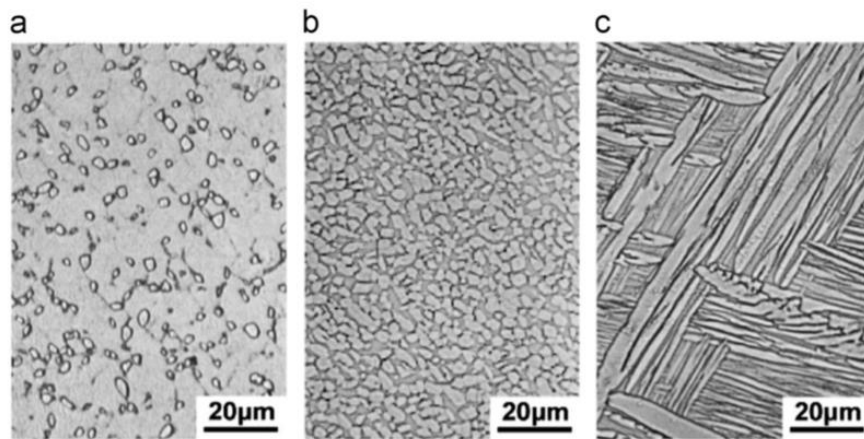


Figure 2. 18 (a) Bi-modal (b) equiaxed (c) lamellar microstructure created by different heat treatment on α_2 phase based alloy^[181].

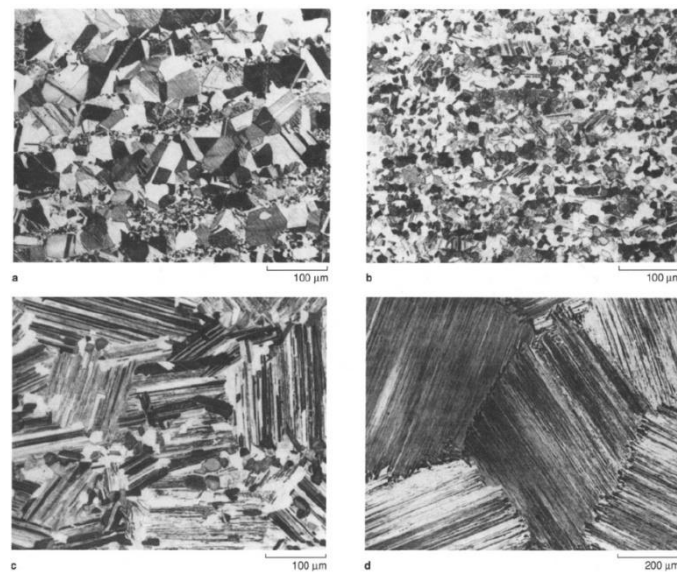


Figure 2. 19 Typical microstructures of post-hot work heat treated γ titanium aluminide alloys. (a) near γ , (b) duplex, (c) near lamellar and (d) fully lamellar^[122].

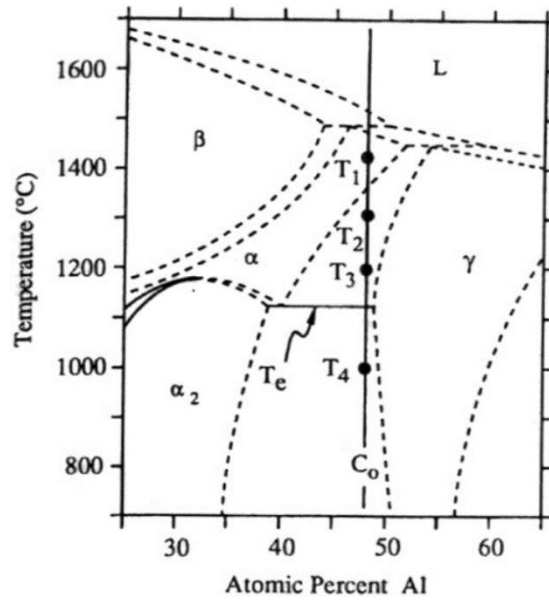


Figure 2. 20 Central portion of the TiAl phase diagram^[115].

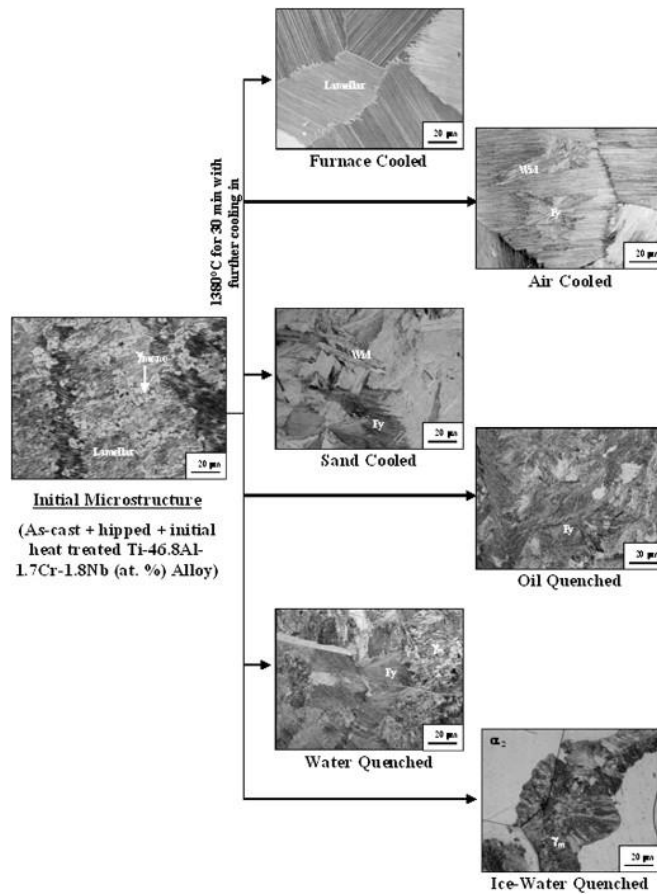


Figure 2. 21 Micrographs of the heat treated Ti-46.8Al-1.7Cr-1.8Nb at 1380 °C for 30 min and then furnace cooled, air cooled, sand cooled, oil quenched, water quenched, and ice-water quenched^[96].

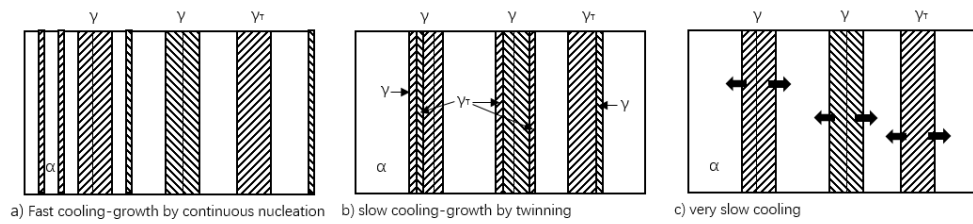


Figure 2. 22 Schematic representation of the possible development mechanisms of lamellar microstructure^[86].

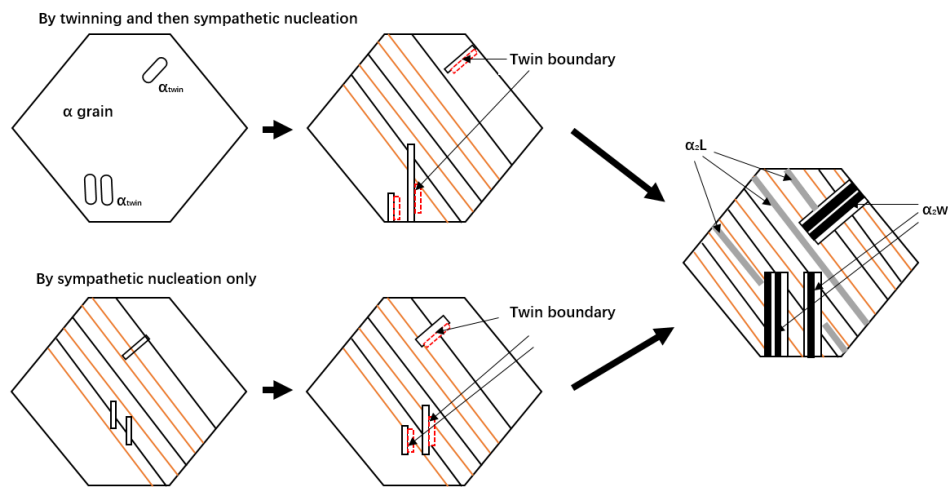


Figure 2. 23 Schematic sketches for Widmannstätten laths nucleation and growth via both twinning then sympathetic nucleation and sympathetic only^[117].

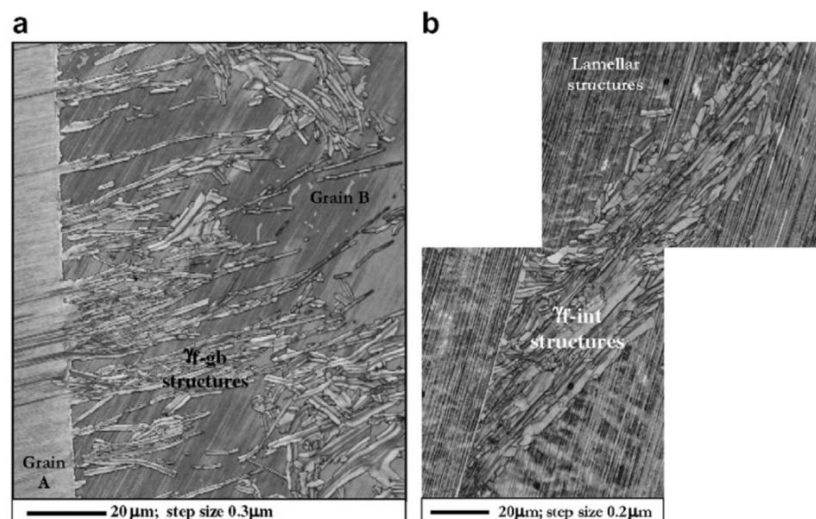


Figure 2. 24 Backscattered electron morphologies of $\gamma_{\text{f-gb}}$ structures and $\gamma_{\text{f-int}}$ structures. (a) $\gamma_{\text{f-gb}}$ structures from ice-water quenched and (b) $\gamma_{\text{f-int}}$ structures in sand cooled GE alloy specimens^[182].

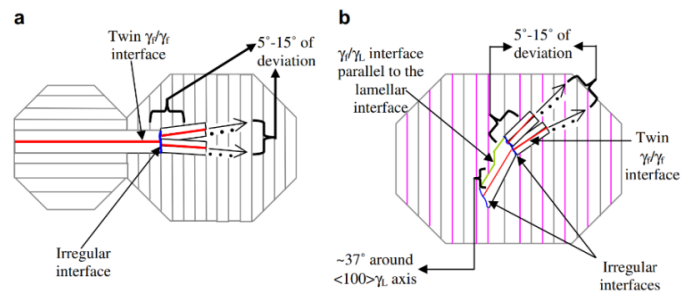


Figure 2. 25 Schematic of feathery like nucleation and growth mechanisms of (a) γ_{f-gb} structures (b) γ_{f-int} structures ^[182].

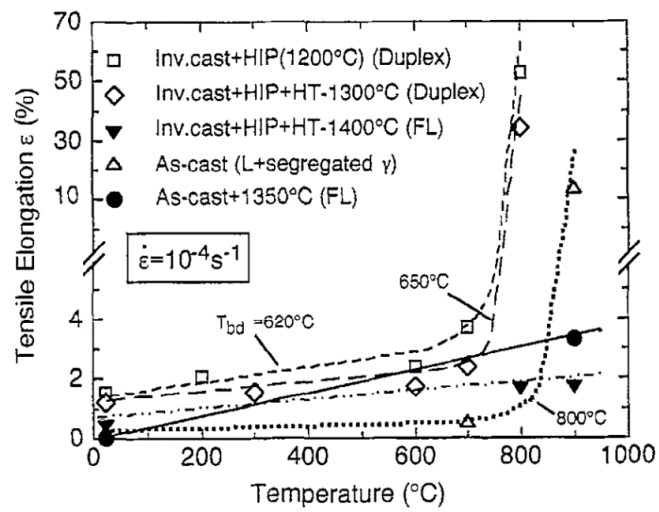


Figure 2. 26 Variation of tensile ductility with temperature for varies microstructures ^[136].

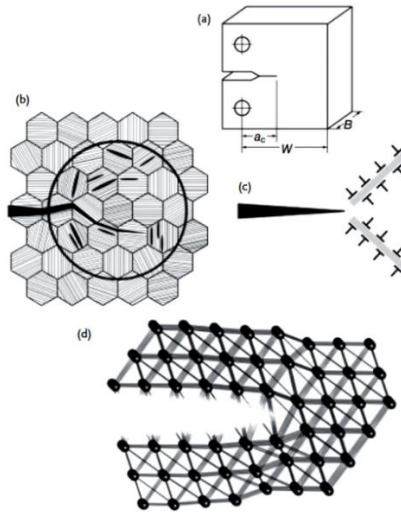


Figure 2. 27 Schematic illustration of the processes determining crack propagation in a lamellar ($\alpha_2 + \gamma$) alloy at temperatures below the brittle to ductile transition temperature. (a) A crack in a macroscopic component; (b) continuum plastic zone involving enough grains; (c) crystal plasticity zone due to dislocation glide and mechanical twinning; (d) actual separation process at the atomic level^[12].

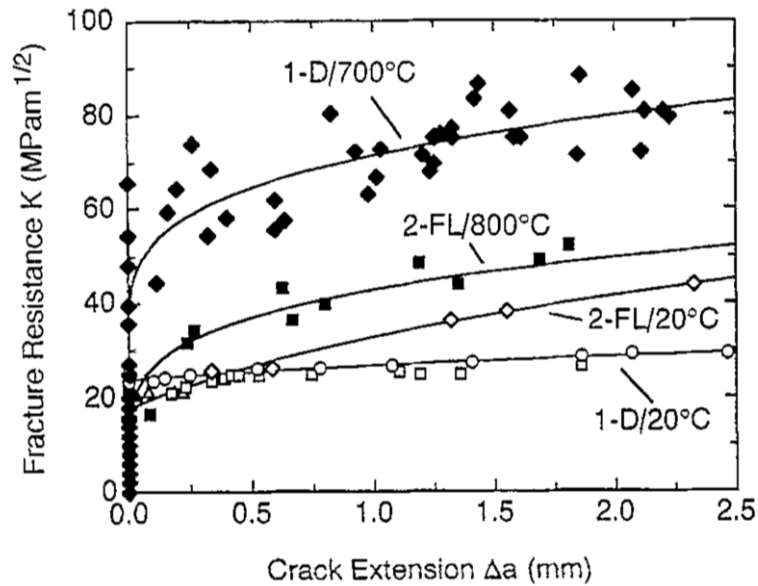


Figure 2. 28 Curves 1: Crack growth resistance curves of investment-cast Ti-48Al-2Cr with duplex microstructure at 20 °C \diamond and 700 °C \square , \circ compact tension (CT)-50 specimens with fatigue pre-cracks and displacement rates of 10 $\mu\text{m/h}$ and 600 $\mu\text{m/h}$, respectively. \triangle CT50 specimens with ECM-slit notch (radius $\sim 50 \mu\text{m}$) and 600 $\mu\text{m/h}$. \blacklozenge : CT-2.6 specimen. 10 $\mu\text{m/h}$. Curves 2: K_R curves of FL Ti-47Al-2.6Nb-2(Cr + V) at 20 and 800 °C; displacement rate $4.2 \times 10^{-2} \text{ /s}$. Data summarized by F. Apple and R. Wagner^[154].

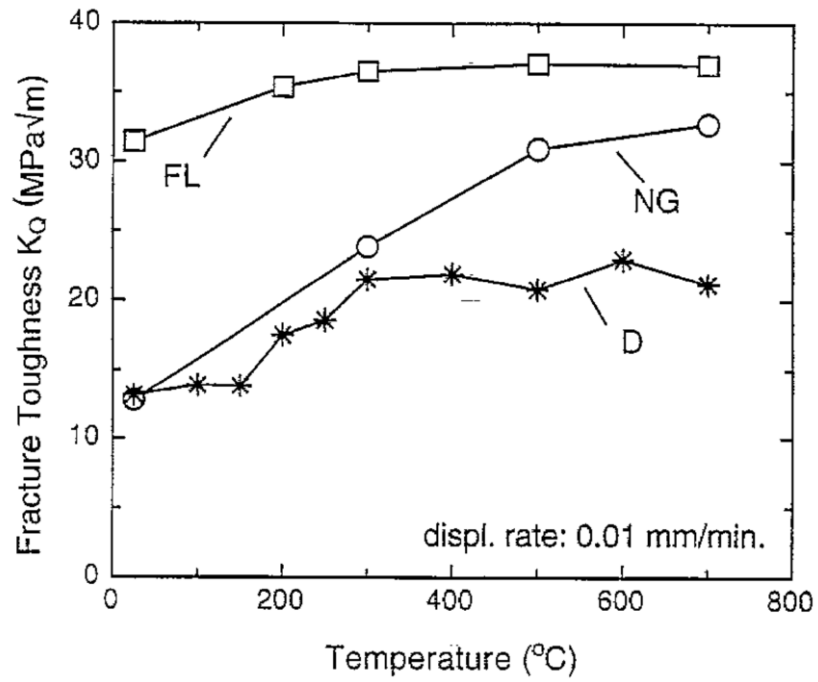


Figure 2. 29 Dependence of the fracture toughness on temperature for two-phase γ -alloys with different microstructures. ■ Ti-47Al-2Cr-0.2Si, lamellar microstructure ($d_L \sim 330$ nm, $\lambda_L \sim 0.05$ – 1 μ m); ○ Ti-47Al-2Cr-0.2Si, near gamma microstructure ($d_\gamma \sim 11$ μ m); * Ti-47Al-1Cr - (Nb, Mn, Si, B), duplex microstructure ($d_\gamma \sim 30$ nm, $d_L \sim 200$ nm) ^[154].

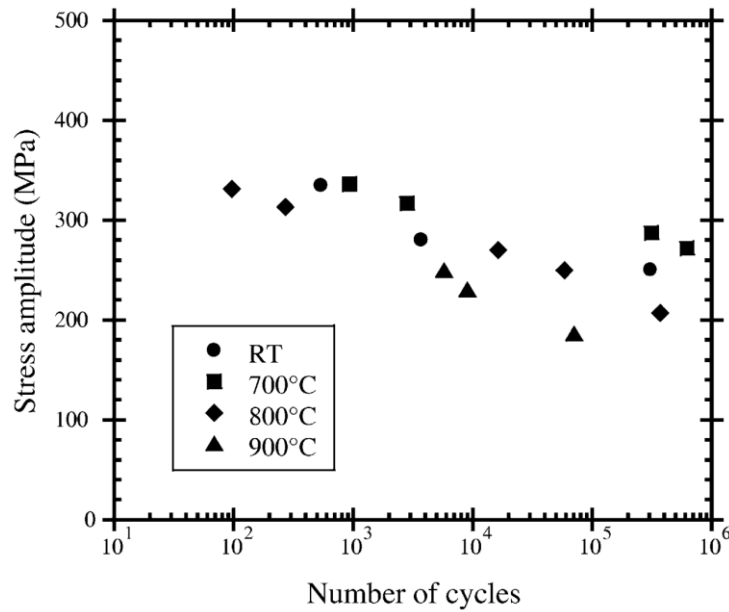


Figure 2. 30 S-N curves of a binary Ti-36.5Al alloy with a lamellar structure at different temperatures ^[154].

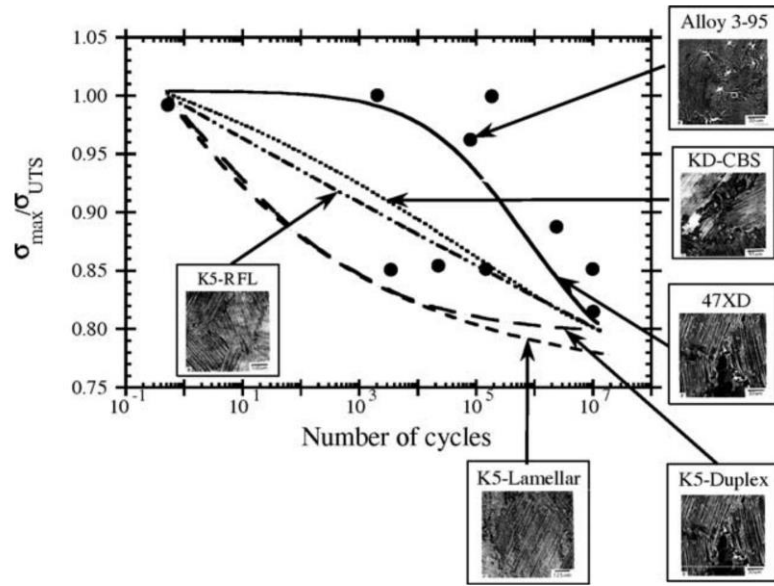


Figure 2.31 S-N curves of alloys with varies microstructures ^[154].

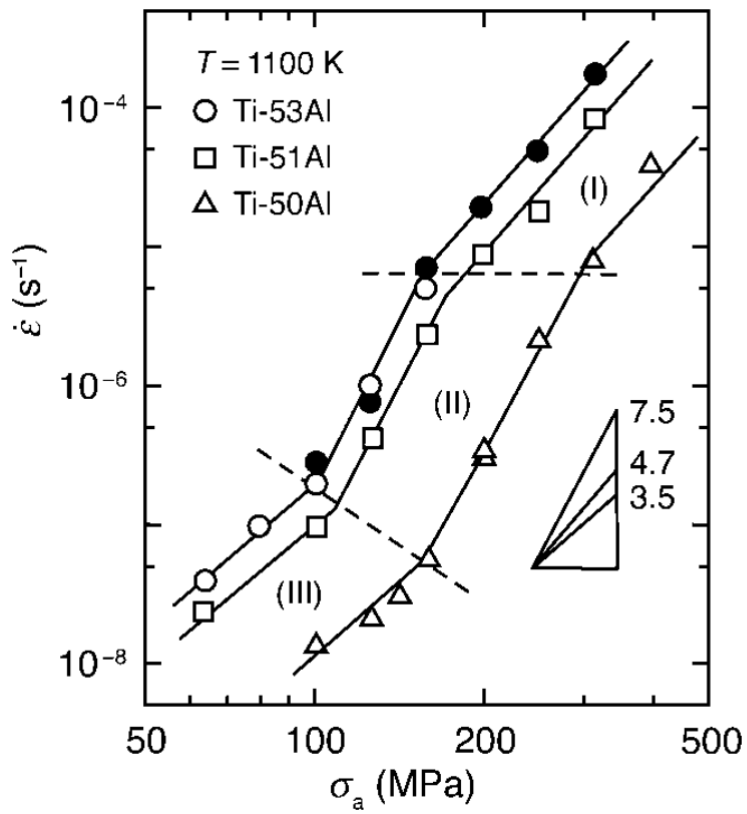


Figure 2.32 Dependence of the minimum strain rate on stress for different single γ -phase alloys ^[154].

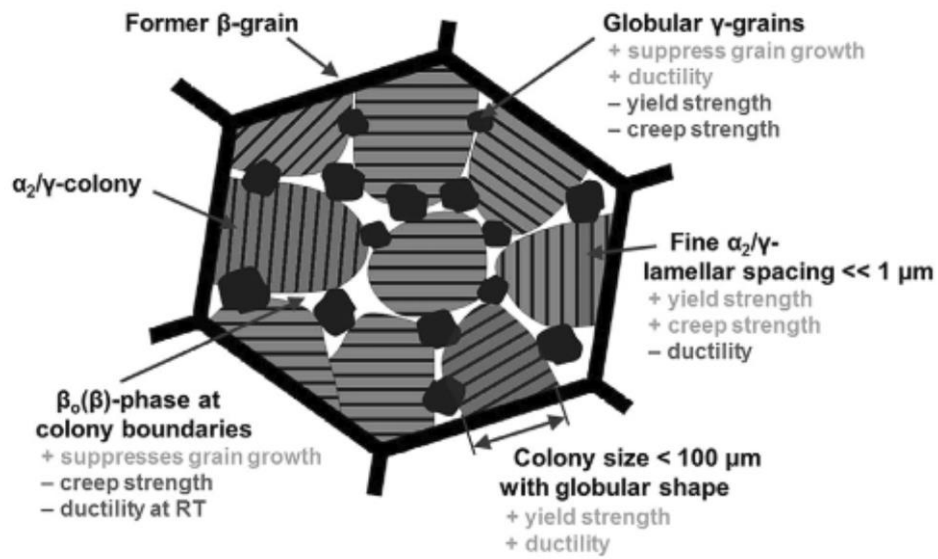


Figure 2. 33 Schematic drawing of a designed NL+ γ microstructure which can be adjusted by a two-step heat treatment in a forged TNM alloy (see text). The influence of the microstructural constituents on the mechanical properties is indicated ^[168].

Boride phases	Space group	Unit cell parameters (nm)
TiB (B27)	Pnma (No. 62)	$a=0.611$ $b=0.305$ $c=0.456$
TiB (B _f)	Cmcm (No. 63)	$a=0.323$ $b=0.856$ $c=0.305$
Ti ₃ B ₄ (D7 _b)	Immm (No. 71)	$a=0.326$ $b=1.373$ $c=0.304$
TiB ₂	P6/mmm (No. 191)	$a=0.303$ $c=0.323$

Table 2. 1 Crystallographic data for the four titanium boride phases ^[41]

CHAPTER 3 EXPERIMENTAL METHOD AND EQUIPMENT

3.1 Alloys Used in This Study

All the experimental samples were modified TNM alloys, which varied by the different concentrations of the elements Al and B. The detailed composition of these samples is as follows: Ti-44Al-4Nb-1Mo-0.3B, Ti-44.4Al-4Nb-1Mo-0.8B, Ti-44.6Al-4Nb-1Mo-0.1B and Ti-45.5Al-4Nb-1Mo-0.3B. All the alloys were cast into Φ 50 mm x 200 mm ingots with permanent moulds, and test bars with a length of 140 mm and a diameter of 15 mm were machined from the ingots, using wire electro discharge machining (EDM).

All these alloys were typical TNM-B alloys and contained three main phases, namely B_2 structure B_2 -Ti phase with their disordered polymorphs, $D0_{19}$ structure- α_2 phase (Ti_3Al) and $L1_0$ - γ phase ($TiAl$). The phases identified by XRD on Ti-44.2Al-4Nb-1Mo-0.8B are shown in Figure 3.1. These four samples exhibit nearly the same BSE mode SEM microstructure images, as shown in Figure 3.2 (0.8B alloy). The microstructure of the as-cast 0.8B alloy presented as $\alpha_2+\gamma$ lamellar colonies with a small number of borides both inside lamellar colonies and at grain boundaries. There was a small number of γ grains and B_2 precipitates located at grain boundaries, which had dark-grey/black and bright contrasts, respectively. The α_2 phase was shown in light grey, and the

rod-shaped/filamentous borides appeared very bright. The ω_0 phase may be also included in the TNM-B alloys, but they were hardly macroscopic by SEM due to their very small size. The ω_0 phase has been observed to precipitate from the B_2 phase^[183, 184]. The size of $\alpha_2+\gamma$ lamellae colonies was about 50 μm in average, which was measured via the intercept method.

3.2 Heat-Treatment Method and Furnace Details

The alloy is designed for high-temperature use on the LPT blade of future aero-engines, in which the working environment can reach 800°C to 850°C. Solution treatment and ageing is the main method to treat the alloy. Thus, the heat-treatment method and furnace details should be described at first.

The purpose of heat treatment is to eliminate or control the size and morphology of weak phase, and to achieve the fully lamellar microstructure with fine lamellae in the alloy, thus improving the mechanical properties^[104, 185]. The main heat treatment process is solution treatment and ageing. The solution treatment was mainly used during the study, which involved heating the alloy to a temperature sufficient for the dissolution of β or γ phases. It was then held for a given time until the cooling phase in which different cooling rates and conditions were used. This variation in cooling conditions was allowed for the control of material microstructures and properties^[90, 122]. Double ageing was used to refine the microstructure, and control the phase nucleation and grain growth during the

study.

All the heat treatment during the study was conducted by using the ELITE BRF 15-5 furnace. The heating temperature ranged from the room temperature to 1500°C. The maximum power was 5.1 KW, and the furnace had a dimensional capacity of 150 mm x 140 mm x 250 mm, which is equivalent to 5 litres. The temperature of the furnace was measured by a type R thermocouple.

The heating sample was normally placed in the middle of the furnace cavity, but the thermocouple fitted in the furnace was not. A small distance may lead to a large temperature difference at the high temperature condition. Therefore, the temperature at the sample position must be calibrated before the heat treatment. The correspondence of sample temperature and furnace reading temperature is shown in Figure 3.3.

Since the cooling rate affects the lamellar microstructure of TiAl alloys, the cooling rate of the furnace was measured during the furnace cooling process. The corresponding temperatures and times were recorded as well. The furnace cooling rate is shown in Figure 3.4.

All the heating temperatures used in this study are actual temperatures, except those specified in particular.

3.3 Preparation of Specimens

Samples used for heat treatment and microstructure observation were cut from the as-supplied bars into 15 mm cylinders. Samples were cut either by using a Struers Accutom cutting machine with a silicon carbide cutting wheel for SEM observation or by using the EDM for TEM observation. The samples were mounted into the conductive Bakelite by using the machine ATM Opal 460, and then ground successively with silicon carbide grinding paper of grit 200-1200 step by step before final polishing. These samples were finished by mechanical polishing with a liquid of active colloidal silica for final polishing of titanium. The Struers DAP-7 polishing machine unit fitted with a pedemin-s automatic polishing head was used for the mechanical polishing. The final polishing was performed for about 10 mins for SEM samples and around 25 mins for EBSD samples^[186]. The polished surface was cleaned with water, detergent and ethanol successively, and then dried with a hair drier on the cool setting.

Some of polish-finished samples were then etched. The standard way is to chemically etch them by using Kroll's reagent of 2 vol.% hydrogen fluoride (HF), 10 vol.% nitric acid (HNO₃) and balance water for about 10 seconds.

Slices of about 1 mm in thickness were sectioned from the heat-treated bars. These slices were thinned by hand grinding on 400-800 grade silicon carbide paper to about 0.3 mm. Discs of 3 mm in diameter were cut from the slices by

using EDM. These discs were carefully held in the TEM sample grinding holder, and then ground on silicon carbide grinding paper of grit 1200 till the thickness was close to 100-150 μm . These foils were electro-polished in a solution of 10% perchloric acid + 90% ethanol at 20V and -20°C , using a twin-jet electro-polisher^[187].

The samples for XRD scan were easier to prepare than SEM, EBSD and TEM samples. The only requirement was to make sure that the samples had a clean and smooth surface, and to keep the scan area away from the edge of the sample to avoid the effect of the oxide layer.

Jominy end quenching was used in the study. The dimensions of the Jominy end quenching bar are shown in Figure 3.5. The standard Jominy quenching apparatus was used. The height of the free water column was set at 65 mm, and the room temperature water was quenched for 10 minutes.

3.4 Equipment Used for Microstructure and Crystal Structure Observation

It is well known that most of the heat-treated samples show a lamellar microstructure or a near lamellar structure. The morphology of the lamellar structure is closely related to the mechanical properties of the alloy. The finer lamellar size and the lamellar spacing could enhance the mechanical properties of the alloy^[20]. Thus, the Scanning Electron Microscope (SEM) JEOL 6060 and

JEOL 7000F were used to take BSE mode SEM images during this study.

The volume fraction of phases in the alloys was determined by X-ray diffraction (XRD) and EBSD. As is well known, there are three main phases in the TNM-based alloys: B₂ structure B₂-Ti phase, D0₁₉ structure- α_2 phase (Ti₃Al) and L1₀- γ phase (TiAl). Transmission electron microscopy (TEM) was also used to confirm the crystal structure of different phases^[188].

3.4.1 The SEMs Used for Microstructure Observation

The JEOL 7000 was used for most of the microstructure observation, because it is a field emission scanning electron microscope, rather than the JEOL 6060 fitted with the tungsten filament. Also, it has the advantage of the better signal-to-noise ratio at the same spot size and better resolution.

The observation on JEOL 7000 included secondary electron (SE), backscattered electron (BSE) and electron backscattered diffraction (EBSD). The secondary electrons that originate from the surface or near-surface regions of the sample were used to inspect the surface topography of the sample. The inelastic interaction between the primary electron beam and the sample could result in the secondary electrons, which are low energy electrons less than 50 eV. The low energy of these electrons can make them easy to be collected by the positive bias grill on the front of the SE detector. The backscattered electrons come from the primary incident beam that is ejected from the sample. There is

no energy loss during the process when electrons are backscattered by the sample. The BSE image shows a high sensitivity to the difference in atomic number, and the higher the atomic number, the brighter the material appears in the image. There is a clear contrast in typical BSE images, due to a significant difference in composition between the phases of the TNM alloy.

3.4.2 Equipment and Method Used for Microstructure and Crystal Structure Identification

The X-ray diffractometer (XRD) used in the study was a Philips XPERT X-ray diffractometer. The target material of this machine was Cu, and the $K\alpha$ of the Cu was 0.150,46 nm. The machine ran under 45 kV and 40 mA at the scanning speed of 6°/min. The scanning results were analysed by the software 'Match', and the output results included the identified phase and phase volume fraction.

The EBSD used in the study was an Oxford EBSD detector fitted on JEOL 7000 SEM. The supporting software used was INCA. The Kikuchi spectra obtained by EBSD phase mapping could identify the crystal structure of different phases, when the thickness of samples was more than 500 nm. However, the width of α_2 lamellar lathes in some samples was less than 500 nm, which means that the EBSD cannot identify these phases clearly. Thus, the EBSD focused on the γ phase analysis while the α_2 phase was analysed by the TEM.

A TEM observation was carried out on the FEI Talos F200X at 200 kV. The Super-X detection system on the Talos F200 consists of four windowless silicon drift detectors (SDD). Three selected area diffraction (SAD) patterns of different zone axes with low index were taken from the same area for identifying the unknown crystal structure. The measured tilting angle between the zone axes should match the theoretical angle. Thus, the tilt distance should be recorded very clearly and carefully, and the tilt angle can be calculated by the equation:

$$\cos\tau = \cos(\alpha_2 - \alpha_1) * \cos(\beta_2 - \beta_1)$$

The calculated angle should be close to the indexed zone angle. The Kikuchi lines were used to help track the tilting direction during the tilt process of TEM samples.

Some phases or particles are too small to be selected by the selected area diffraction pattern. The diffraction patterns of these phases were achieved by High-Resolution TEM (HR-TEM) and convergent beam electron diffraction (CBED)^[189].

3.5 Mechanical Testing

Vickers hardness was measured by an Indentec hardness tester. Due to the uneven grain size of some samples, a high load of 30 kg was used for relative

hardness testing. The final hardness value is the average of five measurements.

The tensile test was carried out by an accredited contractor, EXOVA s.r.o. in Czech Republic, according to the ASTM tensile test standard for metallic materials (ASTM E8/E8M), using round rig test piece of 5 mm x 25 mm in gauge section. The initial strain rate was $1 \times 10^{-4} \text{ s}^{-1}$.

Constant load tensile creep test was performed in air at 700°C and 250MPa for 860h, using round test piece with a gauge section of 4 mm x 20 mm in Swansea University.

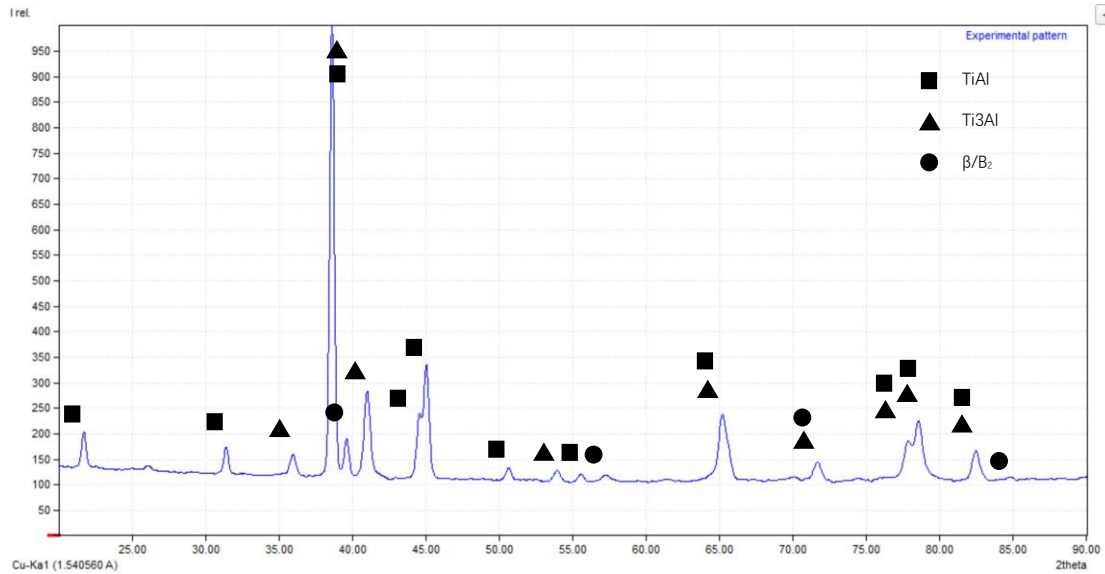


Figure 3. 1 XRD scan result for raw alloy of Ti-44.2Al-4Nb-1Mo-0.8B. It indicates α , β and γ phases contained in this alloy.

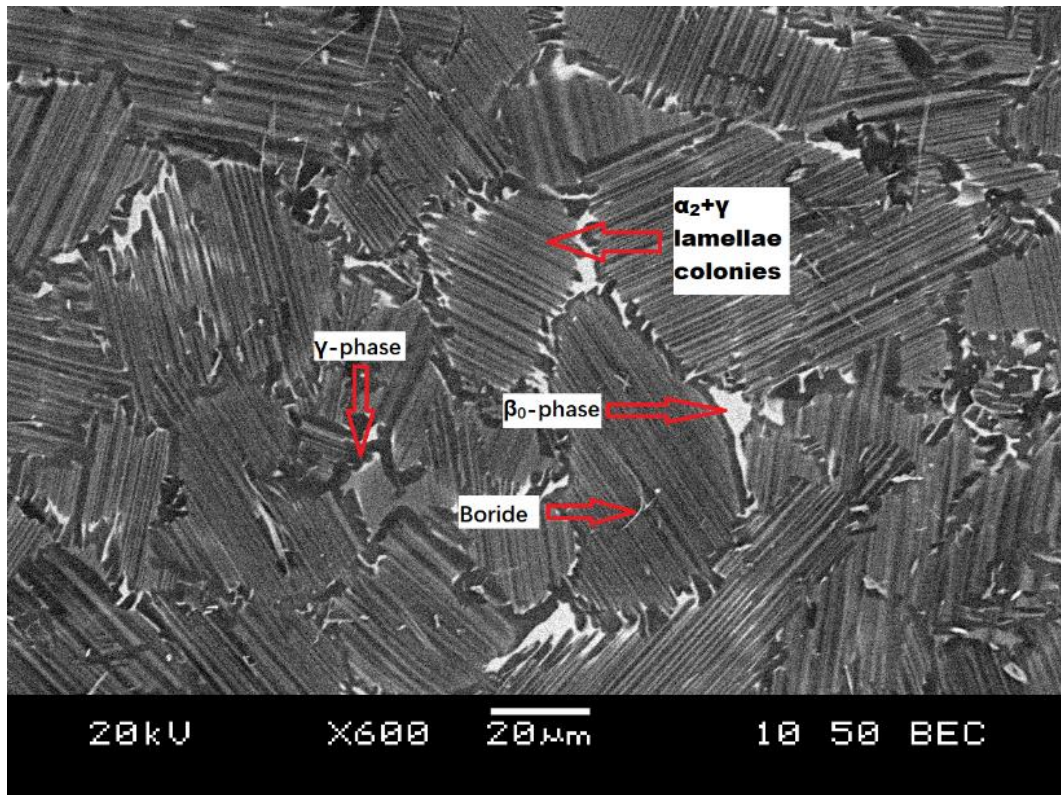


Figure 3. 2 SEM images of raw alloy of Ti-44.2Al-4Nb-1Mo-0.8B under BSE mode. Three phases and boride are indicated by the red arrow.

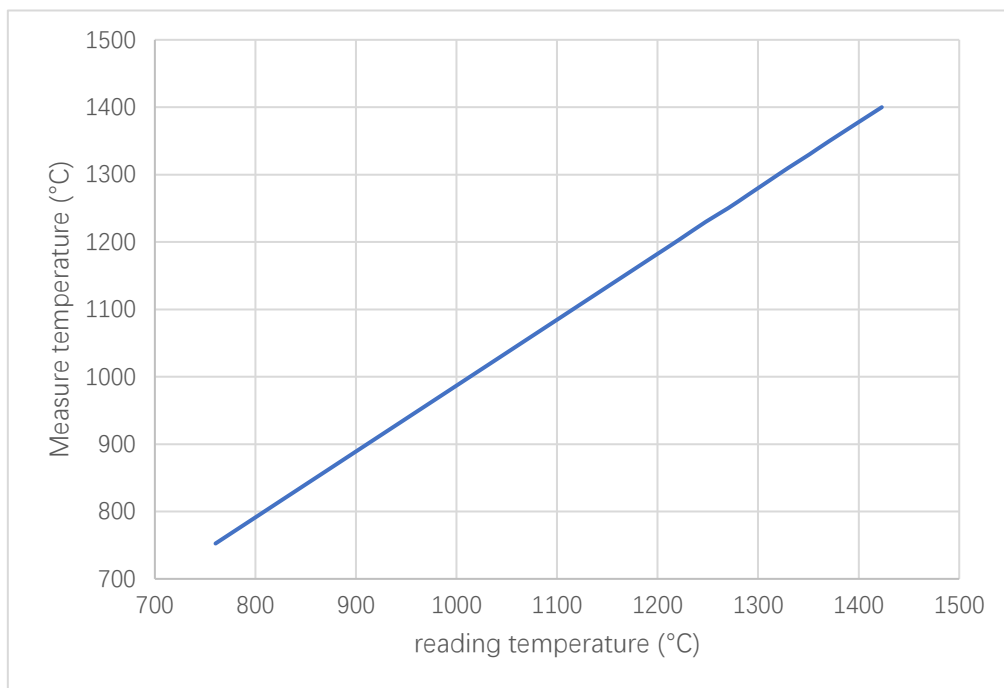


Figure 3. 3 Correspondence diagram of measured temperature and reading temperature.

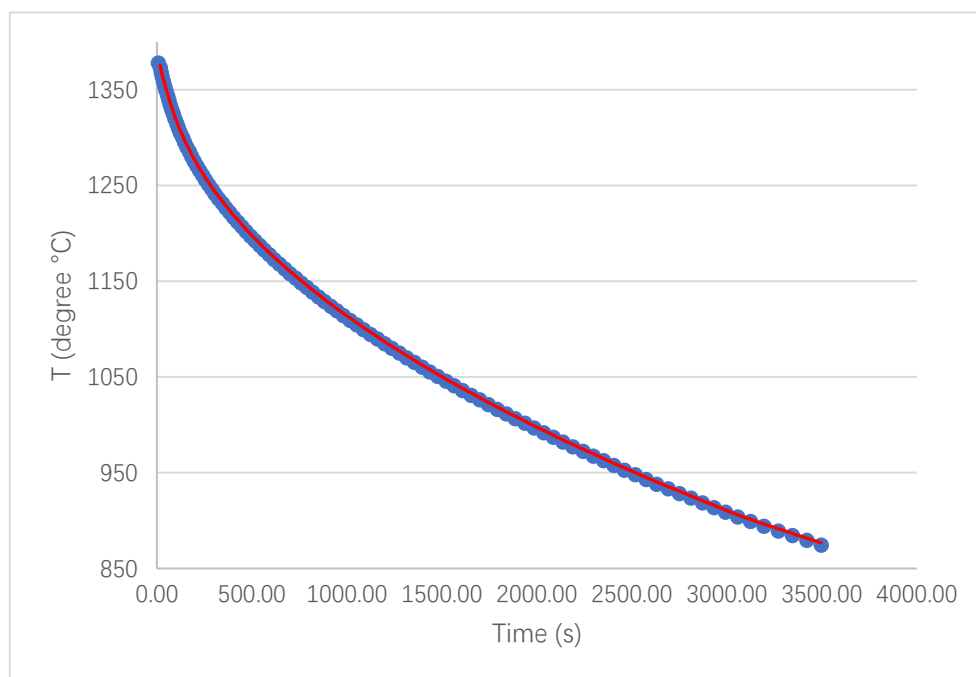


Figure 3. 4 Furnace cooling rate diagram.

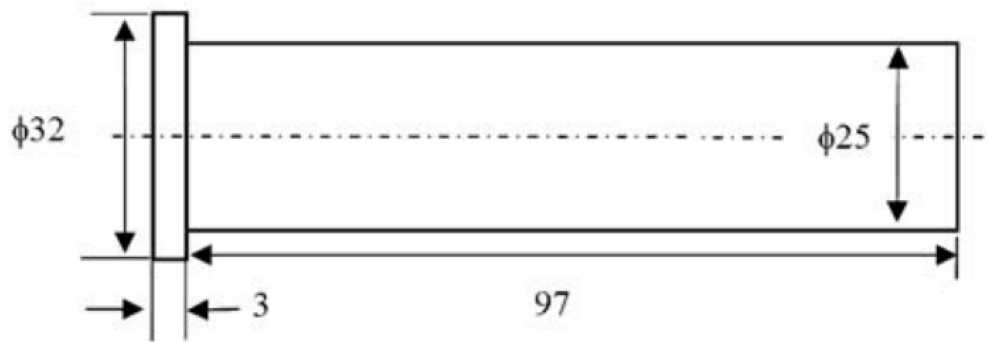


Figure 3. 5 Dimensions of Jominy end quenching specimen.

CHAPTER 4 THE STUDY ON PHASE DIAGRAM

As is well known, the mechanical properties of TNM alloys greatly depend on the arrangement and presence of lamellar colonies. The lamellar colonies of TNM alloys are controlled by two steps in heat treatment^[167]. The first step is solution treatment which controls the grain size by annealing alloys at an appropriate temperature and cooling at an appropriate cooling rate. The second step is ageing at an isothermal stabilisation annealing between 750°C and 900°C. Lamellar spacing can be governed by the cooling rate.

The experimental design in this study can be divided into two main steps. The first step is to construct the phase diagram and select the suitable alloy, during which the solution treatment temperature can be confirmed. The second step is to explore other experimental conditions to determine the solution treatment time, cooling rate/method, ageing/isothermal stabilisation annealing temperature, time and subsequent cooling rate/method, at the same time, to analyse the microstructure changing and infer the feasibility of the heat treatment method.

Some important parameters, such as lamellar grain size, lamellar spacing, grain boundary content, phase content and hardness were measured or counted during the study.

4.1 Experimental Alloy Selection and Phase Diagram Study

The nominal composition of TNM alloy is Ti-43.5Al-4Nb-1Mo-0.1B in at %. Figure 4.1 shows the experimental quasi-binary phase diagram and phase fractions diagram with temperature^[113, 177, 190]. Compared with the original TNM alloy, it is obvious on the phase diagram that the solid phase transformation path and phase fraction diagram of newly designed alloys have changed a lot by increasing the concentration of Al to 44.5%. The solid phase transformation of Ti-(43.8-45.5) Al-4Nb-1Mo-(0.1-0.8) B should follow the pathway: $\beta \rightarrow \beta + \alpha \rightarrow \alpha \rightarrow \alpha + \gamma \rightarrow \alpha + \gamma + \beta \rightarrow \alpha_2 + \gamma + B_2$. And the newly designed alloys have a single α phase field compared with the phase diagram and phase fractions diagram of TNM alloy. This may provide an opportunity to achieve the fully lamellar microstructure via heat treatment, thereby, to improve the mechanical properties and working temperature capacity. Thus, the phase diagram and phase fractions diagram are needed to confirm the inference discussed above.

4.2 Phase Fractions Diagram of TNM-B Alloys

There were four alloys prepared to draft the phase fractions diagram via the metallographic method. The main difference between these four alloys is the concentration of Al. Ti-45.5Al-4Nb-1Mo-0.3B was selected as the reference alloy because the Al concentration of this alloy is very different from the other three alloys. According to the phase diagram shown in Figure 4.1, this alloy should

have a significantly higher α transus temperature and a larger signal α phase range than the other three alloys. Since the only difference between Ti-44Al-4Nb-1Mo-0.3B and Ti-45.5Al-4Nb-1Mo-0.3B is the concentration of Al, the accuracy of the results can be corrected by the comparison of phase diagrams between these two alloys.

Two sets of experiments were designed for phase diagram mapping. The first set of experimental heat treatment temperature was selected from 1152°C to 1387°C for Ti-44Al-4Nb-1Mo-0.3B and Ti-45.5Al-4Nb-1Mo-0.3B, as detailed in Table 4.2. The second set of experimental heat treatment temperature was selected from 1230°C to 1400°C for Ti-44.6Al-4Nb-1Mo-0.1B and Ti-44.2Al-4Nb-1Mo-0.8B, as detailed in Table 4.3. The heat treatment interval for the second set of experiments was less than that for the first set of experiments, because the first set of experiments is used as a reference and more details are required.

All samples were sectioned in the middle to avoid the effect of the oxide layer and mounted in Bakelite after heat treatment. The oxide layer or affected area can reach 2 mm from the outside to inside as measured in Figure 4.2. After well polished, the samples were examined by using JEOL 6060 SEM. The BSE images of these samples are shown in Figure 4.3 and Figure 4.4.

There are many dark areas observed in Figure 4.3 (d) and (f), which may be due

to the segregation of Al. These Al richer fields show darker contrast because the lower atomic number and lighter element give a darker contrast in BSE images^[191].

There are also many dark areas observed in Figure 4.4 (k) and (l), which represent typical γ phase in BSE images. However, it is indicated that no γ phase for Ti-44.2Al alloy exists at a temperature of 1350°C via the phase diagram analysis (Figure 4.1). The alloy has already entered the single α phase at a temperature of 1309°C, as shown in Figure 4.4 (j).

The different BSE images area fractions were counted, and these BSE images were taken from different areas. The final area fractions are the results on average. The area fractions (representing the volume fractions) of constituent phases were measured and summarised in Table 4.4 and Table 4.5. The area fractions of phases against temperature were plotted in Figure 4.5 (Ti-44Al-4Nb-1Mo-0.3B), Figure 4.6 (Ti-45.5Al-4Nb-1Mo-0.3B), Figure 4.7 (Ti-44.6Al-4Nb-1Mo-0.1B) and Figure 4.8 (Ti-44.2Al-4Nb-1Mo-0.8B).

According to the generated phase diagram, the solid phase transformation sequence for these four alloys is as follow: $\beta \rightarrow \beta + \alpha \rightarrow \alpha \rightarrow \alpha + \gamma \rightarrow \alpha + \gamma + \beta$. The original TNM alloy has a β phase in the whole temperature range, but has no 100% α phase field. Thus, there is no way to avoid the β phase in the original TNM alloy. All of these four alloys have a 0% β phase and 100% α phase field.

For these four alloys, the temperature of 0% β phase field is more than 60°C, and the temperature of 100% α phase field varies from 20°C to 50°C, which is related to the Al concentration by comparison of the phase diagram of the alloys. For example, with the increase of Al concentration, the α transus temperature is increased and the range of a single α phase is widened, which is consistent with the phase diagram in Figure 4.1. The single α phase field provides an opportunity in solution treatment, which could be utilised to manipulate the size and morphology of the β phase formed during the cooling process.

The 44.6Al-4Nb-1Mo-0.1B and Ti-44.2Al-4Nb-1Mo-0.8B have a larger single α phase field (about 30°C from 1270°C to 1300°C) than Ti-44Al-4Nb-1Mo-0.3B (about 15°C from 1270°C to 1285°C). The larger the single α phase range, the easier it is to achieve industrial manufacturing. Thus, from the view of industrial manufacturing, the 0.3B alloy should be excluded from the candidates.

The sample of Ti-44.2Al-4Nb-1Mo-0.8B was scanned by XRD and the scan result was analysed by software 'Match' for volume fraction calculation. The analysis results are given in Table 4.6. The XRD volume fraction diagram is compared with the area fraction phase diagram, as shown in Figure 4.9. The accurate phase volume fraction cannot be calculated, even if the two methods are both used. However, the author believes that the results can represent the actual phase volume fraction as a result of the similar results obtained via the

different methods.

4.3 The Assessment of α Grain Size Stability

The experiment regarding the stability of α grain growth has also been done at the same time. It would be meaningless to carry out the solution treatment, if α grains were not stable at high temperature.

In B-containing TiAl alloys, it relies on titanium boride to prevent the continuous growth of α grain through Zener pinning mechanism. The titanium boride prevents the movement of α grain boundaries from the pinning pressure, which counteracts the driving force to push the α grain boundaries. But the boride precipitates will lose pinning power and give way to grain growth if they are coarsened under high-temperature conditions^[29]. Therefore, the assessment of α grain size stability is necessary.

Based on the phase diagram created above, the temperature of 1290°C was determined as the α grain stability temperature for 0.8B and 0.1B alloys, while the temperature of 1270°C was determined as the α grain stability temperature for Ti-44Al-4Nb-1Mo-0.3B. All three alloys could enter the single α phase at the above heat treatment temperatures. The α grains will grow up over time when the samples are held at the above temperatures. The assessment of α grain size stability at different holding temperatures is summarised in Table 4.7.

Apparently, the alloys of Ti-44.6Al-4Nb-1Mo-0.1B and Ti-44Al-4Nb-1Mo-0.3B were not recommended for industrial α solution treatment, whilst great caution should be exercised when carrying out α solution treatment of the 0.3B alloy. The Ti-44.2Al-4Nb-1Mo-0.8B has the highest α grain size stability, and it is very suitable for industrial processing. Thus, it was selected as the experimental alloy.

4.4 Summary

The following conclusions can be summarised during the study on the phase diagram of the four alloys:

- The phase diagrams of the four alternative alloys have been mapped. The results have been found to be close to the published phased diagrams, as shown in Figure 4.1.
- The solution treatment temperature has been selected in this section.
- The alloy of Ti-44.2Al-4Nb-1Mo-0.8B has a single 100% α phase field about 30°C from 1270°C to 1300°C, therefore, the temperature of 1290°C has been selected as the solution treatment temperature for further study.
- The solution treatment time of Ti-44.2Al-4Nb-1Mo-0.8B for 2 hours has been determined for further study, as this alloy is still stable and cannot be coarsened. Longer solution heat treatment time is helpful to the element homogenisation.
- Ti-44.2Al-4Nb-1Mo-0.8B has been selected as the alloy for further study,

since this alloy has the highest α grain stability and the largest temperature range of solution heat treatment.

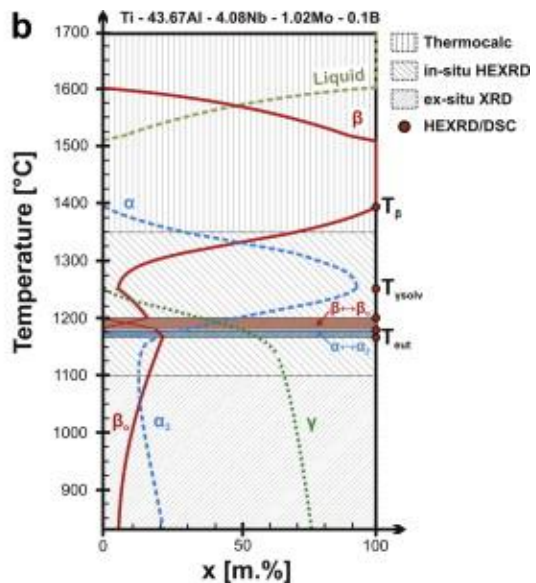


Figure 4.1 Experimental quasi-binary section through the TNM alloying system by Schwaighofer et al. a) The Al-content of the Ti-43.5Al-4Nb-1Mo-0.1B alloy is indicated by a vertical line. b) Course of phase fractions with temperature for the investigated alloy composition Ti-43.67Al-4.08Nb-1.02Mo-0.1B.

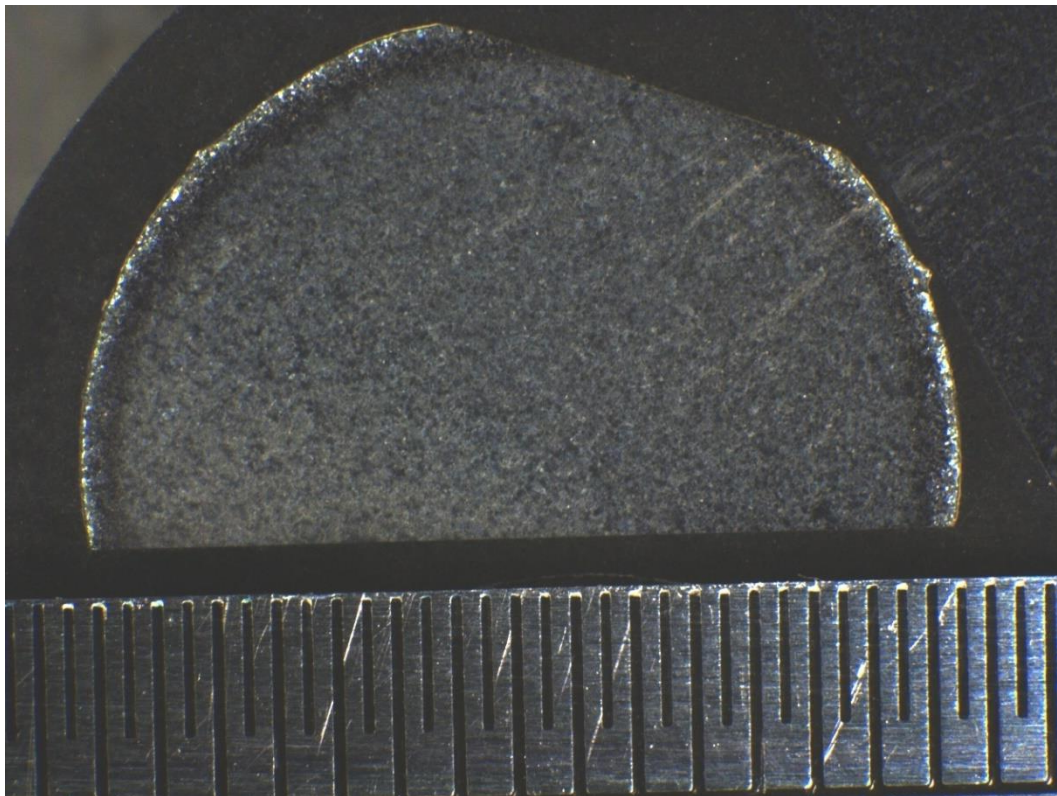

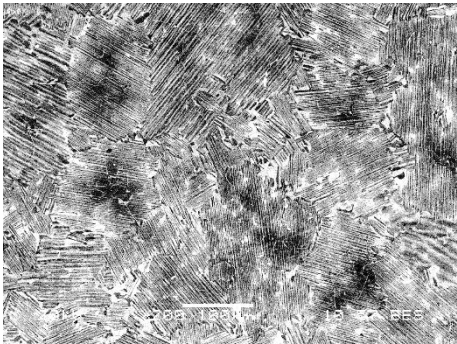
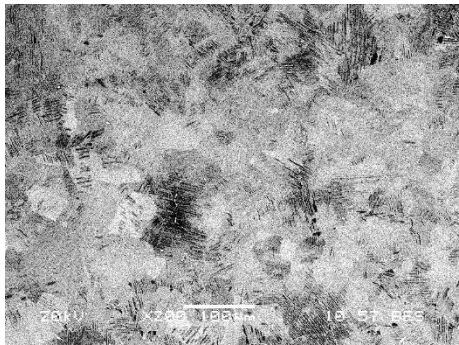
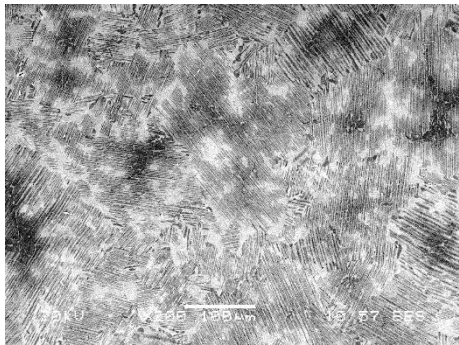
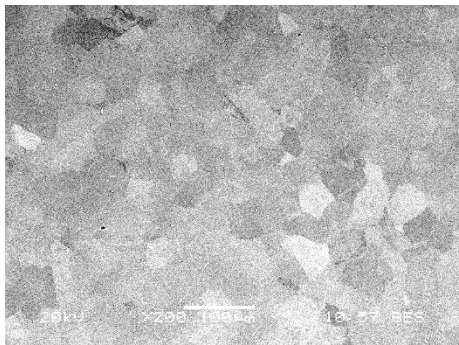
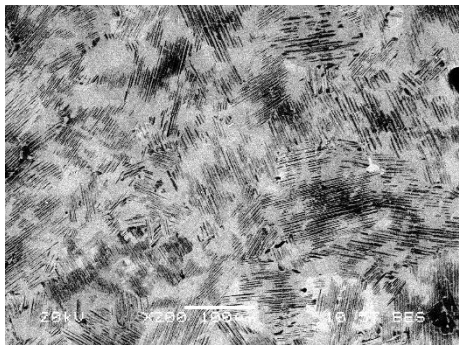
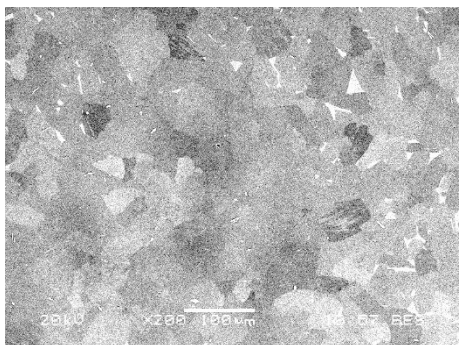
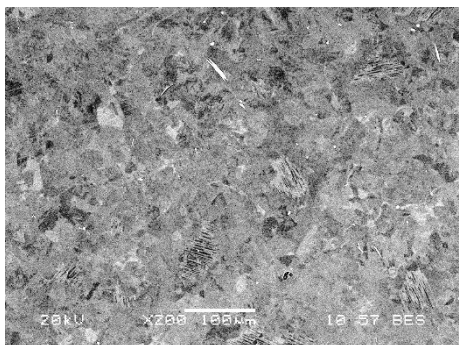
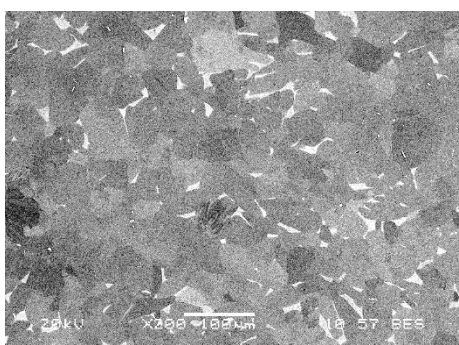
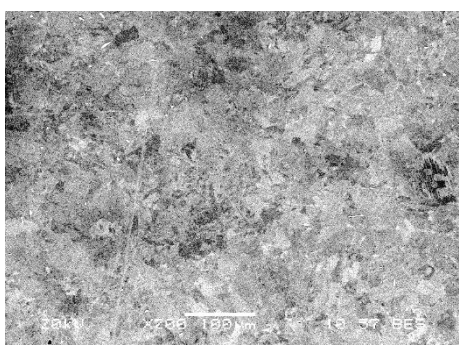


Figure 4.2 The image of long time ageing samples, the oxide layer or oxide effect area up to 2 mm deep from outside to inside.

	Ti-44Al-4Nb-1Mo-0.3B	Ti-45.5Al-4Nb-1Mo-0.3B
1230°C Watch quench	 <p>(a)</p>	 <p>(b)</p>

<p>1250°C Watch quench</p>	 <p>(c)</p>	 <p>(d)</p>
<p>1270°C Watch quench</p>	 <p>(e)</p>	 <p>(f)</p>
<p>1290°C Watch quench</p>	 <p>(g)</p>	 <p>(h)</p>
<p>1310°C Watch quench</p>		

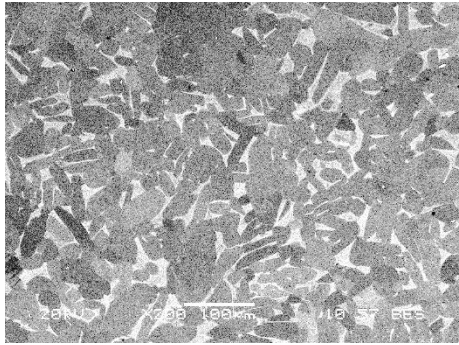
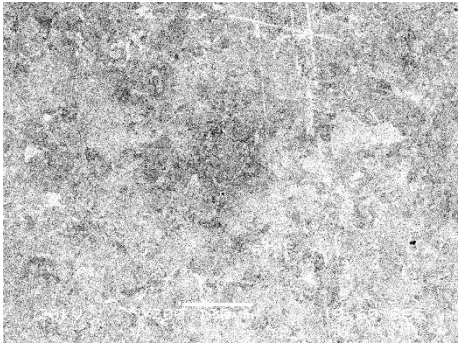
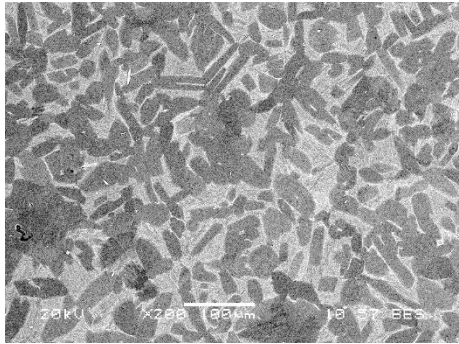
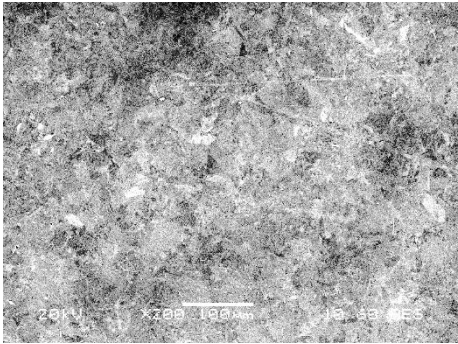
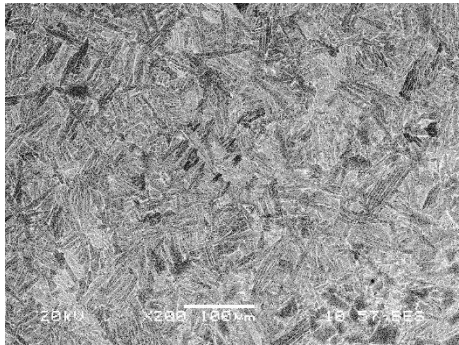
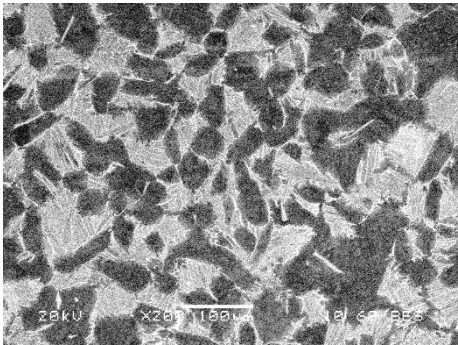
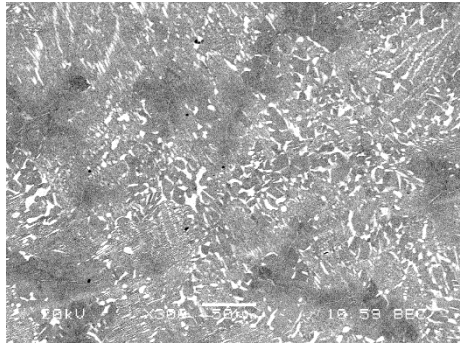
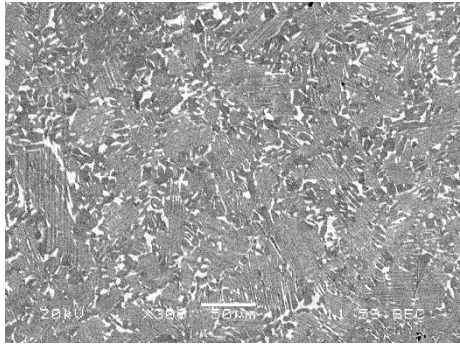
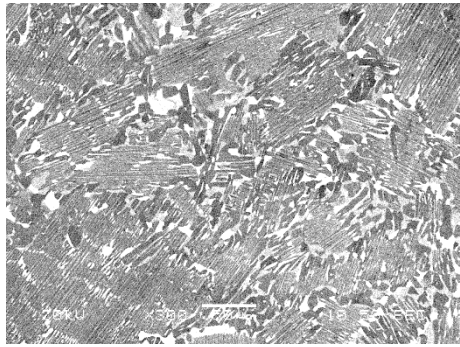
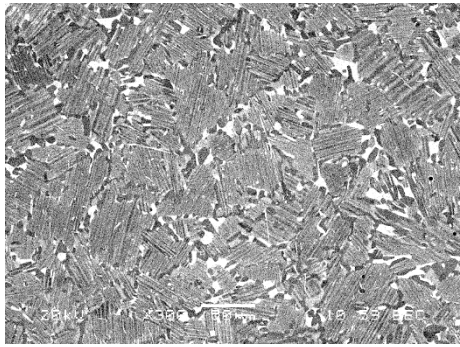
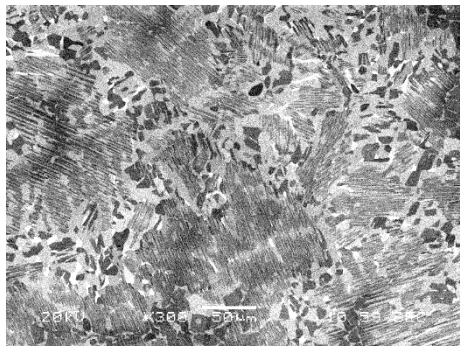
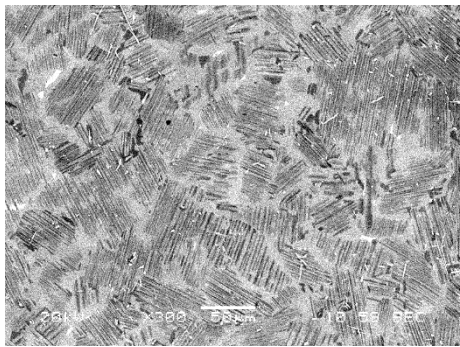
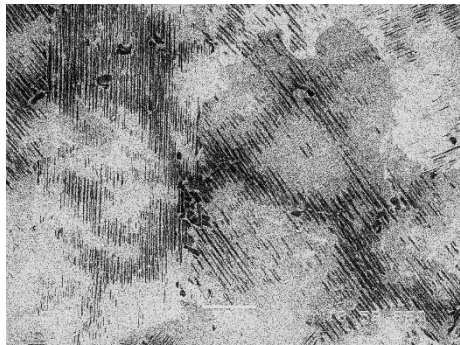
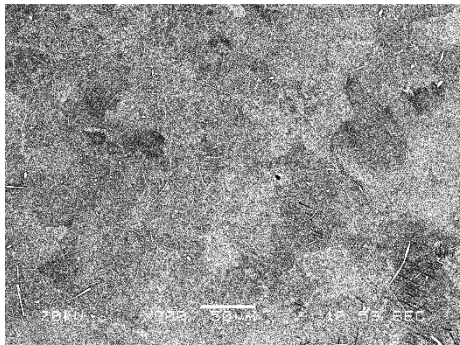
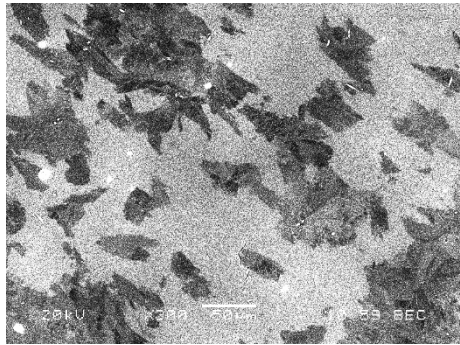
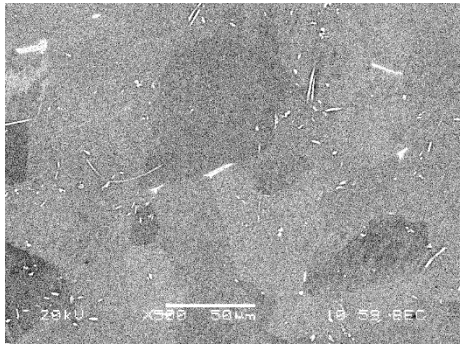
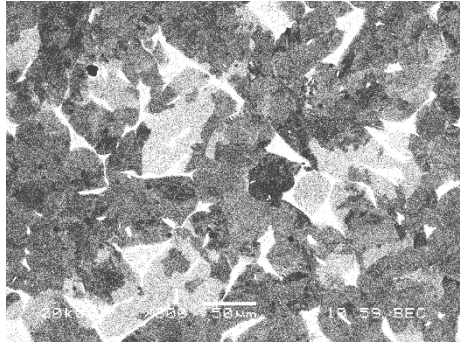
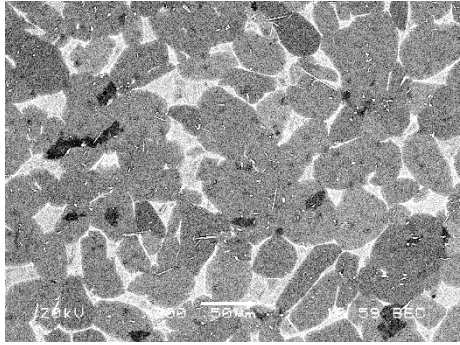
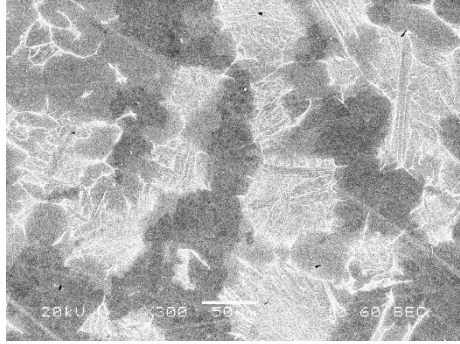
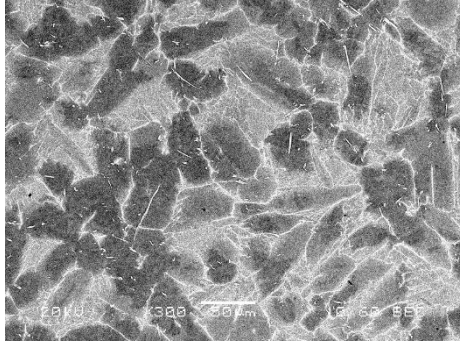
	(i)	(j)
1330°C Watch quench		
	(k)	(l)
1350°C Watch quench		
	(m)	(n)
1400°C Watch quench		
	(o)	(p)

Figure 4.3 BSE images of Ti-44Al-4Nb-1Mo-0.3B and Ti-44.5Al-4Nb-1Mo-0.3B, heat treated at different temperatures and cooled by water quench.

	Ti-44.6Al-4Nb-1Mo-0.1B	Ti-44.2Al-4Nb-1Mo-0.8B
1152°C Watch quench	 <p>(a)</p>	 <p>(b)</p>
1191°C Watch quench	 <p>(c)</p>	 <p>(d)</p>
1231°C Watch quench	 <p>(e)</p>	 <p>(f)</p>

1271°C Watch quench		
	(g)	(h)
1309°C Watch quench		
	(i)	(j)
1349°C Watch quench		
	(k)	(l)
1387°C Watch quench		

	(m)	(n)
--	-----	-----

Figure 4.4 BSE images of Ti-44.6Al-4Nb-1Mo-0.1B and Ti-44.2Al-4Nb-1Mo-0.8B, heat treated at different temperatures and cooled by water quench.

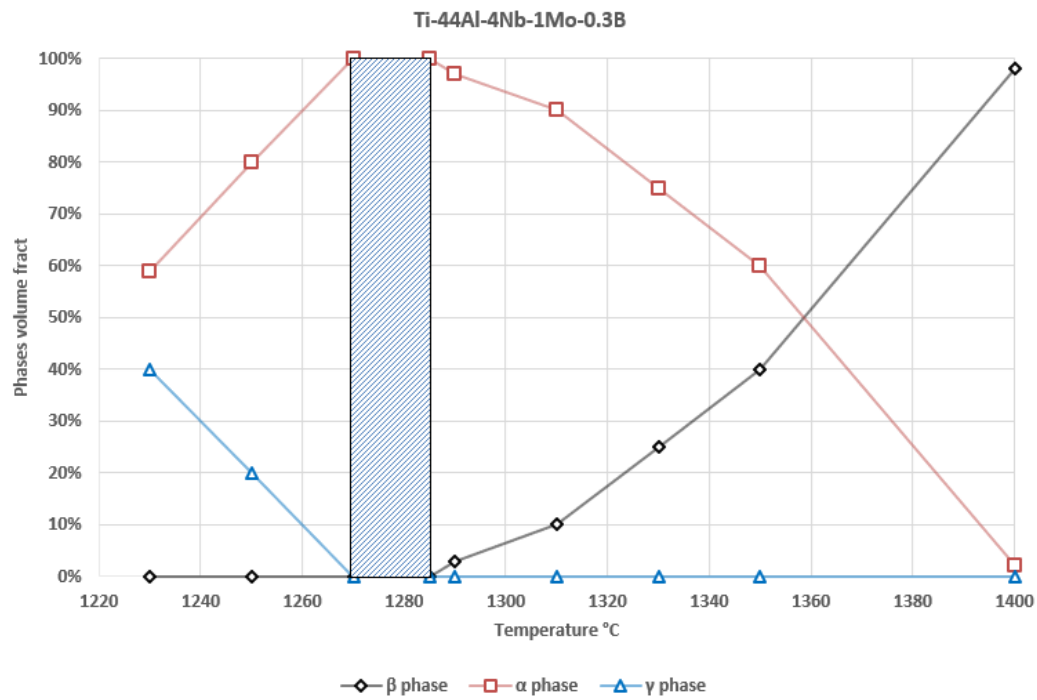


Figure 4.5 Phase diagram of Ti-44Al-4Nb-1Mo-0.3B. The area fraction represents the volume fraction, single α phase from 1270°C to 1285°C.

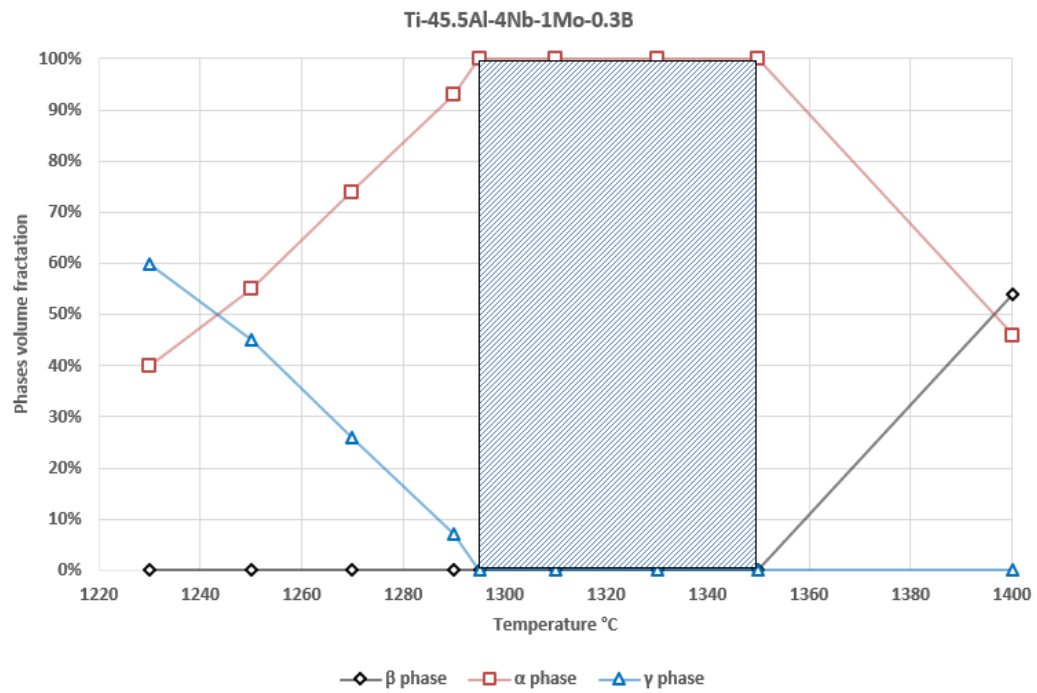


Figure 4.6 Phase diagram of Ti-45.5Al-4Nb-1Mo-0.3B. The area fraction represents the volume fraction, single α phase from 1295°C to 1350°C.

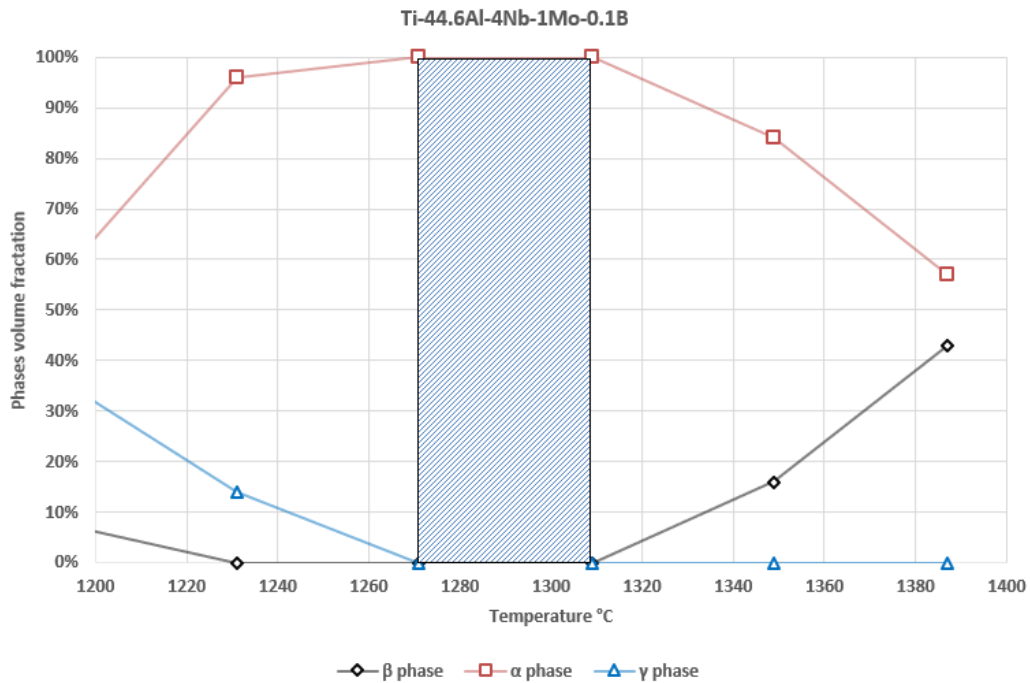


Figure 4.7 Phase diagram of Ti-44.6Al-4Nb-1Mo-0.1B. The area fraction represents the volume fraction, single α phase from 1270°C to 1310°C.

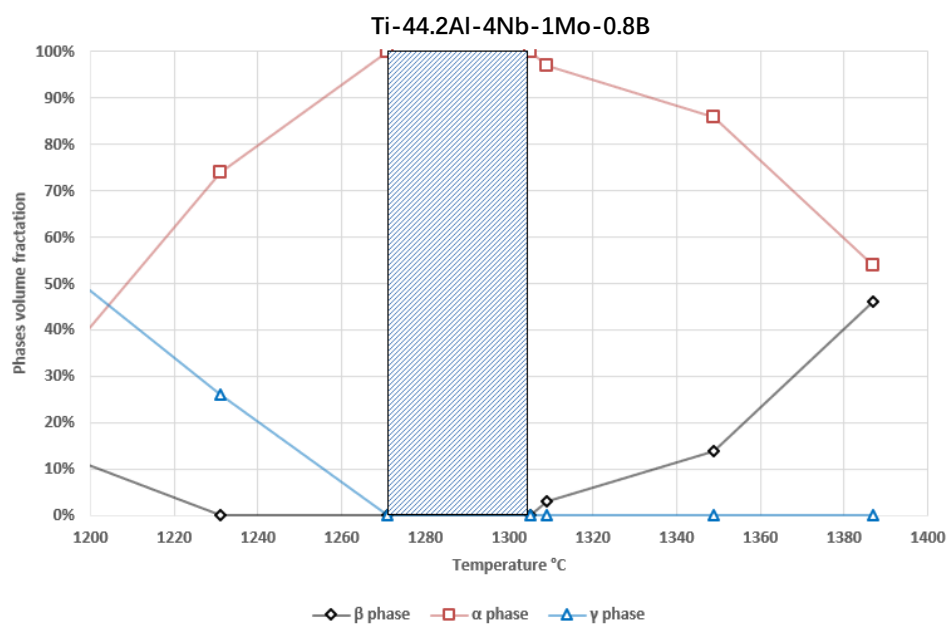


Figure 4.8 Phase diagram of Ti-44.2Al-4Nb-1Mo-0.8B. The area fraction represents the volume fraction, single α phase from 1270°C to 1300°C.

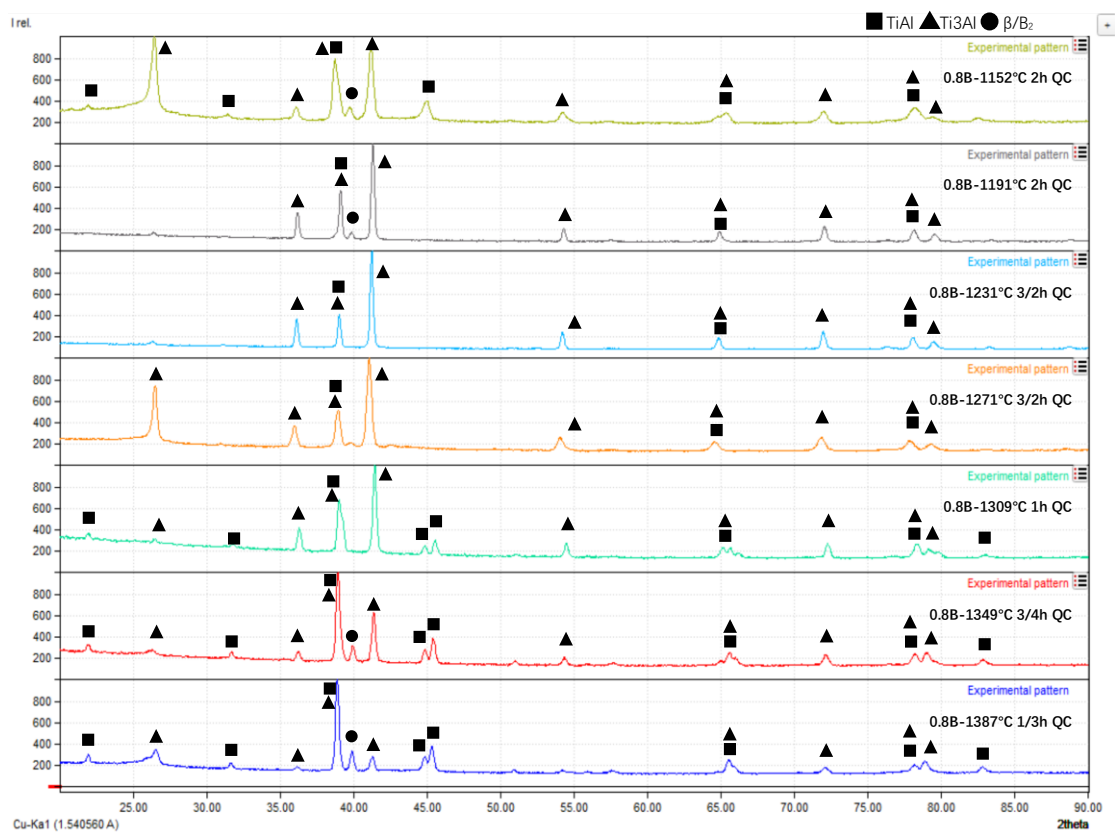


Figure 4.9 XRD curves for 0.8B quenched samples. The heat treatment conditions and phases are indicated in the Figure.

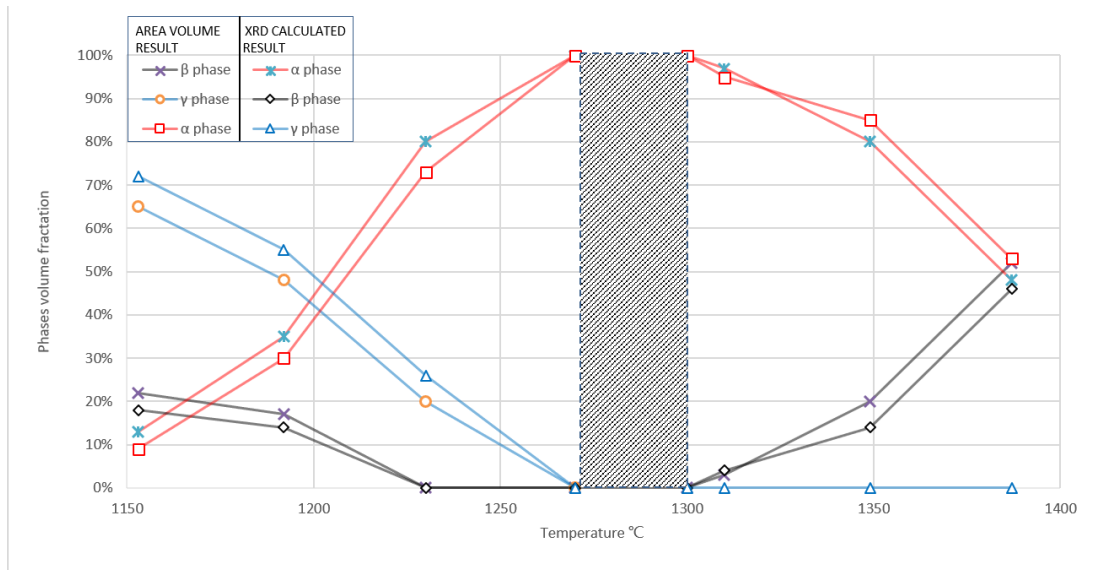


Figure 4.10 Phase diagram of Ti-44.2Al-4Nb-1Mo-0.8B, which is mapped by XRD result compared with the phase diagram mapped by area fraction.

Nominal composition at.%	Condition	Actual composition at.%				
		Ti	Al	Nb	Mo	B
Ti-44Al-4Nb-1Mo-0.3B	As-cast + HIPped	50.44	44.10	4.16	1.04	0.26
Ti-44.2Al-4Nb-1Mo-0.8B	As-cast + HIPped	50.50	43.80	4.00	0.98	0.72
Ti-44.6Al-4Nb-1Mo-0.1B	As-cast	49.93	44.60	4.22	1.04	0.21
Ti-45.5Al-4Nb-1Mo-0.3B	As-cast	49.20	45.40	4.09	1.03	0.28
HIPped at 1260°C, with a HIPping pressure of 150MPa 4 hours, and the heating and cooling rates were 5°C/min above 200°C and 10°C/min below 200°C.						

Table 4.1 Nominal and actual composition of used alloys during the study.

Temperature(°C)	Time(hour)	Cooling method
1230	3	Water quenching
1250	5/2	Water quenching
1270	2	Water quenching
1290	2	Water quenching
1310	3/2	Water quenching
1330	1	Water quenching
1350	1	Water quenching
1400	1/2	Water quenching

Table 4.2 Heat treatment details of Ti-44 Al-4Nb-1Mo-0.3B and Ti-45.5Al-4Nb-1Mo-0.3B.

Temperature(°C)	Time(hour)	Cooling method
1152	2	Water quenching
1191	2	Water quenching
1231	3/2	Water quenching
1271	3/2	Water quenching
1309	2	Water quenching
1349	3/4	Water quenching
1387	1/3	Water quenching

Table 4.3 Heat treatment details of Ti-44.6Al-4Nb-1Mo-0.1B and Ti-44.2Al-4Nb-1Mo-0.8B.

Heat treated temperature(°C)	Ti-44Al-4Nb-1Mo-0.3B			Ti-45.5Al-4Nb-1Mo-0.3B		
	β phase	α phase	γ phase	β phase	α phase	γ phase
1230	0%	59%±4%	40%±3%	0%	40%±2%	60%±4%
1250	0%	80%±3%	20%±1%	0%	55%±1%	45%±2%
1270	0%	100%	0%	0%	74%±2%	26%±3%
1290	3%±3%	97%±3.%	0%	0%	93%±2%	7%±2%
1310	10%±4%	90%±2%	0%	0%	100%	0%
1330	25%±4%	75%±2%	0%	0%	100%	0%
1350	40%±3%	60%±4%	0%	0%	100%	0%
1400	98%±4%	2%±1%	0%	54%±3%	46%±2%	0%

Table 4.4 The area fraction (representing the volume fraction) of the constituent phases for water quenched Ti-44Al-4Nb-1Mo-0.3B and Ti-45.5Al-4Nb-1Mo-0.3B after solution treatment.

Heat treated temperature(°C)	Ti-44.6Al-4Nb-1Mo-0.1B			Ti-44.4Al-4Nb-1Mo-0.8B		
	β phase	α phase	γ phase	β phase	α phase	γ phase
1152	16%±2%	12%±2%	71%±3%	18%±1%	9%±1%	72%±2%
1191	8%±1%	54%±1%	37%±1%	14%±1%	30%±2%	55%±3%
1231	0%	95%±1%	14%±2%	0%	73%±1%	26%±1%
1271	0%	96%±1%	3%±1%	0%	100%	0%
1309	0%	100%	0%	4%±1%	95%±1%	0%
1349	16%±1%	83%±2%	0%	14%±4%	85%±2%	0%
1387	43%±1%	56%±1%	0%	46%±2%	53%±3%	0%

Table 4.5 The area fraction (representing the volume fraction) of the constituent phases for water quenched Ti-44.6Al-4Nb-1Mo-0.1B and Ti-44.2Al-4Nb-1Mo-0.8B after solution treatment.

Heat treated temperature(°C)	Ti-44.2Al-4Nb-1Mo-0.8B		
	β phase	α phase	γ phase
1152	22%±1%	13%±1%	65%±2%
1191	17%±2%	35%±4%	48%±4%
1231	0%	80%±2%	20%±1%
1271	0%	100%	0%
1309	3%±1%	97%±1%	0%
1349	20%±3%	80%±1%	0%
1387	52%±3%	48%±3%	0%

Table 4.6 The volume fraction of Ti-44.2Al-4Nb-1Mo-0.8B. The result is calculated by the software Match automatically.

Alloy	Holding temperature (°C)	Holding Time (h)		
		1	2	4
Ti-44.6Al-4Nb-1Mo-0.1B	1290	NOT STABLE	-	-
Ti-44Al-4Nb-1Mo-0.3B	1270	STABLE	NOT STABLE	NOT STABLE
Ti-44.2Al-4Nb-1Mo-0.8B	1270	STABLE	STABLE	NOT STABLE

Table 4.7 Table of α grain growth stability assessment.

CHAPTER 5 STUDY OF CONTINUOUS COOLING TRANSFORMATION AND TEMPERATURE TIME TRANSFORMATION

5.1 Continuous Cooling Transformation on TNM-B Alloy

The experiments on continuous cooling transformation (CCT) were designed in order to study the effect of the relationship among microstructures, cooling rate, solution treatment time and temperature. Jominy end quenching (JQ), air cooling (AC) and furnace cooling (FC) were used in this section^[192].

5.1.1 Jominy End Quenching on Ti-44.2Al-4Nb-1Mo-0.8B and Ti-45Al-2Mn-2Nb-1B

The method of Jominy end quenching was used for the study of CCT on 0.8B alloy. As a well-established technique in steels for the determination of hardenability, Jominy end quenching was introduced by D. Hu to TiAl alloys in 2004^[90]. According to the study of phase diagram on 0.8B alloy, this alloy had both single β and α phase fields where solution treatment could be carried out.

Three sets of JQ experiments were designed during the study of CCT, including:

- 1) 0.8B alloy Jominy quenched from a single β phase (1400°C/15min/JQ), 2)
- 0.8B alloy Jominy quenched from a single α phase (1300°C/1h/JQ), 3)
- Ti-45Al-2Mn-2Nb-1B (4522XD) alloy Jominy quenched from a single α phase

(1300°C/1h/JQ) as reference. BSE images in Figure 5.1 showed typical microstructures at different locations along the axis of as-quenched bars.

The microstructure at 1mm from the quench end of β phase Jominy quenched 0.8B alloy had a large amount of α phases accompanied with some retained β phases at the grain boundary (Figure 5.1 a). Measured by linear intercept method, the size of α grain size was close to 20-30 μ m. Both α phase Jominy quenched 0.8B alloy and 4522XD alloy had a nearly full α microstructure (Figure 5.1 b, c, e and f) at 1mm and 2mm from the quench end, whose grain sizes were 30-40 μ m and 100-120 μ m respectively. Cooling rate got slower with the increase of distance from the quench end, leading to the transformation of α grain into lamellar colony. The size of the transformed lamellar colony was consistent with that of prior α grain. Thus, β phase solution treatment was an effective way to control the size of lamellar colonies.

As shown in Figure 5.1 d and g, some γ phases could be found in Jominy quenched 0.8B alloy after β phase solution treatment (2-5mm from the quench end).

Significant lamellar microstructures could be found in all three experimental subjects (10-60mm from the quench end). Slower cooling rate resulted in wider lamellar spacing (Figure 5.1 p, q, r, s, t and u). Clear β phase reprecipitates could be observed in α phase Jominy quenched 0.8B alloy whereas no β phase

reprecipitates could be found in 4522XD alloy.

5.1.2 Air and Furnace Cooling on Ti-44.2Al-4Nb-1Mo-0.8B

As mentioned above, microstructures and phases in TiAl alloy were greatly affected by cooling rate after solution heat treatment. Experiments on 0.8B alloy with different cooling methods (air cooling and interrupting furnace cooling) after solution heat treatment were designed.

BSE images of 0.8B alloy treated with air cooling (1290°C 2h AC) and interrupting furnace cooling (1290°C 2h FC 889°C AC) are shown in Figure 5.2 a and b respectively. 2-hour solution treatment at 1290°C was followed by air cooling in the fully lamellar microstructure with fine lamellae which had the average colony size of 70µm and no β phase precipitates. In addition, 2-hour solution treatment at 1290°C was followed by furnace cooling to 889°C and then by air cooling to fully lamellar microstructure, but lamellar spacing was thicker than that in air-cooled samples. However, significant β phase precipitates were found at the grain boundary. Thus, lower cooling rate led to thicker lamellae after the same solution heat treatment.

5.1.3 Interrupting Furnace Cooling Temperature Effect on Microstructure and Phase

Cooling rate exerted an impact on lamellar spacing and the precipitation

temperature of the β phase. From the phase diagram mapped above, the β phase started to reappear below 1225°C in equilibrium, but it should begin to precipitate at lower temperature during continuous cooling. Thus, the experiments at different interrupting temperatures were designed to confirm the precipitation temperature of the β phase during the process of furnace cooling.

The experiment with interrupting furnace cooling at different temperatures was designed in this section. After heat treated at 1290°C for 2 hours, all samples were interrupting furnace cooled to 1182°C, 1085°C, 987°C and 889°C. BSE images are shown in Figure 5.3 (a) 1290°C 2h FC 1182°C AC, (b) 1290°C 2h FC 1085°C AC, (c) 1290°C 2h FC 987°C AC and (d) 1290°C 2h FC 889°C AC. With a similar grain size of about 70 μ m, all samples had lamellar lathes of similar thickness. β phase precipitates could be observed in the samples with furnace cooling ending at all three lower temperatures except for 1182°C.

XRD scanning results shows there are no significant peaks of the β phase was seen in the XRD scanning result of the sample treated with 1290°C 2h FC 1182°C AC. However, the peaks of the β phase could be observed in the results of the samples with furnace cooling ending at all other three lower temperatures, Thus, interrupting furnace cooling at 1182°C suppressed β phase precipitation, but lower interrupting furnace cooling temperature encouraged β phase precipitation at both SEM and XRD levels.

5.2 Temperature Time Transformation on Ti-44.2Al-4Nb-1Mo-0.8B Alloy

As mentioned in the literature review, microstructure was affected by not only cooling rate, but also time and temperature, which thus made it necessary to study temperature time transformation (TTT) on 0.8B alloy.

5.2.1 Ageing with Different Times and Temperatures after Solution Heat Treatment

Ageing is an effective way to refine and stabilise lamellar microstructures and achieve advantageous properties of TiAl alloys. Air-cooled samples showed a highly non-equilibrium microstructure, thereby leading to the change of phases and microstructures during ageing.

TTT heat treatment conditions are shown in Table 5.1. The experiment revealed the relationship among temperature, time and microstructure. The α solution heat treated samples with air cooling were prepared and subsequently aged at different temperatures for different times. Ageing time was settled from 1 to 96 hours and ageing temperature was set to be 792°C and 889°C.

BSE images of these samples are shown in Figure 5.4. Samples aged at different temperatures for the same time displayed significant differences in microstructure. Samples aged at 889°C for short times showed the obvious

precipitation of the β phase and the coarsening of the γ phase at both triple points and lamellar colony boundaries. Almost no β phase precipitation and γ phase coarsening could be observed in the samples aged at 792°C for less than 4 hours. Thus, more volumes of β and γ phases could be produced at higher ageing temperature at lamellar colony boundaries.

Samples aged at the same temperature for different times also displayed significant differences in microstructure. Fine lamellae and no β phase precipitation and γ phase coarsening could be observed in the samples aged at 792°C for less than 2 hours (Figure 5.4 a and c) at both triple points and lamellar colony boundaries. Ageing time would not significantly change lamellar spacing. A significant increase in the volume fraction of β and γ phases was related to the increase of ageing time (Figure 5.4 g, i, k, m, o and q). The same phenomenon also occurred in the samples aged at 889°C. Thus, long ageing time could lead to β phase precipitation and γ phase coarsening at both triple points and lamellar colony boundaries. Similar changes occurred in the samples aged at high temperature (889°C). The only difference was that β phase precipitation and γ phase coarsening could be observed in the samples aged for a short time (1 hour).

The density and size of grain boundary β phase precipitates were counted in the study. Diagrams for the density and grain size of β precipitates during ageing

time are mapped and shown in Figure 5.5 and 5.6 respectively. The method adopted for the density and grain size of β precipitates was the method of counting squares for approximate calculation.

The density of β precipitates increased with the decrease of ageing temperature and decreased with the increase of ageing time probably because adjacent β precipitates were merged during the growth process. Shorter ageing time (4 and 8 hours) and lower ageing temperature at 792°C could contribute to higher nucleation rate. Longer ageing time and higher ageing temperature at 889°C could encourage the growth rate of β phase precipitates.

It was difficult to compare the changes in the lamellar spacing of the samples listed in Figure 5.4 at the SEM level because they had too fine lamellae. However, lamellar spacing had a direct impact on hardness. For example, the smaller the lamellar spacing was, the higher the hardness would be. Therefore, those samples were evaluated by hardness testing. Vickers hardness testing results are shown in Figure 5.7. Two sets of samples heat treated at different temperatures showed similar hardness curves with the lowest and highest values. The lowest value might result from the relaxation of internal stress during ageing. As-cast samples came with high internal stress relaxing in the aging process, leading to the drop of hardness first. The highest value might be caused by the overage and precipitate of the B_2 phase. Extremely fine B_2 phase

might precipitate to form lamellae, leading to the increase of hardness. Then, hardness saw a slight drop again because of the continuous growth of the B₂ phase. The sample aged at 792°C for 40 hours would reach hardness peak and the sample aged at 889°C for around 30 hours would reach hardness peak because higher ageing temperature would speed up the ageing process. The large difference between two curves in hardness was observed at 60 to 96 hours because the β phase precipitated from lamellar colonies in the samples aged at 889°C. β precipitates changed phase content and microstructure, which thus enhanced hardness. The hardness testing results could not simply reflect the change of lamellar spacing in the experiment related to TTT on 0.8B alloy. This was because TTT brought about changes in phase content and microstructure, subsequently resulting in different hardnesses.

It's worth noting that a lamellar grain decomposed at 889°C from 64 hours (Figure 5.4 p and r). Formed from lamellar lathes directly, the particles were more profound after aged for 96 hours, as shown in Figure 5.4 (r) 1290°C 2h AC 889°C 96h AC. The nature of decomposition was not characterised. The precipitates seemed to have an orientation relationship with lamellae because of their fineness and the need for TEM analysis. Further study was discussed in the following chapter.

Solution heat treatment at 1290°C and subsequent furnace cooling to 1182°C

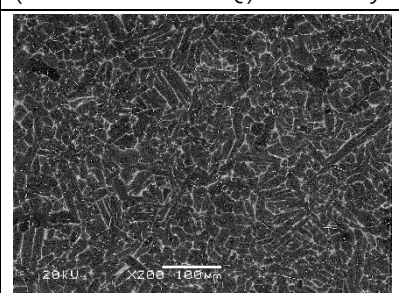
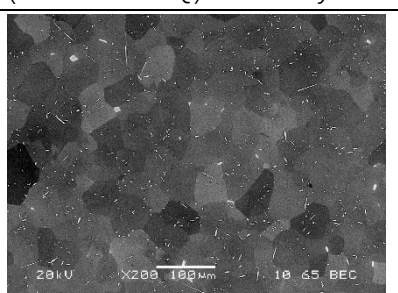
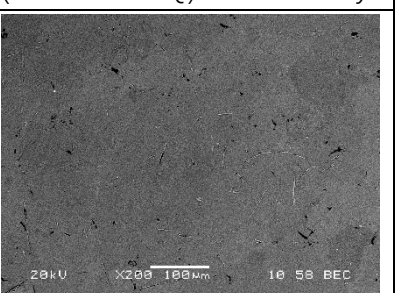
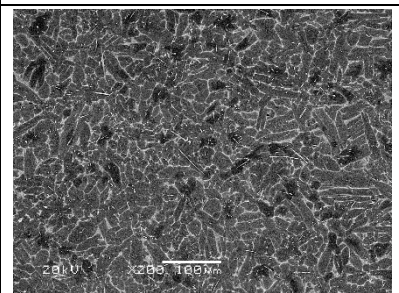
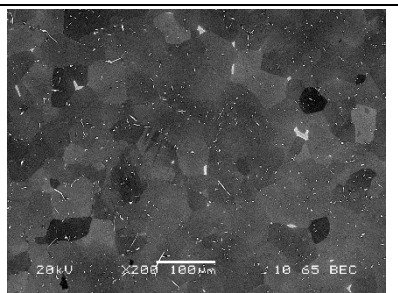
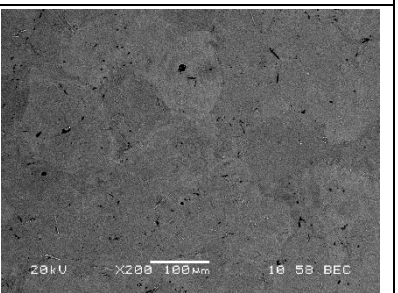
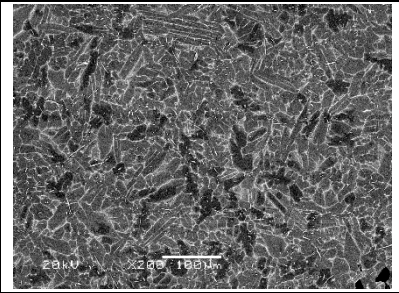
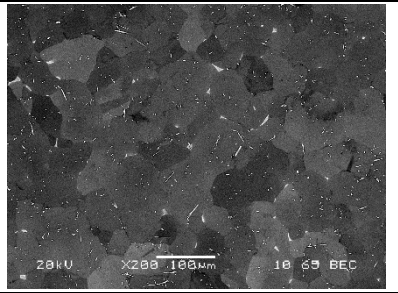
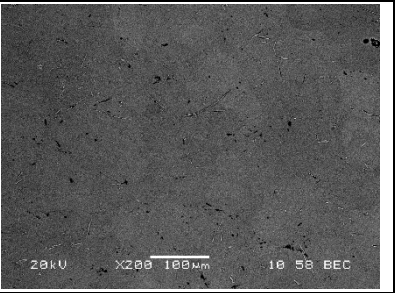
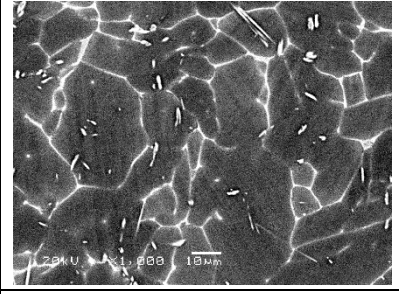
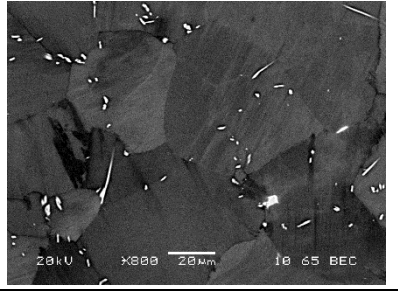
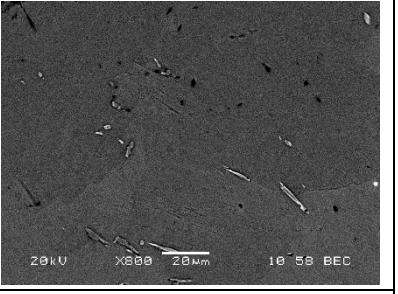
followed by air cooling and subsequent ageing at 792°C and 889°C for 1, 2, 4 and 8 hours were designed for comparison. BSE mode SEM images are shown in Figure 5.9. Furnace-cooled samples had similar lamellar grain size with and thicker lamellar lathes than air-cooled ones. All furnace-cooled samples showed the coarsening of the γ phase. Coarse γ phase grew slowly with the increase of ageing time (Figure 5.9 (a) 1290°C 2h FC 1182°C AC 792°C 1h AC, (g) 1290°C 2h FC 1182°C AC 792°C 8h AC and (b) 1290°C 2h FC 1182°C AC 889°C 1h AC, (h) 1290°C 2h FC 1182°C AC 889°C 8h AC). A small amount of β phases could be observed in the samples aged at lower temperature (792°C). Under the condition of the same ageing time, the higher the ageing temperature was, the larger the size of β phase precipitates generated would be. Under the condition of the same ageing temperature, the longer the ageing time was, the larger the size of β phase precipitates generated would be.

These comparisons revealed a similar result with air-cooled samples. The results could be summarised as follows: Ageing at 792°C for a short time encouraged the nucleation of β phase precipitates. The larger the cooling temperature was, the higher the nucleation density of β phase precipitates would be. For the samples aged for a longer time, ageing at 889°C provided a bigger size of β phase precipitates than that at 792°C. Grain boundary γ and β phases grew up over time during ageing.

5.2.2 Double Ageing on Solution Treated Ti-44.2Al-4Nb-1Mo-0.8B Alloy

As described in the last section, ageing at low temperature for a short time after α solution treatment could encourage the nucleation of β phase precipitates and ageing at high temperature for a short time after α solution treatment could encourage the growth of the β phase for 0.8B alloy. Thus, double ageing at lower temperature first and higher temperature later could contribute to the high nucleation rate and fast growth of β phase precipitates.

Double aged samples (1290°C 2h AC 792°C 2h AC 889°C 2h AC and 1290°C 2h AC 792°C 2h AC 889°C 4h AC) were prepared to compare with long-time single aged ones. BSE mode SEM images of the above double aged samples are displayed in Figure 5.9. The two samples showed very fine lamellae in lamellar colonies with significant volumes of β and γ phases observed at lamellar colony boundaries. By the comparison between images in Figure 5.10 and 5.4, the microstructure of the double aged sample (1290°C 2h AC 792°C 2h AC 889°C 2h AC) was very close to that of the long-time single aged sample (1290°C 2h AC 792°C 96h). It meant that the double aged sample at a lower temperature first and higher temperature later for a short time could produce the same microstructure with the long-time single aged sample.

Ti-44.4Al-4Nb-1Mo-0.8B (1400°C/15min/JQ) 0.8B alloy	Ti-44.2Al-4Nb-1Mo-0.8B (1300°C/1h/JQ) 0.8B alloy	Ti-45Al-2Mn-2Nb-1B (1300°C/1h/JQ) 4522XD alloy
		
(a) 1mm from the quench end	(b) 1mm from the quench end	(c) 1mm from the quench end
		
(d) 2mm from the quench end	(e) 2mm from the quench end	(f) 2mm from the quench end
		
(g) 5mm from the quench end	(h) 5mm from the quench end	(i) 5mm from the quench end
		
(j) 10mm from the quench end	(k) 10mm from the quench end	(l) 10mm from the quench end

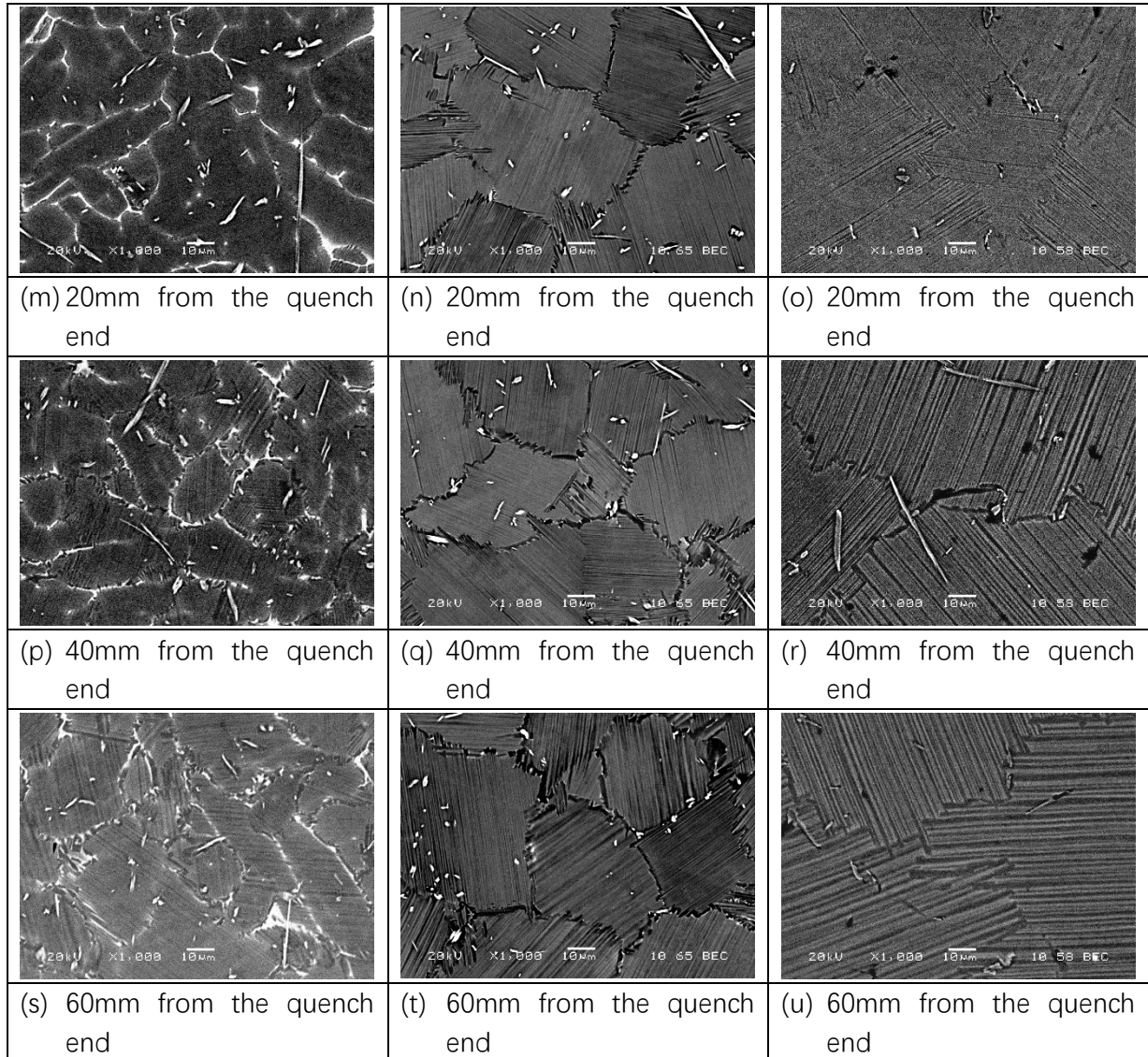


Figure 5. 1 BSE images of β phase Jominy quenched 0.8B alloy, α phase Jominy quenched 0.8B alloy and 4522XD alloy. The images were taken at different distances away from the quench end, as indicated at the bottom of images.

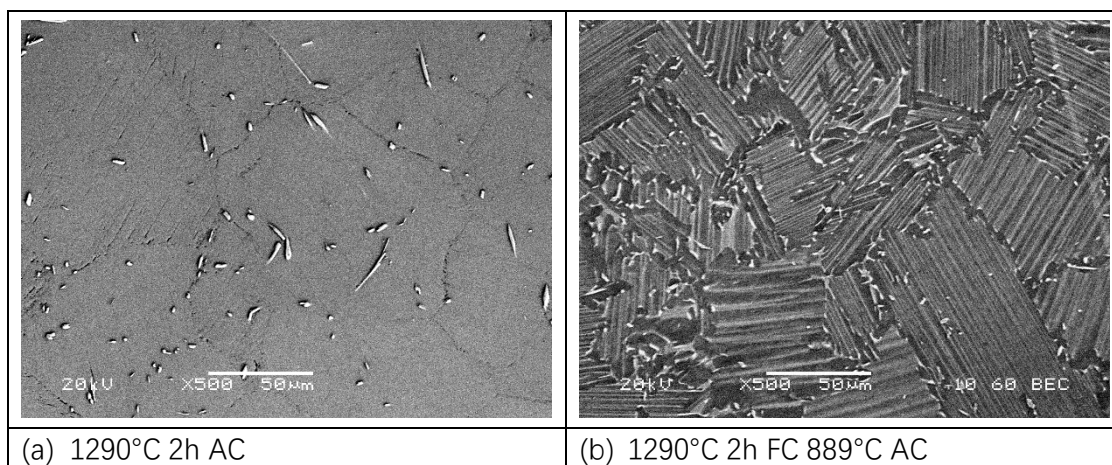


Figure 5. 2 BSE mode SEM images of 0.8B alloy with different cooling rates after α phase solution treatment: (a) Air cooling with hydrofluoric (HF) acid corrosion and (b) Furnace cooling to 889°C and then air cooling.

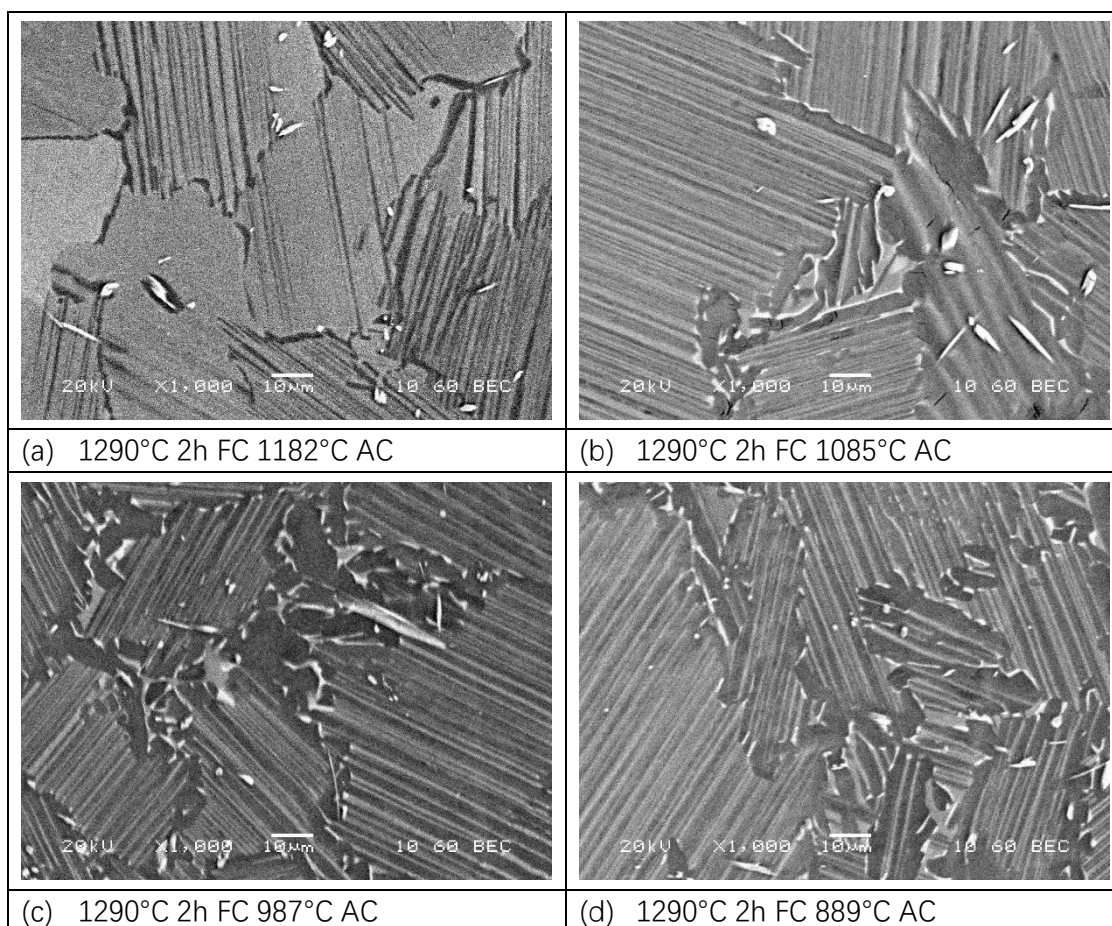
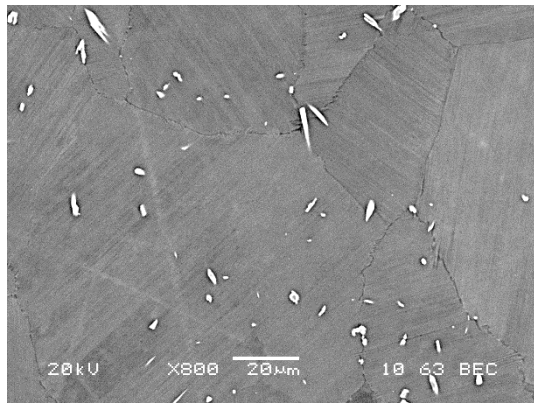
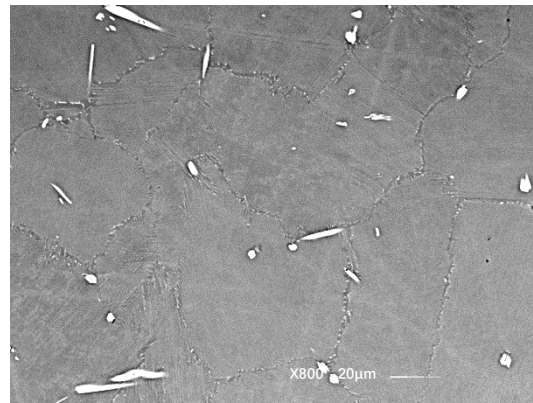


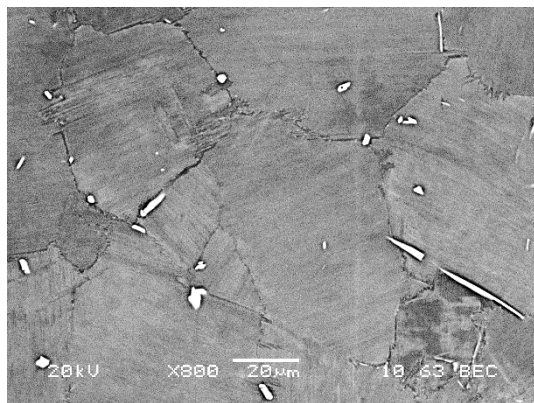
Figure 5. 3 BSE mode SEM images of 0.8B alloy with interrupting furnace cooling at different temperatures after α phase solution treatment. (a) 1290°C 2h FC 1182°C AC, (b) 1290°C 2h FC 1085°C AC, (c) 1290°C 2h FC 987°C AC and (d) 1290°C 2h FC 889°C AC.



(a) 1290°C 2h AC 792°C 1h AC



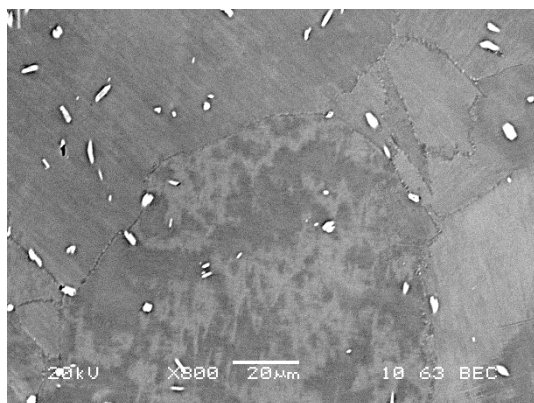
(b) 1290°C 2h AC 889°C 1h AC



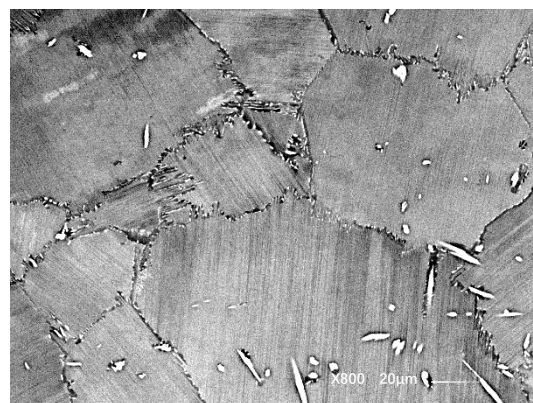
(c) 1290°C 2h AC 792°C 2h AC



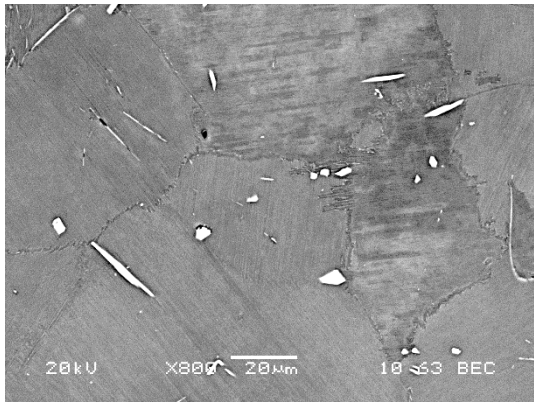
(d) 1290°C 2h AC 889°C 2h AC



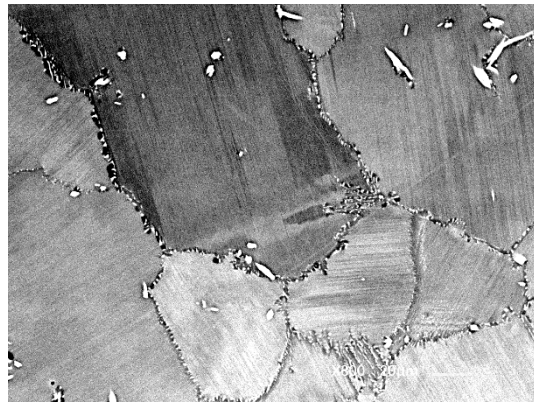
(e) 1290°C 2h AC 792°C 4h AC



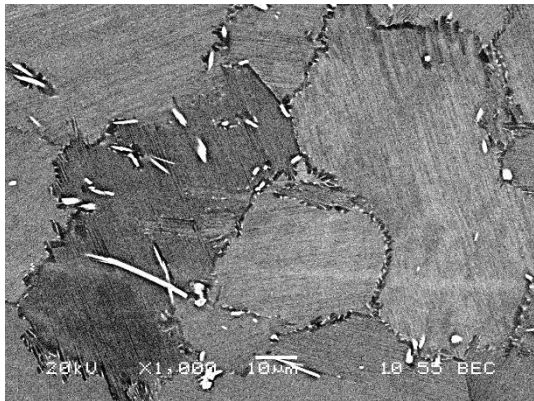
(f) 1290°C 2h AC 889°C 4h AC



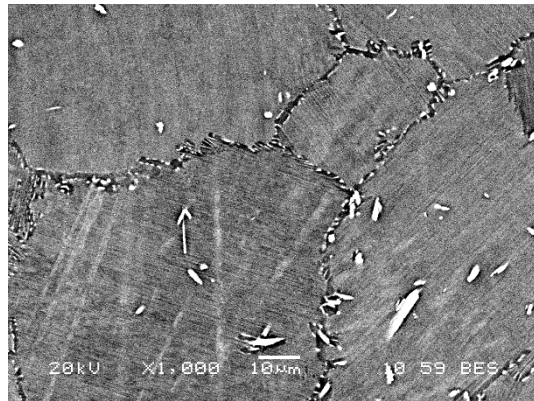
(g) 1290°C 2h AC 792°C 8h AC



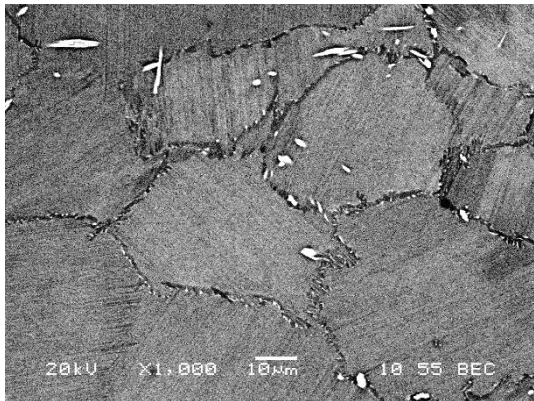
(h) 1290°C 2h AC 889°C 8h AC



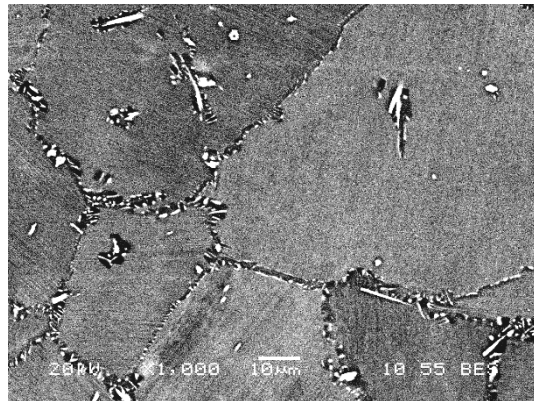
(i) 1290°C 2h AC 792°C 16h AC



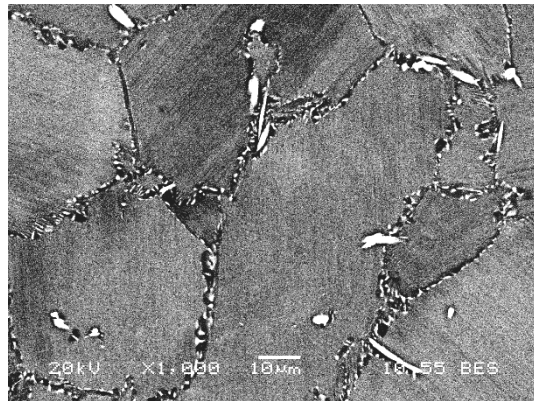
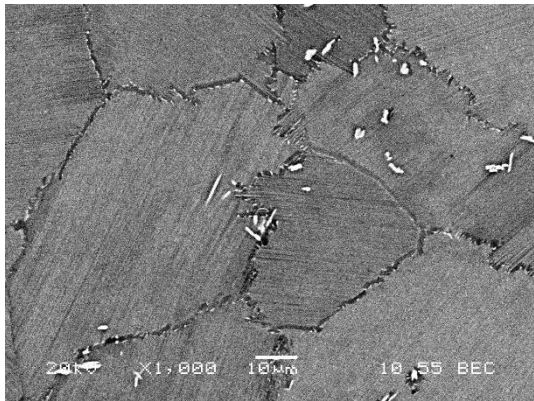
(j) 1290°C 2h AC 889°C 16h AC



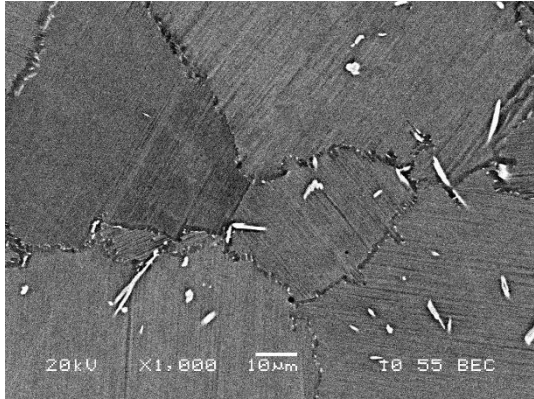
(k) 1290°C 2h AC 792°C 24h AC



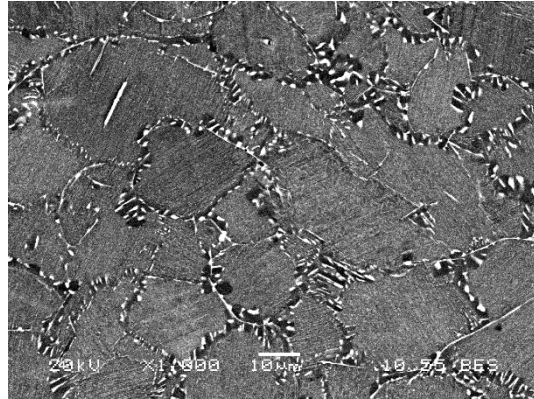
(l) 1290°C 2h AC 889°C 24h AC



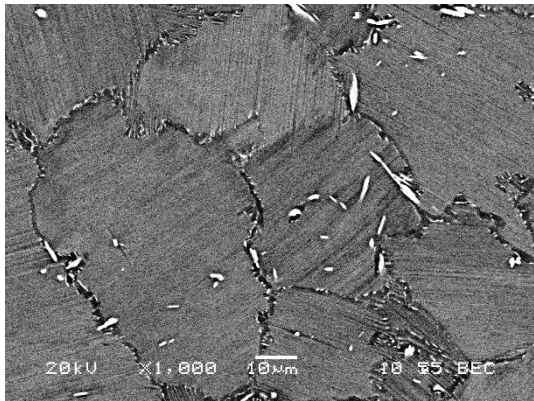
(m) 1290°C 2h AC 792°C 48h AC



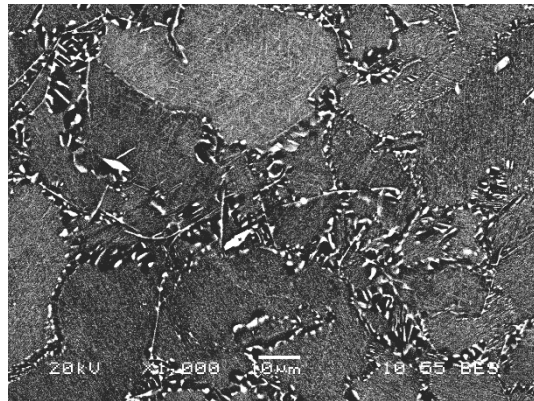
(n) 1290°C 2h AC 889°C 48h AC



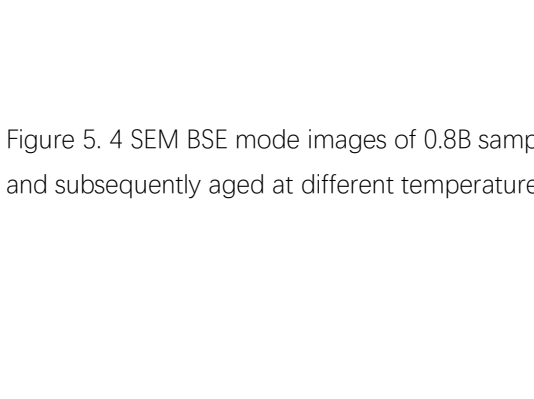
(o) 1290°C 2h AC 792°C 64h AC



(p) 1290°C 2h AC 889°C 64h AC



(q) 1290°C 2h AC 792°C 96h AC



(r) 1290°C 2h AC 889°C 96h AC

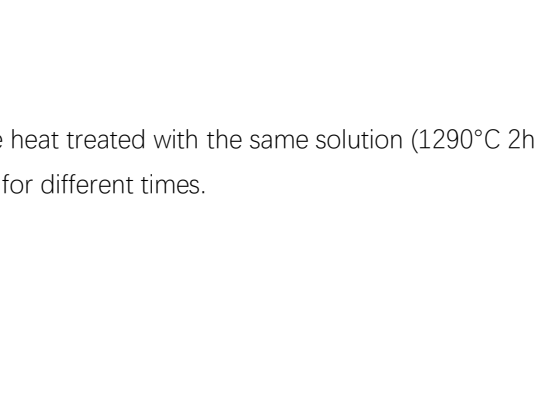


Figure 5. 4 SEM BSE mode images of 0.8B sample heat treated with the same solution (1290°C 2h AC) and subsequently aged at different temperatures for different times.

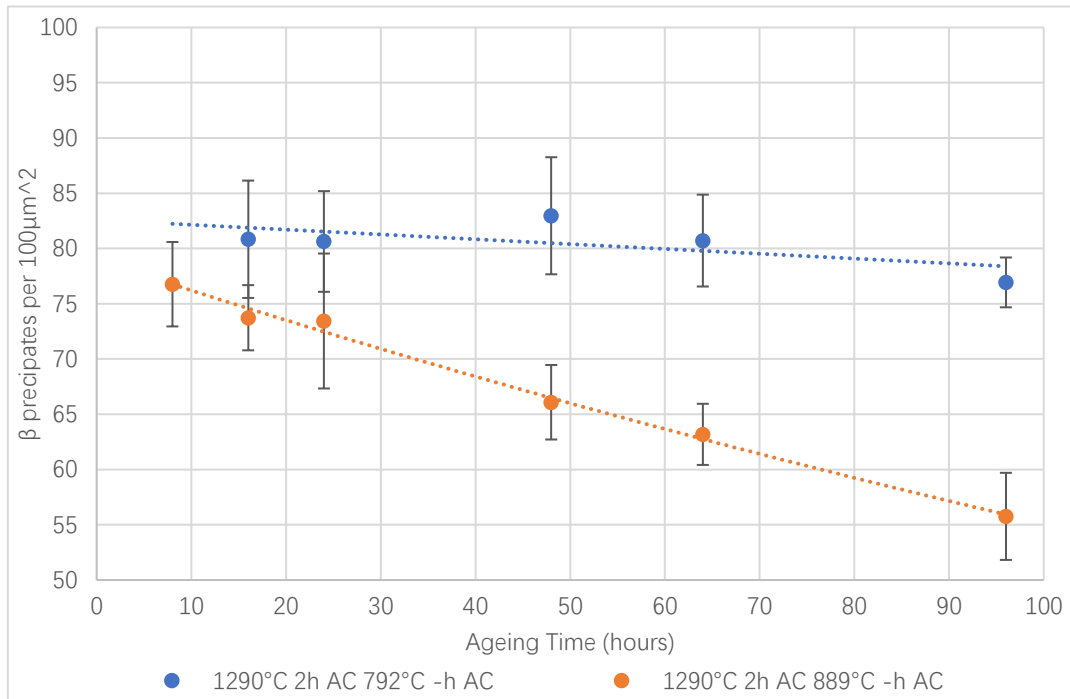


Figure 5. 5 Diagram of β precipitates per $100\mu\text{m}^2$ grain boundary against different ageing times for 0.8B alloy aged at 792°C and 889°C .

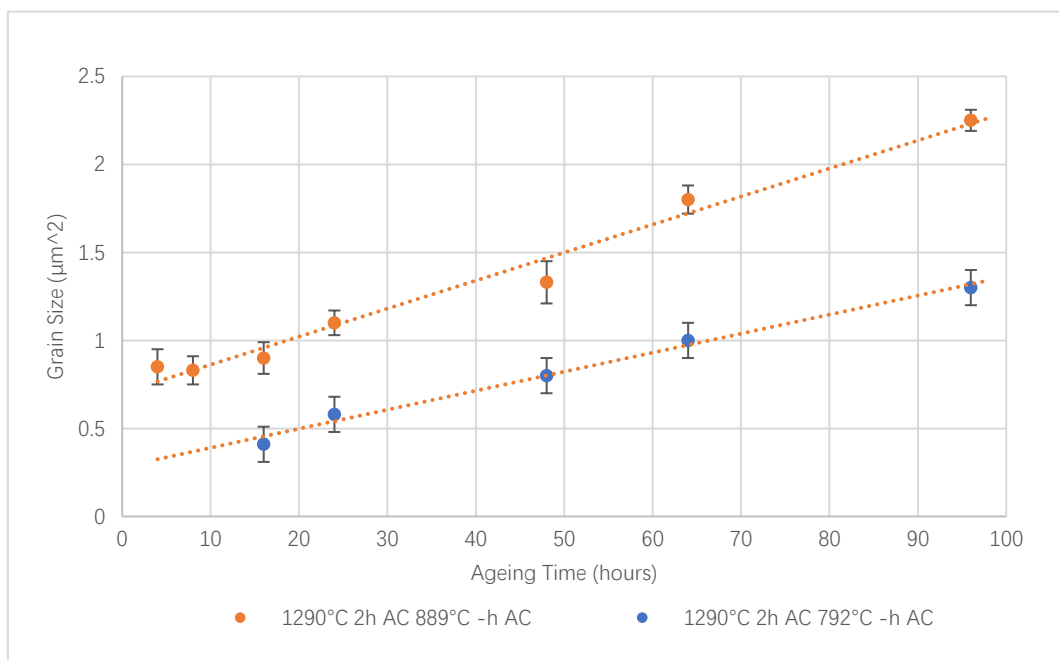
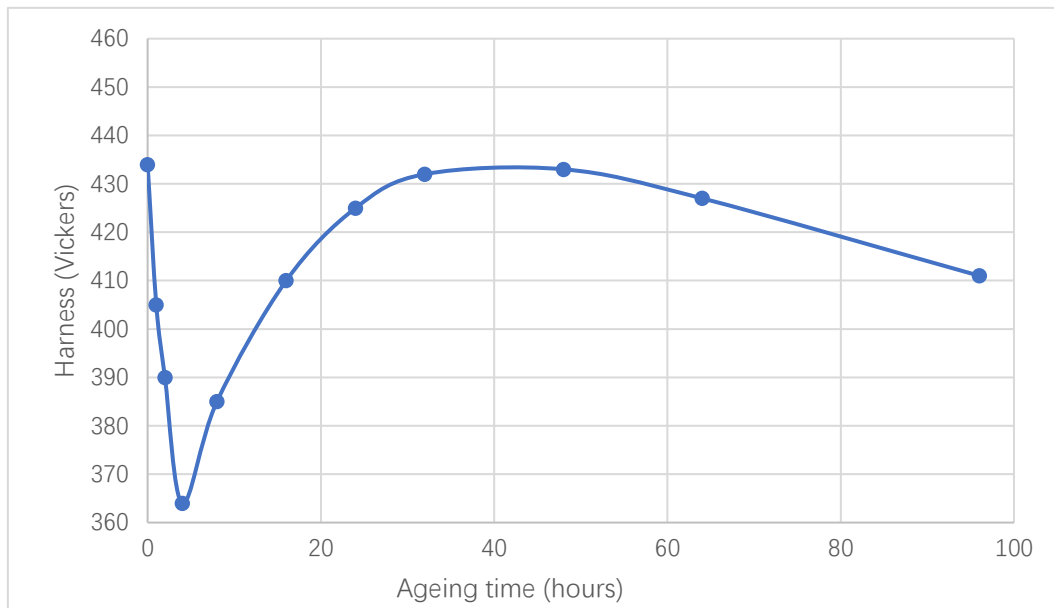
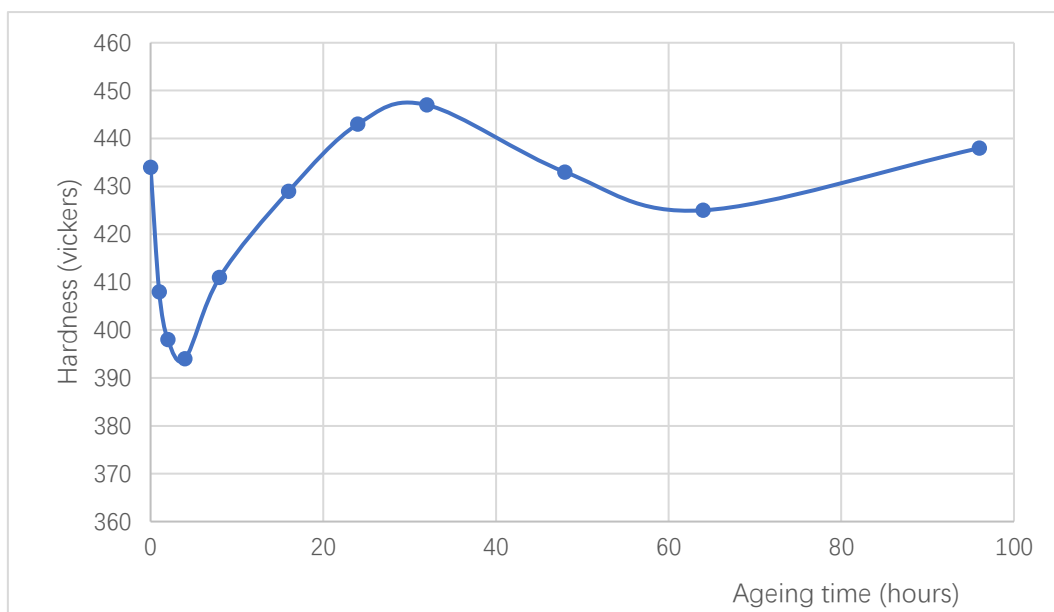


Figure 5. 6 Diagram for the grain size of β precipitates against different ageing times for 0.8B alloy aged at 792°C and 889°C .

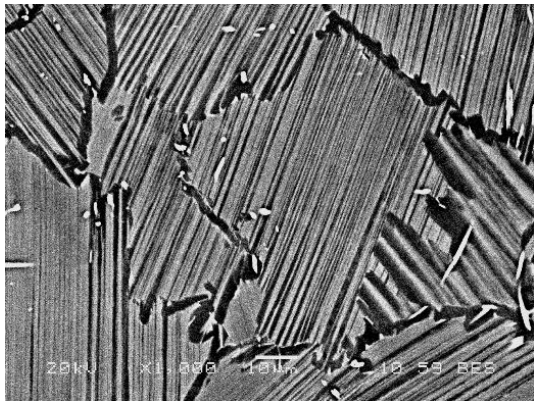


(a) 0.8B alloy-1290°C 2h AC 792°C -h AC

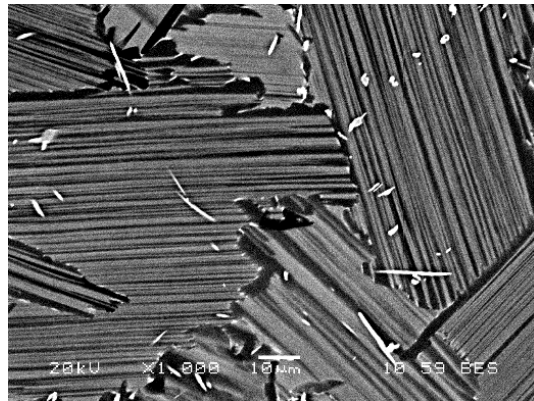


(b) 0.8B alloy-1290°C 2h AC 889°C -h AC

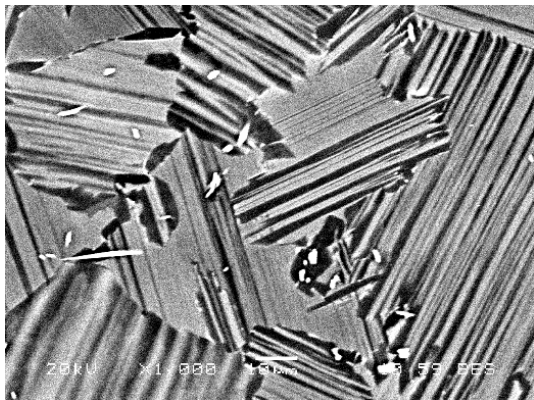
Figure 5. 7 Diagram for the Vickers hardness of 0.8B samples heat treated under the condition of 1290°C 2h AC and subsequently aged at 792°C and 889°C for different times and then air cooling.



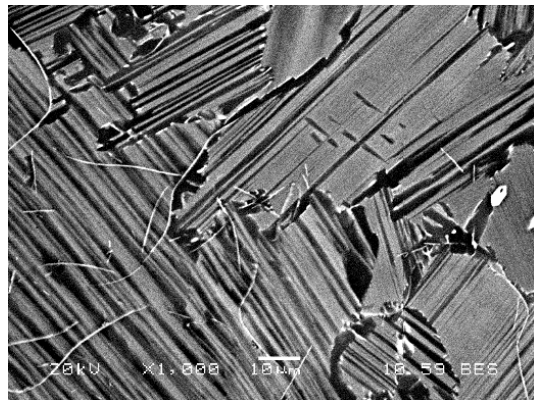
(a) 1290°C 2h FC 1182°C AC 792°C 1h AC



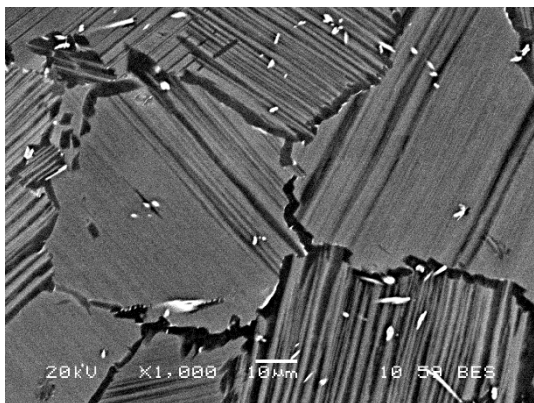
(b) 1290°C 2h FC 1182°C AC 889°C 1h AC



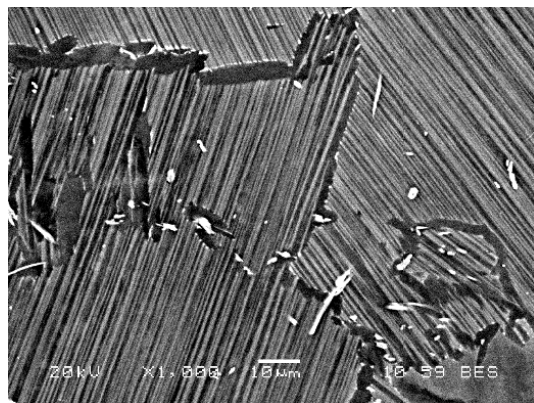
(c) 1290°C 2h FC 1182°C AC 792°C 2h AC



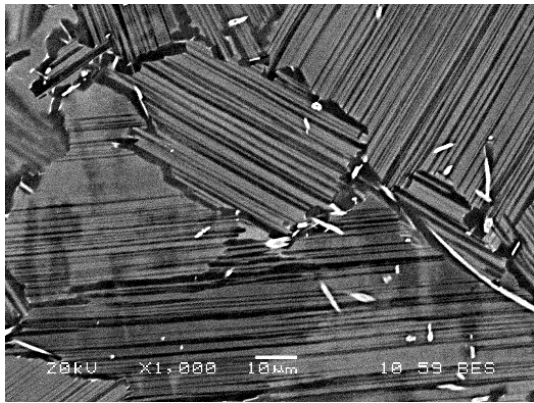
(d) 1290°C 2h FC 1182°C AC 889°C 2h AC



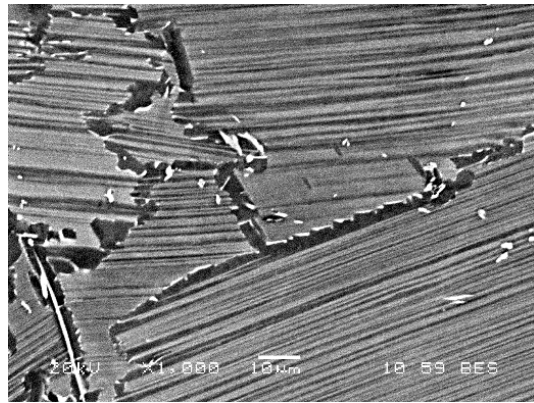
(e) 1290°C 2h FC 1182°C AC 792°C 4h AC



(f) 1290°C 2h FC 1182°C AC 889°C 4h AC

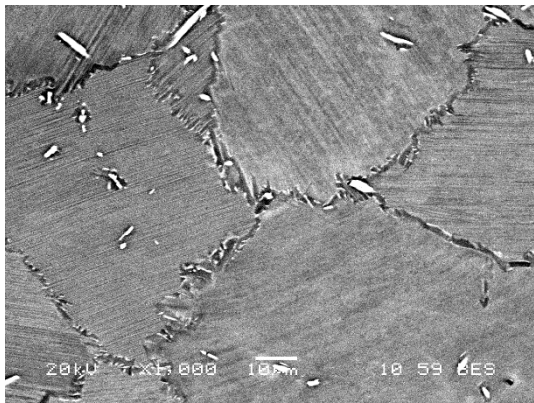


(g) 1290°C 2h FC 1182°C AC 792°C 8h AC

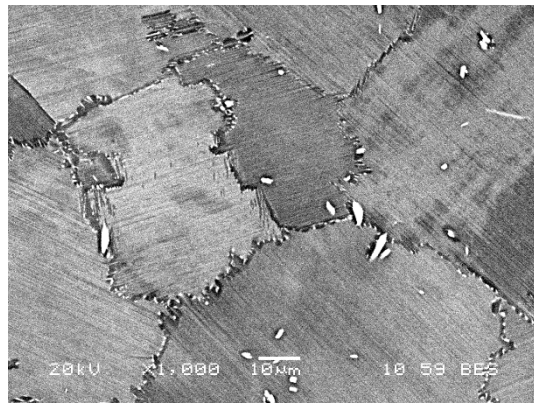


(h) 1290°C 2h FC 1182°C AC 889°C 8h AC

Figure 5. 8 SEM BSE mode images of 0.8B samples heat treated with the same solution (1290°C 2h FC 1182°C AC) but different ageing temperatures ((a),(b),(e) and (g) ageing at 792°C, (a),(b),(e) and (g) ageing at 889°C) and times (1 hour on (a) and (b), 2 hours on (c) and (d), 4 hours on (e) and (f) and 8 hours on (g) and (h)).



(a) 1290°C 2h AC 792°C 2h AC 889°C 2h AC



(b) 1290°C 2h AC 792°C 2h AC 889°C 4h AC

Figure 5. 9 SEM BSE images for 0.8B alloy double aged after α phase solution treatment, which (a) 1290°C 2h AC 792°C 2h AC 889°C 2h AC and (b) 1290°C 2h AC 792°C 2h AC 889°C 4h AC.

Solution treatment Temperature (°C)	Time (h)	Cooling method	Ageing temperature (°C)	Time (h)	Cooling method
1290	2	AC	792	1	AC
1290	2	AC	792	2	AC
1290	2	AC	792	4	AC
1290	2	AC	792	8	AC
1290	2	AC	792	16	AC
1290	2	AC	792	24	AC
1290	2	AC	792	48	AC
1290	2	AC	792	64	AC
1290	2	AC	792	96	AC
1290	2	AC	889	1	AC
1290	2	AC	889	2	AC
1290	2	AC	889	4	AC
1290	2	AC	889	8	AC
1290	2	AC	889	16	AC
1290	2	AC	889	24	AC
1290	2	AC	889	48	AC
1290	2	AC	889	64	AC
1290	2	AC	889	96	AC

Table 5. 1 0.8B samples solution treated at 1290°C for 2 hours, then air cooled, subsequently aged at 792°C and 889°C for different times and then air cooled.

CHAPTER 6 β PHASE AND GRAIN BOUNDARY ANALYSIS ON Ti-44.2Al-4Nb-1Mo-0.8B ALLOY

6.1 Precipitates of the β Phase in Ti-44.2Al-4Nb-1Mo-0.8B Alloy during Cooling and Ageing

As mentioned in chapter 5, the β phase precipitated in 0.8 alloys at the grain boundary and within lamellae during cooling and ageing. The crystal structure of these two β phases precipitated was identified via TEM.

6.1.1 Precipitation of the β Phase at Grain Boundaries and Triple Points

Ageing at 889°C and 792°C for a long time led to the precipitation of new particles. Growing up with the increase of ageing time and forming very bright contrast in BSE mode SEM images shown in Figure 5.4 (long-time aged samples), these particles were predicted to be the β phase in previous work. Because of containing a higher concentration of Ti, the β phase showed the brightest contrast in BSE images. Further EDS and TEM work was designed to verify the composition and crystal structure of these particles.

An EDS map was used to reveal the compositional differences between unknown particles and phases in the samples heat treated at 1290°C AC 2h 889°C 2h AC. EDS mapping results are shown in Figure 6.1. It was distinct that

the concentration of Ti and Al in precipitated particles was very close to that of the α_2 phase, but the particles had a higher concentration of Mo than the α_2 phase. Thus, the particles were likely to be β phase precipitates because Mo was an element stabilising the β phase. The left corner area of the Figure 6.1 contains complex borides which contains Nb, Mo and B.

EDS spot analysis was also used to confirm and compare the compositional differences between known (boride and the γ phase) and unknown phases (the predicted β phase). Three spots are marked in Figure 6.2 (a), including spot A inside boride, spot B inside the γ phase and spot C inside the predicted β phase. Shown in Figure 6.2 (b), EDS spectra displayed similar results with EDS maps (Figure 6.1). Compared to the other two spots, spot A showed a very high content of Nb and B, but a very low content of Al and a fairly low concentration of Ti because Nb was the forming element of borides in this alloy. It was straightforward to show a significant difference between the spectra of spot B and C in Figure 6.2 (b). For example, spot C had a lower concentration of Al but a higher concentration of Mo, which was very close to the compositional difference between B_2 and γ phases, which just proved the unknown phase precipitated from grain boundaries in the previous study was likely to be the B_2/β phase.

EDS line-scan was also used to reveal the composition details of the predicted β

phase. The line-scan results came with the reading of atomic percentage, and composition could be used to identify phases. Figure 6.3 (b) shows some different phases/precipitates observed in the predicted β phase. EDS line-scan across an unknown particle inside the B_2/β phase is shown in Figure 6.3 (c), indicating that B_2/β phase had a lower content of Al and a higher content of Mo and Nb than the γ phase. However, particle B had a higher content of Ti and a lower content of Mo than the predicted β phase, which was likely to be a ω phase precipitated from B_2/β phase during the cooling process.

It was still necessary to confirm the crystal structure of these phases by electron diffraction. Figure 6.4a shows a high angle annular dark field (HAADF) STEM image of the B_2/β phase. Figure 6.4(b), (c) and (d) are corresponding selected area diffraction (SAD) patterns identified to be the B_2 phase with a zone axis of $[110]$, $[111]$ and $[131]$ respectively. The angles between $[110]$ / $[111]$, $[110]$ / $[131]$ and $[111]$ / $[131]$ were 35.26° , 31.48° and 29.50° respectively. The recorded tilting parameters between (b) / (c), (b) / (d) and (c) / (d) were ($\alpha=6.6^\circ$, $\beta=9.2^\circ$), ($\alpha=-27.14^\circ$, $\beta=21.06^\circ$) and ($\alpha=-18.4^\circ$, $\beta=-8.7^\circ$) respectively. By calculation with the formula $\text{angle} = \arccos(\cos(\alpha_2 - \alpha_1) * \cos(\beta_2 - \beta_1))$, the angles between (a)/(b), (b)/(c) and (a)/(c) were 35.53° , 30.90° and 30.41° respectively. The experimental titled angles were very close to the calculated angles, meaning the correctness of the index in Figure 6.4.

High-resolution transmission electron microscopy (HRTEM) images had been taken to identify the particles precipitated from the B₂ phase. Images of 0.8B alloy heat treated with 1290°C AC 2h 889°C 2h AC are shown in Figure 6.5. Three different areas in Figure 6.5c were selected to perform fast Fourier transform (FFT). The FFTed diffraction patterns shown in Figure 6.5d 6.5(e) and 6.5(f) were from the ω phase only, matrix B₂ phase only and ω and B₂ phases respectively. The precipitated particle in the B₂ phase was identified as the hexagonal structure ω phase with $a=0.450$ nm and $c=0.273$ nm. The zone axis of ω and B₂ phases in Figure 6.5 (d) and 6.5 (e) were [0001] and [111] respectively. B₂ and ω phases showed an orientation relationship: $(0\ -11)\ B_2 // (1,1, -2,0)\ \omega$ and $[111]\ B_2 // [0001]\ \omega$, as indicated in Figure (f).

Fig. 6.6 shows TEM/STEM images and different SAD patterns of the grain boundary β/B_2 phase in longer-time aged samples (1290°C 2h AC 889°C 96h AC). Figure 6.6a is a low-magnification bright field (BF) STEM image of the grain boundary β/B_2 phase whose higher-magnification HAADF and BF STEM images are shown in Figure 6.6 b and c respectively. Figure 6.6d is a SAD pattern from a grain boundary β/B_2 phase in Figure 6.6b/c. The diffraction analysis confirmed that the grain boundary phase was the B₂ phase (Figure 6.6d).

According to the above results, the grain boundary β/B_2 particle precipitated during ageing in 0.8B alloy was an ordered cubic ($Pm\bar{3}m$) structure B₂ phase

while the particle precipitated within the B_2 phase was a hexagonal structure ω phase.

6.1.2 Precipitation of the β Phase in Lamellar Colonies

STEM images (Figures 6.6 e and f) showed the formation of the β/B_2 phase within lamellae. SAD pattern from a β/B_2 phase shown in Figure 6.5e is illustrated in Figure 6.6 g, which confirmed that such a particle was the B_2 phase. A dark field TEM image of the precipitates within lamellae is shown in Figure 6.6h.

Many B_2/β phase precipitates were observed in the lamellar colonies of long-time aged samples which were heat treated by ageing at 889°C for 64 hours or even longer time after solution heat-treated with air cooling at 1290°C for 2 hours.

BSE mode SEM images of samples aged for different times are shown in Figure 6.7. No B_2/β phase precipitates were observed in the samples aged at 889°C for a short time (e.g. 4h), as seen in Figure 6.7 (a). Morphologies of B_2/β phase precipitates are shown in Figure 6.7 (b), (c) and (d). As can be seen in SEM images, the precipitates precipitated inside lamellar grains were regularly arranged within lamellar laths and might have an orientation relationship with parent lamellar grains.

TEM EDS map was scanned and used to reveal the compositional differences between the B_2/β phase within lamellae and lamellar colonies. The particles had a similar concentration of Ti and Al with the α_2 phase respectively, as seen in Figure 6.8 (b) and (c). However, these particles contained a higher concentration of Mo compared to the α_2 phase, which thus might be the B_2/β phase because Mo was an element stabilising the B_2/β phase.

EDS line-scan represented the same result with the EDS map. Compared with its parent α_2 phase, the particle had a lower concentration of Ti, but a higher content of Mo, as shown in Figure 6.9 (b). Compared with the nearby γ phase, the particle had a lower concentration of Al, but a higher concentration of Ti and Mo, as shown in Figure 6.9 (d). The composition of α_2 phase precipitates was very close to that of B_2 phase precipitates. Thus, it was very likely that these precipitates were B_2 phase precipitates.

To identify the compositional differences between in-lamellae B_2/β precipitates and grain boundary β precipitates, three different positions and nine different spots were selected for the scanning of EDS spots. The EDS scanning result is shown in Figure 6.10. Spot 'a' and 'd' marked in Figure (a) and (d) were respectively located at the β phase; spot 'b' and "e" marked in Figure (b) and (e) were respectively located at the α_2 phase; spot 'c' and 'f' marked in Figure (c) and (f) were respectively located at the γ phase; spot 'g', 'h' and "" marked in

Figure (g), (h) and (i) were respectively located at the grain boundary β phase. The results of the composition analysis are shown in Figure (j). Curve (a), (d), (j), (h) and (i) almost completely coincided, which meant that these precipitates were likely to be β phases because of owning nearly the same composition with the grain boundary B_2 phase.

S/TEM examination showed the precipitation of the B_2/β particle within γ and α_2 lamellae. Figure 6.11a illustrates an example of the precipitation of the B_2/β particle within the γ lath while Figure 6.11b presents the precipitation of some B_2/β particles within the α_2 lath. A SAD diffraction from a B_2/β particle within the γ lath is shown in Figure 6.12a, which confirmed that the particle was the B_2 phase. Figure 6.13 shows the HRTEM image of a B_2/β particle within the α_2 lath (b) and corresponding FFTed diffraction patterns (c). The analysis of diffraction patterns indicated that the precipitate within the α_2 lath was the B_2 phase. The FFTed diffraction patterns with the index of the adjacent γ phase are shown in Figure (d).

6.2 Analysis of Grain Boundary Morphologies

The 0.8B alloy with lamellar microstructure had two main grain boundary morphologies, namely the discontinuous coarsening (DC) of the grain boundary γ phase and interlock lamellar microstructure of neighbouring colonies, as shown in Figure 6.14 and 6.18.

6.2.1 Coarsening of the γ Phase at the Grain Boundary

DC of the γ phase widely existed in the aged samples after α phase solution treatment in 0.8B alloy. As mentioned in the literature review, the coarsening of lamellae occurred at high temperature, which thus degraded creep resistance significantly. As a result, consideration should be given to grain boundary coarsening during heat treatment.

As mentioned in literature review 2.6, the DC of γ phase at the grain boundary had three morphologies. Typical BSE images are shown in Figure 6.14. The α solution heat treated 0.8B alloys with different cooling rates and aged at 792°C and 889°C for different times was designed to reveal the relationship between cooling speed and grain boundary coarsening in 0.8B alloy. Heat treatment conditions are shown in Table 5.1. Corresponding BSE mode SEM images are shown in Figure 6.15. Apparently, the width of the grain boundary γ phase saw no obvious changes at the SEM level. The widths of the grain boundary γ phase under different heat treatment conditions are plotted in Figure 6.16. For the aged samples after interrupting furnace cooling (Conditions were listed in Table 5.1 and Figure 6.16), the width of the coarse γ phase nearly kept a constant ($\sim 3.1\mu\text{m}$). Thus, no grain boundary γ phase coarsening occurred in the interrupting furnace cooled samples aged at 792°C and 889°C. As already mentioned in chapter 5.1, the width of the coarse γ phase significantly increased with

temperature and time for the aged samples after air cooling (Conditions were listed in Table 5.1 and Figure 5.4) because serious γ phase coarsening would lead to random grain boundary width. Thus, the changes in the volume fraction of the grain boundary γ phase could represent the changes of the coarse γ phase. The grain boundary γ phase volume fraction against different times for air-cooled and furnace-cooled samples is shown in Figure 6.17. The grain boundary γ phase volume fraction of air-cooled 0.8B alloy increased significantly (linearly) over the ageing time. However, the grain boundary γ phase volume fraction of furnace-cooled 0.8B alloy was always close to a constant at 15% over the ageing time. Thus, furnace-cooled samples were more stable than air-cooled ones, which meant that low cooling rate after solution treatment contributed to the stability of 0.8B alloy.

6.2.2 Interlocked-lamellar Colonies

Interlocked lamellar colonies and feathery microstructures were observed in solution-treated and aged samples. As shown in Figure 6.18 (a) and 6.20, lamellae grew into neighbouring lamellar colonies deeply, thus forming interlocked lamellar colonies.

As shown in Figure 6.18, BSE mode SEM images of the samples heat treated with 1290°C 2h AC (Figure 6.18(a)) showed significantly interlocked lamellar colonies A/B (The lamellae in grain A grew into those in grain B deeply) and C/D,

but no inter-lock between B/C and B/E. Further EBSD mapping and pole figures are shown in Figure 6.20. Interlocked lamellar colonies A/B and C/D had the relationship of $\{110\} \gamma_A \parallel \{100\} \gamma_B$ while non-interlocking colonies B/C and B/D had the relationship of $\{100\} \gamma_A \parallel \{100\} \gamma_B$.

A similar relationship was observed in the samples heat treated with 1290°C 2h AC 889°C 2h AC, as shown in Figure 6.19.

A simple orientation relationship could be summarised as follows: Colony A lamellar lathes grew into colony B lamellar lathes, and then the two colonies had the relationship of $\{110\} \gamma_A \parallel \{100\} \gamma_B$ or less than 5°. However, even neighbouring colonies met the condition of $\{110\} \gamma_A \parallel \{100\} \gamma_B$ or less than 5°, and the interlocked morphology might not happen. Non-interlocking colonies had the relationship of at least one set of $\{100\} \gamma_A \parallel \{100\} \gamma_B$ or less than 5°.

Usually showing very fine lamellae in 0.8B alloy, feathery microstructures were often observed due to the extension of the lamellae and similar to interlocked-lamellar colonies. A HAADF image of a feathery microstructure in 0.8B (1290°C 2h AC 792°C 2h AC) alloy with a typical measure angle is shown in Figure 6.20. Resembling lamellar structure, the feathery structure had a common crystallographic orientation relationship with primary α_2 lamellae. For example, the lamellae of the prior α_2 lath within the feathery structure had an angle of less than 15°. Dey et al. suggested that misorientation originated from

elastic stress during sympathetic nucleation.

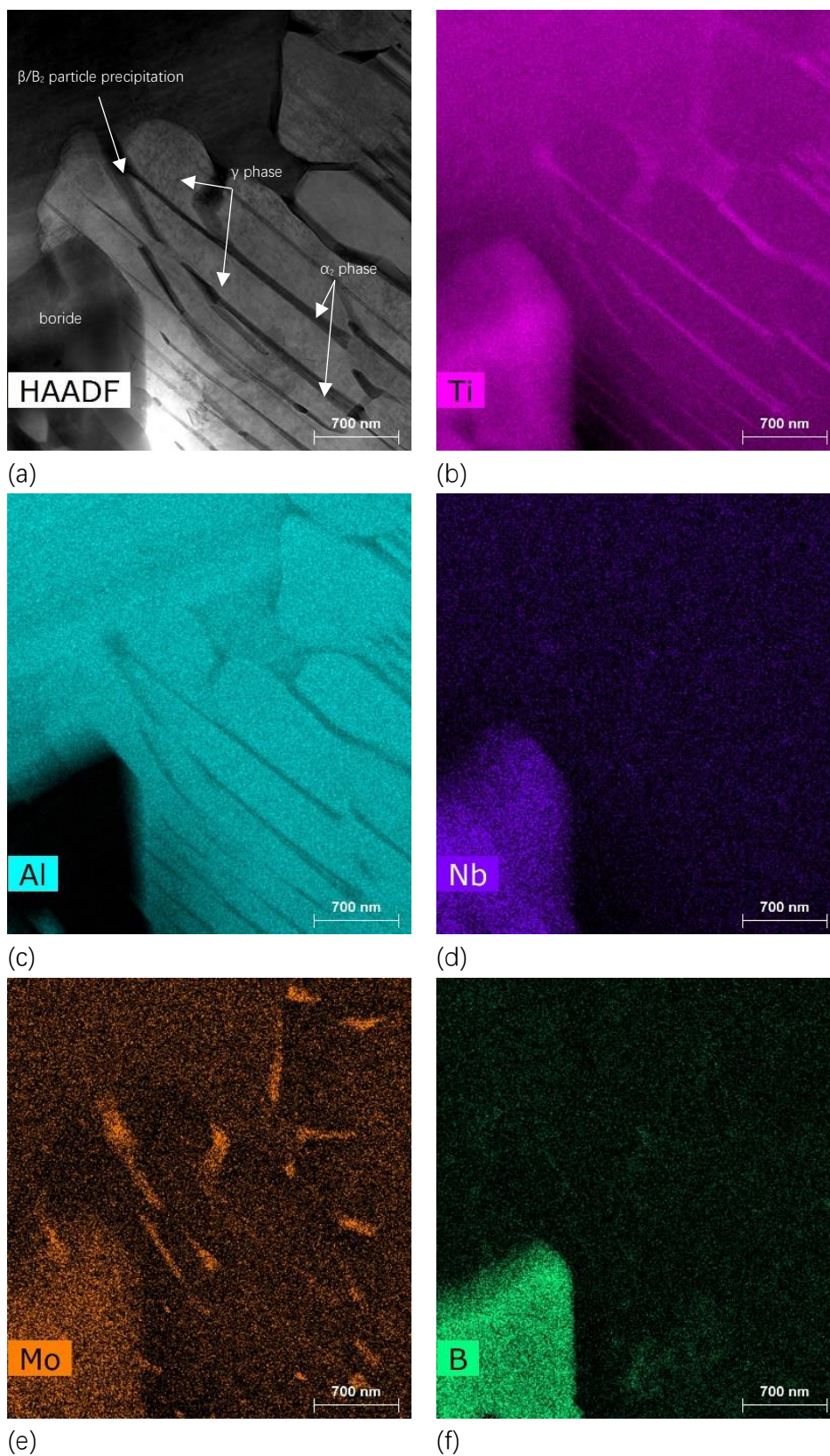
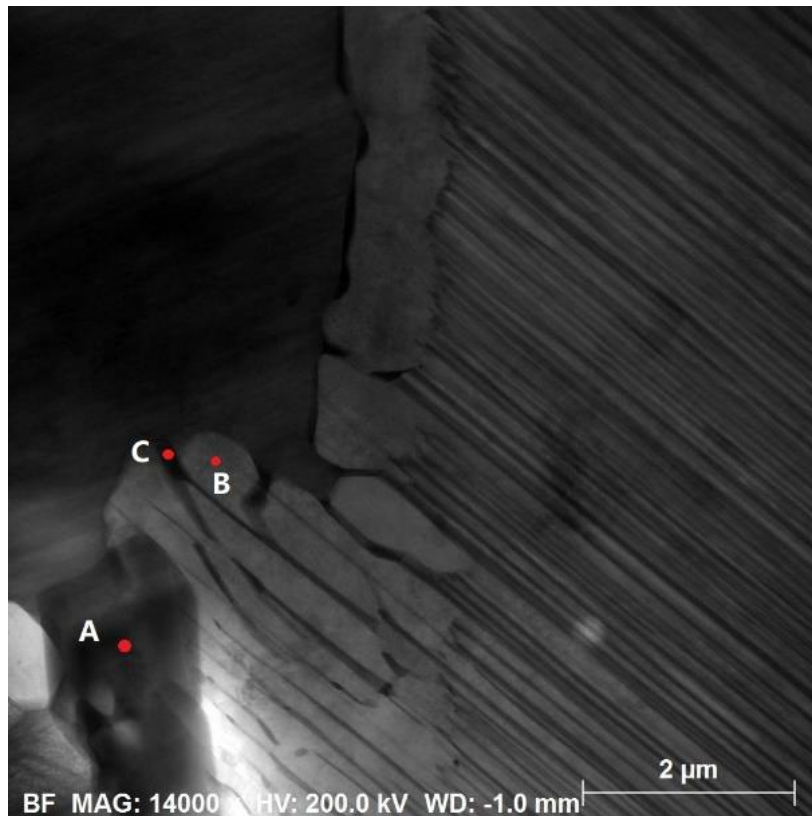
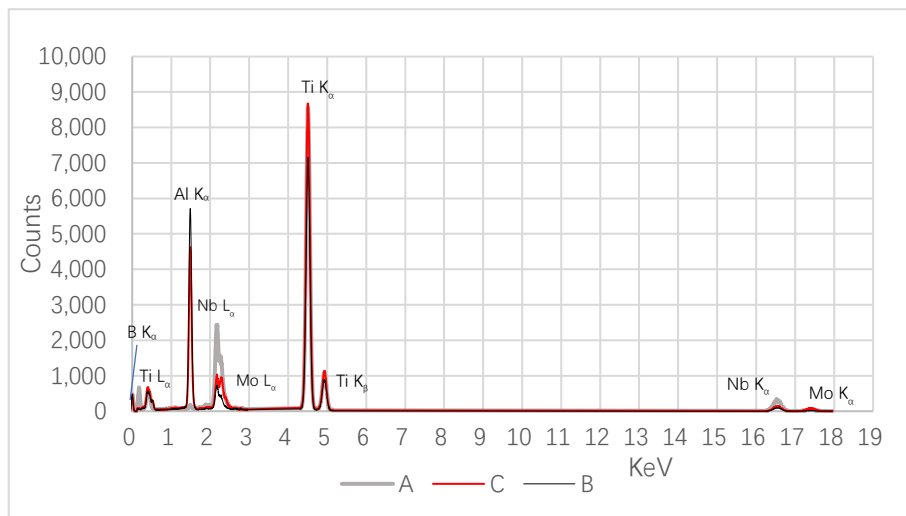


Figure 6. 1 BF-STEM image from and EDS mapping for 0.8B alloy heat treated by condition of 1290°C 2h AC 889°C 2h AC.

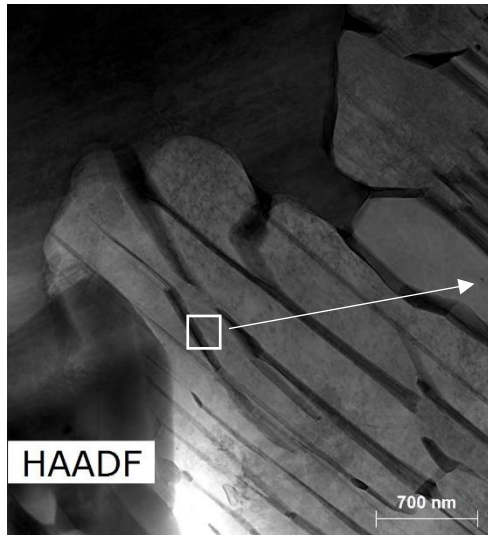


(a)

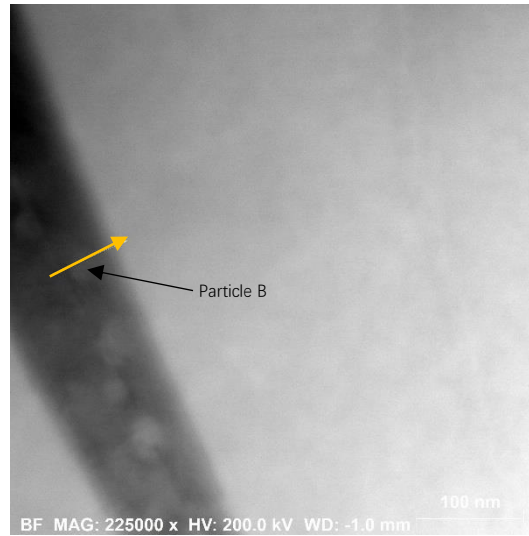


(b)

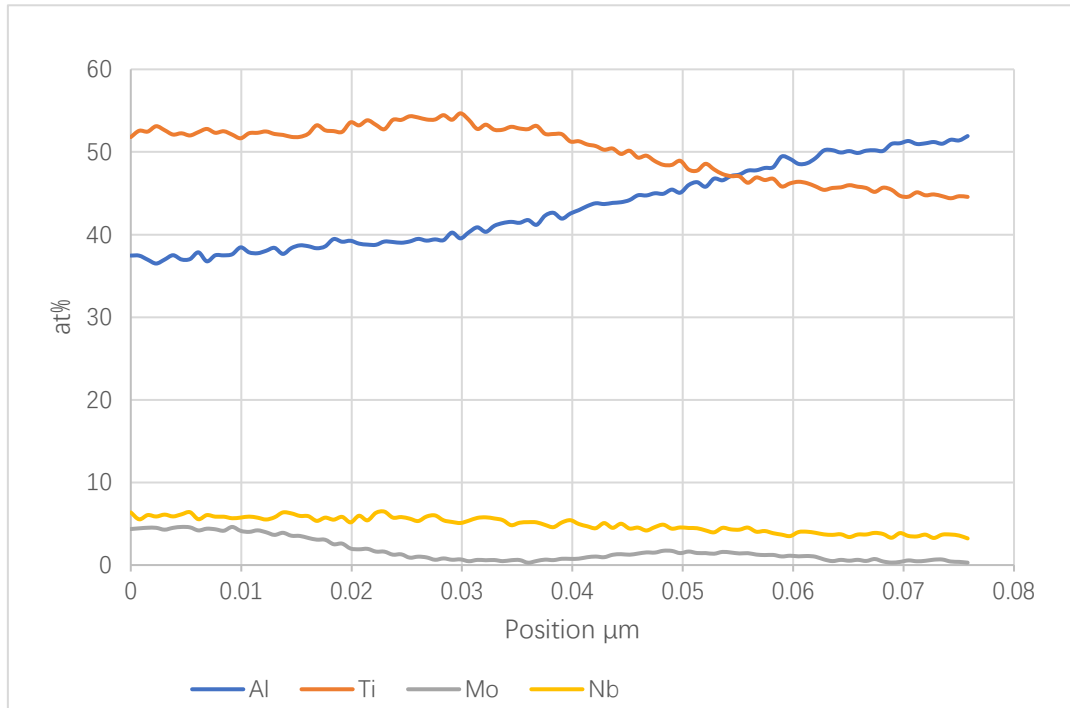
Figure 6. 2 BF-STEM image and EDS spectra from the 0.8B alloy heat treated by condition of 1290°C 2h AC 889°C 2h AC. (a) BF-STEM image showing the positions of EDS spectra. Spot A, C and B located at boride, unknown phases and γ phase respectively. (b) EDS spectra with the highest concentration of Nb, Mo and B but the lowest concentration of Al among spot A, B and C. Spot C contained a higher concentration of Nb and Mo but a lower concentration of Al than spot B.



(a)



(b)



(c)

Figure 6. 3 BF-STEM image from and EDS line-scan for 0.8B alloy heat treated by condition of 1290°C 2h AC 889°C 2h AC. (a) BF-STE image showing the overview of the position for EDS line-scan. (b) EDS line-scan path way indicated by the yellow arrow, the scan started from the predicted β phase, crossed particle B and ended in the γ phase. (c) EDS line-scan results showing that the particle B might be a ω phase.

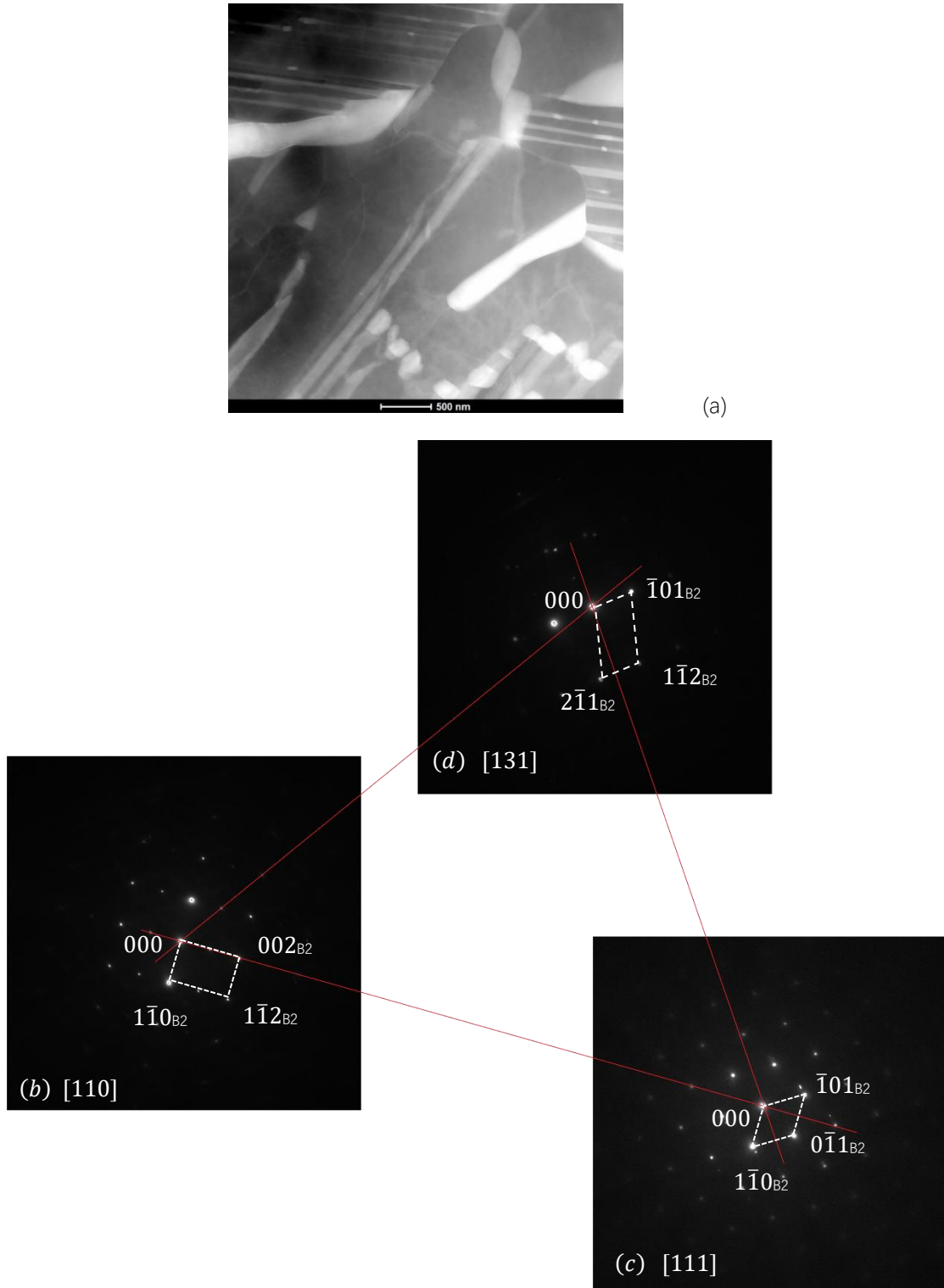
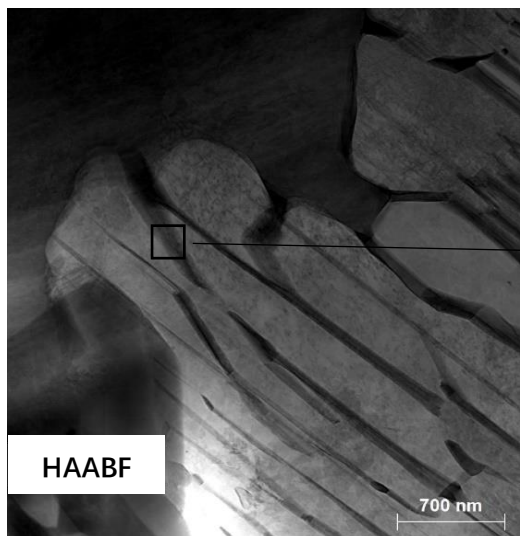
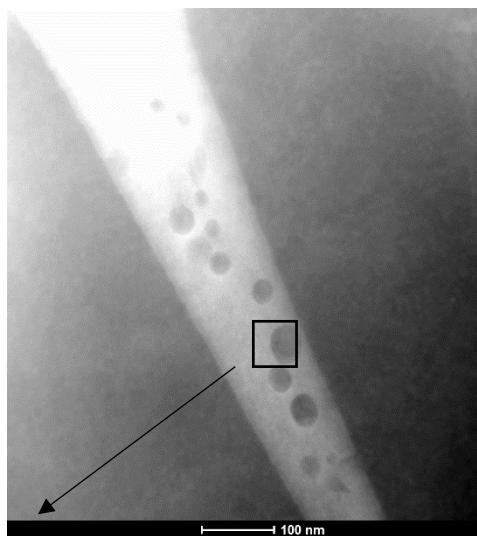


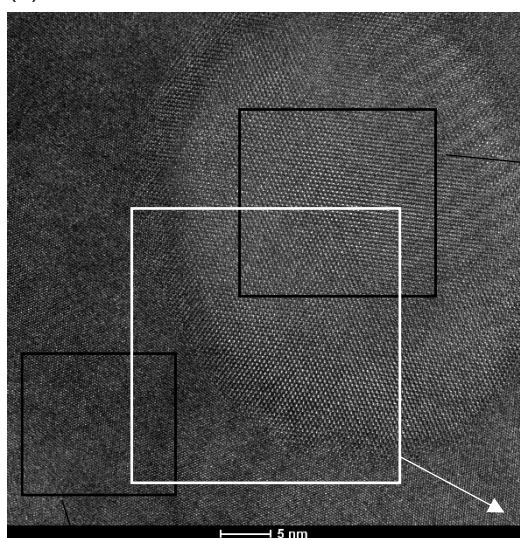
Figure 6. 4 (a) HAADF STEM image of grain boundary β/B_2 phase precipitates (bright grain) in 0.8B alloy heat treated with 1290°C 2h AC 889°C 96h AC, and corresponding SAD patterns with a zone axis of [110] (b), [111] (c) and [131] (d) respectively. The tilting angles between (b) / (c), (b) / (d) and (c) / (d) were 35.26° , 31.48° and 29.50° respectively.



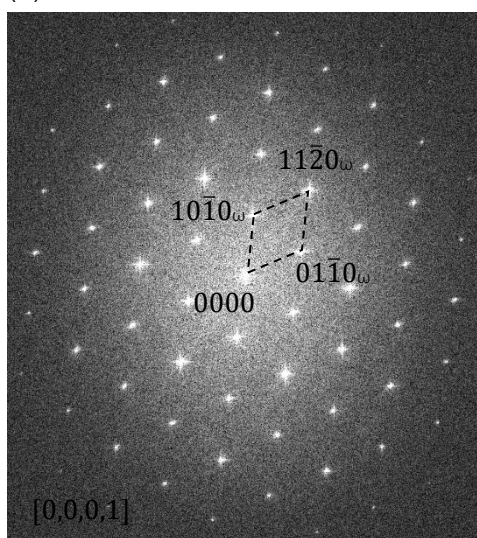
(a)



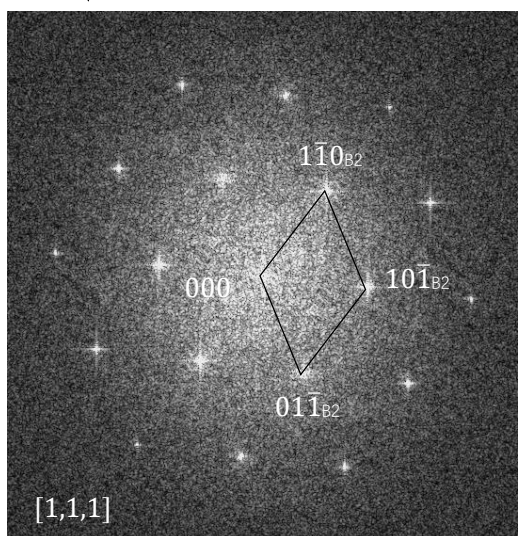
(b)



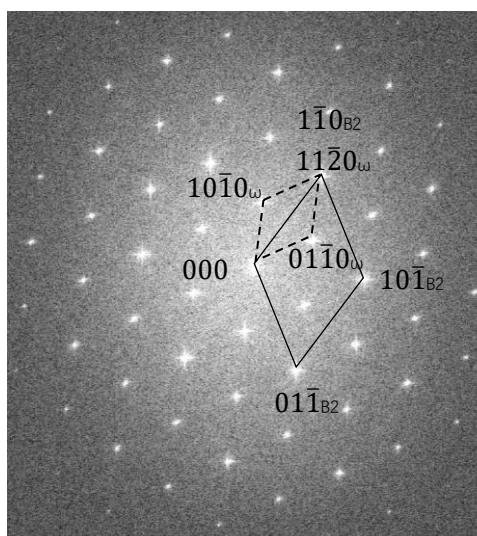
(c)



(d)



(e)



(f)

Figure 6. 5 Identification of ω phase precipitated in the B_2 phase in 0.8B alloy heat treated with 1290°C AC 2h 889°C 2h AC. (a) BF-STEM image, (b) HAADF STEM image of the ω phase precipitated in the B_2 phase, (c) HRTEM images of ω and B_2 phases, (d) FFTed diffraction pattern from the ω phase, (e) FFTed diffraction pattern from the B_2 phase, (f) FFTed diffraction pattern from ω and B_2 phases.

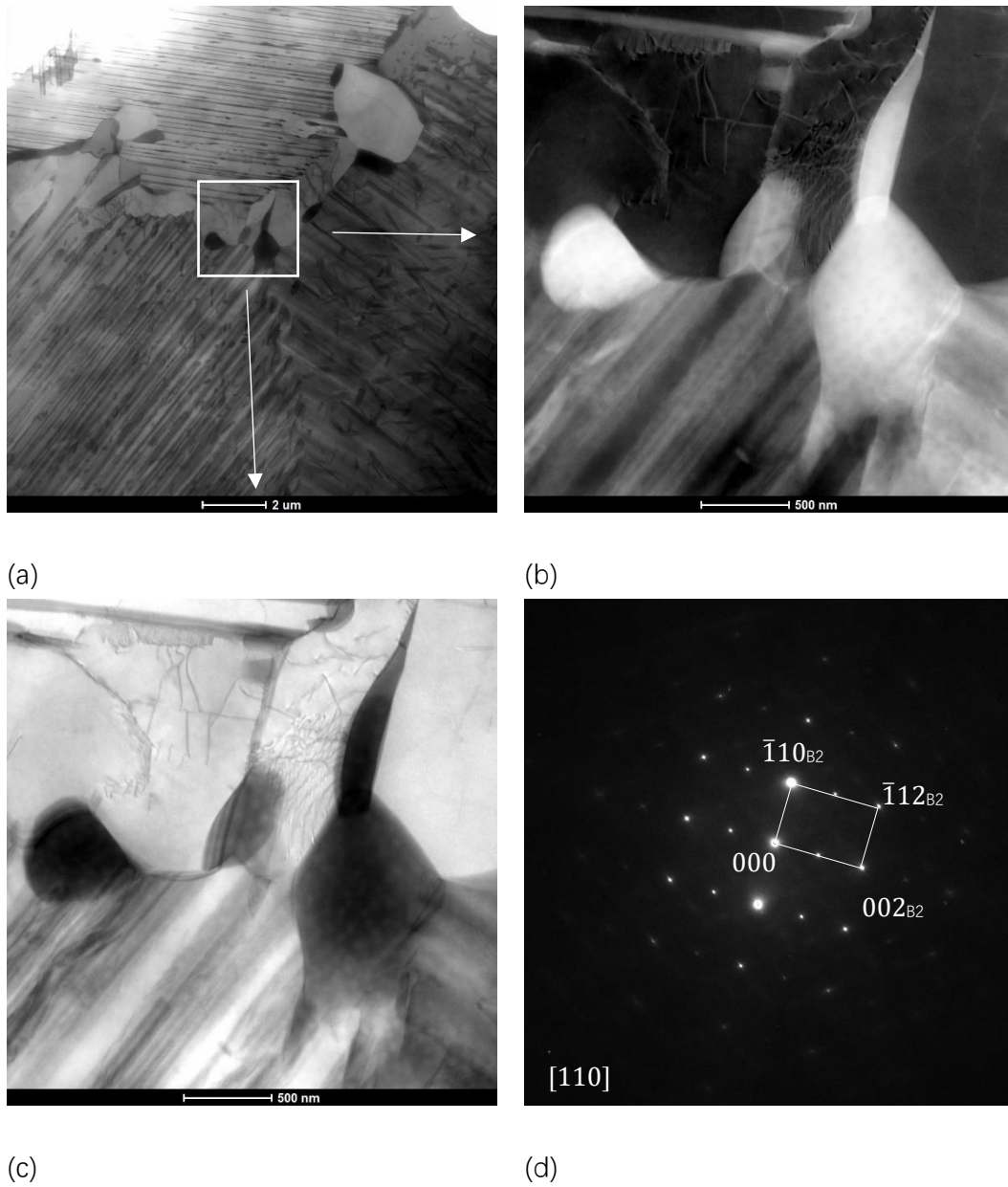
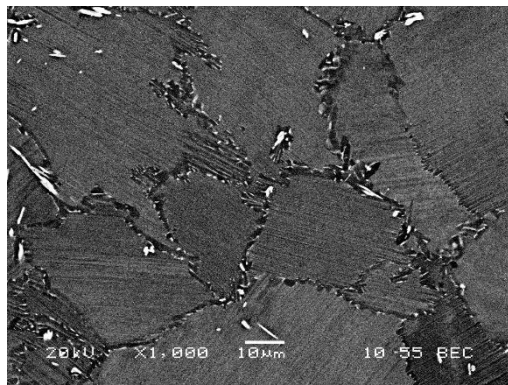
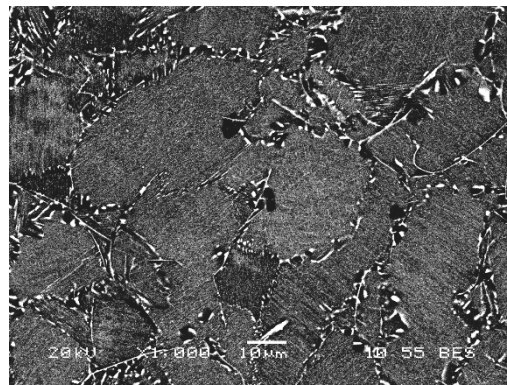


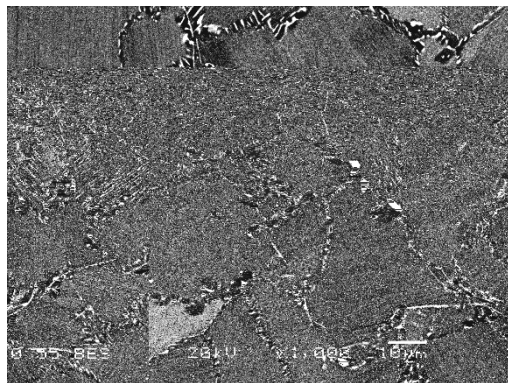
Figure 6. 6 (a) BF-STEM image showing the overview of the grain boundary B_2 phase in heat treated 0.8B alloy (1290°C 2h AC 889°C 96h AC), (b) HAADF and (c) BF STEM images of the grain boundary B_2 phase, (d) [110] SAD pattern from a grain boundary B_2 phase in Figure 6.6b/c.



(a) 1290°C 2h AC 889°C 4h AC



(b) 1290°C 2h AC 889°C 64h AC

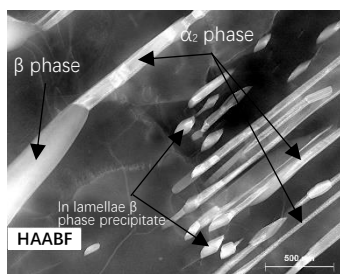


(c) 1290°C 2h AC 889°C 96h AC

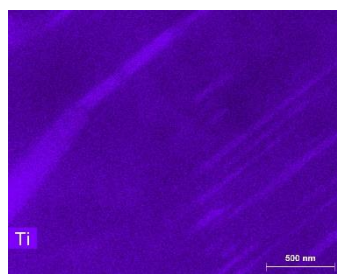


(d) 1290°C 2h AC 889°C 96h AC- X 3000

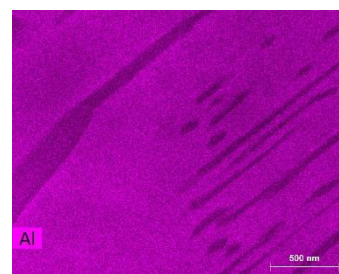
Figure 6. 7β phase precipitates observed in long-time aged samples. The heat treatment conditions of samples were 1290°C 2h AC ageing at 889°C for (a) 4 hours, (b) 64 hours and (c) 96 hours with air cooling. (d) High magnification of (c).



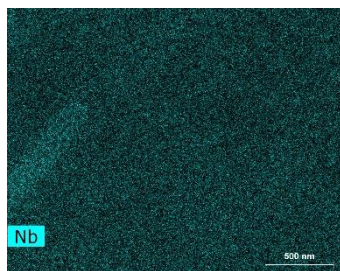
(a)



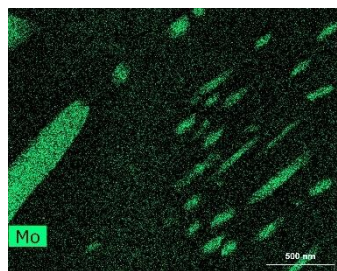
(b)



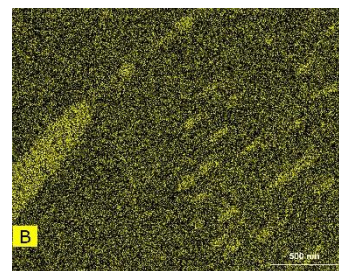
(c)



(d)



(e)



(f)

Figure 6. 8 EDS map of the samples heat treated with 1290°C 2h AC 889°C 96h AC. Known phases were already indicated in (a).

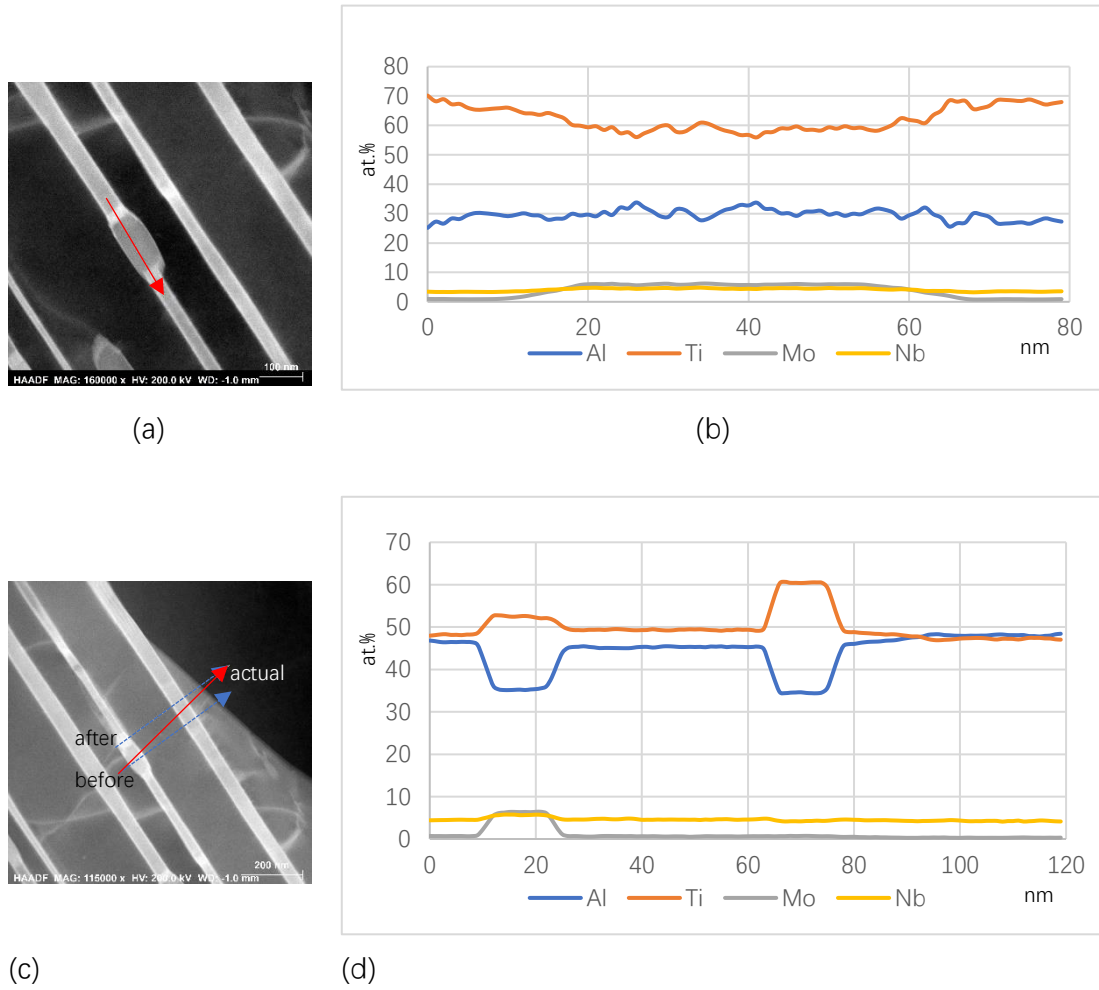
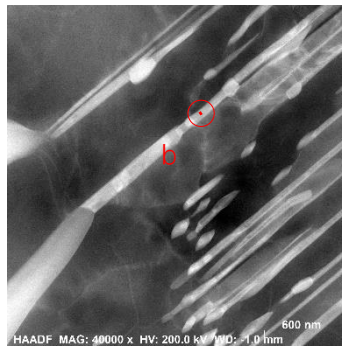


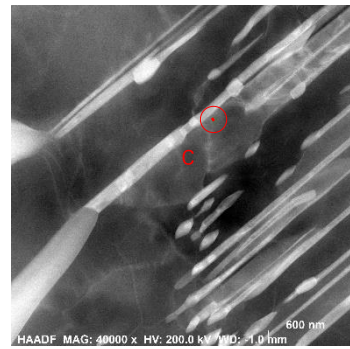
Figure 6. 9 EDS line-scan result crossed β precipitates. (a) EDS line mapping started from the α_2 phase, crossed the β phase and ended in the parent α_2 phase. The scanning result is shown in (b). (c) EDS line mapping started from the γ phase, crossed the β phase, γ and α_2 lathes, and ended in the γ phase. The sample was not very stable during scanning and the real mapping track was indicated by the red arrow. The scanning result is shown in (d).



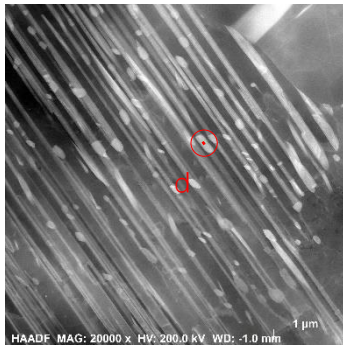
(a)



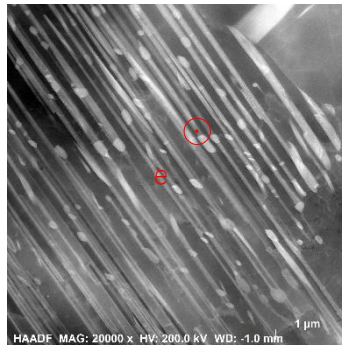
(b)



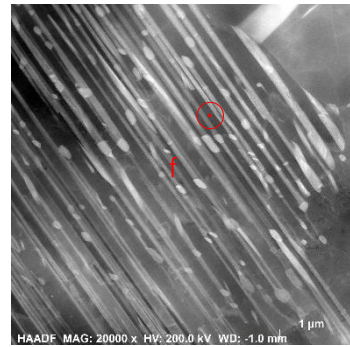
(c)



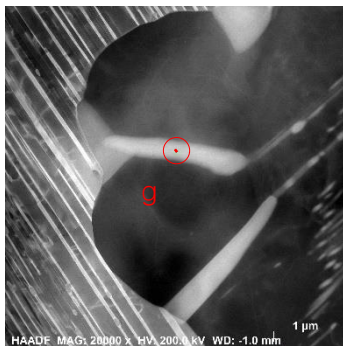
(d)



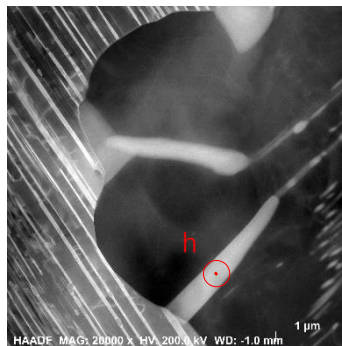
(e)



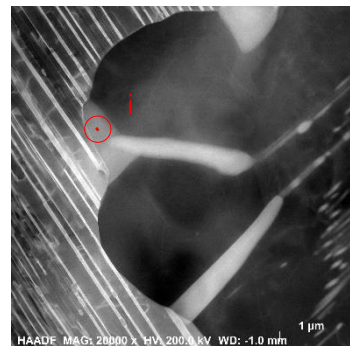
(f)



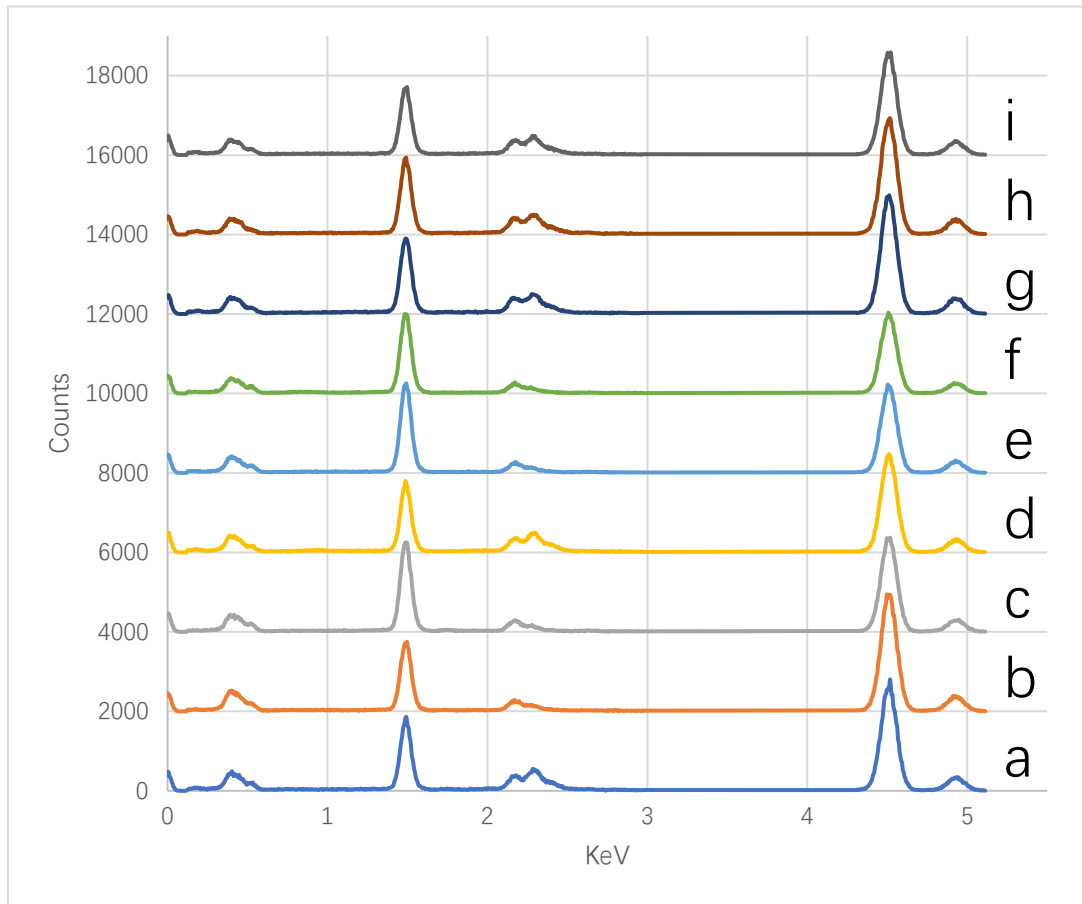
(g)



(h)



(i)



(j)

Figure 6. 10 EDS spot analysis at different areas of the sample heat treated by 1290°C 2h AC 889°C 96h AC. Spot 'a' and 'd' were located at lamellar β precipitates; spot 'b' and 'e' were located at the α_2 phase; spot 'c' and 'f' were located at the γ phase. Spot 'g', 'h' and 'i' were located at the grain boundary B_2 phase. EDS scanning results are shown in (j).

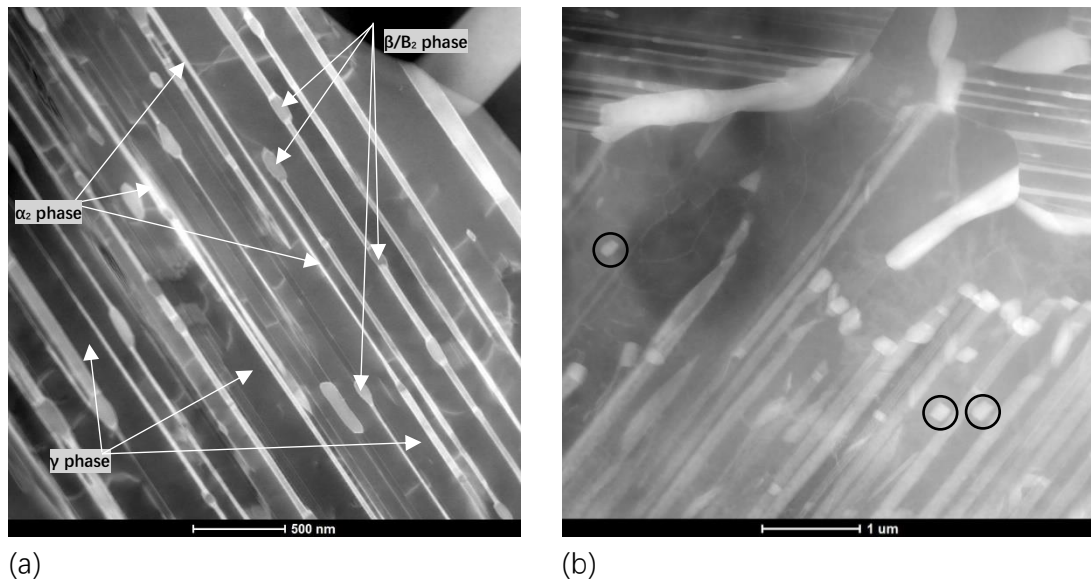


Figure 6.11 HAADF images of in-lamellar precipitated B_2/β particles. (a) B_2/β particles precipitated within α_2 lamellae and (b) B_2/β particles formed in γ lamellae.

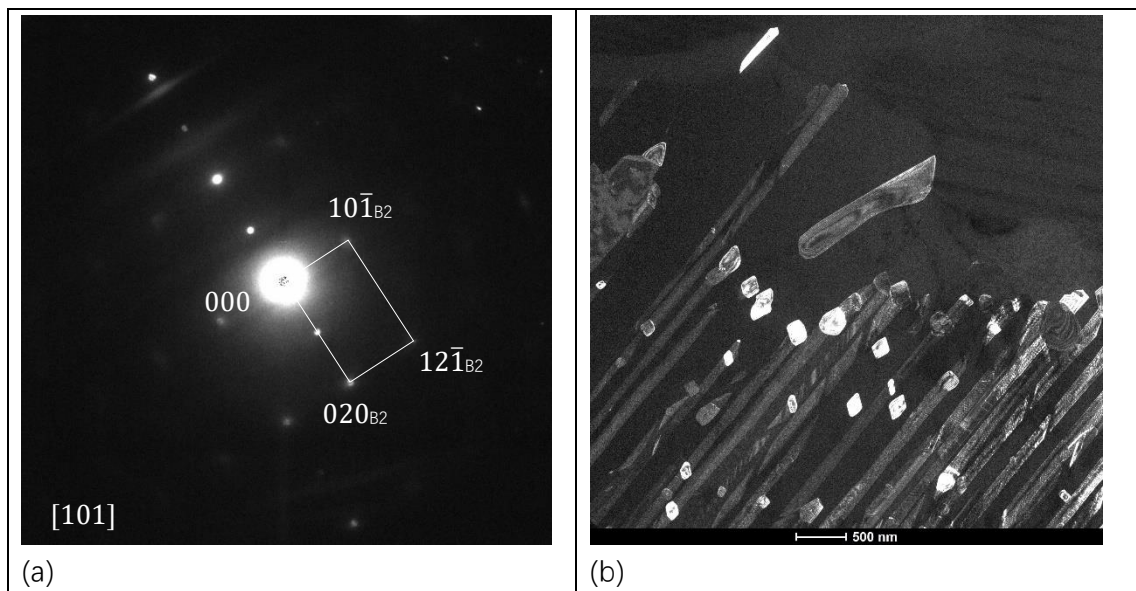
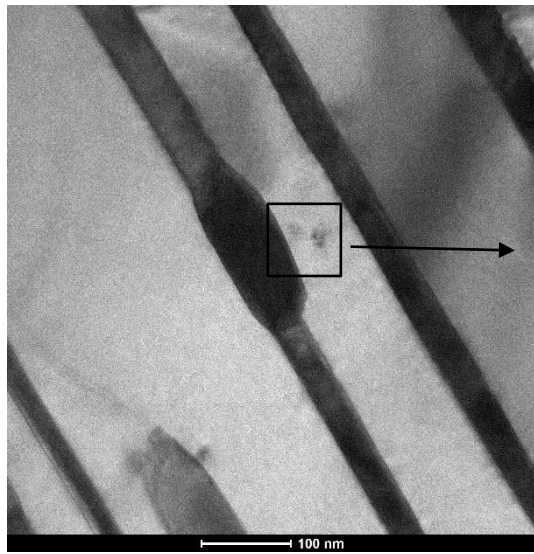
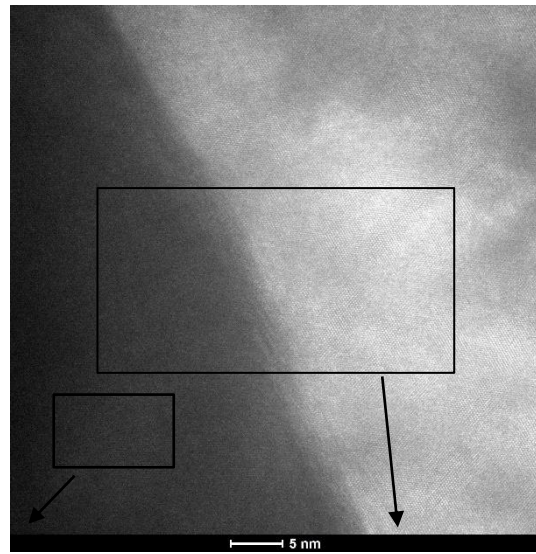


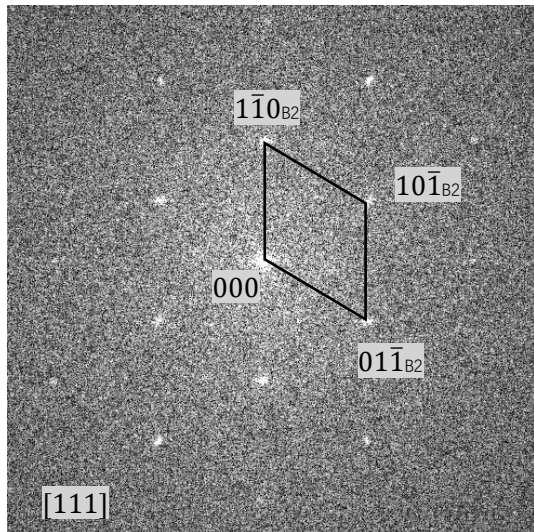
Figure 6.12 (a) $[101]$ A SAD pattern from a B_2 particle within γ lamella shown in Figure 6.11b and (b) a dark field TEM image of the B_2 phase using (010) reflection.



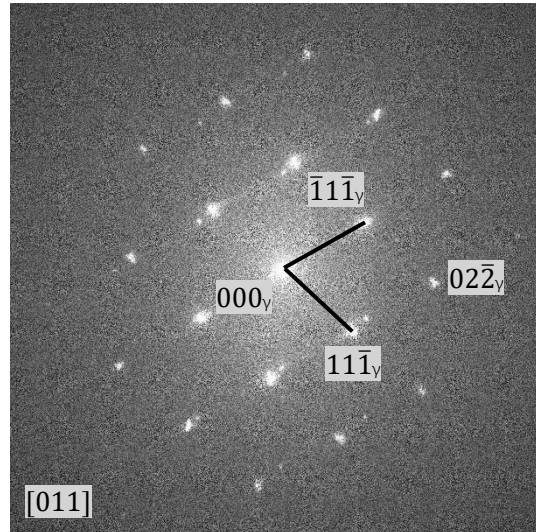
(a)



(b)



(c)



(d)

Figure 6. 13 (a) HAADF STEM image of the analysed β/B_2 particle (b) HRTEM image of a β/B_2 particle within the α_2 lath, (c) and (d) FFT'd diffraction patterns from the γ phase, the particle and two phases (the particle and neighbouring γ laths) respectively.

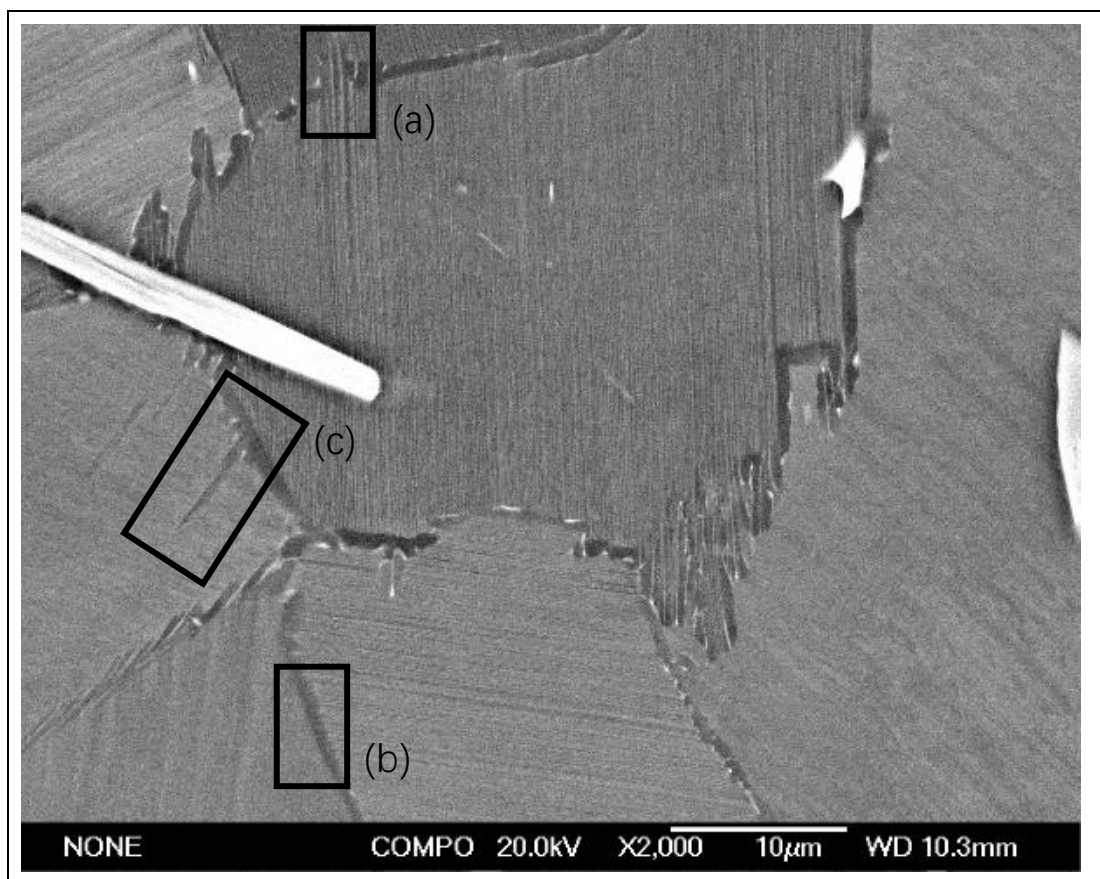
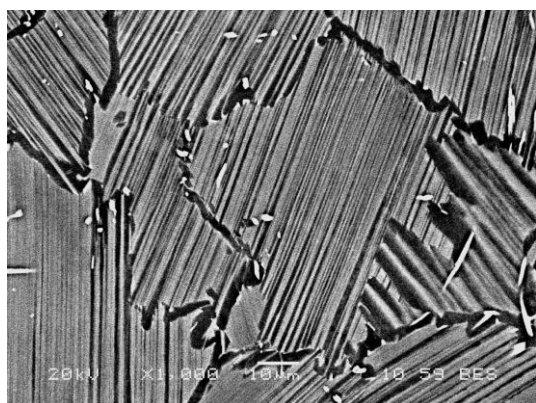
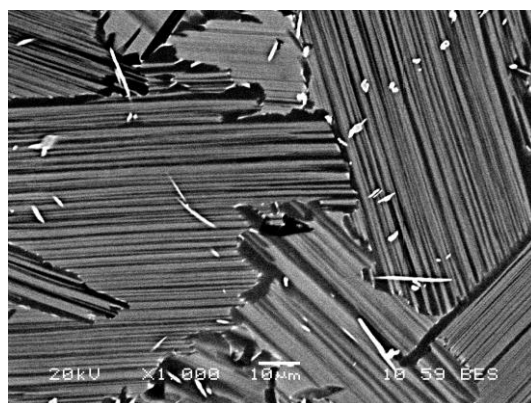


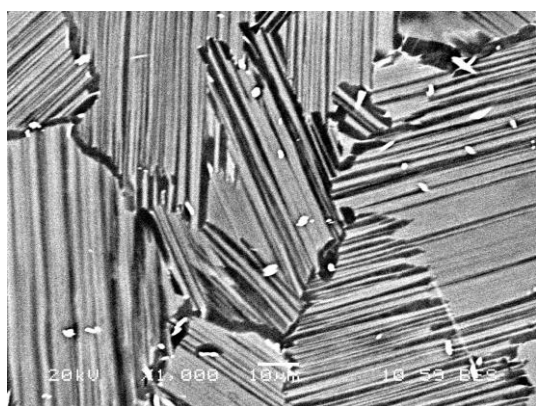
Figure 6. 14 BSE mode SEM image for (1290°C 2h AC 889°C 2h AC) 0.8B alloy, DC of the γ phase with three different morphologies were indicated in the image.



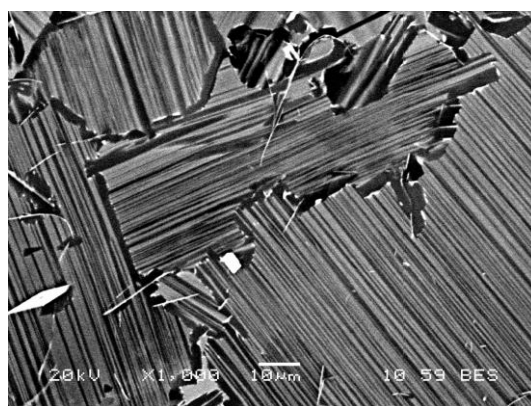
(a) 1290°C 2h FC 1182°C AC 792°C 1h AC



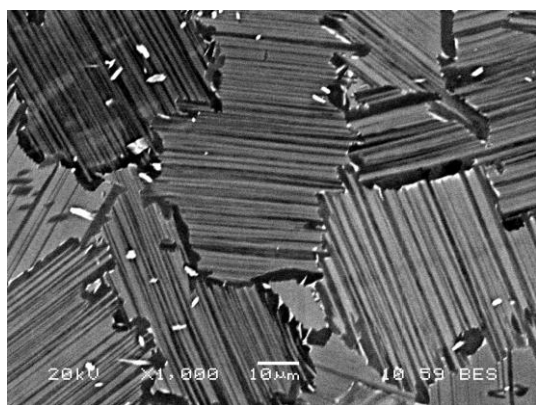
(b) 1290°C 2h FC 1182°C AC 889°C 1h AC



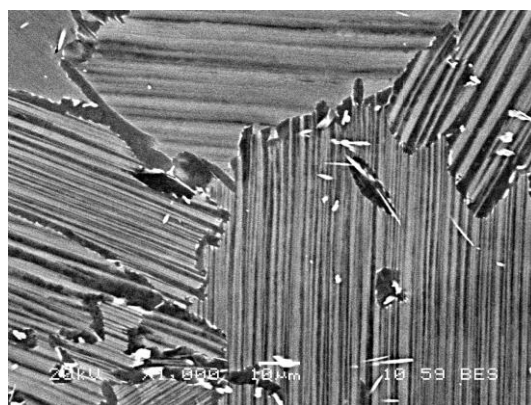
(c) 1290°C 2h FC 1182°C AC 792°C 2h AC



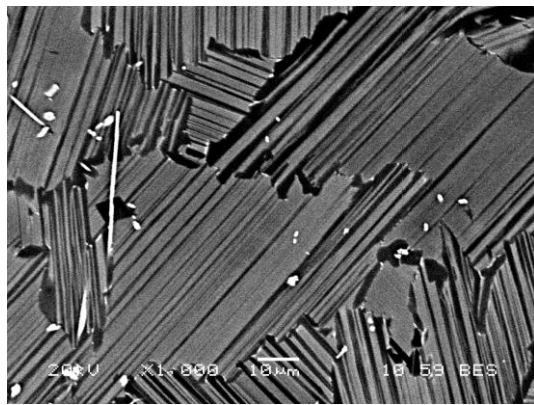
(d) 1290°C 2h FC 1182°C AC 889°C 2h AC



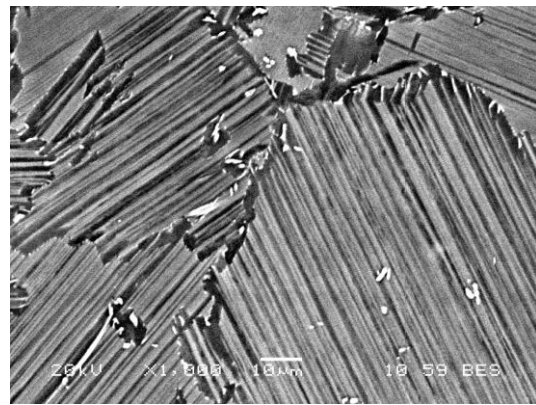
(e) 1290°C 2h FC 1182°C AC 792°C 4h AC



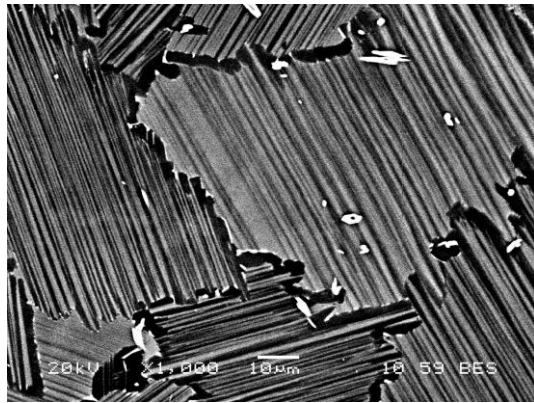
(f) 1290°C 2h FC 1182°C AC 889°C 4h AC



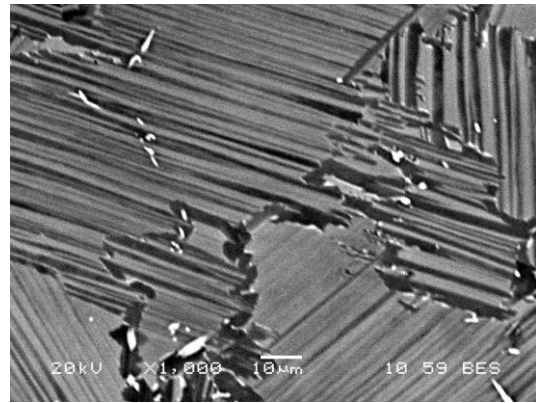
(g) 1290°C 2h FC 1182°C AC 792°C 8h AC



(h) 1290°C 2h FC 1182°C AC 889°C 8h AC



(i) 1290°C 2h FC 1182°C AC 792°C 2h AC 889°C 2h AC



(j) 1290°C 2h FC 1182°C AC 792°C 2h AC 889°C 4h AC

Figure 6. 15 BSE mode images for aged 0.8B samples after interrupting furnace cooling, the detailed heat treatment condition listed in the image.

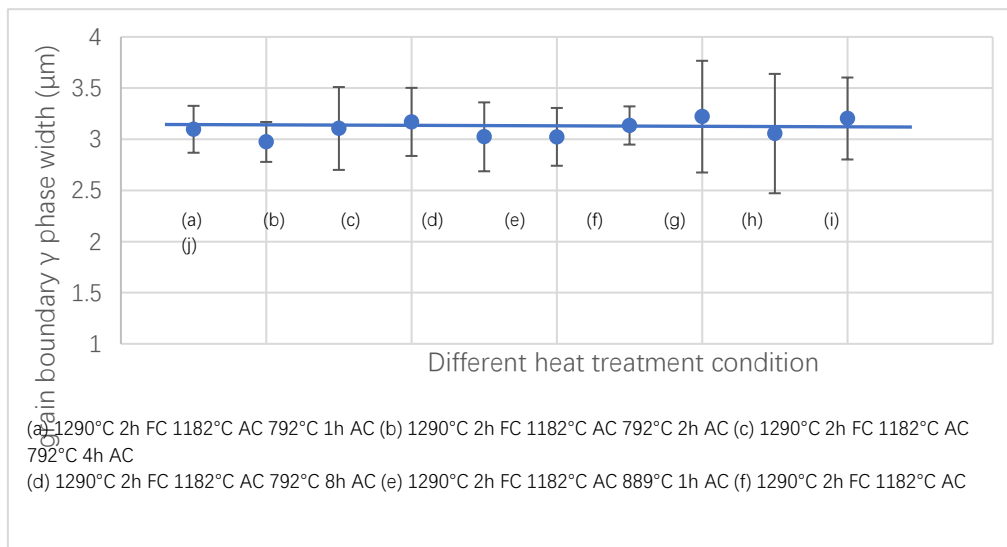


Figure 6. 16 Statistics of the grain boundary γ phase and the width of the aged 0.8B samples after interrupting furnace cooling.

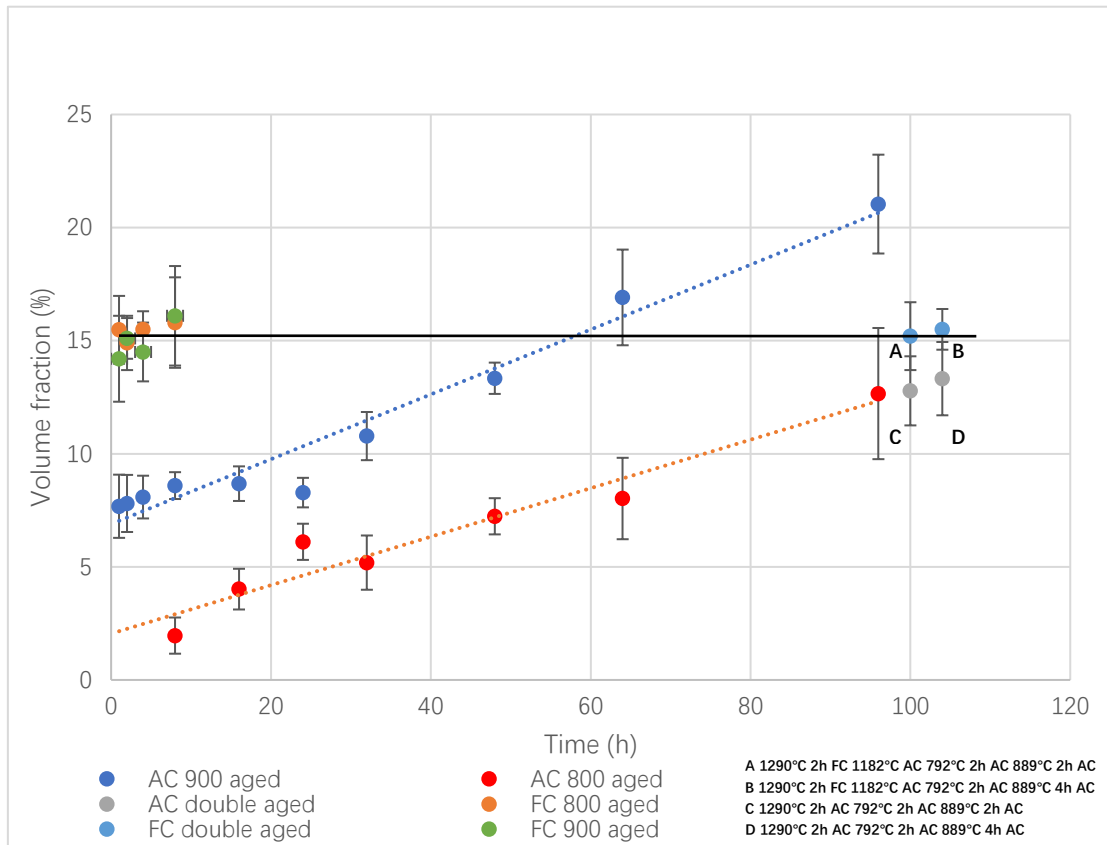
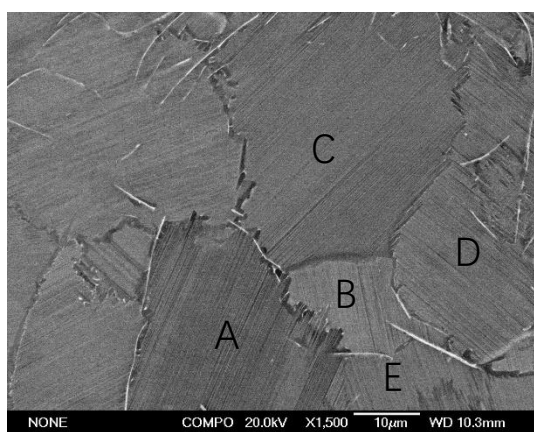
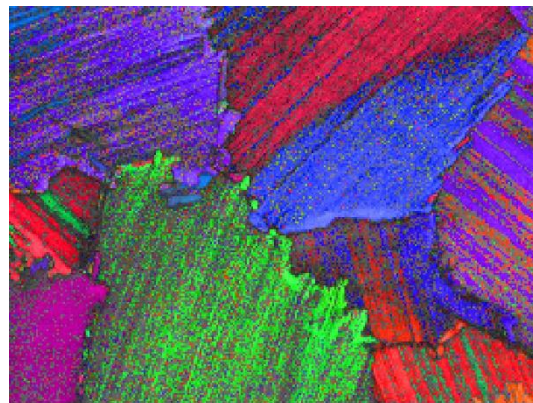


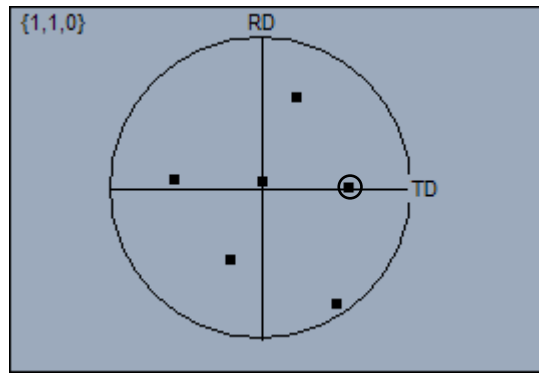
Figure 6. 17 The diagram of grain boundary γ phase volume fraction subject to aged 0.8B samples after interrupting furnace cooling and air cooling.



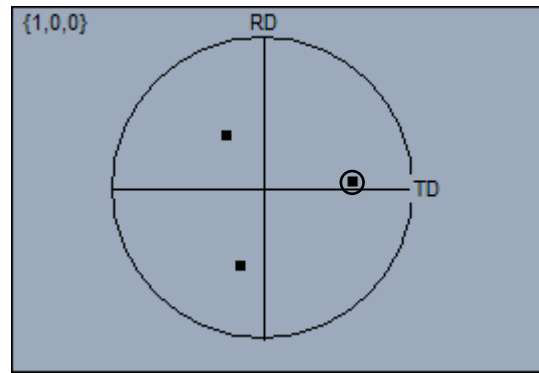
(a) 0.8B alloy 1290°C 2h AC



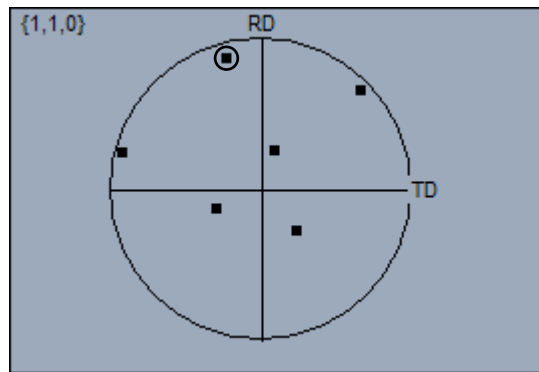
(b)



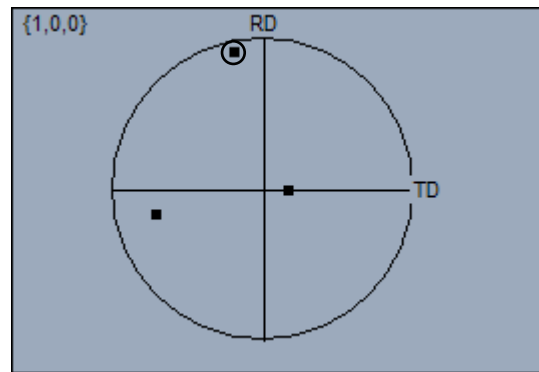
(c) A



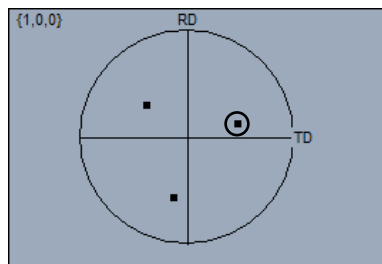
(d) B



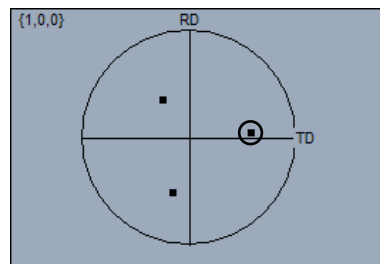
(e) C



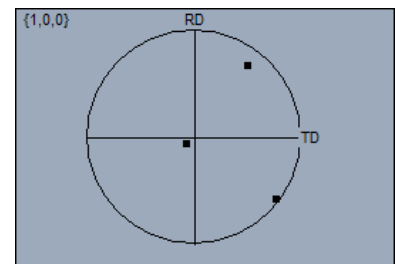
(f) D



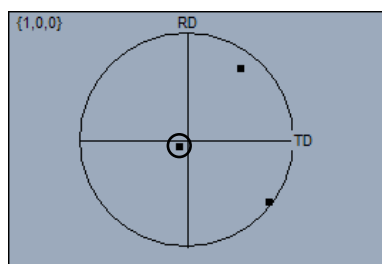
(g) C



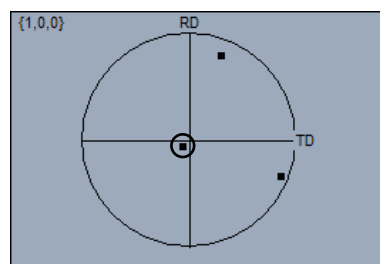
(h) B1



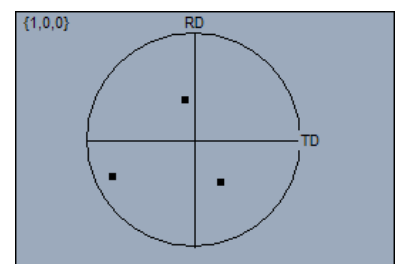
(i) B2



(j) B2

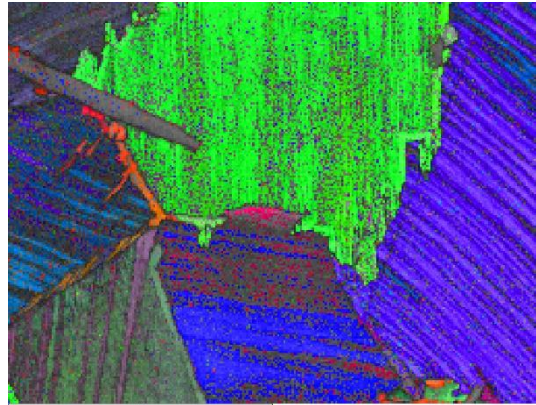
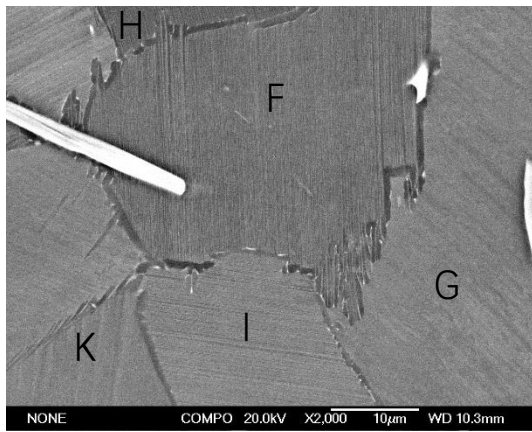


(k) E1

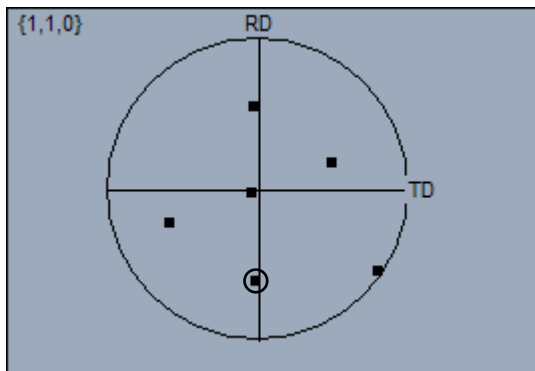


(l) E2

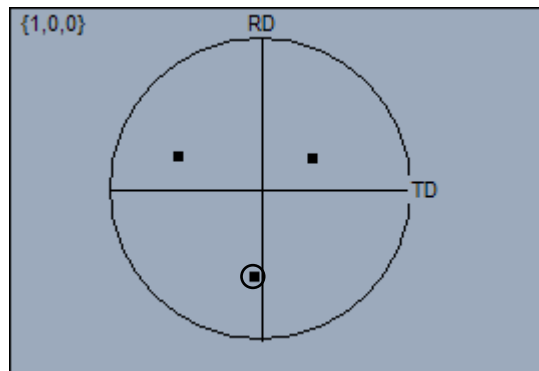
Figure 6. 18 EBSD scan of 0.8B sample treated with 1290°C 2h AC. The BSE image scan area shown in (a) and analysed grains marked with capital letters.



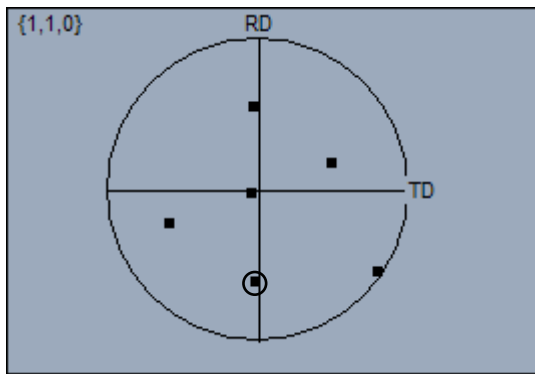
(m)



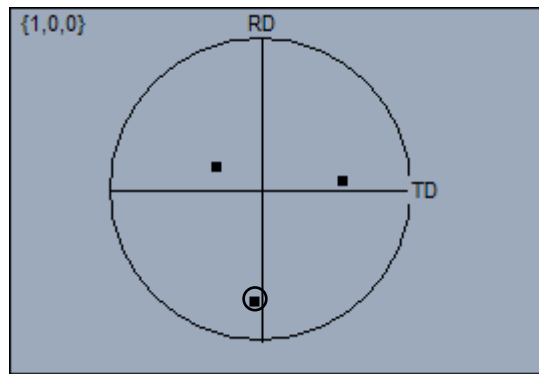
(n)



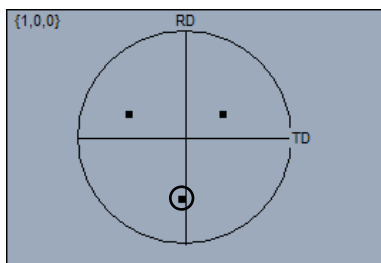
(o) F



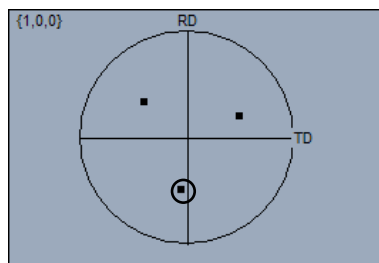
(p) G



(q) F

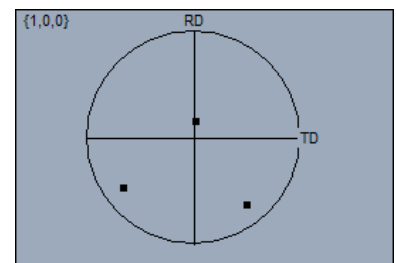


(r) H



(s) G

(t) I1



(u) I2

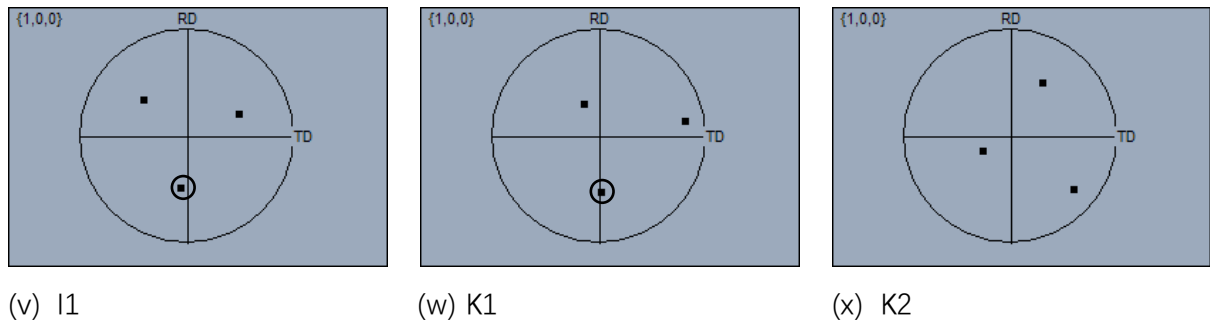


Figure 6. 19 EBSD scan of 0.8B sample treated with 1290°C 2h AC 889°C 2h AC. The BSE image scan area shown in (a) and analysed grains marked with capital letters.

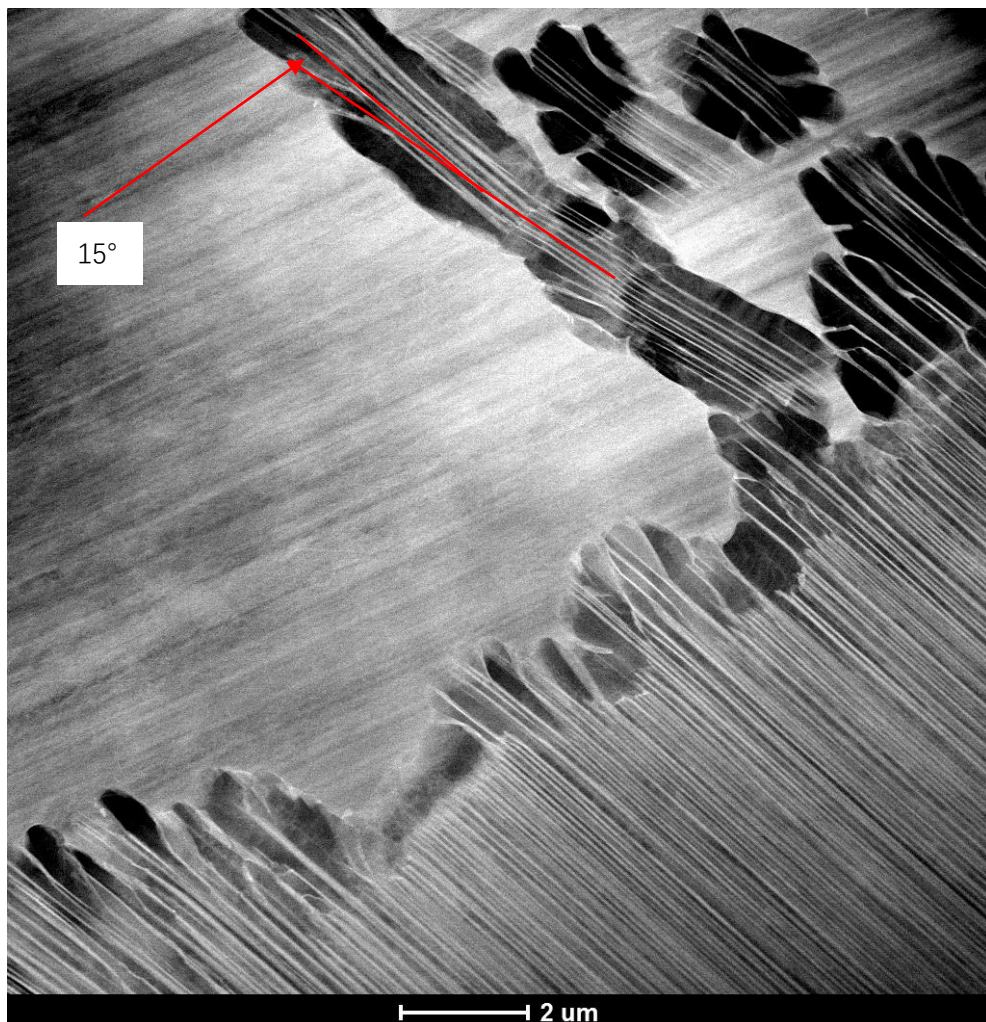


Figure 6. 20 Feathery microstructure with around 15° angle between deviate γ lathes.

CHAPTER 7 HEAT TREATMENT FOR THE IMPROVEMENT OF TEMPERATURE CAPACITY

0.8B alloy with different heat treatment conditions was mechanically tested in this chapter to corroborate the previous results. Heat treatment conditions and microstructures were stated in 7.1 and tensile testing results were discussed in 7.2.

7.1 Heat Treatment Conditions and Microstructures

Based on the previous study, four heat treatment conditions were designed for further mechanical property tests, as seen in Table 7.1. According to the phase diagram of 0.8B alloy (Figure 4.8), 1290°C, 1250°C and 1240°C were selected as three different solution treatment temperatures. 0.8B alloy had a single α phase at 1290°C and $\alpha+\gamma$ phases at 1250°C and 1240°C. The solution was treated for 1 hour to obtain a uniform and small grain size. Both furnace and air cooling methods were used for a single α solution treated sample to obtain different lamellar spacing while air cooling method was adopted for $\alpha+\gamma$ phases solution treated samples. All samples were aged at 889°C for 4 hours.

BSE images of the samples subject to different heat treatment conditions are shown in Figure 7.1. The sample (T119) heat treated with 1290°C 1h FC 1182°C AC 900°C 4h AC had a fully lamellar microstructure with a uniform lamellar

colony size of around 70 μ m. Coarse γ phases were observed at grain boundaries and triple points. The precipitation of a small amount of β phase precipitates was observed in the grain boundary γ phase. The sample (T120) heat treated with 1290°C 1h AC 900°C 4h AC also had a uniform fully lamellar microstructure with a lamellar colony size of close to 70 μ m. Similar with furnace-cooled samples, coarse γ phases were observed at grain boundaries and triple points. The precipitation of a small amount of β phase precipitates was observed in the grain boundary γ phase. The lamellae with smaller spacing were shown in lamellar grains. The sample (T121) heat treated with 1260°C 1h AC 900°C 4h AC had a nearly lamellar microstructure with a larger amount of γ phases and lamellar colonies. A small amount of β phase precipitates were observed within the γ phase and lamellar colony boundary. The sample (T122) heat treated with 1240°C 1h AC 900°C 4h AC had a microstructure similar to T121. The sample also showed a nearly lamellar microstructure with a large amount of β phase precipitates at the grain boundary.

7.2 Tensile Testing on Heat Treated Ti-44.2Al-4Nb-1Mo-0.8B Alloy

Tensile testing was performed on 16 samples with different heat treatment conditions at both room temperature (i.e. 20°C) and high temperature (750°C). The testing results were summarised in Table 7.1.

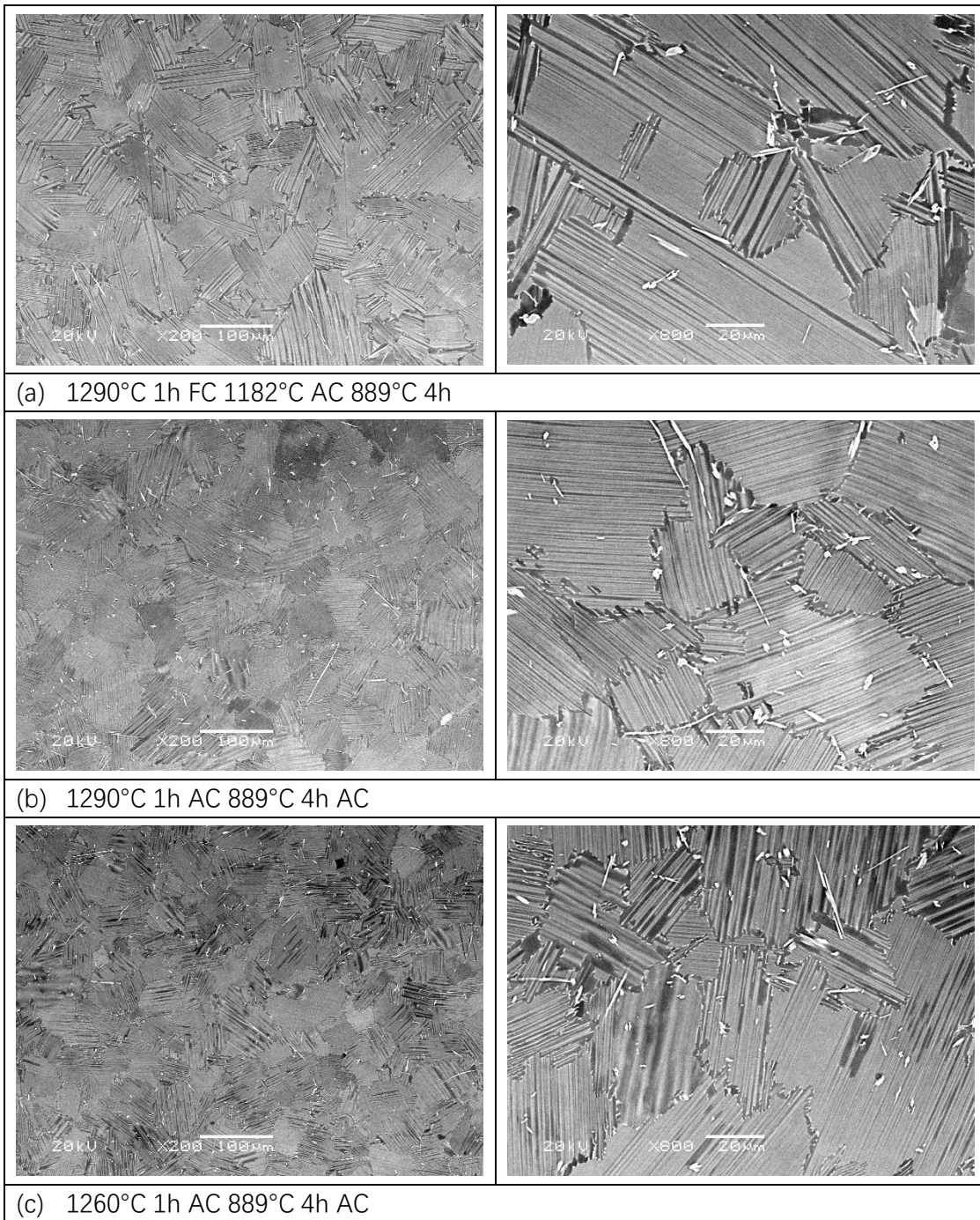
As mentioned in the last section, the single α phase solution treated sample had a fully lamellar microstructure. $\alpha+\gamma$ phase field solution treated samples showed a nearly lamellar microstructure. T119 and T120 samples had a similar microstructure with nearly full lamellae at room temperature. The only difference was lamellar spacing. Sample T120 had finer lamellae which could produce higher yield strength. T121 and T122 samples had the same microstructure with nearly γ lamellae at room temperature. The only difference was the volume fraction of B_2 phase precipitates. With less B_2 phase precipitates, sample T122 showed no γ phase coarsening at grain boundaries. Because of these two factors, T122 showed better yield strength than T121. Sample T120 had better yield strength than sample T122 because the fully lamellar microstructure led to better yield strength than the nearly lamellar microstructure.

The testing results of ultimate tensile strength and elongation were too discrete to analyse. It may be necessary to conduct more tests to get reliable results.

Creep resistance is an extremely important characteristic to be evaluated for the materials with potentially elevated temperature applications. Thus, it is necessary to conduct creep tests on heat-treated samples. Creep curves of the samples with different heat treatment conditions are shown in Figure 7.2. The creep test was performed at 700°C with an applied stress of 250 MPa. In Figure 7.2, all the four samples showed excellent creep resistance. No tertiary creep

stages were observed even when the test time was up to 860 hours. The samples (e.g. T119 and T120) with a fully lamellar structure presented better creep resistance than those (T121 and T122) with adjacent lamellar structure. Sample T120 showed better creep resistance than sample T119 because of its finer lamellae. Thus, the results could be summarised as follows: The fully lamellar microstructure led to better creep resistance than the nearly lamellar microstructure. The finer the lamellae in the fully lamellar microstructure were, the better the creep resistance would be.

As typical lamellar TiAl alloys, all of four samples were brittle in nature, whose ductility shown was largely accompanied by cracks^[72]. The cracking in all samples occurred at the very beginning of plastic deformation. No large extension occurred before the formation of voids and cracks. The low-magnification SEM images of fracture surfaces are shown in Figure 7.3, Similar with common TiAl lamellar alloys, two major fracture modes including interlamellar and translamellar cracking were observed in the higher-magnification SEM images shown in Figure 7.3 (a) and (b). The cracking of lamellar colony boundary was observed in the samples shown in Figure (c). The debonding of boride and matrix was found widely in the samples indicated in the Figure (d).



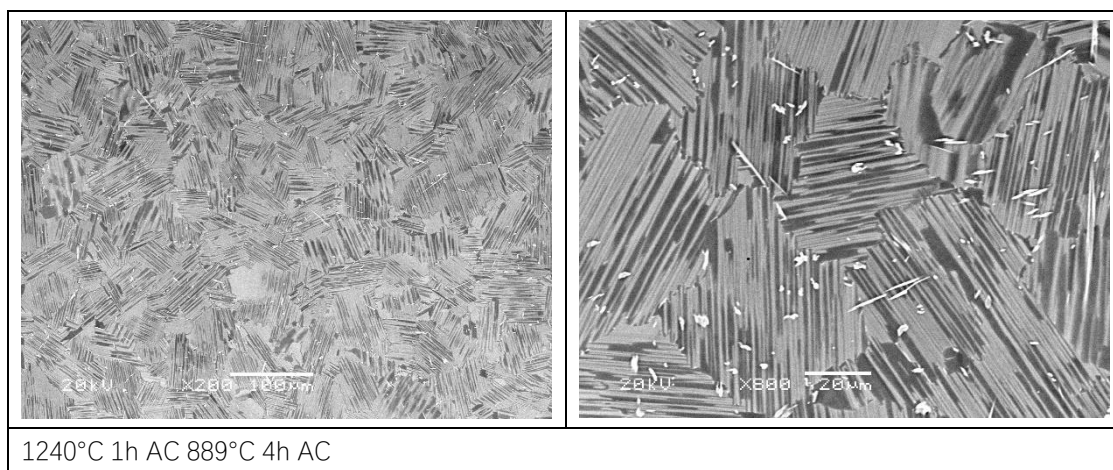


Figure 7. 1 BSE mode SEM images for tensile tested samples.

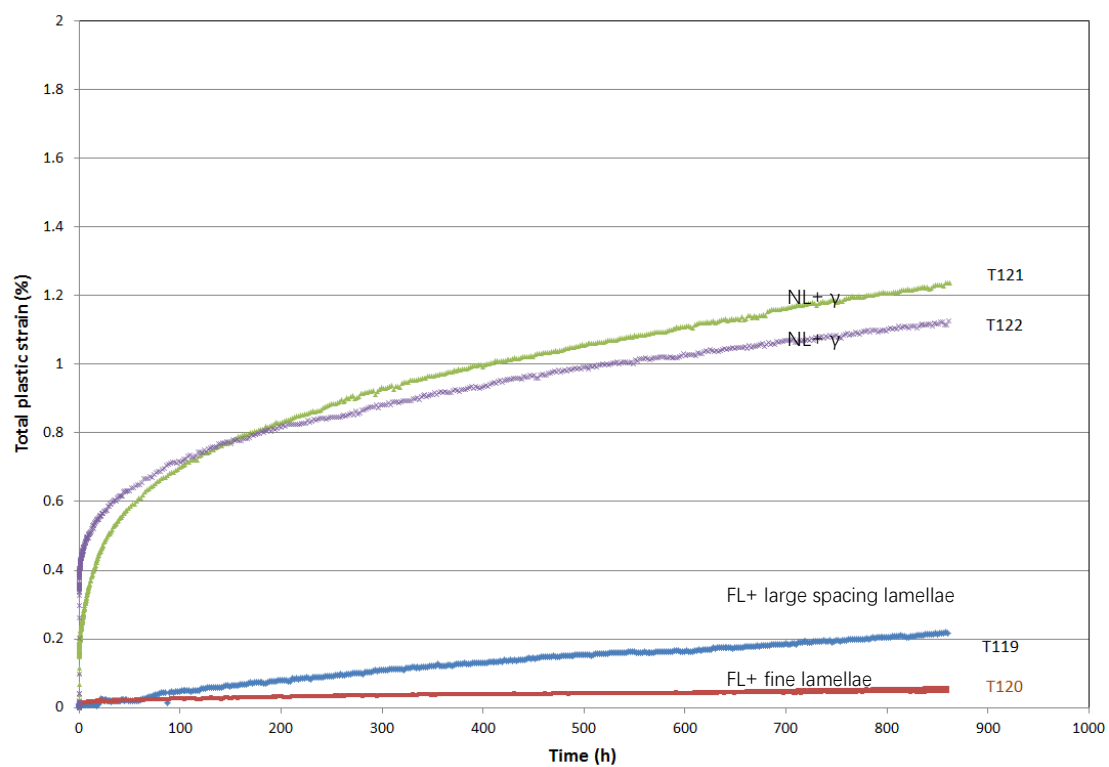
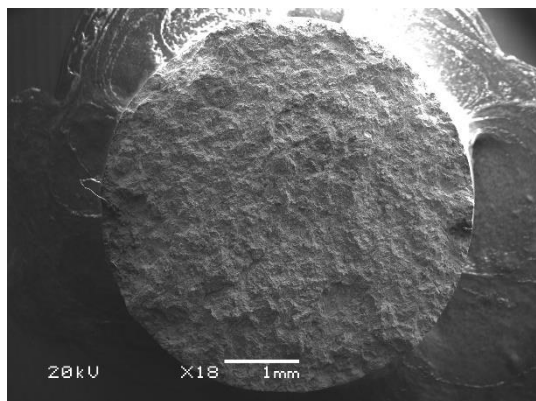
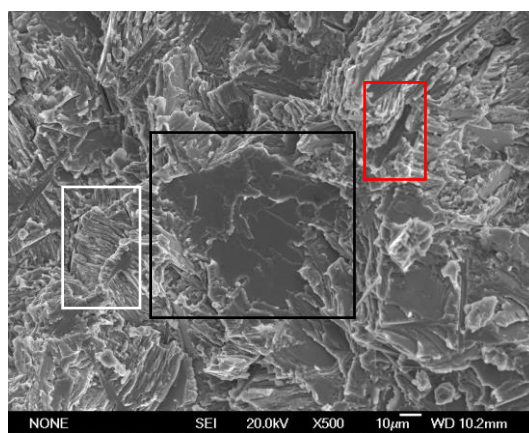


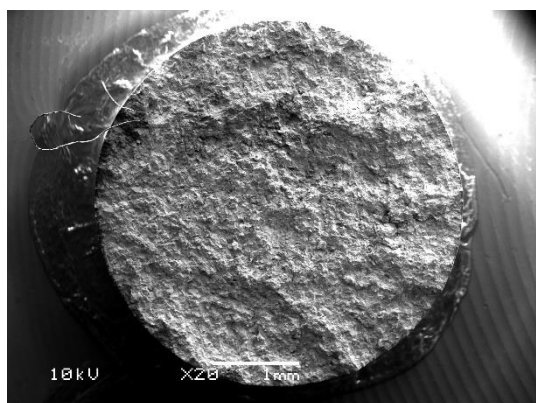
Figure 7. 2 Creep behaviour at 750°C and 250Mpa of mechanical tested samples. Corresponding microstructures were indicated in images.



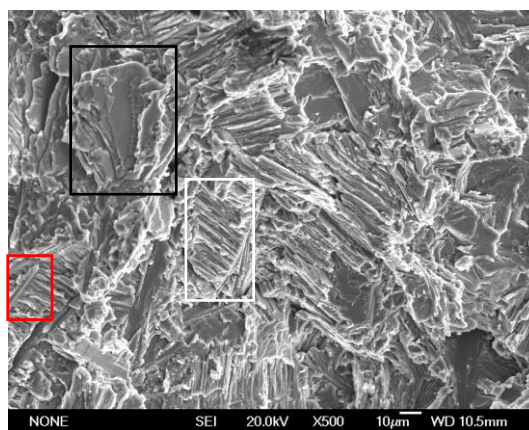
(a)



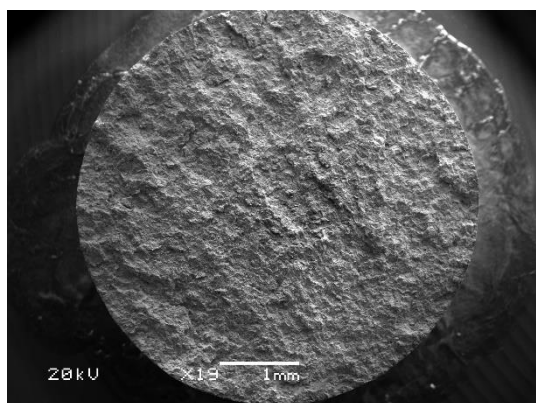
(b)



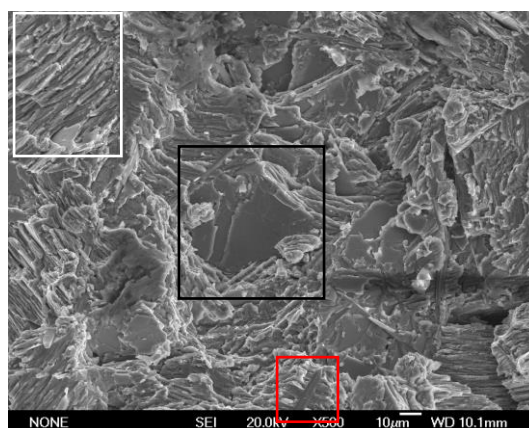
(c)



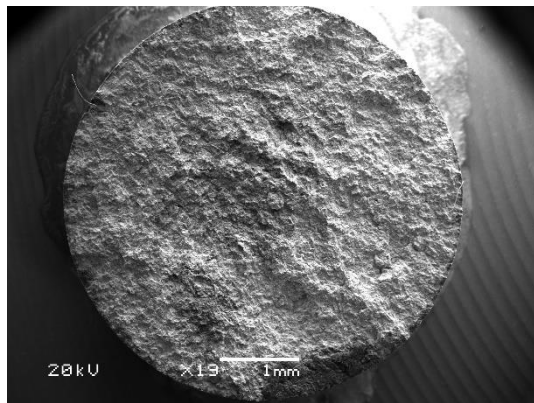
(d)



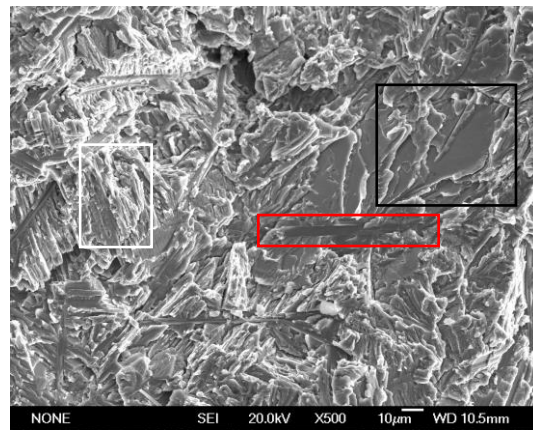
(e)



(f)



(g)



(h)

Figure 7. 3 Low and high-magnification fracture surfaces SEM images for tensile tested samples. Interlamellar and translamellar cracking and debonding of boride were marked by black, white and red frames respectively.

Tensile Testing Samples	T (°C)	YS (MPa)	UTS (MPa)	El. (%)
1310°C/1h/FC to 1200°C/AC+900°C/4h/AC (T119)	20	632	732	0.41
	20	639	674	0.27
	750	466	726	1.26
	750	474	701	0.94
1310°C/1h/AC+900°C/4h/AC (T120)	20	696	771	0.36
	20	781	781	0.20
	750	492	653	0.69
	750	469	732	1.23
1280°C/2h/AC+900°C/4h/AC (T121)	20	619	716	0.48
	20	637	718	0.41
	750	427	723	1.21
	750	422	712	1.20
1260°C/2h/AC+900°C/4h/AC (T122)	20	696	807	0.52
	20	681	754	0.39
	750	497	773	1.30
	750	505	757	1.09

Table 7. 1 Tensile testing conditions and results for selected samples.

CHAPTER 8 GENERAL DISCUSSION

The work reported in chapter 4, 5, 6 and 7 was discussed in two parts. First, phase transformation, relationship of cooling rate, temperature and time with microstructure and specific phase or microstructure of 0.8B alloy was discussed. Second, the method of improving the temperature capacity of 0.8B alloy was discussed.

8.1 Study on Ti-44.2Al-4Nb-1Mo-0.8B Alloy

The detailed study of phase transformation was mainly discussed in this section. The phase diagram of 0.8B alloy was mainly discussed in the first subsection. The study on CCT via Jominy quenching, air cooling and furnace cooling, and TTT via ageing at different temperatures for with different times was discussed in the second subsection.

Compare with the original TNM-B alloy, the heat treated TNM-0.8B alloy come with the excellent creep resistant at high pressure and temperature environment. As shown in Figure 8.1. The heat treated TNM-0.8B represent the very small total plastic strain from during the creep testing up to 850 hours under the testing condition of 250MPa 750°C. The total plastic strains changing of original TNM alloy is up to 0.16% per 100 hours during the 100 hours to 300 hours, but there is no significant plastic strains change (less than 0.02% per 100 hours during 100 to 850 hours) on heat treated TNM-0.8B alloy. Thus, the heat treated 0.8B

alloy has a better creep resistance than original TNM-B alloy. The heat treated TNM-0.8B alloy with fully lamellar microstructure could fulfil the requirements of work at a higher temperature than original TNM-B alloy.

8.1.1 Phase Diagram of TNM-B Alloys

The phase diagram of 0.8B alloy at 1150°C to 1380°C is mapped in Figure 4.8. The sequence of solid phase transformation for 0.8B alloy followed $\beta \rightarrow \beta+\alpha \rightarrow \alpha \rightarrow \alpha+\gamma \rightarrow \alpha+\gamma+\beta$. 0.8B alloy had a 0% β phase field at temperature 1230°C to 1300°C and a 100% α phase field at 1270°C to 1300°C. The 100% α phase field provided an opportunity for the solution treatment which could be utilised to manipulate the morphology and size of the β phase formed during cooling. Thus, 0.8B alloy offered a way to avoid the disadvantages of the original TNM alloy. A large amount of β phases degraded creep strength and room temperature ductility as the original TNM alloy had a β phase in the whole range of temperature. The β phase also led to the formation of globular γ grains, thereby resulting in a further decrease in creep and yield strengths^[168]. Besides, the transformation process of $\beta \rightarrow \beta+\alpha \rightarrow \alpha$ could be utilised to control the size of lamellar colonies. Small lamellar colonies would produce high yield strength and ductility. The single α phase field of 0.8B alloy was up to 30°C and the range met the requirements of industrial operation.

During the study on the phase diagram of different alloys, the followed results

could be summarised as follows: For Ti-(44-45.5) Al alloys, the α transus temperature, 0% β phase field and 100% α phase field depended on the concentration of Al. The higher the concentration of Al was, the higher the α transus temperature would be and the larger 0% β phase field and 100% α phase field would be. These results were consistent with the phase diagram shown in Figure 2.16.

TNM-B alloys relied on titanium boride to prevent the growth of α grains through Zener pinning mechanism. However, the coarsening of boride precipitates at high temperature would lead to the loss of pinning power. The 0.8B alloy showed better α grain stability than 0.1B and 0.3B alloys since excess boron formed more borides of ribbon morphology and the slight coarsening of boride ribbons maintained its Zener pinning mechanism and prevented the growth of α grains.

8.1.2 CCT and TTT on Ti-44.2Al-4Nb-1Mo-0.8B Alloy

Jominy quenching at different temperatures and relatively (1400°C/15min/JQ and 1300°C/1h/JQ) slower cooling rate (furnace and air cooling) was designed to reveal the relationship between cooling rate and microstructure. The results could be summarised as follows: Slower cooling rate would lead to larger lamellar spacing, wider γ grain boundary and more volume of β phase precipitates.

In terms of the phase diagram mapped in Figure 4.08, the β transus temperature

was 1230°C, which meant that the β phase should start to precipitate below 1230°C in equilibrium. However, the starting temperature for the transformation of the β phase should shift to a lower value under the condition of continuous cooling. The B_2 phase should start to precipitate at lower temperature, which depended on cooling rate. No β phase precipitates were observed in the samples heat treated with 1290°C 2h FC 1182°C AC. However, β phase precipitates were observed in the samples heat treated with 1310°C 2h FC 1085°C AC, 1310°C 2h FC 987°C AC and 1310°C 2h FC 889°C AC, which meant that the precipitation temperature of the β phase was close to 1182°C under the condition of furnace cooling. According to the discussion above and the study in 5.1, the schematic CCT diagram for 0.8B alloy is mapped in Figure 8.2.

The experiment of ageing at different temperatures and double ageing after solution treatment was designed to reveal the relationship among ageing temperature, time and microstructure. The results could be summarised as follows: Higher ageing temperature or longer ageing time would lead to larger lamellar spacing, wider γ grain boundary and more volume of β phase precipitates. Ageing at low temperature for a short time had a positive effect on the nucleation of β phase precipitates. Continuous ageing for a long time would lead to the decrease of nucleation rate and the growth of existing precipitates over time. Ageing at a higher temperature exerted a positive effect on the growth

of β phase precipitates. Thus, short-time low and higher-temperature ageing could make long-time aged 0.8B alloy produce a similar microstructure. Double ageing after solution treatment could save a lot of time for industrial production.

For high-temperature aged samples, grain boundary (GB) B_2 phase precipitates formed after 2-hour ageing at the SEM level and the same level of GB phase precipitates were generated after 16-hour ageing at lower temperature. Higher ageing temperature promoted the earlier nucleation of the B_2 phase. The same reaction mechanism should also happen in lamellar (IL) B_2 phase precipitates. Indeed, noticeable IL B_2 phase precipitates were observed in a sample aged at high temperature for a long time (1290°C 2h AC 889°C 64h AC). The IL B_2 phase should precipitate at low temperature (792°C) but for longer ageing time (e.g. more than 96 h). More energy was required by the nucleation of the B_2 phase in lamellar than the grain boundary. Thus, it took longer time for the IL B_2 phase to precipitate compared with the GB B_2 phase. According to the discussion above and the study in 5.2, the schematic TTT diagram for 0.8B alloy is mapped in Figure 8.3.

8.2 Temperature Capacity Improvement via Heat Treatment

As mentioned in the literature review, the fully lamellar microstructure represented the best mechanical property and temperature capacity.

Considering the feasibility of industrial production, TNM-0.8B alloy was advised to receive two-step heat treatment (1290°C 1h AC + 889°C 4h AC) to achieve a fully lamellar microstructure.

The first step: α phase field solution heat treatment with air cooling for 1 hour. The 0.8B alloy entered the single α phase field at 1290°C. 1-hour solution treatment was selected because 1h was enough to complete the transformation to the single α phase and unable to promote the growth of α grains. As borides and reprecipitated β particles impeded the growth of α grains, solution treated 0.8B samples showed a uniform lamellar colony close to 70 μ m with ultra-fine lamellae.

The second step: Long-time ageing at high temperature. Ageing at 889°C for 4 hours was to achieve an equilibrium. Without changing the size of the lamellar colony, ageing promoted the continuous and discontinuous coarsening of the lamellar colony, leading to the increase of lamellar spacing, and the coarsening of the γ phase and the precipitation of γ phase particles at the grain boundary.

8.3 Microstructure and Creep Result Comparison

Compared with the original/as-cast TNM-B alloy, the heat-treated alloy had more uniform grain size, smaller lamellar spacing and narrower grain boundaries, and presented significant differences in grain boundary morphology. The grain boundary of the heat-treated alloy contained a majority of γ phases with a small

amount of uniform and fine B_2 particles. However, the as-cast alloy owned a large amount of β phase plates at the grain boundary.

The heat treated 0.8B alloy with the above heat treatment condition had better creep resistance compared with the reference samples with a nearly lamellar (lamellar + γ) microstructure (T121 and T122 in section 7.2) which was similar to the original TNM alloy. Thus, the reference samples should have similar creep resistance with the original TNM alloy. By referring to the creep curves of the original TNM alloy (Figure 8.4), the follow inference could be obtained: The heat-treated 0.8B alloy was superior to the original TNM alloy in creep resistance. Thus, the heat-treated 0.8B alloy with a fully lamellar microstructure could fulfill the requirements of work at higher temperature than the original TNM alloy.

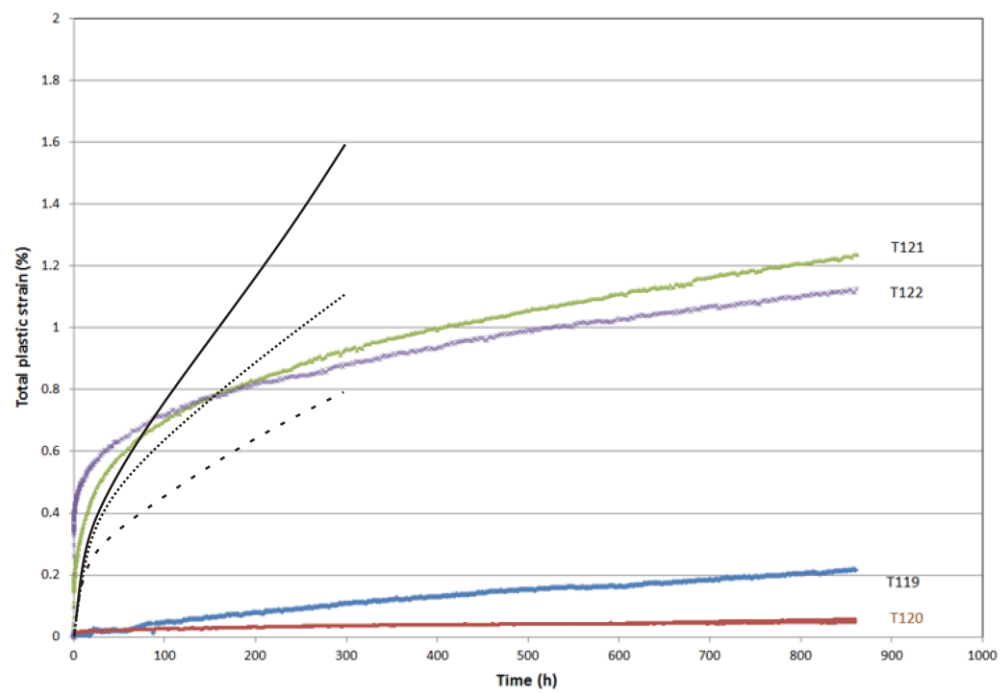


Figure 8. 1 Creep behaviour of the TNM-B (three black curves) and TNM-0.8B alloy (four colour curves). Reference by Figure 7.2 and Figure 8.4. ^[168].

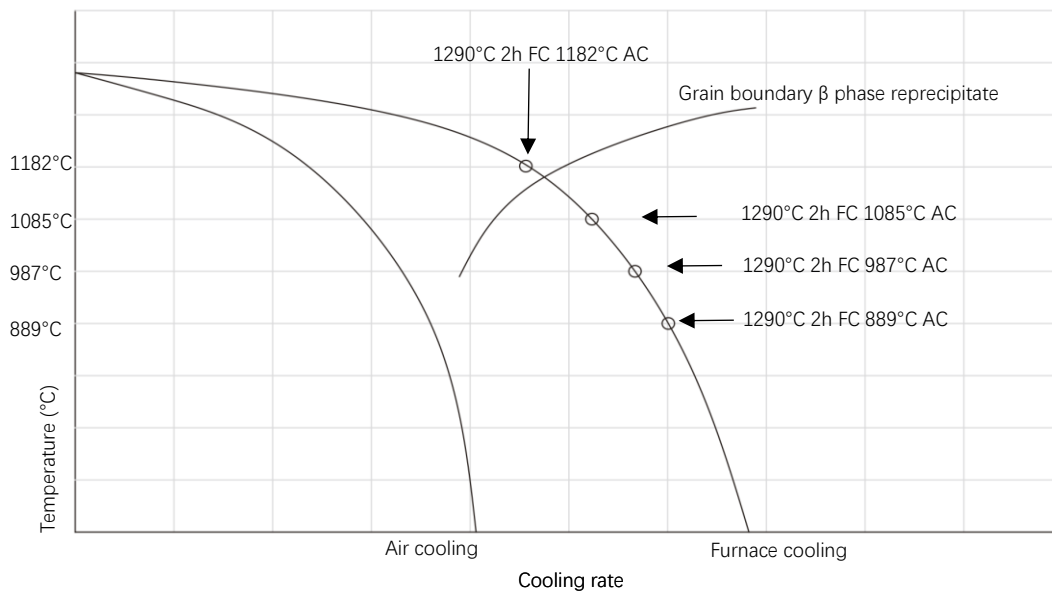


Figure 8. 2 Schematic CCT diagram for 0.8B alloy.

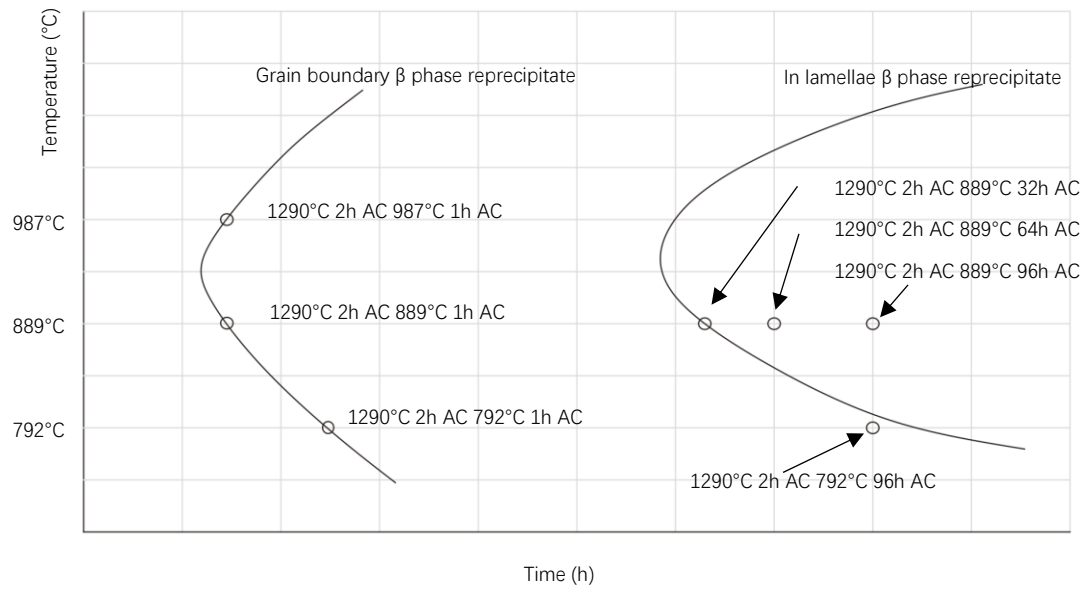


Figure 8. 3 Schematic TTT diagram for 0.8B alloy.

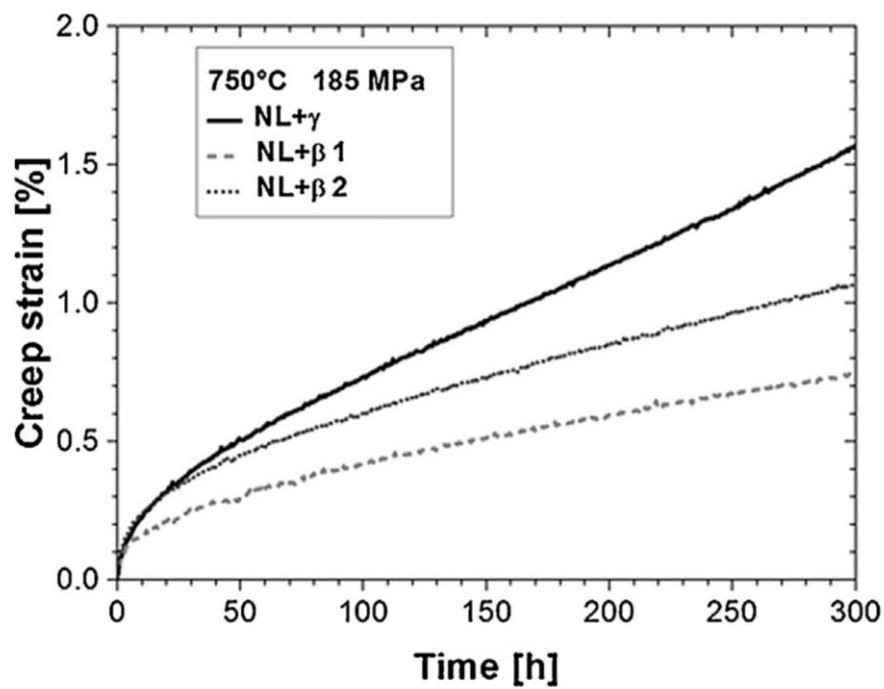


Figure 8. 4 Creep behaviour at 750°C and 185 Mpa of the TNM microstructure NL+ γ (original TNM alloy), NL+ β 1 and NL+ β 2^[168].

CHAPTER 9 CONCLUSIONS AND FUTURE WORK

9.1 Conclusions

The single α phase solution treatment was an effective way to manipulate the microstructure of Ti-44.2Al-4Nb-1Mo-0.8B Alloy.

The fully lamellar microstructure could be achieved by air cooling after single α phase solution treatment.

Finer lamellar spacing could be achieved by faster cooling (e.g. water quenching and air cooling) after single α phase solution treatment.

The β phase transus temperature of the 0.8B alloy was close to 1182°C under the condition of furnace cooling.

The GB β phase could be suppressed by air cooling and interrupting furnace cooling at 1182°C after single α phase solution treatment.

The in-lamellae β phase was observed in the long-time aged 0.8B alloy at high temperature after solution treatment (1290°C 2h AC 889°C 32-96h AC).

Higher GB β phase nucleation could be achieved by ageing at low temperature (792°C).

The faster growth of GB β phase could be achieved by ageing at high temperature (889°C).

Double ageing at low temperature first and high temperature later could contribute to high nucleation rate first and fast growth later, which was an effective way to save the manufacturing time of industrial production.

The 0.8B alloy with a fully lamellar microstructure could be achieved by ageing after α phase solution treatment (1290°C 1h AC 889°C 4h AC).

The heat-treated (1290°C 1h AC 889°C 4h AC) 0.8B alloy had a fully lamellar microstructure with fine lamellae. The size of the lamellar colony was uniform and close to 70 μ m. A small amount of uniform and fine B₂ particles formed at the lamellar colony boundary while ω phase particles existed in the B₂ phase.

Compared with the original TNM alloy, the heat-treated 0.8B alloy showed higher yield strength and creep resistance, which meant that the heat-treated 0.8B alloy could be used at higher temperature than the original TNM alloy. Thus, the heat-treated 0.8B alloy could be considered as a potential material for the LPT of third-generation aero engines.

9.2 Future Work

The design and development of industrial alloys is a complex work and calls for a lot of experiments and testing. A preliminary conception and experiment were

provided in this thesis to manipulate the microstructure of alloys. Suggestions for future work are listed as follows.

1. A detailed CCT and TTT diagrams are needed for 0.8B alloy.

The CCT diagrams are used to represent which types of phase changes will occur in a material as it is cooled at different rates, it represented the relationship between phase transformation and cooling rate, it is necessary to understand the relationship between cooling rate, time and phase transformation. The TTT diagram is useful for understanding the transformations of an alloy at elevated temperatures. It is necessary to understanding the relationship between the heat treatment time, temperature and phase transformation.

2. In-lamellae β phase reprecipitates were observed in long-time aged 0.8B alloy. Appearing to very fine and light at the SEM level, β precipitates might have already precipitated at lower temperature like 1290°C 2h AC 889°C 24h AC and 1290°C 2h AC 792°C (64-96) h AC or for shorter ageing time. Thus, more TEM work remains to be done. As mentioned above, most of β particles precipitated to form α_2 lamellae and a small amount of particles were located in γ lamellae. Thus, the parent phase of in-lamellae β particles remains to be further studied. SEM images displayed the neat and uniform arrangement of in-lamellae β particles, possibly indicating that the β phase had an orientation relationship with the prior phase. These in-lamellae β particles might provide the TiAl alloy with

super mechanical properties because the β phase had higher hardness and uniformly arranged microstructure which normally produced better mechanical properties.

3. GB β phase reprecipitates were normally located at the end of α_2 lamellae.

In-lamellae β phases mostly reprecipitated in α_2 lamellae. It was likely that this type of β phases nucleated in α_2 lamellae and grew up at the expense of α_2 lamellae. The parent phase of the grain boundary and in-lamellae β phases remains to be further studied.

4. It is necessary to conduct more mechanical tests on the heat-treated (1290°C 1h AC 889°C 4h AC) 0.8B alloy. For example: long time creep testing, higher temperature creep testing. Simulate the working environment of LPT to make sure the alloy could be used on LPT of the aero engines.

5. As discussed above, the small size of the lamellar colony with ultra-fine lamellar microstructure for 0.8B alloy may be achieved by short-time β phase solution treatment, interrupting furnace cooling at α single phase field for a certain time and then oil quenching (OQ) like 1400°C×0.25h + FC 1270°C 1h OQ) + 800°C 2h AC. Heating the TNM-0.8B alloy to 1400°C and holding 0.25h to make sure the sample access single β phase, furnace cooling the sample to 1270°C may lead a β to α transformation, the small grain size may be achieved during this process. The untransformed β phase will be transformed to α phase during the

holding at 1270°C, the α grains should not grow up as the holding time is short, the α grains will transform to fine lamella colonies during the oil quenching. The further isothermal stabilisation annealing between 850 and 950°C also needed to increase the γ phase fraction and leading to a significant increase in hardness.

REFERENCES

1. B.P. Bewlay, S. Nag, A. Suzuki, and M.J. Weimer, TiAl alloys in commercial aircraft engines. *Materials at High Temperatures*, 2016. 33(4-5): p. 549-559.
2. M. Ashraf Imam, The 13th World Conference on Titanium (Ti-2015). *JOM*, 2016. 68(9): p. 2492-2501.
3. T. Tetsui and Y. Miura, Heat resistant cast TiAl alloy for passenger vehicle turbocharger. Vol. 39. 2002. 592-615.
4. P. Bartolotta, J. Barrett, T. Kelly, and R. Smashey, The use of cast Ti-48Al-2Cr-2Nb in jet engines. *JOM*, 1997. 49(5): p. 48-50.
5. U. Habel, F. Heutling, C. Kunze, W. Smarsly, G. Das, and H. Clemens. Forged Intermetallic γ -TiAl Based Alloy Low Pressure Turbine Blade in the Geared Turbofan. in *Proceedings of the 13th World Conference on Titanium*. 2016. Wiley Online Library.p. 1223-1227.
6. A. Lasalmonie, Intermetallics: Why is it so difficult to introduce them in gas turbine engines? *Intermetallics*, 2006. 14(10): p. 1123-1129.
7. G.E.R. Schulze. *Metallphysik Ein Lehrbuch*. 1967; Available from: <http://catalog.hathitrust.org/api/volumes/oclc/10015212.html>.
8. A. Bose, *Advances in Particulate Materials*. 2013: Elsevier Science. p5-25.
9. A. Hussain, S. Mehmood, N. Rasool, N. Li, and C.C. Dharmawardhana, Electronic structure, mechanical and optical properties of TiAl₃ (L12 & D022) via first-principles calculations. *Chinese Journal of Physics*, 2016. 54(3): p. 319-328.
10. A. Guitten, H. Kriaa, E. Bouzy, J. Guyon, and N. Maloufi, A Dislocation-Scale Characterization of the Evolution of Deformation Microstructures around Nanoindentation Imprints in a TiAl Alloy. *Materials* 2018, 11, P.305-312.
11. G. Sauthoff, *Intermetallics*. 2008: Wiley. p26-56.
12. F. Appel, J.D.H. Paul, and M. Oehring, *Gamma Titanium Aluminide Alloys: Science and Technology*. 2011: Wiley. p21-50
13. T. Tetsui and Y. Miura, Heat-resistant Cast TiAl Alloy for Passenger Vehicle Turbochargers. Mitsubishi Heavy Industries, Ltd. Technical Review, Feb. 2002. 39: p. 1 -5.
14. D. Zhihai, L. Jinshan, Z. Tiebang, H. Rui, Z. Hong, and C. Hui, Hot Workability and Microstructure Evolution of TiAl Alloy in (α_2 + γ) Dual-phase Field. *Rare Metal Materials and Engineering*, 2013. 42(7): p. 1356-1361.
15. *Intermetallics: Compounds, Principles and Practice*. by JH Westbrook and RL Fleisher (John Willey Sons, NY, 1995), 1995. 1: p. 1126.
16. S. Mayer, E. Schwaighofer, M. Schloffer, and H. Clemens. The use of in-situ characterization techniques for the development of intermetallic titanium aluminides. in *Materials Science Forum*. 2014.

17. P. A. Bartolotta and D. L. Krause, Titanium Aluminide Applications in the High Speed Civil Transport. 1999.
18. S. Djanarthany, J.C. Viala, and J. Bouix, An overview of monolithic titanium aluminides based on Ti3Al and TiAl. *Materials Chemistry and Physics*, 2001. 72(3): p. 301-319.
19. W.J. Zhang, B.V. Reddy, and S.C. Deevi, Physical properties of TiAl-base alloys. *Scripta Materialia*, 2001. 45(6): p. 645-651.
20. G. Lütjering and J.C. Williams, *Titanium*. 2007: Springer Berlin Heidelberg.
21. X. Wu, Review of alloy and process development of TiAl alloys. *Intermetallics*, 2006. 14(10-11): p. 1114-1122.
22. F. Appel, U. Brossmann, U. Christoph, S. Eggert, P. Janschek, U. Lorenz, J. Mullauer, M. Oehring, and J.D.H. Paul, Recent progress in the development of gamma titanium aluminide alloys. *Advanced Engineering Materials*, 2000. 2(11): p. 699-720.
23. A. Gil, H. Hoven, E. Wallura, and W.J. Quadackers, The effect of microstructure on the oxidation behaviour of TiAl-based intermetallics. *Corrosion Science*, 1993. 34(4): p. 615-630.
24. X. Zan, Y.-h. He, Y. Wang, and Y.-m. Xia, Dynamic behavior and fracture mode of TiAl intermetallics with different microstructures at elevated temperatures. *Transactions of Nonferrous Metals Society of China*, 2011. 21(1): p. 45-51.
25. T. Voisin, J.-P. Monchoux, M. Thomas, C. Deshayes, and A. Couret, Mechanical Properties of the TiAl IRIS Alloy. *Metallurgical and Materials Transactions A*, 2016. 47(12): p. 6097-6108.
26. M. Yamaguchi, H. Inui, and K. Ito, High-temperature structural intermetallics. *Acta Materialia*, 2000. 48(1): p. 307-322.
27. A. Brotzu, F. Felli, F. Marra, D. Pilone, and G. Pulci, Mechanical properties of a TiAl-based alloy at room and high temperatures. *Materials Science and Technology*, 2018. 34(15): p. 1847-1853.
28. N. O. Korotkova, A. P. Dolbachev, and T. Akopyan, Analysis of the phase composition and microstructure of a TNM-type alloy by using thermodynamic calculation. *Non-ferrous Metals*, 2017. Vol. 43. P.43-49.
29. D. Hu, Role of boron in TiAl alloy development: a review. *Rare Metals*, Vol. 35. 2016. P.1-14.
30. T. Radchenko, V. Tatarenko, and H. Zapolsky, Statistical Thermodynamics and Ordering Kinetics of D019 Type Phase: Application of the Models for H.C.P.-Ti-Al Alloy. *Solid State Phenomena*, 2008. 138: p. 283-302.
31. J. Wiezorek, X. Zhang, W. Clark, and H. L. Fraser, Activation of slip in lamellae of α_2 -Ti3Al in TiAl alloys. *Philosophical Magazine A*, 2010. July 1: p. 217-238.
32. D. Xu, H. Wang, R. Yang, and A. Sachdev, MD simulation of asymmetric nucleation and motion of $\langle 011 \rangle$ superdislocations in TiAl. *Chinese Science Bulletin*, 2014. 59: p. 1725-1737.
33. T. Hong, T.J. Watson-Yang, A.J. Freeman, T. Oguchi, and J.-h. Xu, Crystal structure, phase stability, and electronic structure of Ti-Al intermetallics: TiAl3. *Physical Review B*, 1990. 41(18): p. 12462-12467.
34. L. Lu and D.P. Pope, Slip and twinning in TiAl PST crystals. *Materials Science and Engineering: A*, 1997. 239-240: p. 126-130.
35. M. Yamaguchi, Y. Umakoshi, and T. Yamane, Plastic deformation of the intermetallic compound Al3Ti. *Philosophical Magazine A*, 1987. 55(3): p. 301-315.

36. M. Yamaguchi, Y. Umakoshi, and T. Yamane, Deformation of the Intermetallic Compound Al_3Ti and Some Alloys with An Al_3Ti Base. MRS Proceedings, 1986. 81: p. 275.
37. D. Hu, Role of boron in TiAl alloy development: a review. Rare Metals, 2016. 35(1): p. 1-14.
38. U. Kitkamthorn, L.C. Zhang, and M. Aindow, The structure of ribbon borides in a Ti-44Al-4Nb-4Zr-1B alloy. Intermetallics, 2006. 14(7): p. 759-769.
39. M. De Graef, J.P.A. Löfvander, C. McCullough, and C.G. Levi, The evolution of metastable Bf borides in a Ti-Al-B alloy. Acta Metallurgica et Materialia, 1992. 40(12): p. 3395-3406.
40. T.T. Cheng, The mechanism of grain refinement in TiAl alloys by boron addition -- an alternative hypothesis. Intermetallics, 2000. 8(1): p. 29-37.
41. W.B. Pearson, Pearson's handbook of crystallographic data for intermetallic phases, P. Villars and L.D. Calvert, Editors. 1985, American Society for Metals: Metals Park, Oh .:
42. G. Sharma, R. V Ramanujan, and G. Tiwari, Interphase precipitation in a γ -TiAl alloy. Materials Science and Engineering A-structural Materials Properties Microstructure and Processing - MATER SCI ENG A-STRUCT MATER, 1999. 269: p. 21-25.
43. J.L. Murray, Phase diagrams of binary titanium alloys. 1987: ASM International.
44. J.C. Schuster and M. Palm, Reassessment of the binary aluminum-titanium phase diagram. Journal of Phase Equilibria and Diffusion, 2006. 27(3): p. 255-277.
45. M. Bram, M.W.T. Ebel, A. P. Cysne Barbosa, and N. Tuncer, ADVANCES IN POWDER METALLURGY: PROPERTIES, PROCESSING AND APPLICATIONS. 2013. p. 520-554.
46. Y.-W. Kim, Microstructural evolution and mechanical properties of a forged gamma titanium aluminide alloy. Acta Metallurgica et Materialia, 1992. 40(6): p. 1121-1134.
47. S.C. Huang, Alloying considerations in gamma-based alloys. 1993, United States: Minerals, Metals and Materials Society.
48. A. Rahmel and P.J. Spencer, Thermodynamic aspects of TiAl and TiSi_2 oxidation: The Al-Ti-O and Si-Ti-O Phase diagrams. Oxidation of Metals, 1991. 35(1): p. 53-68.
49. B.G. Kim, G.M. Kim, and C.J. Kim, Oxidation behavior of TiAl-X (X = Cr, V, Si, Mo or Nb) intermetallics at elevated temperature. Scripta Metallurgica et Materialia, 1995. 33(7): p. 1117-1125.
50. S. Tsuyama, S. Mitao, and K.-n. Minakawa, Alloy modification of γ -base titanium aluminide for improved oxidation resistance, creep strength and fracture toughness. Materials Science and Engineering: A, 1992. 153(1): p. 451-456.
51. T. Noda, M. Okabe, S. Isobe, and M. Sayashi, Silicide precipitation strengthened TiAl. Materials Science and Engineering: A, 1995. 192-193: p. 774-779.
52. U. Hecht, D. Daloz, J. Lapin, A. Drevermann, V. Witusiewicz, and J. Zollinger, Solidification of TiAl-based Alloys. Materials Research Society Symposium Proceedings, 2008. 1128.
53. I. Agote, J. Coleto, M. Gutiérrez, A. Sargsyan, M. García de Cortazar, M.A. Lagos, I.P. Borovinskaya, A.E. Sytshev, V.L. Kvanin, N.T. Balikhina, S.G. Vadchenko, K. Lucas, A. Wisbey, and L. Pambaguian, Microstructure and mechanical properties of gamma TiAl based alloys produced by combustion synthesis+compaction route. Intermetallics, 2008. 16(11): p. 1310-1316.
54. D. Hu and R.R. Botten, Phase transformations in some TiAl-based alloys. Intermetallics, 2002. 10(7): p. 701-715.

55. X. Li, H. Xu, W. Xing, B. Chen, Y. Ma, and K. Liu, Phase Transformation Behavior of a β -Solidifying γ -TiAl-Based Alloy from Different Phase Regions with Various Cooling Methods. *Metals*, 2018. 8: p. 731.
56. C. Hammond and P.M. Kelly, The crystallography of titanium alloy martensites. *Acta Metallurgica*, 1969. 17(7): p. 869-882.
57. D. Hu and H. Jiang, Martensite in a TiAl alloy quenched from beta phase field. *Intermetallics*, 2015. 56: p. 87-95.
58. M. Takeyama and S. Kobayashi, Physical metallurgy for wrought gamma titanium aluminides: Microstructure control through phase transformations. *Intermetallics*, 2005. 13(9): p. 993-999.
59. J.C. Williams, The Science Technology and Applications of Titanium, 1973: p. 1433-1494.
60. C. Li, G. Li, Y. Yang, M. Varlioglu, and K. Yang, α'' Martensitic Twinning in Alpha + Beta Ti-3.5Al-4.5Mo Titanium Alloy. *Journal of Metallurgy*, 2011. 2011.
61. C.R. Feng, D.J. Michel, and C.R. Crowe, Martensites in rolled XD™ titanium aluminide. *Scripta Metallurgica et Materialia*, 1990. 24(10): p. 1913-1917.
62. Q. Xia, J.N. Wang, J. Yang, and Y. Wang, On the massive transformation in TiAl-based alloys. *Intermetallics*, 2001. 9(5): p. 361-367.
63. Y. Yamabe, M. Takeyama, and M. Kikuchi, Gamma Titanium Aluminides, Y.-W. Kim, R. Wagner, and M. Yamaguchi, Eds., TMS, Warrendale, PA, 1995: p. 111-117.
64. Y. Mishin and C. Herzig, Diffusion in the Ti-Al system. *Acta Materialia*, 2000. 48(3): p. 589-623.
65. D. Hu, A.J. Huang, and X. Wu, TEM characterisation of Widmanstätten microstructures in TiAl-based alloys. *Intermetallics*, 2005. 13(2): p. 211-216.
66. Y. Chen, L. Cheng, L. Sun, Y. Lu, G. Yang, H. Kou, and E. Bouzy, Characterization of a New Microstructure in a β -Solidifying TiAl Alloy after Air-Cooling from a β Phase Field and Subsequent Tempering. *Metals*, 2018. 8(3): p. 156.
67. E. Lee, R. Banerjee, S. Kar, D. Bhattacharyya, and H.L. Fraser, Selection of α variants during microstructural evolution in α/β titanium alloys. *Philosophical Magazine*, 2007. 87(24): p. 3615-3627.
68. S. Mitao and L.A. Bendersky, Morphology and growth kinetics of discontinuous coarsening in fully lamellar Ti-44 Al (at%) alloy. *Acta Materialia*, 1997: p. Medium: X; Size: pp. 4475-4489.
69. S.A. Jones and M.J. Kaufman, Phase equilibria and transformations in intermediate titanium--aluminum alloys. *Acta Metallurgica et Materialia*, 1993. 41(2): p. 387-398.
70. W.G. Burgers, On the process of transition of the cubic-body-centered modification into the hexagonal-close-packed modification of zirconium. *Physica*, 1934. 1(7): p. 561-586.
71. U. Dahmen, Orientation Relationships in precipitation systems. Vol. 30. 1982. 63-73.
72. Y. Yang, Variant Selection of $\beta \rightarrow \alpha$ Phase Transformation in Titanium Alloys. *Scripta Materialia*, 1996. 34(8): p. 1281-1286.
73. N. Gey and M. Humbert, Specific analysis of EBSD data to study the texture inheritance due to the $\beta \rightarrow \alpha$ phase transformation. *Journal of Materials Science*, 2003. 38(6): p. 1289-1294.

74. T. Karthikeyan, S. Saroja, and M. Vijayalakshmi, Evaluation of misorientation angle-axis set between variants during transformation of bcc to hcp phase obeying Burgers orientation relation. *Scripta Materialia*, 2006. 55(9): p. 771-774.
75. M.J. Blackburn, Some aspects of phase transformations in titanium alloys, in *The Science, Technology and Application of Titanium*, R.I. Jaffee and N.E. Promisel, Editors. 1970, Pergamon. p. 633-643.
76. M.C. Kim, M.H. Oh, J.H. Lee, H. Inui, M. Yamaguchi, and D.M. Wee, Composition and growth rate effects in directionally solidified TiAl alloys. *Materials Science and Engineering: A*, 1997. 239-240: p. 570-576.
77. R.V. Ramanujan, Phase transformations in γ based titanium aluminides. *International Materials Reviews*, 2000. 45(6): p. 217-240.
78. P. Maziasz and C. T. Liu, Development of ultrafine lamellar structures in two-phase γ -TiAl alloys. Vol. 29. 1998. 105-117.
79. R.D. Doherty, CHAPTER 15 - DIFFUSIVE PHASE TRANSFORMATIONS IN THE SOLID STATE, in *Physical Metallurgy (Fourth Edition)*, R.W. Cahn and P. Haasen†, Editors. 1996, North-Holland: Oxford. p. 1363-1505.
80. Q. Xu, C. Lei, and Y. Zhang, TEM in situ observations of α_2 to α_2/γ phase transformation in a Ti-45 at. pct Al alloy. *Gamma titanium aluminides*, 1995: p. 189-196.
81. S. Zghal, S. Naka, and A. Couret, A quantitative tem analysis of the lamellar microstructure in tial based alloys. *Acta Materialia*, 1997. 45(7): p. 3005-3015.
82. A. Denquin and S. Naka, Phase transformation mechanisms involved in two-phase TiAl-based alloys--I. Lamellar structure formation. *Acta Materialia*, 1996. 44(1): p. 343-352.
83. Y.S. Yang and S.K. Wu, Orientation faults of γ lamellae in a Ti-40 at% Al alloy. *Scripta Metallurgica et Materialia*, 1991. 25(1): p. 255-260.
84. Y.-W.D. Kim, D. M., Effect of Boron Addition on Grain Refinement and Lamellar Formation in Wrought-Processed Gamma TiAl Alloys. *STRUCTURAL INTERMETALLICS -INTERNATIONAL SYMPOSIUM-*, 2001: p. 8.
85. W. Lefebvre, A. Menand, and A. Loiseau, Influence of oxygen on phase transformations in a Ti-48 At. pct Al alloy. *Metallurgical and Materials Transactions A*, 2003. 34(10): p. 2067-2075.
86. S.R. Dey, A. Hazotte, and E. Bouzy, Crystallography and phase transformation mechanisms in TiAl-based alloys – A synthesis. *Intermetallics*, 2009. 17(12): p. 1052-1064.
87. S.R. Singh and J.M. Howe, High-resolution electron microscopy of γ - α_2 interfaces in titanium aluminide. *Philosophical Magazine A*, 1992. 66(5): p. 739-771.
88. L. Xu, Y.Y. Cui, Y.L. Hao, and R. Yang, Growth of intermetallic layer in multi-laminated Ti/Al diffusion couples. *Materials Science and Engineering: A*, 2006. 435-436: p. 638-647.
89. W.J. Zhang, L. Francesconi, E. Evangelista, and G.L. Chen, Characterization of widmanstätten laths and interlocking boundaries in fully-lamellar TiAl-base alloy. *Scripta Materialia*, 1997. 37(5): p. 627-633.
90. A.J.H. D. Hu, A. Grégoire, X.Y. Li, X. Wu, M.H. Loretto, Determining continuous cooling phase transformation behaviour in Ti-46Al-8Nb using jominy end quenching, in

- Proceedings of the 3rd International Conference on Advanced Materials Processing, J.F.N.a.M. Barnett, Editor. 2005.
91. W. Sprengel, N. Oikawa, and H. Nakajima, Single-phase interdiffusion in TiAl. *Intermetallics*, 1996. 4(3): p. 185-189.
 92. X. Wu and D. Hu, Microstructural refinement in cast TiAl alloys by solid state transformations. *Scripta Materialia*, 2005. 52(8): p. 731-734.
 93. D. Hu, A.J. Huang, and X. Wu, On the massive phase transformation regime in TiAl alloys: The alloying effect on massive/lamellar competition. *Intermetallics*, 2007. 15(3): p. 327-332.
 94. X.D. Zhang, S. Godfrey, M. Weaver, M. Strangwood, P. Threadgill, M.J. Kaufman, and M.H. Loretto, The massive transformation in Ti--Al alloys: Mechanistic observations. *Acta Materialia*, 1996. 44(9): p. 3723-3734.
 95. D. Veeraraghavan, P. Wang, and V.K. Vasudevan, Kinetics and thermodynamics of the $\alpha \rightarrow \gamma$ massive transformation in a Ti-47.5 at.% Al alloy. *Acta Materialia*, 1999. 47(11): p. 3313-3330.
 96. S.R. Dey, E. Bouzy, and A. Hazotte, EBSD characterisation of massive γ nucleation and growth in a TiAl-based alloy. *Intermetallics*, 2006. 14(4): p. 444-449.
 97. H. Mecking, U.F. Kocks, and C. Hartig, Taylor factors in materials with many deformation modes. *Scripta Materialia*, 1996. 35(4): p. 465-471.
 98. T.A. Parthasarathy, M.G. Mendiratta, and D.M. Dimiduk, Flow behavior of PST and fully lamellar polycrystals of Ti-48Al in the microstrain regime. *Acta Materialia*, 1998. 46(11): p. 4005-4016.
 99. F. Appel, U. Christoph, and R. Wagner. Structure and stress state of lamellar interfaces in two-phase titanium aluminides. in *Materials Research Society Symposium Proceedings*. 1994. p. 691-696.
 100. M.E. Hyman, C. McCullough, J.J. Valencia, C.G. Levi, and R. Mehrabian, Microstructure evolution in tial alloys with b additions: Conventional solidification. *Metallurgical Transactions A*, 1989. 20(9): p. 1847.
 101. M.E. Hyman, C. McCullough, C.G. Levi, and R. Mehrabian, Evolution of boride morphologies in TiAl-B alloys. *Metallurgical Transactions A*, 1991. 22(7): p. 1647-1662.
 102. D.J. Larson, C.T. Liu, and M.K. Miller, Boron solubility and boride compositions in $\alpha_2 + \gamma$ titanium aluminides. *Intermetallics*, 1997. 5(6): p. 411-414.
 103. H. Okamoto, Al-Ti (aluminum-titanium). *Journal of Phase Equilibria*, 1993. 14(1): p. 120-121.
 104. R.M. Imayev, V.M. Imayev, M. Oehring, and F. Appel, Alloy design concepts for refined gamma titanium aluminide based alloys. *Intermetallics*, 2007. 15(4): p. 451-460.
 105. V. Witusiewicz, A.A. Bondar, U. Hecht, J. Zollinger, L.V. Artyukh, and T.Y. Velikanova, The Al-B-Nb-Ti system: V. Thermodynamic description of the ternary system Al-B-Ti. *Journal of Alloys and Compounds*, Vol. 474. April 2009. P. 86-104.
 106. D. Hu, C. Yang, A. Huang, M. Dixon, and U. Hecht, Grain refinement in beta-solidifying Ti44Al8Nb1B. *Intermetallics*, 2012. 23: p. 49-56.
 107. C. Yang, H. Jiang, D. Hu, A. Huang, and M. Dixon, Effect of boron concentration on phase transformation texture in as-solidified Ti44Al8NbxB. *Scripta Materialia*, 2012. 67(1): p. 85-88.

108. U. Hecht, V. Witusiewicz, A. Drevermann, and J. Zollinger, Grain refinement by low boron additions in niobium-rich TiAl-based alloys. *Intermetallics* Volume 16, Issue 8, August 2008, P.969-978.
109. B. Liu, J. Li, and D. Hu, Solidification and grain refinement in Ti (48–50) Al₂Mn₂Nb₁B alloys. *Intermetallics*, 2018. 101: p. 99-107.
110. H. Clemens, M. Schloffer, E. Schwaighofer, R. Werner, A. Gaitzenauer, B. Rashkova, T. Schmoelzer, R. Pippan, and S. Mayer, Advanced β -Solidifying Titanium Aluminides – Development Status and Perspectives. *MRS Proceedings*, 2013. 1516: p. 3-16.
111. N. Belov and I. S. Chupakhin, Quantitative Analysis of Phase Composition of Alloy TNM-B1 based on TiAl(γ) Titanium Aluminide. *Metal Science and Heat Treatment*, 2014. 55.
112. C. Herzig, T. Przeorski, and Y. Mishin, Self-diffusion in γ -TiAl: an experimental study and atomistic calculations. *Intermetallics*, 1999. 7(3): p. 389-404.
113. E. Schwaighofer, H. Clemens, S. Mayer, J. Lindemann, J. Klose, W. Smarsly, and V. Güther, Microstructural design and mechanical properties of a cast and heat-treated intermetallic multi-phase γ -TiAl based alloy. *Intermetallics*, 2014. 44: p. 128-140.
114. V. Imayev, R. Imayev, T. Khismatullin, T. Oleneva, V. Güther, and H.J. Fecht, Microstructure and processing ability of β -solidifying TNM-based γ -TiAl alloys. *Materials Science Forum*, 2010. 638-642: p. 235-240.
115. K. Kothari, R. Radhakrishnan, and N.M. Wereley, Advances in gamma titanium aluminides and their manufacturing techniques. *Progress in Aerospace Sciences*, 2012. 55: p. 1-16.
116. S.A. Jones and M.J. Kaufman, Phase equilibria and transformations in intermediate titanium aluminum alloys. *Acta Metallurgica et Materialia*, 1993. 41(2): p. 387-398.
117. S. Dey, A. Hazotte, and E. Bouzy, Crystallography and phase transformation mechanisms in TiAl-based alloys – A synthesis. Vol. 17. 2009. 1052-1064.
118. M. Charpentier, A. Hazotte, and D. Daloz, Lamellar transformation in near- γ TiAl alloys-Quantitative analysis of kinetics and microstructure. *Materials Science and Engineering A*, 2008. 491(1-2): p. 321-330.
119. L.C. Zhang, T.T. Cheng, and M. Aindow, Nucleation of the lamellar decomposition in a Ti-44Al-4Nb-4Zr alloy. *Acta Materialia*, 2004. 52(1): p. 191-197.
120. Z.W. Huang, Inhomogeneous microstructure in highly alloyed cast TiAl-based alloys, caused by microsegregation. *Scripta Materialia*, 2005. 52(10): p. 1021-1025.
121. A. Huang, M.H. Loretto, D. Hu, K. Liu, and X. Wu, The role of oxygen content and cooling rate on transformations in TiAl-based alloys. *Intermetallics*, 2006. 14(7): p. 838-847.
122. Y.-W. Kim and D. M. Dimiduk Ph.D, Progress in the Understanding of Gamma Titanium Aluminides. Vol. 43. 1991.
123. S. Karthikeyan, G.B. Viswanathan, P.I. Gouma, V.K. Vasudevan, Y.W. Kim, and M.J. Mills, Mechanisms and effect of microstructure on creep of TiAl-based alloys. *Materials Science and Engineering A*, 2002. 329-331: p. 621-630.
124. J.Y. Jung and J.K. Park, Growth kinetics of discontinuous coarsening of lamellar structure in Ti-44at.%Al(-0.5at.%Cr) intermetallic compounds. *Acta Materialia*, 1998. 46(12): p. 4123-4130.

125. G.W. Qin, K. Oikawa, Z.M. Sun, S. Sumi, T. Ikeshoji, J.J. Wang, S.W. Guo, and S.M. Hao, Discontinuous coarsening of the lamellar structure of γ -TiAl-based intermetallic alloys and its control. *Metallurgical and Materials Transactions A*, 2001. 32(8): p. 1927-1938.
126. V.K. Vasudevan, M.A. Stucke, S.A. Court, and H.L. Fraser, The influence of second phase Ti₃Al on the deformation mechanisms in TiAl. *Philosophical Magazine Letters*, 1989. 59(6): p. 299-307.
127. J.M.K. Wiezorek, X.D. Zhang, A. Godfrey, D. Hu, M.H. Loretto, and H.L. Fraser, Deformation Behavior of α 2-Lamellae in Fully Lamellar Ti-48Al-2Mn-2Nb at Room Temperature. *Scripta Materialia*, 1998. 38(5): p. 811-817.
128. J.B. Singh, G. Molénat, M. Sundararaman, S. Banerjee, G. Saada, P. Veyssiére, and A. Couret, In situ strain investigation of slip transfer across α 2 lamellae at room temperature in lamellar TiAl alloy. *Philosophical Magazine Letters*, 2006. 86(1): p. 47-60.
129. L. Y. and L.M. H., Tensile properties and microstructure of Ti-48Al-2Nb and Ti-48Al-8Nb. *physica status solidi (a)*, 1995. 150(1): p. 271-280.
130. H. Mecking, C. Hartig, and U.F. Kocks, Deformation modes in γ -TiAl as derived from the single crystal yield surface. *Acta Materialia*, 1996. 44(4): p. 1309-1321.
131. M. Yoo, C. Fu, and J. Lee, Deformation Twinning in Ordered Intermetallic Compounds. *MRS Proceedings*, 1989. 133: p. 189.
132. M.H. Yoo, Twinning and mechanical behavior of titanium aluminides and other intermetallics. *Intermetallics*, 1998. 6(7): p. 597-602.
133. D.M.D. Yong Won Kim, Progress in the understanding of gamma titanium aluminides. *JOM*, 1991(August): p. 40-47.
134. M.J.M. G. Babu Viswanathan, Vijay K. Vasudevan, Microstructural effects on the tensile properties and deformation behavior of a Ti-48Al gamma titanium aluminide. *Metallurgical and Materials Transactions A*, 2003. 34A: p. 2113-2127.
135. Y.-W. Kim and D. M. Dimiduk Ph.D, Progress in the Understanding of Gamma Titanium Aluminides. *JOM*, 1991. 43(8): p. 40-47.
136. F. Appel and R. Wagner, Microstructure and deformation of two-phase γ -titanium aluminides. *Materials Science and Engineering: R: Reports*, 1998. 22(5): p. 187-268.
137. G.B. Viswanathan, M.J. Mills, and V.K. Vasudevan, Microstructural effects on the tensile properties and deformation behavior of a Ti-48Al gamma titanium aluminide. *Metallurgical and Materials Transactions A*, 2003. 34(10): p. 2113-2127.
138. R.T. Zheng, Y.G. Zhang, C.Q. Chen, and G.A. Cheng, The ambient temperature tensile behavior of duplex γ -TiAl-based alloys. *Materials Science and Engineering: A*, 2003. 362(1): p. 192-199.
139. Y.-W. Kim, Effects of microstructure on the deformation and fracture of [gamma]-TiAl alloys. *Materials Science and Engineering A*, 1995. 192-193(Part 2): p. 519-533.
140. D. Hu, H. Jiang, and X. Wu, Microstructure and tensile properties of cast Ti-44Al-4Nb-4Hf-0.1Si-0.1B alloy with refined lamellar microstructures. *Intermetallics*, 2009. 17(9): p. 744-748.
141. J.H. Moll and B.J. McTiernan, PM TiAl alloys: the sky's the limit. *Metal Powder Report*, 2000. 55(1): p. 18-22.

142. C.T. Liu, J.H. Schneibel, P.J. Maziasz, J.L. Wright, and D.S. Easton, Tensile properties and fracture toughness of TiAl alloys with controlled microstructures. *Intermetallics*, 1996. 4(6): p. 429-440.
143. S.C.D. W.J.Zhang, G.L.Chen, On the origin of superior high strength of Ti-45Al-10Nb alloys. *Intermetallics*, 2002(10): p. 403-406.
144. T.T. Cheng, M.R. Willis, and I.P. Jones, Effects of major alloying additions on the microstructure and mechanical properties of γ -TiAl. *Intermetallics*, 1999. 7(1): p. 89-99.
145. H. Inui, M.H. Oh, A. Nakamura, and M. Yamaguchi, Room-temperature tensile deformation of polysynthetically twinned (PST) crystals of TiAl. *Acta Metallurgica et Materialia*, 1992. 40(11): p. 3095-3104.
146. K. Chan, Understanding fracture toughness in gamma TiAl. *JOM*, 1992. 44.
147. K.S. Chan, The fatigue resistance of TiAl-based alloys. *JOM*, 1997. 49(7): p. 53-58.
148. Y.-W. Kim, Strength and ductility in TiAl alloys. *Intermetallics*, 1998. 6(7): p. 623-628.
149. K.S. Chan and Y.W. Kim, Effects of lamellae spacing and colony size on the fracture resistance of a fully-lamellar TiAl alloy. *Acta Metallurgica et Materialia*, 1995. 43(2): p. 439-451.
150. R. Gnanamoorthy, Y. Mutoh, and Y. Mizuhara, Fatigue crack growth behavior of equiaxed, duplex and lamellar microstructure γ -base titanium aluminides. *Intermetallics*, 1996. 4(7): p. 525-532.
151. K.T.V.R. J.P. Campbell, R.O. Ritchie, The effect of microstructure on fracture toughness and fatigue crack growth behavior in gamma-titanium aluminide based intermetallics. *Metallurgical and Materials Transactions A*, 1999. 30A(March): p. 563-577.
152. S.M.L. Sastry and H.A. Lipsitt, Fatigue deformation of TiAl base alloys. *Metallurgical Transactions A*, 1977. 8(2): p. 299.
153. J. Larsen, A. Rosenberger, B. Worth, K. Li, D. Maxwell, and W. Porter, Assuring reliability of gamma titanium aluminides in long-term service. *Minerals, Metals and Materials Society/AIME, Gamma Titanium Aluminides 1999(USA)*, 1999: p. 463-472.
154. G. Hénaff and A.L. Gloanec, Fatigue properties of TiAl alloys. Vol. 13. 2005. 543-558.
155. C. Choi, Y.T. Lee, and C.S. Lee, Microstructural influence on the fatigue crack propagation of a γ -TiAl alloy. *Scripta Materialia*, 1997. 36(7): p. 821-827.
156. J.P. Campbell, R.O. Ritchie, and K.T. Venkateswara Rao, The effect of microstructure on fracture toughness and fatigue crack growth behavior in γ -titanium aluminide based intermetallics. *Metallurgical and Materials Transactions A*, 1999. 30(3): p. 563-577.
157. Y.S. Park, S.W. Nam, S.K. Hwang, and N.J. Kim, The effect of the applied strain range on fatigue cracking in lamellar TiAl alloy. *Journal of Alloys and Compounds*, 2002. 335(1): p. 216-223.
158. M. Roth and H. Biermann, Thermo-mechanical fatigue behaviour of a modern γ -TiAl alloy. *International Journal of Fatigue*, 2008. 30(2): p. 352-356.
159. V. Bauer and H.J. Christ, Thermomechanical fatigue behaviour of a third generation γ -TiAl intermetallic alloy. *Intermetallics*, 2009. 17(5): p. 370-377.
160. M.H. Wayne E. Voice, Edward F.J. Shelton, Xinhua Wu, Gamma titanium aluminide, TNB. *Intermetallics*, 2005. 13: p. 959-964.

161. T. Klein, S. Niknafs, R. Dippenaar, H. Clemens, and S. Mayer, Grain Growth and β to α Transformation Behavior of a β -Solidifying TiAl Alloy. *Advanced Engineering Materials*, 2015. 17(6): p. 786-790.
162. D. Zhang, G. Dehm, and H. Clemens, Effect of heat-treatments and hot-isostatic pressing on phase transformation and microstructure in a β /B2 containing γ -TiAl based alloy. *Scripta Materialia*, 2000. 42(11): p. 1065-1070.
163. J. Morris, M. Ye, and C. Fu. Advanced Intermetallic-Based Alloys. in *MRS Symposia Proceedings*. 2007.
164. S. Mayer, Intermetallic titanium aluminides in aerospace applications – processing, microstructure and properties AU - Clemens, Helmut. *Materials at High Temperatures*, 2016. 33(4-5): p. 560-570.
165. F. Appel, J.D.H. Paul, M. Oehring, U. Fröbel, and U. Lorenz, Creep behavior of TiAl alloys with enhanced high-temperature capability. *Metallurgical and Materials Transactions A*, 2003. 34(10): p. 2149-2164.
166. D. Huber, H. Clemens, and M. Stockinger, Near Conventional Forging of an Advanced TiAl Alloy. *MRS Proceedings*, 2012. 1516: p. 23-28.
167. P. Erdely, P. Staron, E. Maawad, N. Schell, J. Klose, H. Clemens, and S. Mayer, Design and control of microstructure and texture by thermomechanical processing of a multi-phase TiAl alloy. *Materials & Design*, 2017. 131: p. 286-296.
168. S. Mayer, P. Erdely, F.D. Fischer, D. Holec, M. Kastenhuber, T. Klein, and H. Clemens, Intermetallic β -Solidifying γ -TiAl Based Alloys – From Fundamental Research to Application *Advanced Engineering Materials*, 2017. 19(4): p. 1600735.
169. M. Schloffer, F. Iqbal, H. Gabrisch, E. Schwaighofer, F.-P. Schimansky, S. Mayer, A. Stark, T. Lippmann, M. Göken, F. Pyczak, and H. Clemens, Microstructure development and hardness of a powder metallurgical multi phase γ -TiAl based alloy. *Intermetallics*, 2012. 22: p. 231-240.
170. H. Clemens and S. Mayer, Design, Processing, Microstructure, Properties, and Applications of Advanced Intermetallic TiAl Alloys. *Advanced Engineering Materials*, 2013. 15(4): p. 191-215.
171. J. Bryant, L. Christodoulou, and J.R. Maisano, Effect of TiB₂ additions on the colony size of near gamma titanium aluminides. *Scripta Metallurgica et Materialia*, 1990. 24: p. 33-38.
172. F. Appel, U. Lorenz, M. Oehring, U. Sparka, and R. Wagner, Thermally activated deformation mechanisms in micro-alloyed two-phase titanium amminide alloys. *Materials Science and Engineering: A*, 1997. 233(1): p. 1-14.
173. F. Appel, H. Clemens, and F.D. Fischer, Modeling concepts for intermetallic titanium aluminides. *Progress in Materials Science*, 2016. 81: p. 55-124.
174. W. Wallgram, T. Schmölzer, L. Cha, G. Das, V. Güther, and H. Clemens, Technology and mechanical properties of advanced γ -TiAl based alloys. *International Journal of Materials Research*, 2009. 100(8): p. 1021-1030.
175. H. Clemens, W. Wallgram, S. Kremmer, V. Güther, A. Otto, and A. Bartels, Design of Novel β -Solidifying TiAl Alloys with Adjustable β /B₂-Phase Fraction and Excellent Hot-Workability. *Advanced Engineering Materials*, 2008. 10(8): p. 707-713.

176. L. Cha, H. Clemens, and G. Dehm, Microstructure evolution and mechanical properties of an intermetallic Ti-43.5Al-4Nb-1Mo-0.1B alloy after ageing below the eutectoid temperature. *International Journal of Materials Research*, 2011. 102: p. 703-708.
177. E. Schwaighofer, M. Schloffer, T. Schmoelzer, S. Mayer, J. Lindemann, V. Guether, J. Klose, and H. Clemens, Influence of Heat Treatments on the Microstructure of a Multi-Phase Titanium Aluminide Alloy. *Practical Metallography*, 2012. 49(3): p. 124-137.
178. S. Bolz, M. Oehring, J. Lindemann, F. Pyczak, J. Paul, A. Stark, T. Lippmann, S. Schrüfer, D. Roth-Fagaraseanu, A. Schreyer, and S. Weiß, Microstructure and mechanical properties of a forged β -solidifying γ TiAl alloy in different heat treatment conditions. *Intermetallics*, 2015. 58: p. 71-83.
179. J. Sieniawski, W. Ziája, K. Kubiak, and M. Motyka, Microstructure and mechanical properties of high strength two-phase titanium alloys. *Titanium Alloys - Advances in Properties Control*, 2013. 69-80.
180. A. Denquin and S. Naka, Phase transformation mechanisms involved in two-phase TiAl-based alloys—II. Discontinuous coarsening and massive-type transformation. *Acta Materialia*, 1996. 44(1): p. 353-365.
181. N. Reinhard, *Intermetallics*. Von G. Sauthoff. VCH Verlagsgesellschaft, Weinheim. *Angewandte Chemie*, 1996. 108(6): p. 726-727.
182. S.R. Dey, E. Bouzy, and A. Hazotte, Features of feathery γ structure in a near- γ TiAl alloy. *Acta Materialia*, 2008. 56(9): p. 2051-2062.
183. M. Schloffer, B. Rashkova, T. Schöberl, E. Schwaighofer, Z. Zhang, H. Clemens, and S. Mayer, Evolution of the two phase in a β -stabilized multi-phase TiAl alloy and its effect on hardness. *Acta Materialia*, 2014. 64: p. 241-252.
184. R. Strychor, J.C. Williams, and W.A. Soffa, Phase transformations and modulated microstructures in Ti-Al-Nb alloys. *Metallurgical Transactions A*, 1988. 19(2): p. 225-234.
185. A. Godfrey, D. Hu, and M.H. Loretto, Properties and microstructure of TiAl-based alloys. *Materials Science and Engineering: A*, 1997. 239-240: p. 559-563.
186. M. Nowell, R. A. Witt, and B. W. True, EBSD Sample Preparation: Techniques, Tips, and Tricks. *Microscopy today*, Vol. July. 2005. P.44.
187. C.H. Tung, G. T. T. Sheng, and C.Y. Lu, TEM Sample Preparation Techniques. *ULSI Semiconductor Technology Atlas*, 2005: p. 90-139.
188. A. Suzuki, M. Takeyama, and T. Matsuo, Transmission electron microscopy on the phase equilibria among β , α and α_2 phases in Ti-Al binary system. *Intermetallics*, 2002. 10(9): p. 915-924.
189. M. Vijayalakshmi, S. Saroja, and R. Mythili, Convergent beam electron diffraction — A novel technique for materials characterisation at sub-microscopic levels. *Sadhana*, 2003. 28(3): p. 763-782.
190. H. Clemens, B. Boeck, W. Wallgram, T. Schmoelzer, L.M. Droessler, G.A. Zickler, H. Leitner, and A. Otto, Experimental Studies and Thermodynamic Simulations of Phase Transformations in Ti-(41-45)Al-4Nb-1Mo-0.1B Alloys. *MRS Proceedings*, 2008. 1128: p. 1128-U03-06.
191. G. E. Lloyd, Atomic Number and Crystallographic Contrast Images with the SEM: A Review of Backscattered Electron Techniques. Vol. 51. 1987. 3-19.

192. J. Yang, B. Cao, Y. Wu, Z. Gao, and R. Hu, Continuous cooling transformation (CCT) behavior of a high Nb-containing TiAl alloy. *Materialia*, 2019. 5: p. 100169.